

1. LEG 202 SUMMARY¹

Shipboard Scientific Party²

ABSTRACT

More than 7 km of long and relatively continuous sediment sequences from 11 sites in the southeast and equatorial Pacific were recovered during Leg 202 for the study of the Earth's climate and biogeochemical systems on scales that range from tectonic (millions of years) to orbital (tens to hundreds of thousands of years) and centennial to millennial (hundreds to thousands of years). These materials will be used to test a broad set of hypotheses on (1) the evolution of the South Pacific Ocean as it responds to and modulates the effects of major tectonic and climatic events, such as the opening of the Drake Passage, uplift of the Andes Mountains, closure of the Isthmus of Panama, and major expansion of polar ice sheets; (2) linkage between climate and biogeochemical changes in the high latitudes and the equatorial Pacific, related to rhythmic changes in Earth's orbit, and the relationship of such changes to well-known glacial events of the Northern Hemisphere; and (3) global and regional changes in climate, biota, and ocean chemistry on timescales of centuries to millennia to millions of years.

Three sites (1236, 1237, and 1241) targeted sequences with relatively low sedimentation rates of <30 m/m.y. to obtain long records of climate and oceanographic change representing the Neogene and, in some cases, the late Paleogene that are not subject to severe burial diagenesis. Two sites (1238 and 1239) targeted moderate sedimentation rates of 30–80 m/m.y. to assess orbital-scale climate and biogeochemistry oscillations at a resolution suitable for the tuning of timescales and examination of changing responses to orbital forcing during the late Neogene. Six sites (1232 through 1235, 1240, and 1242) recovered sediments that accumulated rapidly, at rates of 80–2000 m/m.y., near the equator and in the higher southern latitudes to assess equator-to-pole climate and biogeochemical linkages at centennial, millennial, and orbital timescales.

¹Examples of how to reference the whole or part of this volume.

²Shipboard Scientific Party addresses.

Drilling strategy and near real-time stratigraphic correlation played significant roles in the successful recovery of these sequences. Drilling multiple holes at each site and extensive use of overdrilling with the advanced piston corer (APC) provided long records with continuous recovery. Innovative use of rapid core logging allowed for real-time optimization of drilling strategies that maximized recovery and minimized redundant coring. Analysis of core expansion, as well as core-log integration and double extended core barrel (XCB) coring at some sites, facilitated the assembly of cores into a depth framework that will improve the quantitative analyses of sediment accumulation rates.

On Nazca Ridge, Site 1237 provides a continuous sediment sequence, recovered in overlapping APC cores, that spans >30 m.y. (modern to middle Oligocene). Exceptional preservation of the flora and fauna in this long, continuous record indicates that this site will provide a much-needed stratigraphic reference in the southeast Pacific. Abrupt changes in the presence of volcanic ash layers here document an increase in tectonic activity during the late Miocene, while nearly at the same time an increase in dust flux and biogenic components associated with productive upwelling systems, such as diatoms, are associated with late Cenozoic cooling that may be associated with uplift of the Andes. Site 1236 provides an equally good record from shallower water depths for the last 28 m.y. that, when paired with Site 1237, will document variations of deep, intermediate, and surface water masses in the subtropical South Pacific.

Near the equator, Sites 1238–1241 provide evidence for rhythmic oscillations of pelagic and hemipelagic sediments on the scale of Earth's orbital cycles, which will help to test hypotheses on tropical vs. polar origins of the well-known 100-k.y. climate cycle that characterizes the late Pleistocene, as well as the response of the equatorial Pacific to closure of the Isthmus of Panama over millions of years. Again, complete recovery of long and well-preserved sediment sequences will provide unprecedented resolution of biotic and environmental changes.

Century- to millennial-scale climate changes can be addressed with the records from rapidly accumulating (40–200 cm/k.y.) sediments recovered at Sites 1233–1235 from the central Chile margin. These sites will provide important data related to the southern westerlies and Antarctic Intermediate Water variability. A detailed record of paleomagnetic intensity and secular variability will link these records into a global chronological framework. At Site 1232, in the Chile Basin, a rapidly accumulating Pleistocene sequence documents terrigenous sediments eroded from the southern Andes and transported to the deep via turbidity currents. Near the equator, Sites 1240 and 1242 have moderately high sedimentation rates (~8–13 cm/k.y.), which will help to test linkages of millennial-scale climate changes between low and high latitudes.

Together, the array of sites recovered during Leg 202 provides a new view of Southern Hemisphere and tropical climate variability and biogeochemical systems across a broad range of spatial and temporal scales in a region of the ocean that has received relatively little study in the past.

INTRODUCTION

Leg Objectives

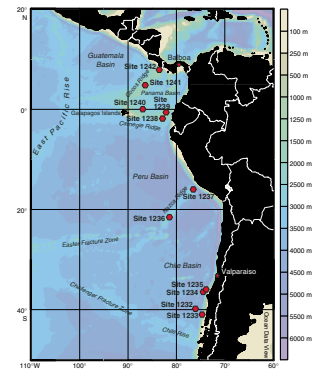
The primary scientific objectives of Leg 202 are to assess climate and oceanographic changes and to investigate the role of such changes in biogeochemical systems in the southeast Pacific. The drilling experiment contained three major elements that probe the Earth's system on three different but compatible scales: tectonic (millions of years), orbital (tens to hundreds of thousands of years), and centennial to millennial (hundreds to thousands of years). The sediment records obtained during Leg 202 will allow the testing of a broad set of hypotheses on these three timescales:

1. The evolution of the South Pacific as it responds to and modulates the effects of major tectonic and climatic events, such as the opening of the Drake Passage (creating a circumpolar current), uplift of the Andes Mountains (modifying wind systems), closure of the Isthmus of Panama (separating the Atlantic and Pacific Oceans), and major expansion of polar ice sheets in the high latitudes of the Southern and Northern Hemispheres at different times. Biogeochemical and climatic responses of this oceanic region can have far-reaching effects.
2. Linkages between climate and biogeochemical changes in the high southern latitudes and the equatorial Pacific, related to rhythmic changes in Earth's orbit, and the relationship of such changes to well-known glacial events of the Northern Hemisphere.
3. Global and regional changes in climate, biota, and ocean chemistry on timescales of centuries to millennia. Such features have been detected in selected locations around the world, but how these regions are linked, or whether the driving mechanisms originate in the high or low latitudes, remains unknown.

On each of these scales, we obtained sediment records suitable for the study of upper-ocean circulation, subsurface water masses, continental climate as reflected in eolian and fluvial inputs to the ocean, the role of biogeochemical fluxes in a changing system, and processes related to chemical diagenesis.

Our operational goals were to maximize the depth and latitude range of sites to sample different parts of the water column and upper-ocean currents from southern Chile to Central America (Fig. F1; Tables T1, T2). We targeted sites with a range of time spans and sedimentation rates appropriate to the scale of questions to be addressed (Fig. F2). Some sites (1236, 1237, and 1241) targeted lower sedimentation rates of <30 m/m.y. to obtain long sequences of climate and biogeochemical change in the Neogene and, in some cases, the late Paleogene that are not subject to severe burial diagenesis. Other sites (1238 and 1239) targeted moderate sedimentation rates of 30–80 m/m.y. to assess orbital-scale climate and biogeochemical oscillations at a resolution suitable for the tuning of timescales and examination of changing responses to orbital forcing during the late Neogene. Sediments that accumulated rapidly, at rates of 80–2000 m/m.y., were recovered from high southern latitudes (Sites 1232–1235) and near the equator (Sites 1240 and 1242) to assess equator-to-pole climate linkages at both millennial and orbital scales. At all Leg 202 sites, we recovered and verified continuous sedi-

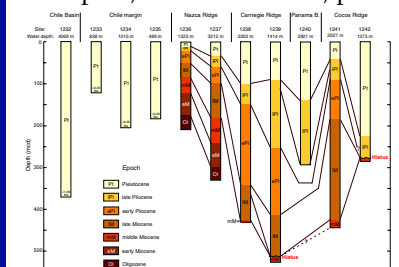
F1. Latitudinal range of Leg 202 drill sites, p. 73.



T1. Leg 202 coring summary by site, p. 142.

T2. Leg 202 coring summary by hole, p. 143.

F2. Cored intervals, ages, and water depths, Sites 1232–1242, p. 74.



mentary sections as long as possible by drilling multiple advanced piston corer (APC) holes and assembling composite sections in real time as drilling progressed.

Here, we summarize the shipboard results of Leg 202 and highlight the progress made at sea in each of the three experimental time frames and within a broad range of processes related to changing climate, ocean circulation, and biogeochemical systems.

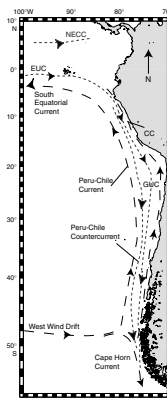
Modern Oceanographic Setting

Near-surface waters of the eastern Pacific exhibit enormous spatial variability, reflecting the influence of the Peru-Chile Current, the largest and most continuous eastern boundary current in the global oceans (Fig. F3). Off southern Chile, cool waters of the Antarctic Circumpolar Current impinge on the continent and form a transition zone between the southward-flowing Cape Horn Current and the northward-flowing Peru-Chile Current. Here, the westerly winds bring heavy rainfall to the coastal mountains and the Andes, resulting in high fluvial sediment fluxes to the ocean (Lamy et al., 1998, 2001). Cool and relatively low-salinity waters of the Peru-Chile Current are advected northward from Chile to offshore reaches of Peru (Strub et al., 1998) (Fig. F4A). Coastal upwelling driven by southerly winds along the coast of central Chile and Peru helps to maintain this cool flow and brings nutrients to the sea surface (Fig. F4B) to feed highly productive ecosystems (Toggweiler et al., 1991). These eastern boundary waters merge to feed the westward-flowing South Equatorial Current (Fig. F3), which is in turn maintained by equatorial upwelling and known as the equatorial cold tongue (Fig. F4A) (Wyrтки, 1981; Bryden and Brady, 1985). On scales ranging from decades to tens of thousands of years, changes in the rate of wind-driven advection of cool water off the eastern boundary contribute to major variations in the strength of the cold tongue, with recognizable effects extending to the western Pacific (Liu and Huang, 2000; Pisiias and Mix, 1997; Feldberg and Mix, 2002).

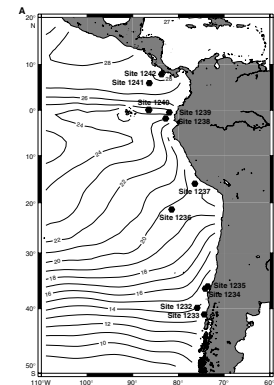
Near the equator east of the Galapagos Islands, the Equatorial Front separates the cold, salty waters of the Peru Current from warmer and fresher tropical waters of the Northern Hemisphere. The Panama Basin region is noted for its extreme warmth (often $>30^{\circ}\text{C}$), exceptionally low salinity (~ 32) (Fig. F4C), and a strong, shallow pycnocline (typically centered near 20–40 m depth). These features north of the equator and under the influence of the Intertropical Convergence Zone (ITCZ) reflect high rainfall relative to evaporation (Magaña et al., 1999), which stabilizes the water column and diminishes vertical mixing of heat and other properties. Some of the net freshwater flux to the Panama Basin originates in the Atlantic or Caribbean (Jousaumme et al., 1986), so low salinities here are also associated with the transport of freshwater from the Atlantic to Pacific Basins via the atmosphere. The dynamics of this transport are important because this relatively small transport of freshwater helps to maintain the relatively high salinity of the Atlantic Ocean—a key parameter in maintaining the global thermohaline “conveyor belt” circulation dominated by North Atlantic Deep Water (Zaucker et al., 1994; Rahmstorf, 1995).

Subsurface circulation of the southeast Pacific is illustrated in cross sections of dissolved oxygen, phosphate, and salinity in a meridional transect of the eastern Pacific (Fig. F5). At present, bottom water enters eastern basins of the South Pacific from the south, below 3 km depth (Lonsdale, 1976; Tsuchiya and Talley, 1998). After transiting north, ac-

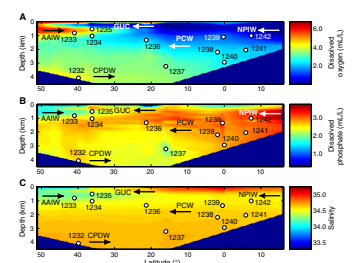
F3. Schematic of upper-ocean currents off the west coast of South America, p. 75.



F4. Modern annual average values of sea-surface temperature, sea-surface phosphate, and sea-surface salinity, p. 76.



F5. Cross section of subsurface water masses, characterized by dissolved oxygen, dissolved phosphate, and salinity, p. 79.



cumulating nutrients and losing oxygen in the North Pacific, much of the Pacific Deep Water is returned southward as Pacific Central Water (PCW) between 1 and 3 km. This middepth return flow and its importance to Pacific (and global) distributions of nutrients have been known for nearly 30 yr (Reid, 1973), but how this outflow from the North Pacific changes through time remains a mystery. Debate centers on the role of Southern Hemisphere winds in maintaining global thermohaline circulation (Toggweiler and Samuels, 1993). Much of the advective export of phosphate and nitrate from the North Pacific occurs in the southward return flow between 1 and 3 km depth in the eastern Pacific, where concentrations of these nutrients are highest (Wunsch et al., 1983). Thus, changes in this flow have the potential to change the budget of nutrients in the Pacific Ocean and the global ocean (Berger et al., 1997).

At intermediate water depths, water mass properties of the Pacific Ocean are highly asymmetric. Antarctic Intermediate Water (AAIW) is relatively depleted in phosphate and contains abundant oxygen because it forms in substantial contact with the atmosphere. This combination of processes results in relatively high $\delta^{13}\text{C}$ of dissolved inorganic carbon (DIC) in AAIW (Kroopnick, 1985). At present, AAIW is for the most part restricted to the Southern Hemisphere. North Pacific Intermediate Water (NPIW), which forms in the northwest Pacific with relatively little interaction with the atmosphere (Talley, 1993), contains abundant nutrients but is relatively low in oxygen and has low $\delta^{13}\text{C}$ in its DIC. An exceptionally steep property gradient between the southern- and northern-source water masses occurs, at present, near the equator. These intermediate water masses are found in the eastern Pacific, typically at depths of ~500–1000 m.

At a few hundred meters water depth, the classical oxygen minimum zone (OMZ) is driven by the degradation of organic matter sinking out of the euphotic zone and modified by ocean circulation (Wyrтки, 1962). North of the equator, the OMZ is extremely intense (<0.2 mL/L O_2 between 200 and 900 m depth). The broad depth range of this OMZ reflects the presence of NPIW, which is depleted of oxygen because it exchanges relatively little with the atmosphere in its northern source areas, as well as the exceptionally high export of organic matter from productive upwelling systems along the eastern boundary of the North Pacific (Tsuchiya and Talley, 1998). A relatively shallow and abrupt pycnocline below low-salinity surface waters helps to maintain the shallow oxygen minimum north of the equator.

Near the equator, the OMZ is shallower (300–400 m depth) and oxygen values return to typical deep Pacific values of 1 mL/L by ~700 m depth (Fig. F5A). Farther south, off central Chile, a “double” OMZ reflects southward advection of oxygen-depleted waters from the Peru margin at ~200–500 m depth in the poleward-flowing Gunther Undercurrent (GUC) above the relatively oxygen-rich AAIW near ~500–1000 m. PCW of Northern Hemisphere origin comprises the deeper oxygen minimum from ~1500–2000 m depth. Oxygen is slightly higher and nutrient contents are lower (Fig. F5B) in the deep basin because of the incursion of Circumpolar Deep Water (CPDW) below ~3000 m.

The large pools of oxygen-poor water at intermediate depths in the modern eastern Pacific (Tsuchiya and Talley, 1998), both north and south of the equator, are major sites of denitrification and represent collectively the largest sink for nitrogen in the world’s oceans. By acting as governors of the average oceanic nitrate concentration, these regions (along with the Arabian Sea) have the potential to act as climate rheo-

stats by altering the fertility and thus the rate of photosynthetic CO₂ fixation in the ocean. Indeed, temporal decreases and increases in export production off northwestern Mexico, off Peru, and in the Arabian Sea do appear to have modulated the oxygen content in upper intermediate-depth waters and the consequent intensity of denitrification during the late Quaternary (e.g., Codispoti and Christensen, 1985; Ganeshram et al., 1995). Whether or not such variations occurred on a broad scale over long time periods remains an open question. For example, it is unclear whether biological production of the eastern tropical Pacific was higher (Lyle et al., 1988) or lower (Loubere, 2000) than at present during the last ice age.

The equatorial region is highly productive but is significant in the world's oceans for not consuming all nutrients at the sea surface (Fig. F4B). High phosphate concentrations in tropical surface waters here (Levitus et al., 1993) are now thought to reflect biological limitations associated with iron or other so-called micronutrients. This is significant because any change in the net nutrient utilization would also cause a change in the net flux of CO₂ and other biologically mediated gases from the sea surface (Mix, 1989; Jasper et al., 1994; Farrell et al., 1995a).

Tectonic Setting

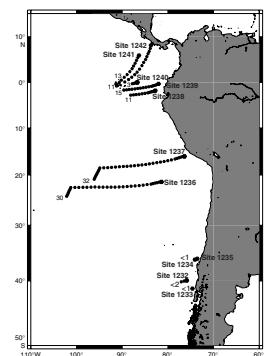
Most of the sites drilled during Leg 202 examine sediments overlying oceanic crust formed either at oceanic spreading centers (Sites 1232 and 1240) or on bathymetric ridges formed by hotspot volcanism (Sites 1236–1239, 1241, and 1242). Three sites are located on the continental margin of Chile (Sites 1233–1235). These sites may have been influenced by local tectonic effects of subduction at the Peru-Chile Trench, but the time spans covered by those records (a few hundred thousand years at most) are short enough that tectonic movements at these margin sites can be ignored.

The sites off the margin cover longer time spans, and all are subject to plate tectonic movements. These sites can be “backtracked” to estimate their paleogeographic position relative to South America (Fig. F6), using poles of rotation for the Nazca and Cocos plates (Pisias et al., 1995). The sites may also be backtracked in water depth, assuming they have subsided in response to long-term cooling of the underlying crust (Parsons and Sclater, 1977). Such estimates work reasonably well for normal oceanic crust but are more difficult to apply to oceanic ridges and plateaus that may have experienced different thermal, tectonic, and volcanic histories than the regional oceanic spreading centers (Detrick and Crough, 1978).

Age constraints on the volcanic crust are based mostly on seafloor magnetic lineations (Hey et al., 1977; Lonsdale and Klitgord, 1978; Heron et al., 1981; Cande and Leslie, 1986), along with basal sediment ages developed by shipboard biostratigraphy. For quantitative age estimates, we use the magnetic anomaly age model of Cande and Kent (1995), which is in reasonable agreement with orbitally tuned sedimentary age models of the last 5 m.y. and with radiometric dates at older intervals.

The absolute poles for South America were added to the absolute poles for each respective crustal plate to calculate the paleoposition of each drill site relative to South America. Movement of South America in the absolute framework is very small compared to the oceanic plate motions, so these backtrack paths approximate real geography. Sites on the

F6. Plate tectonic backtrack of Leg 202 drill sites, p. 80.



Nazca and Cocos plates' backtrack paths for 0 to 19 Ma are based on the analysis of Piasias et al. (1995). Absolute poles of rotation for the Cocos plate (Sites 1241 and 1242) were calculated using the pole of relative rotation between the Cocos and Pacific plates (36.823°N, 108.629°W; $\Omega = 2.09^\circ/\text{m.y.}$ [DeMets et al., 1990]), and absolute poles for the Pacific plate (0- to 5-Ma pole, 61.6°N, 82.5°W, $\Omega = 0.97^\circ/\text{m.y.}$; for the 5- to 20-Ma pole, 70.3°N, 74.4°W, $\Omega = 0.73^\circ/\text{m.y.}$ [Cox and Engebretson, 1985]). Absolute poles for the Nazca plate (Sites 1232 and 1236–1240) were calculated using relative motions between the Pacific and Nazca plates (pole = 55.58°N, 90.10°W; $\Omega = 1.42^\circ/\text{m.y.}$) and the absolute Pacific poles noted above.

Major tectonic events undoubtedly influenced the environments of the southeast Pacific. Evaluating these effects is a major element of the Leg 202 experiment. The Drake Passage likely began to open ~29 Ma, and a deepwater connection between ocean basins was present by ~23–24 Ma (Barker and Burrell, 1977). Numerical models predict a decrease of the Peru-Chile surface current and a distinct decrease in Antarctic deep- and bottom water export to the north as water masses are entrained into a growing circumpolar circulation (Mikolajewicz et al., 1993).

Uplift of the Andes would have caused significant changes in atmospheric circulation and wind-driven oceanic surface circulation. Because it is difficult to separate tectonic and climatic influences on sedimentation, regional elements of this uplift history are controversial. Nevertheless, sedimentation in the tropical Atlantic, as well as hiatuses and paleobotanical evidence on land, suggest major Andean uplift events in the last 10 m.y. (Curry, Shackleton, Richter, et al., 1995; Gregory-Wodzicki, 2000; Harris and Mix, 2002).

Neogene tectonic closure of the Central American Isthmus from 13.0 to 2.7 Ma resulted from the subduction of the Pacific, Cocos, and Nazca plates, and hotspot volcanics of the Cocos and Carnegie Ridges beneath the North and South American plates and later the Caribbean plate (Duque-Caro, 1990; Dengo, 1985; Collins et al., 1996). The final closure has always been an attractive candidate for the ultimate cause of the Pliocene intensification of Northern Hemisphere glaciation since ~3.1 Ma, but the details of the isthmus formation and the climatic mechanisms that govern the response to this remain uncertain.

OPERATIONAL INNOVATIONS

As with previous paleoceanographic sampling missions, the main operational goal of Leg 202 was to recover complete stratigraphic sections at the preselected sites with as little coring disturbance as possible and as efficiently as possible. Preferred use of the APC coring system over rotary systems, coring of multiple holes at a site to ensure a complete record, and shipboard construction of stratigraphic composite sections and sampling splices became standard strategies over the last several ODP drilling legs that addressed paleoceanographic objectives. During Leg 202, we employed techniques and concepts to further optimize these strategies in order to obtain longer APC sections, to correlate data from multiple holes faster for real-time control on coring offsets and thus to minimize redundant coring, and to correlate and integrate data from cores and downhole logs.

Maximizing APC Penetration: Drilling Over

Two coring systems were used during Leg 202: the APC and the XCB. The APC, a “cookie-cutter” type system that cuts cores with minimal coring disturbance, was always the preferred coring system. The drill pipe is pressurized to shear one or two pins that hold the inner barrel attached to the outer barrel. The inner barrel strikes out and cuts the core. The driller can detect a successful cut, or “full stroke,” on the pressure gauge on the rig floor.

When “APC refusal” occurs in a hole before the target depth is reached, the XCB is generally used to advance the hole. The XCB is a rotary system with a small cutting shoe extending below the large rotary bit. The smaller bit can cut a semi-indurated core with less torque and fluid circulation than the main bit and thus optimizes recovery. XCB coring disturbs the cores, as the torque of the drill rotation shears and breaks the core into segments. In this process, voids fill with drill slurry and short sections of core appear as “biscuits” that range from a few centimeters to decimeters in length. The degree of XCB disturbance depends strongly on the lithology. Disturbance is most severe in partly lithified sediments that are not stiff enough to maintain their integrity under a rotating bit. Given this disturbance, an operational goal during Leg 202 was to continue APC coring as long as possible before switching to the XCB.

APC refusal is conventionally defined in two ways: (1) a complete stroke (as determined from the pump pressure reading) is not achieved by the piston because the formation is too hard and (2) excess force (>60 klb) is required to pull the core barrel out of the formation because the sediment is too cohesive or “sticky” (formation pressure develops a tight grip on the core barrel). In cases where full stroke can be achieved but excessive force cannot retrieve the barrel, the core barrel can be “drilled over” (i.e., after the inner core barrel is successfully shot into the formation, the rotary bit is advanced to total depth to free the APC barrel).

During Leg 202 we generally accepted only the first APC refusal criterion (incomplete stroke) for the transition to XCB operations. Drilling over stuck APC barrels allowed us to advance many holes significantly deeper with the APC than if the second criterion had been applied (Table T3). A total of 101 core barrels were drilled over during Leg 202, which is more than during any previous leg. These drill-over operations consumed time (in some cases >1 hr per core in addition to normal operations), and in a few cases resulted in damaged core barrels. Nevertheless, we found that these investments of time and equipment paid substantial dividends in terms of enhanced APC penetration. At the Leg 202 sites dominated by carbonate-rich lithologies and characterized by low to moderate sedimentation rates (Sites 1237–1241), overdrilling increased the APC penetration by 12% to 126% (average = 77%) in those 10 holes that were cored to APC refusal. At two sites, APC penetration was pushed to >300 meters below seafloor (mbsf), and at another two sites to >200 mbsf. In addition, by reserving XCB coring for sediments that were substantially lithified, we maximized the quality of recovery within those intervals, in most cases resulting in high-quality cores suitable for developing composite depth sections through most of the sedimentary sections at each site.

T3. Summary of APC drilling over, p. 144.

Stratigraphic Correlation

Guiding Coring Offsets and Use of a “Fast Track”

During Leg 202, as during several previous Ocean Drilling Program (ODP) legs with paleoceanographic emphasis, multiple APC holes were drilled at each site to ensure recovery of a complete stratigraphic sequence, despite coring gaps that are present in any one hole. A meters composite depth (mcd) scale for each site was constructed through inter-hole correlation using closely spaced core logging measurements. The mcd scale accommodates core expansion and coring gaps and can be used to define a shipboard splice, a stratigraphically continuous sediment sequence consisting of undisturbed segments from different holes.

The assembly of composite depth sections with an mcd scale, in principle, can be done with two holes, but in most cases three or more holes are needed because the position of coring gaps is not uniform (and is often unpredictable) as drilling advances downhole. Variations in bit depth may be caused by tides, ship heave (which is not compensated for with APC coring), and limited precision in defining the depth of the drill bit based on the visual observation of pipe advances. To optimize the depth offsets between holes, it is desirable to control bit position on a core-by-core basis. This requires knowing the position of a core relative to cores in the previously drilled hole(s) in near real time such that the relative offset of the subsequent core can be estimated and communicated to the driller. Rapid core logging that keeps pace with drilling is an essential requirement of this strategy.

To provide information on core depths for real-time adjustments in bit depth, an automated “fast track” magnetic susceptibility core logger was provided by Oregon State University (OSU) for Leg 202. This track was installed in the *JOIDES Resolution* core laboratory near the catwalk so that whole-round cores could be analyzed as soon as they entered the laboratory. The OSU Fast Track employs a Bartington MS2 susceptibility meter that was zeroed before each section scan. The usual sampling interval was 5 cm, although intervals were adjusted as needed to keep pace with drilling. Where possible, a 1-s integration time was used. Using this setting, full cores (seven sections) could be analyzed in ~15 min. However, several of the Leg 202 sites had little terrigenous material and low magnetic susceptibility. At these sites, a 10-s integration time was needed and this increased the logging time to ~40 min per core. Even with this slow setting, the OSU Fast Track processed cores significantly faster than the ODP multisensor track (MST), which was configured to maximize natural gamma ray counting, and was fast enough to keep up with drilling under most circumstances.

The availability of the Fast Track magnetic susceptibility data, in many cases, allowed us to verify complete recovery of the APC-cored interval with two holes or with a third hole that was spot cored to cover specific gaps. By minimizing redundant drilling, the Fast Track strategy effectively preserved time for deeper penetration with the APC by overdrilling and for occupying three alternate sites that added greatly to the overall scientific results of Leg 202. Use of the OSU Fast Track for most composite section development and drilling offset decisions had an additional scientific benefit, as it allowed the ODP MST to be run more slowly to optimize data quality. This strategy allowed us to increase the use of the slower MST sensors, such as the natural gamma counters, which provided a useful data set for core-log integration. Effectiveness

of stratigraphic correlation and core logging would have been seriously compromised without the extra core logging track on Leg 202. Based on our experience, we recommend that future operations requiring rapid verification of complete recovery employ a similar Fast Track strategy.

Corrected Meters Composite Depth and Mass Accumulation Rates

Composite depth scales typically are expanded by 10%–20% when compared to drilled intervals because of the expansion of cores upon recovery as a result of elastic rebound, expansion of volatile hydrocarbons (mostly biogenic methane), and mechanical stretching during the coring process. In cohesive, fine-grained sediment, this expansion is assumed to occur without significant uptake or loss of interstitial water per unit mass of dry sediment. If this assumption is correct, sediment densities determined by wet and dry mass and volume measurements are most compatible with those measured in situ. Calculations of mass accumulation rate (MAR) require information on both sediment density and linear sedimentation rate (LSR). LSR is typically based on the mcd scale, which suffers from core expansion. A corrected LSR can be calculated either by using corrected meters composite depth (cmcd) for the age-depth series or by correcting the mcd-based LSRs directly with the appropriate mcd growth rates for each depth interval. To facilitate the calculation of MAR, we established the cmcd scale for each site during Leg 202, adjusting the mcd scale for empirically observed expansion. A cmcd datum is produced by dividing the mcd value by the average expansion of the mcd scale relative to the mbsf scale over a sufficiently long interval so that random variations in drill pipe advance are negligible. The cmcd scale provides a complete stratigraphic sequence that is the same length as the total depth cored. The cmcd scale is a close approximation of actual drilling depths, and unless further corrected by logging data, the cmcd scale should be used when calculating LSR or MAR.

Equivalent Logging Depth

At three sites (1238, 1239, and 1241), logging operations produced data sets that were of sufficient quality to allow for core-log integration. Core-log integration produces yet another depth scale, equivalent logging depth (eld). This depth scale has the advantage that it corrects for stretching and squeezing within cores. The disadvantage is that it is rarely a complete data set for correlation of the entire hole. The eld scale typically begins at ~100 mbsf, where the drill pipe usually is positioned during logging operations. If logging data are available and of sufficient quality, the eld is the best estimate of in situ depth and is ideal for calculating MAR.

To determine eld, logging and whole-core MST data were imported into the Sagan software package (version 1.2) and culled as necessary to remove extraneous errors associated with voids in cores or with poor sensor contact with the borehole. Because core logging data generally have a higher resolution than downhole logging data, it is necessary to smooth the core logs before comparing them with downhole logs. Sagan allows the correlation of individual cores within different holes with the data series recovered from logging. We found that Formation MicroScanner (FMS) data integrated around the borehole using 64 buttons was particularly useful because its high depth resolution compared

well with that of core gamma ray attenuation (GRA) density measurements (Fig. F7). We also found good agreement in some intervals between natural gamma data measured in cores and in the borehole with different tools (Fig. F8) and between GRA bulk densities measured both in cores and in the borehole (Fig. F9).

Tidal Effects on Coring Offsets

Because we had near real-time Fast Track magnetic susceptibility data to assess coring depth offsets between holes, we attempted to make adjustments in drilling depth as coring progressed. As we scrutinized the data to make these decisions, we noticed that the differential offsets appeared to vary systematically through a daily cycle. We hypothesized that these variations were due to variations in water depth resulting from the tides.

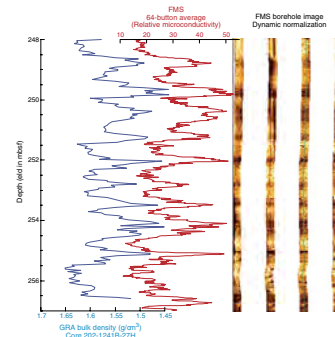
Site 1240 illustrates variations in drilling depths well because we APC cored the entire recovered section and were able to construct a splice that spans a 2.5-day-long time interval of operations. We obtained a deep-ocean tide prediction for the drill site courtesy of Dr. Gary Egbert at OSU. A comparison of the two (Fig. F10) shows that local tides and differential drilling offsets are related to each other and share a 12-hr period with a similar magnitude (~2 m) over the period of operations. As coring proceeds at a site, tides can either add to or subtract from the depth offsets, depending on the time at which two holes are begun relative to the tidal cycle (i.e., on a rising or falling tide). We imagine that in the future tidal predictions could be used to adjust drill pipe advances as needed to maintain coring overlap in multiple holes. Effective implementation of this strategy, along with the provision for heave compensation during APC coring, would likely provide for complete recovery in two holes at a site, rather than the three to five holes per site that are typically needed in current operations.

Use of Color Reflectance Spectroscopy in Lithostratigraphy

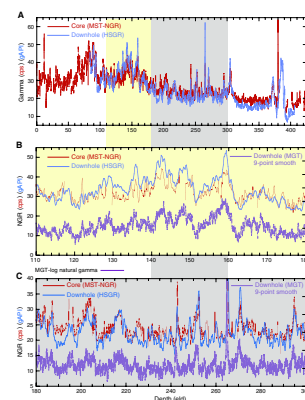
Physical properties are the expression of the lithologic, textural, and structural variations in sediments, and, in many cases, they can be used to empirically infer specific sediment components over long intervals at much higher resolution than can be practically measured using traditional laboratory-based direct measurements on discrete samples. During Leg 202, reflectance spectroscopy data were calibrated with direct geochemical measurements to provide rapid optical estimates of carbonate and total organic carbon (TOC) concentrations in sediments as well as relative abundance of oxides, such as hematite and goethite, and organic pigments known as chlorins.

The reflectance spectroscopy data included 31 reflectance values over the visual spectrum (400 to 700 nm) averaged over 10-nm intervals. First derivatives of these data with respect to wavelength are commonly used to emphasize variations in spectral shape. Empirical equations were calibrated based on least-squares multiple regressions fit to discrete chemical data. Regression terms were selected with a stepwise procedure and were retained in the equations only if they exceeded the 95% significance level. The advantages of using this technique in real-time during the cruise were to quickly provide us with (1) a better understanding of sediment composition and physical properties and (2) a detection of scales of variability in calcium carbonate and TOC that

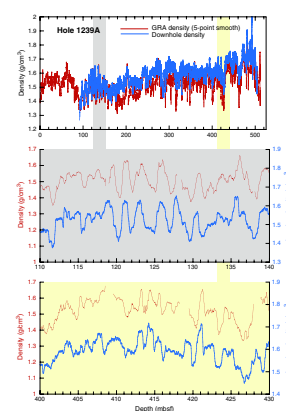
F7. Core-log integration, p. 81.



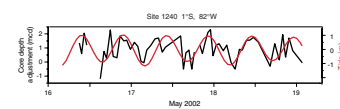
F8. Comparison of natural gamma radiation data from core logging and downhole logging, Site 1238, p. 82.



F9. Comparison of GRA bulk density data from core logging and downhole logging density, p. 83.



F10. Depth offsets of sequential cores vs. time of coring operation, Site 1240, p. 84.



could not be attained rapidly at sea based on direct measurements with low depth resolution. Variations detected by the detailed optical data set can be targeted rapidly for manual sampling to make sure that extreme events are verified with precise chemical techniques. One example of the successful use of reflectance spectroscopy estimates of lithology during Leg 202 is the detection at Site 1237 of rhythmic variations in estimated TOC at scales of 5 to 10 m (Fig. F11). Based on preliminary shipboard age models, such variations may be associated with known ~400-k.y. cycles of Earth's orbit and suggest a climatic and biogeochemical response to this external forcing.

Digital Imaging of Cores

A new digital imaging system (DIS) implemented by ODP in 2002 and installed on the *JOIDES Resolution* during Leg 198 was used routinely for the first time during Leg 202. Essentially, all cores were imaged with this tool. As would be expected with a new, custom-made measurement system, we encountered some problems and came up with some recommendations for the operation of the system and use of the data as well as some recommendations for future improvements that would maximize the benefit of such measurements at sea. Although we found the digital images extremely useful for purposes of basic visual description (especially for postdescription review when the cores were not easily available for viewing), we also found that the digital image calibration was not sufficiently stable or reliable when using the digital data as a measure of quantitative brightness or color.

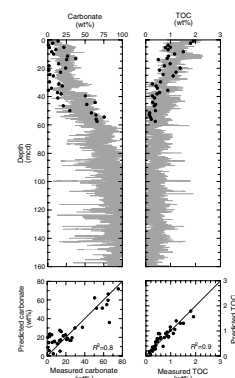
We found systematic millimeter- and centimeter-scale stripes in the digital images that result from the system's attempt to adjust image exposure based on calibration pixels at the site of the digital array. These pixels were inadvertently aligned with millimeter and centimeter marks on reference rulers along the sides of each core section. This problem can be mitigated by careful alignment of the camera or by using low-contrast markings on reference rulers that will not trigger automatic adjustments in camera calibration.

Significant variations in the brightness of digital images from the top to the bottom of core sections occurred because of variations in ambient lighting in the laboratory. Such ambient lighting effects may be corrected in one of three ways: (1) by enclosing the imaging system in a sealed box that shades the core sections from ambient light, (2) by increasing the brightness of the lamps that illuminate the core sections so that ambient light is overpowered by a constant source, or (3) by modifying the system to move core sections under a fixed camera so that ambient light is effectively constant rather than having the system move the camera over fixed core sections as the system is now designed.

By analyzing standard materials, we also found that small (millimeter scale) variations in camera-to-core distance (which inevitably result from irregularities in cut core surfaces) result in variations in the brightness of core images. Such an effect could be mitigated by increasing the distance between the light source and the camera system relative to the core surfaces so that small variations in the core surface are negligible relative to the total system geometry. Increases in the core-to-lamp distance, however, work against the goal of increasing light intensity to overpower ambient light, and this effect must also be considered.

Significant temporal drift in the calibration of the digital camera system relative to white standards dictates frequent recalibration of the camera system. Ideally, such calibrations should be done automatically

F11. Reflectance spectroscopy-derived CaCO_3 and TOC contents compared to directly measured quantities, Site 1237, p. 85.



between each run. Calibration standards could include multiple gray levels that would compensate for nonlinear responses of the camera system across its full range of brightness.

Finally, we found it awkward and error-prone to set the camera's aperture (and the corresponding setting in the software) manually in sediment sequences that vary significantly in their reflectance or geometry. Although manual settings are fine for occasional measurements, a greater degree of automation in camera settings and calibrations would be beneficial for ODP operations in which the camera is used continuously for long periods of time by a variety of operators who are working under stressful conditions at sea.

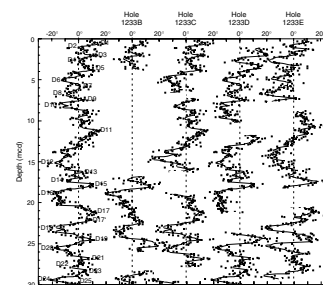
Use of a Nonmagnetic Core Barrel

Drilling-induced magnetic overprints are ubiquitous in ODP paleomagnetism and have been known to exist since the beginning of the program. In some cases, these overprints are easily dealt with. In other cases, they may completely compromise the paleomagnetic objectives of a leg (e.g., Leg 154). Observations and experiments made during Leg 202 demonstrate that substantial magnetic overprints superimposed on the sediment natural remanent magnetization (NRM) as a result of the use of steel core barrels and the time the sediment spends within it. The use of the APC temperature (APCT) tool, which extends the duration of the coring process by 15 min for each core, induced a substantially larger overprint as compared to cores recovered without the use of this tool. It is thought, based on laboratory experiments, that this large overprint is not APCT specific, but rather due to the extra time the sediment rests in the core barrel (see [Lund et al.](#), this volume). Alternating the use of a nonmagnetic core barrel (e.g., on Cores 2, 4, 6, etc.) with a normal magnetized (steel) core barrel (e.g., on Cores 1, 3, 5, 7, etc.) within a hole, at sites throughout the leg, demonstrated a reduced overprint with the nonmagnetic core barrel. The improvement of the magnetic record due to the use of the nonmagnetic core barrel was most dramatic in relatively coarse siliciclastic sediments from the continental margin of Chile. The effect, though less dramatic, was still noticeable in fine-grained, open-ocean pelagic carbonate sediments and, in some cases, resulted in the recognition of polarity chrons that were obscured when cores were recovered by the steel core barrel.

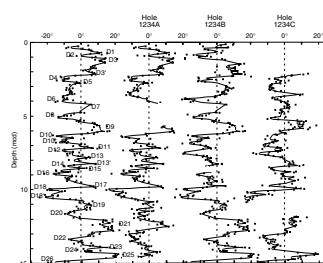
HOLOCENE–LATE PLEISTOCENE GEOMAGNETIC FIELD BEHAVIOR (SITES 1233–1235)

Paleomagnetic measurements made during Leg 202 on cores from the Chile margin Sites 1233, 1234, and 1235 document that these sites may provide the highest-resolution long-term record of paleomagnetic secular variation (PSV) and excursions field behavior ever recovered. They also will provide some of the very first records that document high-resolution paleomagnetic field behavior in the Southern Hemisphere. Shipboard measurements indicate that reproducible records of directional PSV have been recovered from four independent holes at Site 1233 (Fig. F12) over the entire 137 mcd, from the uppermost 30 mcd of three independent holes at Site 1234 (Fig. F13), and from the uppermost 15 mcd of three independent holes at Site 1235. The prospect is good that even better final PSV records from these intervals ex-

F12. PSV records, Site 1233, p. 86.



F13. PSV records, Site 1234, p. 87.



tending to greater depths at Sites 1234 and 1235 will be developed with shore-based paleomagnetic studies.

Shipboard paleomagnetic measurements also clearly suggest that magnetic field paleointensity variations can be determined from these cores. Initial relative paleointensity estimates determined by normalizing the sediment NRM to magnetic susceptibility have been developed for all of Site 1233. The Site 1233 shipboard relative paleointensity and directional PSV records (Fig. F14) are thought to have the potential to provide the longest and highest-resolution “total-vector” PSV record ever observed. A close-up of the total-vector PSV record (Fig. F15) from Site 1233 shows that remarkable cyclicity, on the scale of ~3 m (equivalent to ~2 k.y. based on preliminary shipboard age models), exists in both the directional PSV and paleointensity records for more than 30 k.y. of the late Pleistocene. This total-vector PSV record, when finally developed, should provide important new insights into the working of the Earth’s outer-core dynamo, which generates the Earth’s magnetic field.

The directional PSV data from Sites 1233 and 1234 also document at least one and possibly two magnetic field excursions. The younger of these excursions probably occurred ~41 k.y. ago, based on an initial timescale (Fig. F14) determined by correlation of the paleointensity data with other sites around the world, and is almost certainly the Laschamp Excursion (Fig. F16). The PSV record of the Laschamp Excursion at Site 1233 is ~2 m in width (documented in three separate holes) and probably spans a time interval of <1500 yr. That makes this one among the highest-resolution paleomagnetic records of an excursion ever recovered. Moreover, a similar excursion is also recorded at Site 1234, more than 400 km away, and the patterns of more frequent directional PSV are comparable between the two sites (Fig. F16). Further shore-based paleomagnetic studies of these Laschamp Excursion records should provide valuable new insight into the workings of the Earth’s magnetic field during times of anomalous behavior that may be related to the geomagnetic field reversal process, as well as magnetostratigraphic information in unprecedented detail that will likely provide reference stratigraphic sections for the region and for the world.

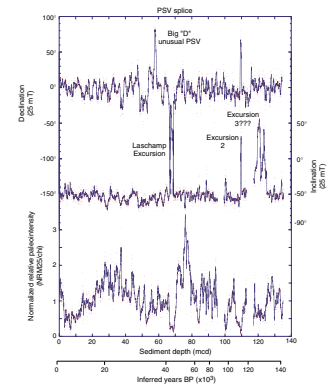
CENOZOIC BIOSTRATIGRAPHIC AND MAGNETOSTRATIGRAPHIC REFERENCE SECTIONS (SITES 1237 AND 1241)

Shipboard data suggest that two of the sites with long stratigraphic records, Sites 1237 and 1241, have great potential to provide not only a well-constrained chronological framework for studying the long-term tectonic, climatic, and biogeochemical history of the region, but also excellent stratigraphic reference sections in the Pacific Ocean.

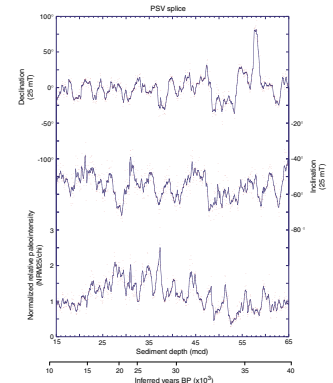
Site 1237

The 360.65-mcd-thick pelagic sequence recovered at Site 1237 spans the last ~31 m.y. (the Holocene through the early Oligocene) without any detectable stratigraphic breaks. The composite depth section based on the four APC-drilled holes at the site documents complete recovery for the entire sequence, which is dominated by biogenic components

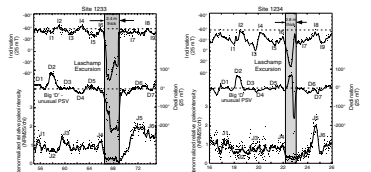
F14. Variations in paleomagnetic declination, inclination, and paleointensity at Site 1233, 0–136 mcd, p. 88.



F15. Variations in paleomagnetic declination, inclination, and paleointensity at 1233, 15–65 mcd, p. 89.



F16. Comparison of paleomagnetic inclination, declination, and paleointensity, Sites 1233 and 1234, p. 90.



with a minor terrigenous (probably eolian) component that decreases downhole.

Calcareous nannofossils and foraminifers are generally abundant or common and well to moderately well preserved throughout the sequence. Diatoms are abundant and well preserved down to ~60 mcd, but abundance decreases and preservation deteriorates below ~69 mcd, and diatoms are absent below ~174 mcd. Most of the standard nannofossil and planktonic foraminiferal zonal markers, as well as some non-standard nannofossil markers, can be used to establish a relatively detailed biostratigraphy. Diatoms provide additional biostratigraphic control down to ~137 mcd. All fossil groups examined during the cruise provide relatively consistent age assignments (Fig. F17). Shore-based biostratigraphic studies will refine biostratigraphic datums and identify additional events.

The paleomagnetic stratigraphy at Site 1237 includes the clear definition of all chrons and subchrons for the 0- to 5- and 7- to 13-Ma intervals. Some fine-scale features and short polarity subchrons are also apparent within the Matuyama Chron. Although the assignments of chrons and subchrons in the intervals from 5 to 7 Ma and from 13 to 31 Ma are not certain yet, shore-based paleomagnetic studies are expected to provide a detailed magnetostratigraphy for most or all of the sequence.

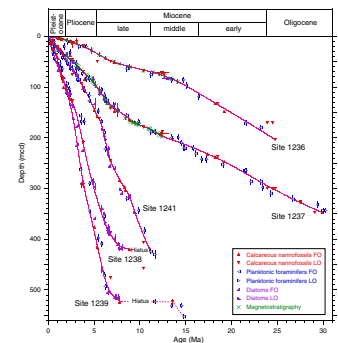
Based on the preliminary biostratigraphic and magnetostratigraphic age model, the sedimentation rate generally increases from ~1 cm/k.y. prior to ~7 Ma to ~2 cm/k.y. after ~7 Ma (Fig. F18A). Despite the relatively low sedimentation rates, the opportunities for an astronomical calibration of the Neogene timescale are good, as core logging data are characterized by high-frequency fluctuations in lithology. First frequency spectra of GRA density fluctuations clearly identified pronounced cycles at orbital periods of precession and obliquity for the time interval from 3 to 4 Ma (Fig. F19), although bioturbation may have smoothed the primary signal at low sedimentation rates ranging from 1.5 to 2 cm/k.y.

Site 1237 should provide not only a well-constrained chronological framework for studying the long-term history of Andean uplift and continental climate, as well as the evolution of upwelling, sea-surface, and intermediate-water properties in the southeast Pacific and the sequence of biotic events, but will also provide an outstanding stratigraphic reference section for improving integrated biostratigraphic, magnetostratigraphic, and cyclostratigraphic timescales.

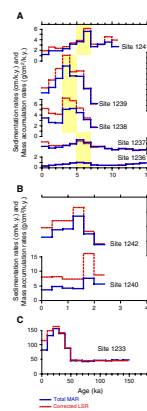
Site 1241

This site on Cocos Ridge was triple APC cored, and a complete Pleistocene to upper Miocene sequence (0–360 mcd) that is unaffected by burial diagenesis was recovered. Calcareous nannofossils are abundant and well preserved within the sequence of the last 9 m.y. Planktonic foraminifers are abundant to common and reasonably well preserved. Although rare above ~184 mcd, diatoms are consistently present and show better preservation and higher abundance below this depth. Standard nannofossil, planktonic, foraminiferal, and diatom index markers provide tight biostratigraphic age control from the Pleistocene to latest Miocene (~8 Ma) (Fig. F17). The Pleistocene–lower Pliocene sequence has a sedimentation rate of ~2 cm/k.y. From 3 to 6 Ma, the sedimentation rate increases to ~6 cm/k.y. Below this level (7–9 Ma), the sedimentation rate decreases again to an average rate of ~3 cm/k.y.

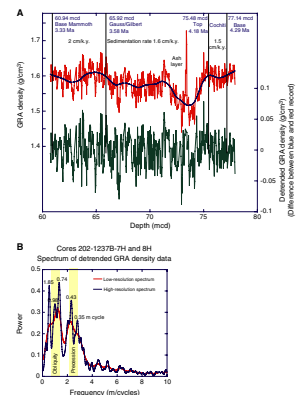
F17. Age models for Leg 202 sites, p. 91.



F18. LSRs and MARs at Leg 202 sites, p. 93.



F19. Site 1237 frequency spectrum of GRA density fluctuation for the time interval of ~3–4 Ma, p. 94.



Site 1241 offers an excellent potential to derive an orbitally tuned timescale that can be tied to the biostratigraphy in order to establish a late Neogene reference section for the equatorial East Pacific. The new timescale will provide integration and intercalibration of datums from both calcareous and siliceous microfossil groups within a single regional chronological framework. It will also provide a useful link between tropical and subtropical biostratigraphic schemes for the Pacific and between timescales from different oceans (such as the Leg 154 orbitally tuned timescale). The timescale will also serve as the basis for high-resolution studies that aim to reconstruct sea-surface and intermediate-water characteristics in the eastern Pacific, to retrace the history of the closure of the Panamanian seaway, to decipher the interaction between tropical and high-latitude circulation systems, and to delineate the evolution of various groups of marine biota.

AGE MODELS AND MASS ACCUMULATION RATES OF LEG 202 SITES

Preliminary age models were created using shipboard biostratigraphic and paleomagnetic data (Fig. F17) to aid initial interpretation of the recovered sediment sequences and sampling of the cores. It is expected that postcruise studies will significantly improve the models by establishing oxygen isotope stratigraphy and orbitally tuned cyclostratigraphy, as planktonic and benthic foraminifers are abundant enough throughout the Holocene to Oligocene sequences and most sites are marked by cyclic changes in lithology.

At Chile margin Sites 1232–1235, where we recovered high-resolution Pleistocene records <0.26 Ma, the common stratigraphic approach provided no additional age control points to refine the age models. Sites 1233–1235, however, revealed unprecedented high-resolution records of pronounced centennial- to millennial-scale variability in paleomagnetic intensities. Here, future studies are expected to strike a new path in establishing a high-resolution late Pleistocene stratigraphy, as centennial- to millennial-scale fluctuations in paleomagnetic secular variation and intensity are global in extent and on such scales may provide a more powerful tool than stable isotope stratigraphy. Following this approach resulted in an improved preliminary shipboard age model for the upper Pleistocene sequence at Site 1233.

Using our shipboard stratigraphic framework (Fig. F17), LSRs and MARs were computed as described in “Age Models and Mass Accumulation Rates,” p. 41, in the “Explanatory Notes” chapter and in the “Age Model and Mass Accumulation Rates” sections of the site chapters and as summarized in Figures F18 and F19. The late Cenozoic variability in LSRs and MARs at Leg 202 sites responds to both long-term tectonic drift of the sites relative to the continental margin and to variations in local environments that drive changes in production and preservation of biogenic sediment components and the supply of terrigenous sediments.

Chile Margin (Sites 1232–1235)

At Sites 1232–1235, located in the Chile Basin and on the Chile margin, upper Pleistocene sediments that accumulated rapidly and at extremely high rates were recovered. At Chile Basin Site 1232, paleomag-

netic and biostratigraphic age control suggests a basal age of >0.46 and <0.78 Ma for the turbidite-dominated sediment sequence. A conservative estimate of the LSR is, therefore, ~ 475 m/m.y. As a first approximation, the average recurrence time of turbidites would be on the order of hundreds of years, possibly triggered by large earthquakes and instabilities at the continental slope associated with climate-induced century- to millennial-scale fluctuations in sediment supply from the continent.

The almost turbidite-free hemipelagic sediment sequences recovered from the Chile margin Sites 1233–1235 are all younger than 0.26 Ma, and the average LSR is estimated to be 82 cm/k.y. at Site 1233, ~ 79 cm/k.y. at Site 1234, and ~ 70 cm/k.y. at Site 1235. A more detailed age model was developed at Site 1233. Here, good correlations to a nearby ^{14}C -dated Holocene sequence (Lamy et al., 2001) and to a previously dated magnetic paleointensity record (Stoner et al., 2002) as well as the presence of the well-dated Laschamp Excursion justified the transfer of additional age control points (for details, see [“Age Model and Mass Accumulation Rates,”](#) p. 16, in the “Site 1233” chapter). This preliminary shipboard model suggests a basal age of ~ 0.17 Ma for the sediment sequence at site 1233. The late Pleistocene to Holocene LSRs and MARs range from 40 to 160 cm/k.y. and from 40 to 150 g/cm²/k.y., respectively (Fig. 18C).

The input of siliciclastic material accounts in general for $>90\%$ of the total sediment deposition at Site 1233 and largely reflects the predominantly fluvial supply of terrigenous material from the Andes and the Coastal Range province (see [“Lithostratigraphy,”](#) p. 5, in the “Site 1233” chapter). A pronounced maximum in MARs between 50 and 10 ka (up to ~ 150 g/cm²/k.y.) (Fig. F18C) suggests enhanced terrigenous sediment discharge during marine isotope Stages 3 and 2, possibly associated with temporal changes in continental rainfall patterns and/or refocusing of fluvial sediment discharge during the glacial sea level lowstand. Distinctly lower rates mark the late Pleistocene interval from 50 to 170 ka (40 g/cm²/k.y.) and the Holocene (~ 60 g/cm²/k.y.). We cannot exclude the possibility that the tripling of noncarbonate MARs during MISs 2 and 3 is a random event, perhaps driven by a newly formed channel that favored a higher sediment flow to Site 1233.

The MARs of carbonate and organic carbon range from 1 to 9 g/cm²/k.y. and from 0.3 to 1.2 g/cm²/k.y., respectively (see [“Age Model and Mass Accumulation Rates,”](#) p. 16, in the “Site 1233” chapter). Such high rates clearly reflect the influence of the high-productivity region off southern Chile. Both carbonate and organic MARs suggest a maximum in biogenic productivity for the LGM and, although slightly reduced, a high level for the Holocene.

Nazca Ridge (Sites 1236 and 1237)

The sediment sequences recovered at Nazca Ridge span the entire Neogene and the Oligocene to ~ 28 Ma at Site 1236 and to ~ 31.5 Ma at Site 1237 without any detectable stratigraphic breaks (Fig. F17). The age models are based on a framework of paleomagnetic datums and biostratigraphy (for details, see [“Age Model and Mass Accumulation Rates,”](#) p. 19, in the “Site 1236” chapter and [“Age Model and Mass Accumulation Rates,”](#) p. 25, in the “Site 1237” chapter). Sites 1236 and 1237, currently located near the outer edges of the oligotrophic subtropical gyre and the nutrient-rich eastern boundary Peru upwelling system, re-

spectively, exhibit relatively low LSRs (0.4–2.4 cm/k.y.) and MARs (<2.5 g/cm²/k.y.) throughout their late Cenozoic history (Fig. F18A).

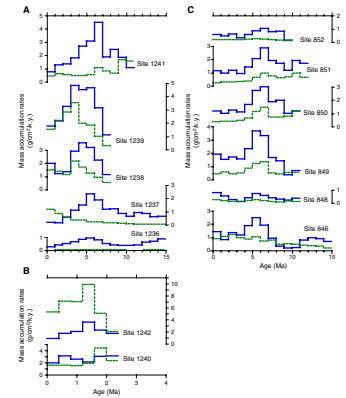
Carbonate MARs and total MARs are nearly identical at Site 1236, as carbonate concentrations are >90%. Slightly elevated carbonate MARs between 25 and 12 Ma (Fig. F20A) resulted from gravity-driven transport of predominantly calcareous neritic material to the site rather than from an increase in productivity or preservation, as Site 1236 was located in the center of the oligotrophic subtropical gyre well above the lysocline during its early history.

A major characteristic of both sites is the simultaneous increase in carbonate MAR at ~9 Ma that culminated in a brief maximum at ~7 to 5 Ma followed by a decrease into the Pleistocene (Fig. F20A). Given no detectable changes in the preservation of calcareous nannofossils, the late Miocene to early Pliocene maximum suggests an interval of enhanced surface productivity. A similar increase and maximum in carbonate MAR is also recognized at equatorial East Pacific sites from Leg 138 (Fig. F20B) and is often referred to as the Miocene to early Pliocene biogenic bloom (Farrell et al., 1995b). Sites 1236 and 1237 trace this event for the first time into the southern East Pacific. At equatorial Sites 849–851 (Leg 138), this event was also accompanied by a pronounced maximum in biogenic opal MAR (Fig. F21), which is not observed at Nazca Ridge. Instead, biogenic opal MARs at Site 1237 dramatically increased over the last ~6 m.y. from 0.02 to 0.8 g/cm²/k.y. (Fig. F21B). Organic carbon MARs at Site 1237 strongly increased over the last 4 m.y., when organic carbon contents increased from the detection limit of 0.1 wt% (using shipboard techniques) to 1.9 wt%.

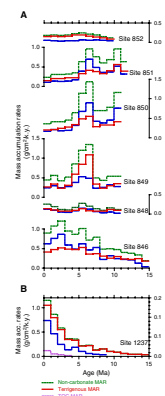
The long-term Pliocene to Holocene increase in both organic carbon and biogenic opal MAR is considered to be associated with the progressive paleodrift of the site toward the eastern boundary upwelling system (Fig. F6), as farther westward at Site 1236 diatoms are almost absent and organic carbon contents are <0.1 wt%. The paleodrift of both sites and the modern regional changes in surface nutrients and productivity along their track would predict a slight and continuous increase in productivity over the last ~30 Ma at Site 1236 and a fourfold increase at Site 1237 (Figs. F22, F23). Although this cannot explain the late Miocene to early Pliocene maximum in productivity, the predicted increase in nutrients, especially in silicate, at ages <7 Ma may serve as an explanation for the observed increase in biogenic opal MARs at Site 1237 (Fig. F21B).

The nonbiogenic MAR at Site 1236 is the lowest of the Leg 202 sites (<0.05 g/cm²/k.y.) (Fig. F20A) and reflects a minimal amount of eolian siliciclastics (biogenic opal and organic carbon contents are negligible). This is consistent with the site's position far away from the Atacama Desert, the major dust source for this area. At Site 1237, the Oligocene and early Miocene siliciclastic MARs are as low as at Site 1236 but slightly increase at ~13 Ma to a higher level of ~0.1 g/cm²/k.y. and then increase more rapidly from ~9 Ma to a late Pleistocene/Holocene maximum of 1 g/cm²/k.y. The enhanced supply of eolian siliciclastics since ~13 Ma may partly result from the eastward migration of Nazca Ridge, which moved Site 1237 closer to the dust source. Although tectonic drift can account for the general increase, it cannot account for short-term changes in dust flux, which likely reflect regional changes in aridification, wind strength, and wind direction.

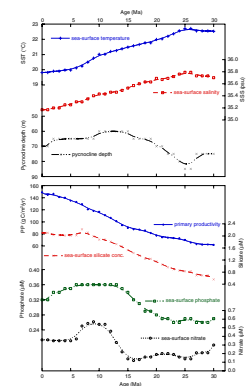
F20. Carbonate and noncarbonate MARs, p. 95.



F21. Biogenic opal and terrigenous sediment MARs as components of the noncarbonate MAR, p. 96.



F22. Modern ocean properties at backtrack locations, Site 1236, p. 97.



Carnegie Ridge (Sites 1238 and 1239)

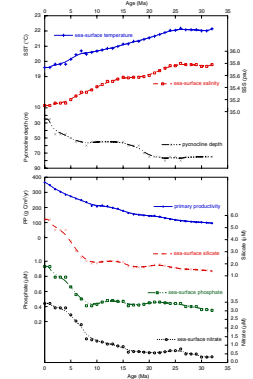
The sediment sequences recovered from Carnegie Ridge range in age from the Holocene to ~11 Ma (Site 1238) and to ~15 Ma (Site 1239). The construction of the age models relies primarily on calcareous microfossil datums and suggests an upper Miocene hiatus at Carnegie Ridge (Fig. F17) encompassing the interval from ~13.5–8 Ma at Site 1239 and extending from the base of Site 1238 to ~8 Ma (for details, see “Age Model and Mass Accumulation Rates,” p. 23, in the “Site 1238” chapter and “Age Model and Mass Accumulation Rates,” p. 22, in the “Site 1239” chapter)

Sites 1238 and 1239 are currently located just south of the equator on the easternmost flanks of Carnegie Ridge. The tectonic backtrack path moves the sites to the west almost parallel to the equator (Fig. F6), and thus both sites remained within the highly productive equatorial upwelling zone throughout their history. Accordingly, Sites 1238 and 1239 are marked by relatively high Neogene LSRs (up to 10 cm/k.y.) (Fig. F18A). Site 1239, closer to the equator and to the continent and at shallower depths, exhibits MARs (2–8 g/cm²/k.y.) that are higher than those at Site 1238 (1–5 g/cm²/k.y.) except in the interval 0–1 Ma.

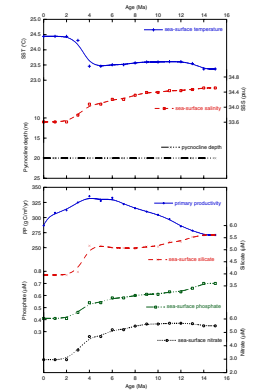
Both sites are characterized by similar trends in carbonate and non-carbonate MARs with distinctly higher values at Site 1239 (Fig. F20A). Rates of carbonate deposition gradually increased from the end of the hiatus (~8 Ma), peaked at 6–3 Ma, and then progressively declined over the last 3 m.y. The maximum in carbonate MARs occurred ~1 m.y. later and persisted ~2 m.y. longer than that observed between 7 and 5 Ma at Sites 1236, 1237, and 1241 and at most of the Leg 138 sites (Fig. F20). This temporal difference may partly result from the paleodrift of Sites 1238 and 1239. The modern pattern of local changes in sea-surface characteristics along the track of Site 1239 would predict a maximum in biogenic productivity from 6 to 3 Ma terminated by the eastward drift of the site out of the highly productive equatorial cold tongue (Fig. F24). The drift-related trends for Site 1238 would predict a generally higher productivity than at Site 1239, thus higher carbonate MARs, and a mid-Pleistocene productivity maximum (Fig. F25), which is in conflict with both absolute values and major trends in carbonate MARs. Hence, regional and temporal oceanographic changes and nutrient budgets may have contributed to the observed variations in carbonate MARs at Carnegie Ridge but cannot explain the full pattern. An additional explanation for the relatively young peaks in carbonate MARs at Sites 1238 and 1239 is their relatively shallow water depth, compared to the Leg 138 sites, which suggests progressive development of corrosive bottom waters through Neogene time.

The noncarbonate MARs at Carnegie Ridge exhibit a broad maximum between 6 and 1 Ma, with highest values between 4 and 3 Ma (Fig. F20A). For this interval, the results from Leg 138 (Fig. F20B) suggest an interesting eastward shift (~4.4 Ma) in the locus of maximum noncarbonate and biogenic opal MARs along the equatorial high-productivity belt from 110°W (Sites 849 and 850) into the Galapagos region (Site 846). At Sites 849 and 850, maxima in both noncarbonate and biogenic opal MARs correspond to the interval of the biogenic bloom between ~7 and 5 Ma. Further eastward and closer to Sites 1238 and 1239, maxima in noncarbonate and biogenic opal MARs occurred between 3 and 1.5 Ma, with a distinct peak at ~1.9 Ma (Farrell et al., 1995b). The maximum in noncarbonate MAR at the easternmost Sites 1238 and 1239, however, occurred in the early Pliocene interval just be-

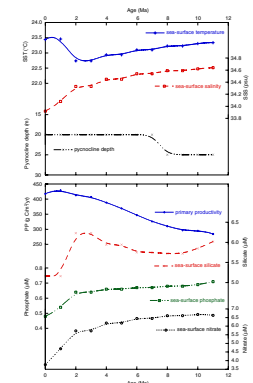
F23. Modern ocean properties at backtrack locations, Site 1237, p. 98.



F24. Modern ocean properties at backtrack locations, Site 1239, p. 99.



F25. Modern ocean properties at backtrack locations, Site 1238, p. 100.



tween the maxima observed at the Leg 138 sites. Whether the trends in noncarbonate MARs at Carnegie Ridge can be ascribed to biogenic opal or terrigenous siliciclastic MARs is difficult to assess without any precise biogenic opal contents. Careful inspection of smear slide data suggests a strong variability in biogenic opal contents on shorter timescales. A distinct trend is only recognized at Site 1238, suggesting a phase of enhanced biogenic opal deposition between 1 and 3.5 Ma, which would closely match the maximum in biogenic opal MARs observed in the Galapagos region (Site 846). An exceptionally strong minimum in grain density data at both sites consistently suggests a short-term interval of enhanced biogenic opal deposition at ~1.9 Ma. Although the documentation of this event will require finer-resolution age control, such a maximum was also recognized in the Galapagos region (Site 846) and the Panama Basin (Site 1240).

At present, long-term variations in siliciclastic MARs at Carnegie Ridge cannot be assessed, except for the younger part of the record. The significant late Pliocene to Holocene increase in magnetic susceptibility may indicate that the supply of siliciclastics dominated the noncarbonate MARs at Carnegie Ridge during that interval.

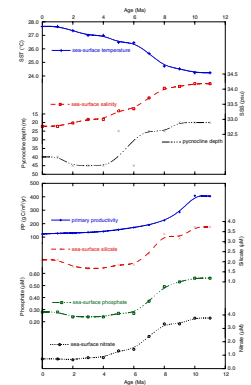
Panama Basin and Cocos Rise (Sites 1240–1242)

At Panama Basin Site 1240, an extended sequence of upper Pliocene (~2.8 Ma) to Holocene sediments was recovered. Age control was excellent and relied primarily upon magnetostratigraphy and calcareous nannofossil datums (Fig. F17B). The site remained below the highly productive equatorial upwelling zone during its entire history. Accordingly, the sediment deposition is largely controlled by variations in biogenic opal and carbonate accumulation and reflects high LSRs and MARs that range between 7 and 16 cm/k.y. and between 4 and 8 g/m²/k.y. (Fig. F18B). Most remarkable is a pronounced maximum in carbonate and noncarbonate MARs at the Pliocene/Pleistocene boundary between 2 and 1.6 Ma (Fig. F20B). The maximum in noncarbonate MARs largely results from high contents in organic carbon (as much as 3 wt% and biogenic opal as indicated by smear slide data, high porosities, and low grain densities (see “Lithostratigraphy,” p. 5, in the “Site 1240” chapter). This interval of enhanced biogenic productivity was also recognized at Carnegie Ridge (Sites 1238 and 1239) and in the Galapagos region (Site 846) although less pronounced and dominated by biogenic opal deposition. This event seems to be restricted to the easternmost equatorial Pacific, as it is not documented farther westward at sites from Leg 138.

Sites 1241 and 1242 at Cocos Ridge recovered continuous sediment sequences that reach back into the middle Miocene (11–12 Ma) and the Pliocene (~2.5 Ma), respectively. The construction of the age model was primarily based on calcareous nannofossil datums (Fig. F17). Magnetic data were useful back to ~1 Ma at Site 1241.

At Site 1241, the Miocene to Pliocene LSRs are relatively high (3–6 cm/k.y.) and decrease in the Pliocene interval to <3 cm/k.y. (Fig. F18A). This general trend is consistent with the northeastward paleodrift of the site away from the highly productive equatorial upwelling zone (Fig. F6). The modern pattern of local changes in productivity along the track of Site 1241 would predict high rates in biogenic productivity from ~11–10 Ma that rapidly drop between 10 and 7 Ma to a relatively low level in productivity at ages <7 Ma (Fig. F26). This trend is mainly reflected by the noncarbonate MAR but not by the carbonate MAR (Fig.

F26. Modern ocean properties at backtrack locations, Site 1241, p. 101.



F20A). The oldest interval from 11 to 9 Ma is marked by the relatively high concentrations of organic carbon and biogenic opal (see “**Biostratigraphy**,” p. 10, and “**Geochemistry**,” p. 15, both in the “Site 1241” chapter) suggesting that the maximum in noncarbonate MARs during this period reflects high biogenic productivity when the site was near the equator. Benthic and planktonic foraminiferal tests appear strongly affected by carbonate dissolution over this sequence, which corresponds to a well-known interval of poor carbonate preservation in the equatorial east Pacific and in the Caribbean, the “Miocene carbonate crash” (Lyle et al., 1995).

A major characteristic of the carbonate MAR is the pronounced maximum at 7–5 Ma (Fig. **F20A**) that is mirrored by the noncarbonate MAR and accompanied by increased deposition of biogenic opal from 6 to 7 Ma (see “**Lithostratigraphy**,” p. 5, in the “Site 1241” chapter). This maximum in productivity is not predicted by the tectonic backtrack but is a widespread feature that has been documented in sediment records from the eastern equatorial Pacific (Leg 138; Farrell et al., 1995b) (Fig. **F20B**) and in the eastern South Pacific at Sites 1236 and 1237 (Fig. **F20A**).

The Pliocene and Pleistocene interval is marked by a continuous decrease in total and carbonate MARs, with the lowest rates in the upper Pleistocene to Holocene interval. This trend is not shown at Site 1242, where all rates exhibit a pronounced and broad maximum between 2.5 and 0.5 Ma, with peak values centered at 1.6–1.2 Ma. Noncarbonate MARs are higher than carbonate MARs by a factor of three. Distinct minima in grain density values and in siliciclastic contents at ~1.4–1.6 Ma (see “**Lithostratigraphy**,” p. 5, in the “Site 1242” chapter) suggest that the maximum in noncarbonate MAR may result primarily from increased biogenic opal contents rather than from a maximum in terrigenous sediment supply. The inferred maximum in biogenic MAR may provide evidence for variations in upwelling and biological production on the Costa Rica margin.

BIOGEOCHEMICAL CONSTRAINTS

The oceanographic and geographic settings of Leg 202 sites influence their biogeochemical environments, as reflected in the volatile hydrocarbon, interstitial water, and sediment geochemistry. The latitudinal range for Leg 202 (from ~41°S to ~7.5°N) is significantly larger than those ranges for earlier ODP legs that focused on the productive regimes of major eastern boundary currents: Leg 167 sites from the California Current region (~30–40°N) and Leg 175 sites from the Benguela Current region (~4°–32°S). Water depths at the Leg 202 sites range from 489 to 4072 m, affecting the delivery of organic matter to the sediment/water interface. Linear sedimentation rates range over at least two orders of magnitude, from <1 to >100 cm/k.y.

The oxidation of organic matter is the major influence on interstitial water geochemistry, with resulting effects on volatile hydrocarbon geochemistry and on authigenic carbonate mineralization reactions. In addition to the prevailing influence of organic matter degradation, two sites are affected by methane hydrates (Sites 1233 and 1235), and a third site shows the signature of fluid flow in the underlying basement (Site 1240).

Organic Matter Oxidation: Sulfate Reduction, Methanogenesis, and Nutrient Regeneration

Organic matter oxidation in marine sediments proceeds by a sequence of reactions typically observed with increasing depth below the seafloor (aerobic respiration, denitrification, manganese reduction, iron reduction, sulfate reduction, and methane fermentation). The geochemical sampling and analytical strategies employed during Leg 202 are best suited to observing the effects of organic matter oxidation through the depletion of sulfate, an oxidant, and the production of methane, a product of methane fermentation. On the basis of sulfate profiles (Fig. F27), Leg 202 sites can be divided into three categories:

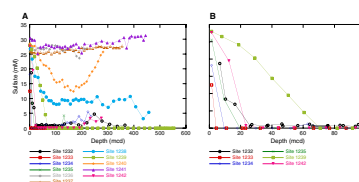
1. Those with no to limited sulfate reduction (Nazca Ridge Sites 1236 and 1237 and the deeper Cocos Ridge Site 1241);
2. Those with an intermediate degree of sulfate reduction (the deeper Carnegie Ridge Site 1238); and
3. Those with complete sulfate reduction (Chile Basin Site 1232, Chile margin Sites 1233–1235, and the shallower Carnegie Ridge and Cocos Ridge Sites 1239 and 1242).

Previous studies including those at some Peru margin sites have found a relationship between interstitial sulfate gradients with depth and bulk sedimentation rates, with steeper sulfate decreases (i.e., shallower depth of sulfate disappearance) related to faster sedimentation rates. This relationship appears to be generally true for Leg 202 sites, with deeper sulfate “zero” depths for the shallower of the Carnegie Ridge and Cocos Ridge sites relative to the more rapidly accumulating Chile margin and Chile Basin sites (Fig. F27). However, further evaluation of this requires definition of sedimentation rates for the Chile margin and Chile Basin sites, all with relatively shallow sulfate disappearance depths of <30 mcd (Table T4).

The categorization of sites by sulfate profiles is clearly linked to the production of methane, as the presence of interstitial sulfate is known to inhibit methanogenesis in marine sediments (Claypool and Kvenvolden, 1983). The sites with limited sulfate reduction and thus high sulfate concentrations had very low methane concentrations, whereas the deeper Carnegie Ridge site (1238) with intermediate sulfate concentrations had only low to moderate levels of measured methane (Table T4). In contrast, all the sites with complete sulfate depletion had high measured methane values, with high methane concentrations being reached at depths coincident with or just deeper than the depth of sulfate disappearance (Table T4). Note that the limited depth resolution of both interstitial water and volatile hydrocarbon sampling makes a more detailed assessment impossible.

Because the oxidation of organic matter is important in the production of alkalinity in interstitial waters, the values of the alkalinity maxima for these sites also follow the division on the basis of the sulfate profiles. Sites with limited sulfate reduction have relatively low peak alkalinity values (2 to >5 mM), the site with intermediate sulfate reduction has a moderately high alkalinity maximum (>17 mM), and the sites with complete sulfate reduction have the largest alkalinity maxima (>25 mM to as high as 60 mM) (Table T4) because of strong organic matter oxidation. The regeneration of phosphorus (as dissolved phosphate) and nitrogen (as dissolved ammonium) are also closely linked to

F27. Interstitial sulfate concentrations vs. depth, p. 102.



T4. Summary of Leg 202 geochemistry, p. 145.

organic matter oxidation, and the peak values at the sites follow the same division by redox intensity (Table T4).

Sedimentary Organic Matter: Competing Influences and the Importance of Dilution

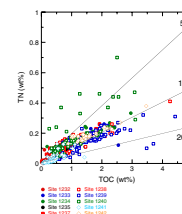
A primary objective of Leg 202 is the study of variations in biological production in this eastern boundary current region and their role in modifying subsurface water masses characteristics such as oxygenation and nutrient inventories through time. TOC concentrations determined aboard ship were therefore used to give first insights about the richness of sediments in organic material and export production. TOC/total nitrogen (TN) ratios and Rock-Eval pyrolysis parameters were used to help identify the quality of the organic matter (e.g., origin and preservation).

In contrast to the wide ranges of sulfate reduction, alkalinity generation, and methane production, the sedimentary organic carbon concentrations have a much narrower range for Leg 202 sites. Organic carbon concentration maxima do not exceed 4.5 wt%, even for sites at shallower water depths where biological production in the overlying waters is known to be high, such as in coastal upwelling areas. Average organic carbon concentrations are typically lowest for the three sites with limited degrees of sulfate reduction (Sites 1236, 1237, and 1241). Higher methane concentrations and partial to complete sulfate reduction are found at sites where sedimentary organic carbon concentrations are higher, with maximum values of at least 1.5 wt% (Sites 1233–1235, 1238–1240, and 1242). This indicates that the supply of labile organic matter controls the redox state of these sediments (Table T4). The availability of oxidants during diagenesis may also change both the quantity and composition of the organic matter in the upper several hundred meters of marine sediments.

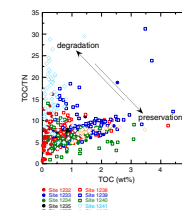
TOC/TN ratios are commonly used to discriminate between marine and terrestrial organic matter. Marine organic materials have atomic TOC/TN ratios between 4 and 10, and terrestrial organic matter TOC/TN ratios are above 20. Whereas degradation during sinking and burial diagenesis can increase TOC/TN ratios, in Leg 202 sediments they are usually ~10 (Fig. F28), indicating that organic matter buried in sediments is mainly of marine origin along the southeast Pacific margin. One exception is Site 1241, where higher TOC/TN ratios are found. These high ratios may result from degradation, because the supply of land-derived organic matter is expected to be negligible at this site located on a ridge and away from the coast.

Many sites show an initial decline of organic carbon concentrations with increasing depth, consistent with organic matter oxidation. However, the competing influences of organic carbon supply from primary productivity, the effects of water depth at a site on organic carbon delivery to sediments, and the importance of dilution by detrital and biogenic sediments based on site location make simple generalizations about site organic carbon concentrations difficult. For instance, the degradation process would be dominant in driving TOC changes if TOC decreases are associated with increases in TOC/TN ratios, whereas preservation would be the dominant process if an inverse correlation had been observed. The lack of a clear correspondence between these two parameters (Fig. F29) may indicate that both processes significantly influence the preservation of TOC. Results of Rock-Eval analyses of selected samples from several sites confirm this.

F28. TN vs. TOC concentrations, p. 103.



F29. TOC/TN ratios vs. TOC concentrations, p. 104.



Dilution by siliciclastics appears to play an important role in controlling organic matter concentration in many of the sites, particularly at Sites 1233–1235 from the Chile margin, where sedimentation rates are extremely high (>50 cm/k.y. to >1 m/k.y.). Although the high concentrations of volatile hydrocarbons at these three sites indicate that the burial flux of metabolizable organic matter is very important, TOC concentrations are low compared to other eastern boundary sites where coastal upwelling occurs, such as along the coastal branch of the Benguela Current. At the Chile margin sites, variations in TOC contents are mainly influenced by extremely high terrigenous sediment supply as a result of enhanced fluvial discharge in response to continental rainfall.

Results from two cores from the central Chile margin, close to Sites 1233–1235, document a decrease in TOC concentrations from the Holocene to the last glacial state (MIS 2) Hebbeln et al. (2002). The MARs of organic carbon, however, reveal a reversed pattern. Organic carbon MARs were higher during MIS 2 than during the Holocene as a consequence of higher glacial sedimentation rates. This pattern is very similar to that observed at Site 1233. Hence, the effect of dilution and varying sedimentation rates has to be considered for paleoproductivity reconstructions from Leg 202 sites, and a multiproxy approach should be preferred.

At Site 1237 on Nazca Ridge, the increase in TOC concentrations since 3.5 Ma can be attributed to a change in export production. A larger influence of degradation or preservation is unlikely according to the variations observed in TOC/TN ratios and Rock-Eval data. Dilution by calcium carbonate is minor. In addition, dilution by siliciclastics can be excluded because the supply of siliciclastics also increased over the last ~3.5 m.y. The increase in TOC contents could be the result of an intensification of coastal upwelling or the plate tectonic migration that moves Site 1237 closer to the coastal upwelling zone.

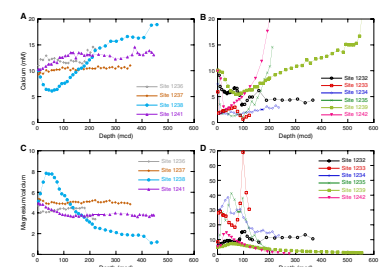
Similarly, export production and thus organic material delivery to the sediments seem to be the dominant factors in driving TOC variations in the sedimentary sequences of Sites 1238–1240 along the equatorial divergence. For instance, in these three sites, an organic-rich interval corresponding to Pliocene–Pleistocene times has been found. The generally good correlation between TOC variations and the presence of microfossils (diatoms in particular) in these intervals support this hypothesis.

Authigenic Mineralization: Calcium and Magnesium Profiles in Interstitial Waters

Alkalinity produced by organic matter oxidation can drive carbonate mineralization reactions, including precipitation and replacement reactions producing calcite and/or dolomite. If precipitation reactions are sufficiently intense, they can result in substantial decreases in interstitial calcium, in contrast to the more typical conservative increases of calcium with depth driven by reactions in basement seen in many marine sediments. Decreases in calcium can drive large increases in magnesium/calcium ratios, and high values of this ratio appear to be necessary to promote authigenic dolomite formation.

At sites with little to no sulfate reduction, interstitial calcium typically is constant or increases with increasing depth (Fig. F30A) and magnesium/calcium ratios are constant or decrease with increasing depth (Fig. F30C). In contrast, the deeper Carnegie Ridge site (1238) with an intermediate degree of sulfate reduction (Table T4) has a cal-

F30. Interstitial calcium and magnesium/calcium profiles vs. depth, p. 105.



cium minimum ~40% lower than seawater values, and magnesium/calcium ratios increase to nearly 8 just shallower than the sulfate minimum (Fig. F30A, F30C). The depletion of calcium is more pronounced at sites with complete sulfate reduction and with minimum calcium concentrations at least 80% lower than seawater concentrations (Fig. F30B). The depth of the calcium minimum is typically shallower than the alkalinity maximum (Table T4). The large decreases in calcium drive substantial increases in magnesium/calcium ratios to values as high as 40 (Fig. F30D). Higher magnesium/calcium ratios more effectively promote dolomite formation, which acts as a sink for magnesium. Sites with more intense sulfate reduction via organic matter oxidation are likely to be influenced more heavily by authigenic carbonate mineralization reactions, and this must be considered when evaluating their utility for ocean history reconstructions.

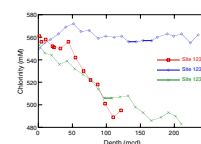
Chloride Profiles: Gas Hydrates in Two Chile Margin Sites

The two shallower Chile margin sites (1233 and 1235) show clear evidence of the influence of methane hydrates in interstitial chloride profiles based on the large decreases in chloride with increasing depth (Fig. F31). These gradients are significantly larger than those observed at the deeper water, midslope Peru margin basin sites drilled during Leg 112 (Sites 682, 683, 685, and 688; site water depths range from 3072 to 5071 m). Decomposition of gas hydrates could explain the observed chloride decreases as a result of dilution, either through in situ decomposition at depth in the sediment column below the hydrate stability zone or as an artifact during sediment recovery. In contrast to Sites 1233 and 1235, the deeper-water Chile margin site (1234) has a more conservative chloride gradient with depth (Fig. F31).

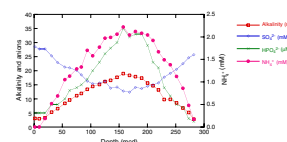
Fluid Flow in Basement: Panama Basin Site 1240

A Panama Basin site (1240) has a relatively thin total sediment cover, and drilling reached basement at 289.2 mcd. Organic matter diagenesis influences the interstitial water chemistry, as indicated by the sulfate profile (Fig. F32). The decline in interstitial sulfate with depth is accompanied by increases in alkalinity, phosphate, and ammonium (Fig. F32). However, sulfate reduction is not complete at this site. The return of sulfate and alkalinity values toward seawater values near the sediment/basalt interface, along with those of other elements, indicates flow of relatively unaltered seawater in the underlying basement. Large-scale horizontal advection of such waters through oceanic crust in the central equatorial Pacific has been inferred from interstitial water geochemistry (Oyun et al., 1995) and is thought to be responsible for the low conductive heat flow (i.e., low thermal gradients) observed in that region. This influence of advective flow at Site 1240 means that any estimates of the influence of processes like authigenic mineralization based on interstitial water geochemistry may tend to underestimate their effects at this site. The incomplete sulfate reduction is not because of lack of oxidizable organic matter, as indeed the middepth sediments at this site are relatively organic carbon rich, but is the result of the effectiveness of the resupply of sulfate from above and below the sediment column, resulting in distinctive interstitial profiles (Fig. F32).

F31. Interstitial chloride vs. depth for Chile margin sites, p. 106.



F32. Interstitial water profiles vs. depth, Site 1240, p. 107.



TECTONICS AND CLIMATE

One of the most perplexing questions in climate is why global climate over the past 40 m.y. changed from very warm conditions (the “Greenhouse World”) to conditions of unipolar (Southern Hemisphere) and later bipolar glaciation (the “Icehouse World”). Partial answers include plate tectonic processes, elevation and erosion of vast plateaus, opening and closing of oceanic gateways, and changing concentrations of atmospheric greenhouse gases. The southeast Pacific is a key location for examining the Neogene and Paleogene response of climate, oceanography, and biogeochemical systems to events such as the closure of the Isthmus of Panama and the uplift of the Andes.

Andean Uplift, Eolian Dust, Volcanism, Climate Change, and Biogeochemistry

The Neogene uplift of the Andes Mountains is expected to have caused extensive changes in South American climate, wind-driven oceanic surface circulation, and, hence, productivity by reorganizing the pattern of atmospheric circulation and the hydrological cycle. But the timing and consequences for climate and ocean circulation, possibly responding to critical thresholds in the uplift history, are poorly constrained.

Continued uplift raised the Andes to an altitude of >4000 m by the end of the Neogene, establishing a barrier for southeast trade winds in the subtropics and for westerly winds in the midlatitude regions of South America (Lenters et al., 1995). Today, the blocking of the westerly winds results in enhanced precipitation on the western side of the mountain range (Chilean and Patagonian glaciers) and causes a strong rain shadow on the eastern side (Patagonian desert). A reversed rainfall pattern marks the low-latitude regions, where the barrier leads to enhanced precipitation from the trade winds on the eastern side of the mountain chain. Heavy rainfalls form a major source for the Amazon River, which drains its sediment load into the Atlantic. The western side suffers from a rainshadow effect and drier climate conditions, as expressed in the Atacama Desert. Moreover, the interplay between the uplift of the Andes and the semipermanent subtropical high-pressure cell over the southeast Pacific may have significantly amplified the aridification along the western margin of South America, as suggested by theoretical studies (Hay, 1996). The Andes constrict the counterclockwise flow on the east side of the high-pressure cell and force low-level high-velocity winds to follow the coast line. This results in enhanced coastal upwelling, lower sea-surface temperatures, reduced evaporation, and increased onshore aridity.

Marked changes in the erosion history of the Andes were detected during Leg 154 (Ceara Rise), which drilled the Atlantic side of South America. The increase in the Amazon River’s supply of terrigenous sediments and its change in clay mineralogy indicate major uplift phases from 12 to 8 Ma and since ~4.6 Ma (Curry et al., 1995), as well as substantial regional climate changes (Harris and Mix, 2002). Uplift over the past ~10 m.y. is consistent with paleobotanical reconstructions from the central and Colombian Andes (Gregory-Wodzicki, 2000) and from ~4.6 Ma (Hooghiemstra and Ran, 1994; van der Hammen et al., 1973). The early Pliocene phase is paralleled by the subduction of Cocos Ridge at ~5 Ma, which formed during the passage of the Cocos plate over the

Galapagos hotspot and dramatically elevated the Central American volcanic arc and led to the final phase of the closure of the Isthmus of Panama (Dengo, 1985). Unfortunately the land record can not be used to assess the details of Neogene water mass changes that respond to mountain building, as the land record of uplifted marine sediments contains major hiatuses, for example in Chile between 10 and 3.5 Ma (Martinez-Pardo, 1990).

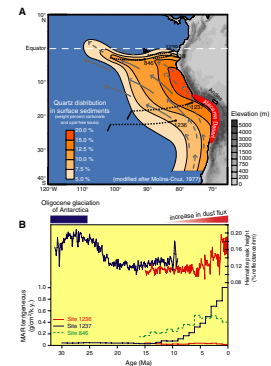
During Leg 202, we recovered a latitudinal transect of sediment records off the Pacific coast of South America that spans the time interval of the last 32 m.y. and offers an opportunity to assess the impact of Andean uplift on long-term changes in volcanic activity, continental aridity, upwelling/productivity, trade winds, and dust transport.

The long-term history of eolian deposition in the subtropical southeastern Pacific is best recorded at Sites 1236 and 1237 (Fig. F33). Today, both sites underlie the path of eolian transport from the Atacama Desert in Chile. The southeast trade winds are the major dust carriers as indicated by the pattern of quartz distribution in southeast Pacific surface sediments (Molina-Cruz, 1977). The presence of terrigenous hematite and goethite, as well as other mainly clay-sized siliciclastics at Sites 1236 and 1237 (Fig. F33), is indicative of a far-field eolian component (Pye, 1987). The combined records of these tracers suggest that eolian dust has accumulated in the subtropical southeast Pacific since at least the late Oligocene. Shipboard data from Site 1236 provide no information about eolian deposition for the sediments older than middle Miocene because the sediment deposition was dominated by supply from a nearby carbonate platform. Conversely, at Site 1237, the iron oxide signal is lost, probably diagenetically, in sediments younger than ~8 Ma.

From ~31 to ~15 Ma, before the major uplift of the Andes, Site 1237 was located nearly parallel to its modern latitudinal position farther westward (a result of plate tectonic movement), ~2200–1500 km away from the South American coast, and thus received less dust (Fig. F33). Siliciclastic accumulation rates were lower than today by an order of magnitude and indicate no significant trend over this interval. The hematite record, however, indicates a change in the source region of dust, which was significantly enriched in hematite during the Oligocene and depleted during the Miocene. This gradual change between 26 and 22 Ma may indicate a change in weathering conditions that was possibly associated with a major change in global climate, when late Oligocene warming (~25 Ma) reduced the extent of Antarctic ice and led to warmer conditions that prevailed until the middle Miocene (Zachos et al., 2001). The timing of this shift in eolian sedimentation is also roughly coincident with the opening of the Drake Passage from 39 to 22 Ma (Barker and Burrell, 1977), which established a deepwater connection between oceans and the Antarctic Circumpolar Current. The presence of dust far away from the South American coast suggests that arid or semiarid conditions existed in subtropical South America prior to the uplift of the Andes. Aridity in this region could have been the result of loss of humidity by the southeast trade winds along their continental path across South America and the presence of the adjacent cool Peru-Chile Current (Frakes, 1979). Before the major uplift of the Andes, the trade winds probably had a more zonal distribution that allowed deposition of eolian hematite at Site 1237.

For the period between ~15 and ~8 Ma, a hematite record exists at both sites. Higher hematite content at Site 1237 during this interval is consistent with its closer proximity to a potential South American dust source area. A first slight increase in siliciclastic accumulation rates oc-

F33. Quartz distribution in surface sediments, siliciclastic accumulation rates, and hematite peak height, p. 108.



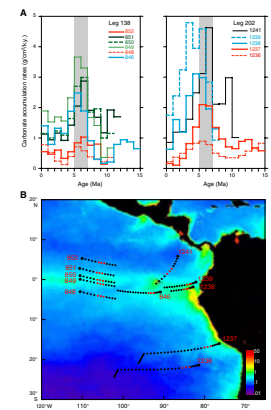
curred at ~14 Ma. This may reflect the onset of aridity in the Atacama Desert, as suggested by Alpers and Brimhall (1988) to occur sometime between 15 and ~8 Ma, possibly in response to the uplift of the Andes. However, the increase in siliciclastic accumulation rates since ~14 Ma may also result from strengthened trade winds in response to enhanced global cooling during the Miocene from ~14 to 10 Ma, associated with the reestablishment of a major ice sheet on Antarctica (Zachos et al., 2001), or from the eastward migration of Nazca plate, which moves Site 1237 closer to the dust source (Fig. F33).

The abrupt loss of the iron oxide signal at Site 1237 (~8 Ma) appears to result from diagenetic reduction processes due to an increase in productivity and enhanced rain of organic matter to the seafloor rather than to reflect a change in the dust source area. This is corroborated by the fact that the reddish color signal of the iron oxides persists into the Pleistocene sequence at Site 1236, located ~500 km to the southwest of Site 1237, and thus had an even larger distance to the dust source.

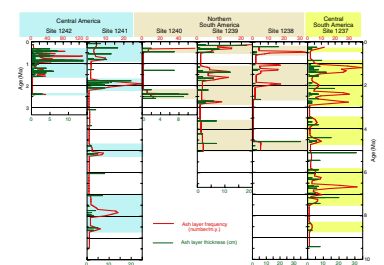
Since the late Miocene and Pliocene, eolian iron oxides are complemented by a significant eolian siliciclastic fraction. Since ~8 Ma, increases are evident in both hematite content at Site 1236 and total dust flux at Site 1237, indicating enhanced eolian deposition (Fig. F33). In accordance, recent sedimentological data from middle Miocene to upper Pliocene successions in the modern Atacama Desert indicate that desertification commenced at ~8 Ma and was punctuated by a phase of increased aridity at ~6 Ma (Hartley and Chong, 2002). Moreover, the increase in eolian deposition and aridification is paralleled by a pronounced increase in productivity (reaching a maximum at ~6 Ma) along the equatorial upwelling belt (Sites 1239 and 1241 and Leg 138 sites) and in the southeast Pacific, in a region outside the major coastal upwelling zone but within the influence of the Peru-Chile Current (Sites 1236 and 1237) (Fig. F34). A change in atmospheric circulation could explain these features. Intensified trade winds would enhance equatorial upwelling/productivity and the northward advection of nutrient-rich waters transported by the Peru-Chile Current. Modern upwelling along the Peru continental margin occurs over a broader region than just a very narrow coastal strip (Fig. F34). This may be because the wind stress curl associated with the topographically steered winds (the result of an effective mountain barrier) is positive, creating a broader upwelling zone than a strictly uniform wind with an equatorward component (Pickard and Emery, 1990). Thus, the late Miocene paleoposition of Site 1237 was possibly influenced by upwelling features. Enhanced coastal upwelling, in turn, would have led to increased aridification of the Atacama Desert.

The inferred enhancement in wind speed at ~8 Ma is consistent with a coarsening in eolian sediments at south equatorial Sites 848 and 849 (Hovan, 1995), which were recovered during Leg 138. At about the same time, the first occurrence of discrete ash layers in sediments of the South Pacific record the onset of intense volcanism in the central Andes and possibly a phase of major uplift that led to the deposition of 55 ash layers at Site 1237 over the last 9 m.y. (Fig. F35). Taken together, this chain of evidence may indicate a critical threshold in the uplift history at ~8–9 Ma by forming an effective topographic barrier that enhanced the steering of trade winds along the coast, resulting in stronger meridional flow, enhanced eolian transport, coastal upwelling, and biogenic productivity. This event is also recorded in the Atlantic Ocean as a rapid increase in the chlorite:kaolinite ratio off the Amazon, suggesting an

F34. Mean calcium carbonate accumulation rates vs. age and annual chlorophyll-a concentrations, p. 109.



F35. Ash frequency, Sites 1237–1242, p. 110.



abrupt increase in physical weathering following uplift (Harris and Mix, 2002).

Paleobotanical evidence as summarized by Gregory-Wodzicki (2000) suggests a different uplift history for the central and northern Andes. These data suggest that the central Andes had attained no more than half of the modern elevation by ~10 Ma and imply surface uplift on the order of 2000–3500 m since the late Miocene. Major uplift of the Colombian Andes has been suggested to occur at a later stage, between 2 and 5 Ma, reaching no more than 40% of its modern elevation by ~4 Ma and a modern height by ~2.7 Ma. The temporal distribution of ash layers along the latitudinal transect of the Leg 202 sediment records might be a useful proxy for tracing the different evolution of the mountain range from Central to South America, if major uplift phases were accompanied by intense volcanism. The sediment records of Leg 202 comprise >200 volcanoclastic horizons that were deposited during the last ~9 m.y. (Fig. F35). Maxima in ash layer frequency occurred at ~8–6 Ma off the coast of southern Peru (~16°S). Farther to the north, between 2°S and 8°N, significant amounts of ash layers did not occur before ~5 Ma. The Miocene occurrence of ash layers at north equatorial Site 1241 is interpreted to reflect the volcanic activity of the Galapagos hotspot based on the presence of black lapilli-sized scoria. The deposition of such ash layers ceased at ~6 Ma, probably because of the northeastward movement of Site 1241 away from the Galapagos hotspot. The interval of the last 5 m.y. is marked by ash layers enriched in clear glasses, possibly originating in Central America.

Another maximum in ash layer frequency marks the interval of the last 3 m.y. at all sites along the transect between 16°S and 8°N. The late appearance of ash layers in the northern sediment records during the Pliocene might be indicative of the major uplift phase in the northern Andes between 5 and 2 Ma.

However, it is difficult to conclusively prove a primary teleconnection between the uplift of the Andes and the observed changes in volcanism and atmospheric and oceanic circulation because the inferred uplift rates have limited confidence in absolute paleoelevation and age control. Even if the timing and identification of major changes in the uplift history are known, thresholds for profound changes in climate and ocean circulation are unknown. Furthermore, it is difficult to distinguish the initial climate response in equatorial and southeast Pacific sediment records from effects that may result from the plate tectonic drift of site locations toward the continent. Nevertheless, the sediment records recovered during Leg 202 have an excellent potential to provide detailed insights into the complex tectonics-climate connection.

Additional insights are thought to result from a comparison of sediment records from the southeast Pacific and southeast Atlantic off the coast of Namibia (Leg 175 and proposed for Leg 208). These regions share strong similarities. Both coasts are bordered by highlands that force the meridional component of the southeast trade winds in connection with the subtropical high-pressure cell to cause enhanced coastal upwelling and desertification (Namib and Atacama Deserts). However, the highlands along the coast of Namibia rise to an altitude of no more than 2000 m and thus may serve as a modern analog to the late Miocene elevation of the Andes and its impact on atmospheric and oceanic circulation. We mention these thoughts here in the hope of encouraging further research into the tectonic linkages, especially experiments with general circulation models, to test the sensitivity of atmospheric circulation patterns to progressive mountain uplift in the

midlatitudes and their effect on oceanic heat transfer via the eastern boundary currents.

Closure of the Isthmus of Panama

The Neogene tectonic closure of the Central American isthmus from 13.0 to 2.7 Ma (Duque-Caro, 1990; Collins et al., 1996) resulted from the subduction of the Pacific Cocos and Nazca plates beneath the North and South American plates and later the Caribbean plate. The early phase of the closure restricted the exchange of deep and intermediate water between the Pacific and the Atlantic and is considered as a potential cause for the carbonate crash near the middle/late Miocene boundary (Lyle et al., 1995). This interval is characterized by periods of severe carbonate dissolution and has been documented in sediment records from the eastern equatorial Pacific (~9–11 Ma) and the Caribbean (~10–12 Ma). The dissolution events are more recently interpreted to reflect an intensified influx of corrosive southern source water from the Atlantic into the Caribbean and into the equatorial east Pacific, both in response to a strengthened global thermohaline circulation associated with enhanced production of North Atlantic Deep Water (Roth et al., 2000). However, the major phase of the carbonate crash occurred ~1 m.y. earlier in the Caribbean than in the Pacific, leaving open several questions concerning the timing and mechanisms.

In addition, the closure has always been an attractive candidate for the ultimate cause of the Pliocene intensification of the Northern Hemisphere glaciation since ~3.1 Ma (Mikolajewicz and Crowley, 1997). Closure-induced changes in global thermohaline circulation have been invoked to be the cause either for the onset (Berggren and Hollister, 1974) or for the delay (Berger and Wefer, 1996) or for setting the preconditions of the Northern Hemisphere glaciation (Haug and Tiedemann, 1998; Driscoll and Haug, 1998).

Although the link between the isthmus closure and the Northern Hemisphere glaciation is still a matter of debate, recent studies clearly identify a close link between the formation of the Isthmus of Panama and major oceanographic changes that occurred between 4.6 and 4.2 Ma, when the Panamanian sill shoaled to a water depth of <100 m (Haug and Tiedemann, 1998). The chain of evidence suggests the development of the modern Pacific-Atlantic salinity contrast of ~1‰ (Haug et al., 2001), a reorganization of the equatorial Pacific surface current system, the intensification of Upper North Atlantic Deep Water formation, and the development of the modern chemical Atlantic-Pacific asymmetry, which is reflected in a strong increase in Caribbean/Atlantic carbonate preservation and a remaining strong carbonate dissolution in the Pacific (Farrell et al., 1995b; Haug and Tiedemann, 1998; Haug et al., 2001). This major salinity contrast between ocean basins, driven in part by net freshwater transport as vapor across the Isthmus of Panama, is likely responsible for maintaining the global thermohaline “conveyor belt” circulation, which is dominated by North Atlantic Deep Water (Gordon, 1986; Broecker, 1991).

In contrast to Leg 138, the equatorial sediment records from Leg 202 provide only limited evidence for the middle–late Miocene carbonate crash, probably due to the shallower site locations. All information about the Pacific carbonate crash is based on records deeper than 3000 m water depth, a depth level that is highly sensitive to fluctuations in the carbonate compensation depth (CCD) in the eastern equatorial basins (Lyle et al., 1995). However, Site 1241 on Cocos Ridge was affected

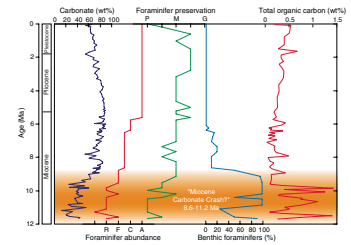
by enhanced carbonate dissolution between ~9 and 12 Ma (Fig. F36), although positioned in a water depth of ~2200 m, well above the modern CCD. The tectonic backtrack moves Site 1241 southwestward, closer to its origin at the Galapagos hotspot into the equatorial high-productivity belt, and into a water depth that was probably several hundred meters shallower during the middle to late Miocene than it is today.

The Miocene interval from ~9 to 12 Ma is marked by low carbonate accumulation rates (Fig. F34) and low carbonate concentrations averaging ~40 wt% (Fig. F36) but relatively high mean sedimentation rates of ~50 m/m.y. Biogenic opal, organic carbon, and siliciclastics became significant contributors to the sediment composition. The preservation of calcareous nannofossils, planktonic foraminifers, and even benthic foraminifers was affected strongly by carbonate dissolution (Fig. F36). The overall increase in biogenic opal (including laminated diatom oozes), organic carbon (up to 1.5 wt%), and sedimentation rates is indicative of high surface productivity and enhanced organic carbon rain. Fluctuations in the lysocline depth associated with a change in carbonate vs. biogenic opal productivity ($>C_{org}/CaCO_3$ -flux) and supralysocline carbonate dissolution in response to organic matter degradation are considered as major contributing factors to the carbonate dissolution events. These findings may revitalize the discussion about the mechanisms that contributed to the carbonate crash. At this stage of results, however, it is difficult to postulate any link to the closure of the Isthmus of Panama.

The most prominent feature of long-term changes in the Leg 202 sediment records is a pronounced late Miocene to early Pliocene maximum in biogenic accumulation rates, suggesting an interval of enhanced oceanic surface productivity between ~8 and ~4 Ma with a maximum at ~6 Ma (Fig. F34). A similar but shorter interval of rapid biogenic accumulation (6.7–4.5 Ma) was found at equatorial east Pacific sites during Leg 138 and is often referred to as the late Miocene to early Pliocene biogenic bloom (Farrell et al., 1995b). Compelling evidence that the biogenic bloom occurred throughout the entire tropical Indo-Pacific is summarized in Farrell et al. (1995b). The ultimate cause of the rise and fall of this bloom is unknown but has been linked to a variety of previous hypotheses including sea level variations, continental weathering, deepwater circulation, trade wind fluctuations, and the closure of the Isthmus of Panama. Sites 1236 and 1237 trace the productivity maximum for the first time farther south and suggest an early onset of this event in the eastern boundary current of the South Pacific. The onset and continuation of the productivity event was probably associated with an increase in trade wind circulation since ~8 Ma as discussed in the context of Andean uplift in the previous section. Whether the wind-driven northward advection of cool and nutrient-rich Southern Ocean waters via the eastern boundary current and its injection into the South Equatorial Current is a possible source for this biogenic bloom will be studied postcruise.

The fall of this event was possibly associated with a decrease in the strength of the southeast trade winds as indicated by grain-size studies on eolian sediments from south equatorial Sites 848 and 849 (Hovan, 1995). The grain-size records, spanning the interval of the last 10 m.y., reveal a pronounced early Pliocene minimum, inferring a decrease in wind speed. Site 1237 underlies the path of eolian transport from the Atacama Desert and is ideally located to verify this hypothesis. In addition to changes in atmospheric circulation, the emergence of the Isthmus of Panama may have played a critical role because the end of the

F36. $CaCO_3$ concentration, foraminifer abundance and preservation, benthic foraminifer percentage, and TOC concentration, Site 1241, p. 111.



bloom, at ~4.5 Ma, coincides with a critical threshold in the closure history that led to a decrease in equatorial east Pacific sea-surface salinities (Haug et al., 2001) and an eastward shift of maximum biogenic opal productivity (Farrell et al., 1995b). The preliminary results from Leg 202 provide no clear timing for the Pliocene fall of the productivity event (Fig. F34) because the carbonate accumulation rates continued to decrease into the Pleistocene at Sites 1236, 1237, and 1241. At Carnegie Ridge, off the coast of Ecuador, the picture is even more complicated because here the biogenic bloom persisted until ~3 Ma and Site 1238 and perhaps until ~2 Ma at Site 1239. However, equatorial Sites 1238, 1239, and 1241 are ideally located to monitor changes in biogeochemical cycles and equatorial oceanography that may result from the closure history of the Isthmus of Panama.

ORBITAL-SCALE CLIMATE VARIABILITY

Sites drilled during Leg 202 will provide an opportunity to examine the details of regional climate responses to the onset and amplification of Pleistocene ice age cycles at orbital scales over the last 5 m.y. Evidence from the Southern Ocean (Imbrie et al., 1993) and from the equatorial Pacific (Pisias and Mix, 1997; Lea et al., 2000) suggests that near-surface changes in these areas precede those at high northern latitudes. Thus, climate changes here do not passively respond to Northern Hemisphere glaciation but could be part of the chain of responses that led to Northern Hemisphere glaciation.

Especially important for Leg 202 will be to assess the linkages between changes observed at higher southern latitudes (e.g., Leg 177) with those along the equator (Sites 1238–1240). Site 1237 will provide a useful monitor of the advective link between the high and low latitudes, by monitoring the strength of the cool Humboldt Current at orbital scales of 10^4 – 10^6 yr. Comparison of benthic water mass tracers from sites at intermediate depths (Sites 1239 and 1242) with those at greater depths (Sites 1238 and 1240) will help to document the role of changing Pacific intermediate waters of northern and southern sources in large-scale climate change (Mix et al., 1991).

Within Pleistocene time, the origin of the large 100-k.y. climate cycle ~1 m.y. ago remains puzzling. A number of mechanisms have been proposed, including a threshold response of high-latitude glaciers to gradual long-term cooling associated with uplift of mountain ranges (Ruddiman and Raymo, 1988) or reduction of greenhouse gases (Maasch and Saltzman, 1990); a transition from land-based to marine-based ice sheets (Pisias and Moore, 1981; Berger and Jansen, 1994); erosion of soft sediment below Northern Hemisphere glaciers to expose bedrock, allowing larger glaciers to grow by increasing basal friction (Clark and Pollard, 1998); atmospheric loading of cosmic dust to trigger a response to rhythmic changes in the plane of Earth's orbit (Muller and MacDonald, 1997); and long-term cooling of the deep sea at polar outcrops, which influenced sea ice distributions (Gildor and Tziperman, 2001).

A 100-k.y. cycle of climate may also originate independently of polar climate changes via the responses of tropical climate systems to orbital changes in seasonal insolation (Crowley et al., 1992). Evidence exists for rhythmic 100-k.y. cycles of sedimentation in the eastern tropical Pacific that, if climatically significant, could have provided a "template" for a climate cycle that was later picked up by the global ice sheets (Mix et al., 1995). A range of evidence suggests that tropical climate changes

at orbital scales preceded those of the Northern Hemisphere ice sheets and must vary independently from the high northern latitudes (Imbrie et al., 1989; McIntyre et al., 1989; Pisias and Mix, 1997; Harris and Mix, 1999; Lea et al., 2000).

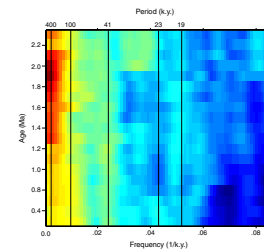
One prediction of climate models that create climate cycles of a 100-k.y. period from a tropical response to orbital precession is that strong cycles of ~400-k.y. duration must also be found. Although shipboard age models are not sufficiently refined to allow interpretation of all the orbital cycles, preliminary data from Leg 202 demonstrate the likely existence of orbital-scale variability in lithologies. Evolutive spectra of the optical lightness parameter L^* at Site 1239 (which here tends to mimic calcium carbonate concentrations in the sediment) reveal substantial changes in orbital-scale cycles through time (Fig. F37). Prior to ~1.2 Ma, large variations in sediment L^* occurred most strongly within a long period (~400-k.y.). Near ~1.0 Ma, this ~400-k.y. cycle broadens to include variability near the ~100-k.y. period. Rhythmic variations with ~400-k.y. periodicity are also present in reflectance-predicted TOC content at Site 1237 (Fig. F11), and in an interval with a well-constrained paleomagnetic age model, variations in GRA density at the orbital periods of tilt (~41 k.y.) and precession (~23 and 19 k.y.) are well defined (Fig. F19).

MILLENNIAL-SCALE CLIMATE CHANGES: POLAR, TROPICAL, OR EXTRATERRESTRIAL CAUSES?

A primary initiative for ODP is to understand the causes and consequences of millennial-scale climate change. Such changes, including the well-known “Heinrich” events at ~5- to 10-k.y. intervals and “Dansgaard-Oeschger” events of ~1- to 3-k.y. periods, are well documented in rapidly accumulating North Atlantic sediments (e.g., Labeyrie and Elliot, 1999; Clark et al., 2000). This regional expression of rapid climate change has led to hypotheses that millennial-scale changes are driven either by instabilities in Northern Hemisphere ice sheets that surround the North Atlantic region (MacAyeal, 1993), by oscillations in the formation of North Atlantic Deep Water (Broecker et al., 1990), or, in some cases, perhaps by rhythmic solar forcing that is expressed in the changing climate of the North Atlantic (Bond et al., 1997, 2001). Similar millennial-scale climatic oscillations have been detected in the northeast Pacific (e.g., Hendy and Kennett, 1999, 2000a, 2000b), suggesting the transmission of rapid climate change events from their North Atlantic origins into the Pacific (Mikolajewicz et al., 1997).

An alternative (but perhaps not mutually exclusive) hypothesis to explain the occurrence of millennial-scale climate change is that rapid climate oscillations may emanate from the tropics, where they originate as unstable responses to insolation (McIntyre and Molino, 1996). A likely tropical source of rapid climate variability may be modulation of interannual to decadal climate changes of the eastern tropical Pacific (Cane and Clement, 1999), a region well known for El Niño Southern Oscillation (ENSO) events. The tropical hypothesis is plausible, given lake and ice core records from South America that suggest long-term changes in the mean state of ENSO events (Thompson et al., 1998; Rodbell et al., 1999), glacial-interglacial sea-surface temperature changes that mimic spatial patterns of change associated with modern La Niña events (Pisias and Mix, 1997; Mix et al., 1999b; Beaufort et al., 2001),

F37. Evolutive spectra of the lightness parameter L^* , Site 1239, p. 112.



and model results suggesting the sensitivity of long-term average oceanic condition to changes in El Niño frequency forced by orbital insolation (Clement et al., 1999). It remains unclear how changes in the high latitudes and low latitudes interact, however.

On an interannual to decadal scale, Liu and Huang (2000) argue that warming in the equatorial Pacific over the past 50 yr is related to reduction of the wind-driven advection of cool water from the eastern boundary current and that such effects that dominate the eastern tropical Pacific extend even to the western Pacific and perhaps elsewhere. On longer (glacial–interglacial) timescales, a similar linkage between the equatorial Pacific and the eastern boundary current seems to be important (Pisias and Mix, 1997; Feldberg and Mix, 2002).

If the tropical hypothesis is true, we expect that millennial-scale climate events will be clearly recorded in sites with high sedimentation rates from the eastern equatorial Pacific, particularly near the Galapagos Islands, a region sampled at Site 1240. If the connection to the eastern boundary current is important in driving such changes, we might also expect to find similar patterns of variability in sites to the south, including Sites 1233, 1234, and 1235.

We already know, based on continental paleoenvironmental records in midlatitude Chile such as glacier advances in the southern Andes correlated to Northern Hemisphere climate events (Lowell et al., 1995; Denton et al., 1999), vegetation changes during both Termination 1 and marine isotope Stage 3 (MIS 3) (Heusser et al., 1999; Moreno et al., 2001), and weathering activity in the Chilean Norte Chico (27°S) (Lamy et al., 2000), that this region is very sensitive to rapid climate change. However, so far it has proven difficult to compare such changes unambiguously to those of the Northern Hemisphere because of limitations in dating.

Short marine cores from the region reveal that surface ocean properties also varied significantly within the southern Peru-Chile Current. Sea-surface temperature reconstructions based on the U^{k}_{37} method reveal pronounced millennial-scale oscillations during both the late glacial period (Kim et al., 2002) and the Holocene (Lamy et al., 2002). Similar variations in sea-surface salinity (SSS) reconstructed for the Holocene at Site 1233 indicate close links to continental climate changes, as SSS within this region is strongly influenced by freshwater input in the southern Chilean fjord region (Lamy et al., 2002).

Recent data, especially from the northeast Pacific (Behl and Kennett, 1996; Mix et al., 1999a; Lund and Mix, 1998) also affirm the importance of understanding Pacific deep and intermediate water circulation on millennial timescales. Broecker (1998) points to the existence of a “bipolar seesaw” effect, in which millennial-scale changes in Antarctic temperature are out of phase with (leading) Northern Hemisphere events. This inference is buttressed by data from the Southern Ocean (Charles et al., 1996) and by comparison of ice core $\delta^{18}\text{O}$ or ^2H data from both hemispheres synchronized with the methane record (Blunier et al., 1998). Because the patterns of change are significantly different in the Northern and Southern Hemispheres, we can use the pattern of ventilation events on the millennial scale as a “fingerprint” of their source.

In the Pacific, Northern Hemisphere sites such as Site 893 from the Santa Barbara Basin provide compelling evidence of millennial-scale events of enriched oxygen content (i.e., unvarved sediments containing oxic benthic foraminiferal assemblages), which are approximately correlated with cold events in the North Atlantic (Kennett and Ingram,

1995; Behl and Kennett, 1996; Cannariato et al., 1999). Off Oregon, Site 1019 (980 m water depth) suggests that regional productivity effects could contribute to variations in the oxygen minimum zone off California (Mix et al., 1999a) and that ventilation of intermediate water masses is stronger during warm (e.g., Bølling-Allerød) climate events than it is during cold (e.g., Younger Dryas) climate events. At greater water depths, a possible Southern Hemisphere connection is found, as variations in benthic foraminiferal $\delta^{13}\text{C}$ appear linked to the Antarctic Cold Reversal, which precedes Younger Dryas cooling of the Northern Hemisphere (Blunier et al., 1997). With these data alone, the processes responsible for millennial-scale climate changes in the Pacific remain unclear.

Leg 202 sites will contribute to the understanding of millennial-scale climate changes by providing records of high sedimentation rates from sites off central Chile (Sites 1233, 1234, and 1235), within the equatorial cold tongue (Site 1240), and on the Costa Rica margin (Site 1242).

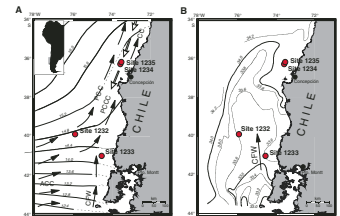
The sites drilled along the Chile continental margin at 41°S (Site 1233) and ~3°S (Sites 1234 and 1235) (Fig. F38) provide sediment sequences with the potential for unprecedented ultra-high-resolution records of surface and deep-ocean conditions as well as continental paleoclimates during the last two glacial-interglacial cycles.

Sites 1233–1235 are particularly well located for assessing variations in the strength of AAIW through time (Fig. F39). Site 1235 monitors the boundary between the GUC (the poleward undercurrent, a relatively low-oxygen water mass), and AAIW (a relatively high oxygen water mass). Site 1233 is located roughly in the core of AAIW and thus should provide the best available record of AAIW properties relatively close to its source in the Antarctic Subpolar Front. Finally, Site 1234 monitors the deeper boundary of AAIW in its zone of mixing with PCW (a relatively low oxygen water mass).

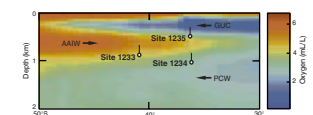
Together, these records will fill a crucial gap in the paleoceanographic archive because there are no existing high-resolution cores capable of monitoring the intermediate waters that upwell at low latitudes and influence productivity and carbon outgassing to the atmosphere (Broecker and Peng, 1982). The temperature changes deduced from benthic foraminiferal oxygen isotopes at Sites 1233–1235 should provide a sensitive monitor for assessing the effect of intermediate-depth temperature changes on tropical climate over millennial to decadal timescales. Thus, Sites 1233–1235 afford an excellent opportunity to examine the role of chemical changes in high-latitude surface waters that can be transferred to the tropics via AAIW (e.g., Oppo and Fairbanks, 1989; Ninnemann and Charles, 1997).

Shipboard biostratigraphic data indicate that the bases of Sites 1233–1235 are younger than 260 ka. Additional tentative stratigraphic markers are derived from analyses of paleomagnetic variations, such as the Laschamp Excursion at ~41 ka, which is particularly pronounced at Sites 1233 and 1234 (see “**Cenozoic Biostratigraphic and Magnetostratigraphic Reference Sections (Sites 1237 and 1241)**,” p. 14, and “**Age Models and Mass Accumulation Rates of Leg 202 Sites**,” p. 16. These data indicate that sedimentation rates are generally >50 cm/k.y. reaching >1 m/k.y. in major parts of the recovered sequences, particularly at Sites 1233 and 1235. Such high sedimentation rates at key locations provide an outstanding opportunity to explore atmospheric and oceanographic variability in the Southern Hemisphere on the relatively short timescales from millennia to centuries and perhaps even decades.

F38. Surface water temperature and salinity contours, Sites 1232–1235, p. 113.



F39. Locations of Sites 1233–1235 on subsurface oxygen contours, p. 114.



Sediments at all three sites are dominated by lithologically homogeneous fine-grained terrigenous material with very high magnetic susceptibilities (Fig. F40). Minor amounts of biogenic components, mostly well preserved for paleoceanographic studies, are present throughout nearly the entire recovered sequences. The high sedimentation rates can be explained by extremely high terrigenous sediment supply due to enhanced fluvial discharge in response to heavy continental rainfall (Lamy et al., 2001). Probably in response to northward decreasing precipitation, sedimentation rates appear to be lower at Sites 1234 and 1235 when compared to Site 1233, particularly during MISs 2 and 3. However, this pattern might have been different in the older parts of the records, either indicating a different contribution of syndepositional sediment focused within the local basins or different rainfall patterns during MISs 5 and 6.

The magnetic susceptibility records of all sites document pronounced variability both on Milankovitch and sub-Milankovitch timescales. Higher magnetic susceptibility appears to be characteristic of glacial intervals, which might indicate increased terrigenous sediment input due to higher rainfall during regional cold phases. This is consistent with findings from marine sediment cores off central and northern Chile (Lamy et al., 1998, 1999).

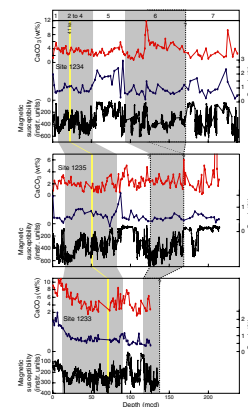
Even as the Leg 202 cores were being analyzed at sea, we were able to develop preliminary age models based on correlation of magnetic susceptibility data from Site 1233 and from a ^{14}C -accelerator mass spectrometry (AMS)-dated gravity core taken previously at the site that spans the last ~8000 yr (Lamy et al., 2001). In addition, shipboard paleomagnetic data revealed a major excursion of Earth's magnetic field, which we correlated to the well-known Laschamp Excursion at ~41 ka. The shipboard chronologies do not yet allow us to link specific variations in magnetic susceptibility at Sites 1233–1235 to climate changes recorded in either the Northern Hemisphere or Southern Hemisphere ice sheets. Nevertheless, it is already clear that such linkages are likely to be found. For example, within the interval of the last ~45 k.y., Site 1233 displays strong sub-Milankovitch variability with general patterns similar to those observed in polar ice cores (Fig. F41). By analogy to variations within the Holocene (Lamy et al., 2001) and to longer-period glacial–interglacial variations in the region, we expect that the variations in magnetic susceptibility at Site 1233 are related to changes in continental rainfall, which probably reflect latitudinal shifts of the southern westerly winds.

Shipboard data on diatom abundance and assemblage composition reveal pronounced sub-Milankovitch variability, possibly reflecting changes in upwelling and biological production at Site 1233. Furthermore, significant changes in continental freshwater input seem to be indicated by the abundance of freshwater diatoms.

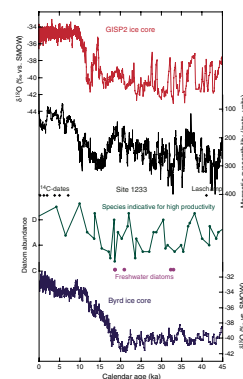
In the tropics, Site 1240 is ideally located to assess rapid variations in equatorial upwelling, perhaps related to long-term stability of ENSO events (Clement et al., 1999; Beaufort et al., 2001). Here, sedimentation rates are near 10 cm/k.y., suggesting that climate changes on the scale of centuries may be well recorded here.

Site 1242 will provide for analyses of sea-surface salinities in the Panama Basin, related to excess precipitation relative to evaporation near the intertropical convergence. This region of the Panama Basin is noted for its extreme warmth (often $>30^\circ\text{C}$), exceptionally low salinity (near 32), and a strong, shallow pycnocline (typically centered near 20–40 m depth). These features all reflect high rainfall relative to evaporation

F40. Shipboard correlation of data, Sites 1233–1235, p. 115.



F41. Millennial-scale variability, Site 1233, p. 116.



(Magaña et al., 1999), which stabilizes the water column and diminishes vertical mixing of heat and other properties. A portion of the net freshwater flux to the Panama Basin originates in the Atlantic or Caribbean (Jousaumme et al., 1986), so low salinities here partially reflect the transport of freshwater from the Atlantic to Pacific Basins via the atmosphere. The dynamics of this transport are important because this relatively small transport of freshwater helps to maintain the relatively high salinity of the Atlantic Ocean—a key parameter in maintaining the global thermohaline “conveyor belt” circulation dominated by North Atlantic Deep Water production (Zaucker et al., 1994; Rahmstorf, 1995). Thus, a millennial-scale record of sea-surface salinity variation at Site 1242 will help to test the tropical hypotheses of rapid climate change and will evaluate a possible mechanism that would link climate changes of the tropics via the hydrological cycle to those of the high latitudes through the control of oceanic salinity budgets on deepwater formation.

Variations in paleomagnetic secular variation and NRM intensity observed at Sites 1233–1235 and 1240 will likely facilitate synchronization of these important Southern Hemisphere sedimentary records to high-resolution records from the Northern Hemisphere, and this will provide a test of the phasing of millennial-scale climate changes between the two hemispheres.

SUMMARY AND PERSPECTIVES

Leg 202 set out to study the oceanic, climatic, and biogeochemical systems in the southeast Pacific. Drilling probed these systems on scales that range from tectonic (millions of years) to orbital (tens of hundreds of thousands of years), and centennial to millennial (hundreds of thousands of years). The experiment addressed hypotheses on (1) the response of the South Pacific to major tectonic and climatic events, such as the opening of the Drake Passage, uplift of the Andes Mountains, closure of the Panama Isthmus, and major expansion of polar ice sheets; (2) linkage between climate changes in the high latitudes and the equatorial Pacific related to rhythmic changes in Earth’s orbit and the relationship of such changes to known glacial events of the Northern Hemisphere; and (3) regional changes in climate, biota, and ocean chemistry on scales of centuries to millennia. The southeast Pacific is a relatively unstudied area, so Leg 202 opened study of new regional elements of the global climate system.

A total of 7081 m of sediment was recovered at 11 sites that form a latitudinal transect from 41°S to 8°N as well as a transect of intermediate to deep water masses at water depths of 490–4070 m. Sediments range in age from early Oligocene (~31.5 Ma) to Holocene (Tables T1, T2; Fig. F2). Operational successes during Leg 202 include the ability to make real-time drilling decisions by using a rapid-scanning core logging track. Based on the availability of these logging data, efficient planning of operations made time for extensive drilling over of APC cores that improved recovery. As a result, at all sites, we documented essentially complete recovery in some of the longest APC-cored intervals in ODP history (six holes >250 m and three holes >300 m). In some instances, recovery was nearly complete in double XCB-cored intervals at even greater depth. Other innovative operations included the use of a non-magnetic core barrel, which significantly improved the quality of shipboard paleomagnetic data. The combination of detailed magnetic strati-

graphies with excellent biostratigraphies based on all major microfossil groups provided a unified chronologic framework at sites that range from cool subtropical to warm tropical settings.

The diversity of sites as a function of latitude, water depth, sedimentation rate, and biological production of overlying waters yielded a unique opportunity to understand the role of organic matter oxidation on interstitial water chemistry. These findings provide significant geochemical constraints on the interpretation of climate and biogeochemical changes from sedimentary records. For example, sites with complete sulfate reduction (1232–1235, 1239, and 1242) are likely to be influenced more heavily by authigenic carbonate remineralization. Sites with little or no sulfate reduction (1236, 1237, and 1241) have very little remineralization of carbonates and offer opportunities for development of exceptionally long pelagic records. Two shallower sites on the Chile margin (1233 and 1235) gave clear evidence of methane hydrates based on chloride decreases in interstitial waters, whereas one site (1240) revealed active fluid flow in the underlying basement.

The sedimentary imprint of the gradual plate tectonic drift of sites relative to the continental margin is clear, but superimposed on these long-term trends are substantial variations in local environments that drive changes in the production and preservation of biogenic sediment components and modify the supply of terrigenous sediments. For example, the slow drift of Site 1237 (Nazca Ridge) toward South America resulted in increasing terrigenous and opaline sediments at younger ages. Noncarbonate sediments also generally increased at younger ages at Sites 1238 and 1239 (Carnegie Ridge) as they approached South America, but gradual changes were punctuated by high sedimentation rates ~2–5 Ma. In contrast, Site 1241 (Cocos Ridge) recorded a long-term decrease in noncarbonate sedimentation at younger ages, as this site drifted to the northeast away from the productive equator.

An interval of low carbonate accumulation from 11 to 9 Ma has been referred to in the equatorial Pacific as a carbonate-crash event of poor preservation, perhaps related to deep-sea circulation. Our finding of low carbonate accumulation within this interval at Site 1236, which occupied relatively shallow paleo-water depths (<1000 m), suggests that low production may also have contributed to the carbonate-crash event.

A stepwise increase in terrigenous dust flux (Site 1237) and hematite contents (Site 1236) since 8 Ma may reflect a critical threshold in the history of Andean uplift, which strengthened the equatorward trade wind circulation and enhanced coastal upwelling and productivity. At approximately the same time, discrete ash layers began to appear at Site 1237, perhaps recording the onset of intense volcanism that accompanied the tectonic uplift of the Andes. More than 200 volcanoclastic horizons were deposited during the last ~9 m.y. at this site. Maxima in ash layer frequency occurred at ~8–6 Ma and during the last 3 m.y.

An interval of distinctly high carbonate accumulation rates, with an essentially synchronous onset near 7 Ma at Sites 1236–1239 and 1241 and at other equatorial Pacific sites (Legs 130 and 138), is thought to represent a widespread Miocene interval of high production and is often referred to as a biogenic bloom. Our finding of this carbonate bloom event at all water depths confirms production as the cause. Furthermore, our discovery of the event in the southeast Pacific proves that the event is not uniquely associated with equatorial upwelling as some previous hypotheses suggested, but instead may be linked to sub-

stantial changes in the eastern boundary current system or regional nutrient budgets.

The termination of the bloom event appears to be diachronous, as early as 5 Ma at the deepwater sites (e.g., Sites 849 and 850 drilled during Leg 138) but as late as 3 Ma at Site 1238 and, perhaps, even 2 Ma at Site 1239, two relatively shallow sites on Carnegie Ridge. Such diachrony associated with water depth points to the influence of decreasing carbonate preservation through Pliocene time, perhaps a response to shoaling and final closure of the Panama Isthmus and the development of the global “conveyor belt” deep circulation between the Atlantic and Pacific.

Most of the sequences recovered during Leg 202 reveal clear lithologic changes in meter and decimeter scales that are most likely related to orbitally induced changes in precession and obliquity. If so, these cycles provide a basis for (1) developing orbitally tuned age models and (2) testing the phase relationships between major climate and oceanographic components to assess the role of South Pacific oceanography and biogeochemistry within a chain of climate forcing mechanisms related to orbital changes in the capture of insolation. An apparent ~400-k.y. cycle of lithologic change at several sites, especially prior to 1 Ma, is consistent with low-latitude climate oscillations driven by orbital precession, which can induce such long-period variations from responses to shorter-period orbital changes.

An especially exciting result of Leg 202 was the successful recovery of unprecedented ultra-high-resolution records from the Chile continental margin between 41° and 36°S at water depths between 490 and 1115 m (Sites 1233–1235). Shipboard stratigraphic data indicate that these records have exceptionally high sedimentation rates of up to 160 cm/k.y., apparently driven by extremely high terrigenous sediment supply in response to heavy continental rainfall. Dominance of siliciclastic sediments here also yielded a highly refined record of paleomagnetic variations. The Laschamp magnetic event at ~41 ka is particularly pronounced (e.g., covering an interval of ~2 m at Site 1233). These extraordinary paleomagnetic records provide opportunities for high-resolution regional and global correlation of marine and terrestrial records using paleomagnetic secular variation and paleointensity variation. This synchronization strategy will help to establish the relative phasing of millennial-scale climate changes in the Southern and Northern Hemispheres and offer the potential for fundamental advances in understanding the dynamics of Earth’s magnetic field. Together with a rich array of well-preserved biogenic and mineralogic tracers of paleoclimate utility, these sites provide a unique chance for understanding the role of South Pacific oceanography and Southern Hemisphere climate in a global context on scales from millennia to centuries, and perhaps even decades.

In the tropics, rapid climate change and oceanographic changes on the scale of centuries and millennia are recorded at Site 1240 in the Panama Basin and at Site 1242 on Cocos Ridge. Both sites provide a complete stratigraphic sequence of the last ~2.6 m.y. with sedimentation rates varying in the range of at least 5–17 cm/k.y. Persistent decimeter- to meter-scale variability in core logging data (bulk density and magnetic susceptibility) are mainly related to changes in the relative supplies of carbonate, biosiliceous, and siliciclastic material and are tentatively interpreted to reflect millennial-scale changes in equatorial productivity and/or climate.

As with most ODP legs that focus on paleoceanographic objectives, rigorous tests of hypotheses must await detailed shore-based studies. Isotopic, geochemical, magnetic, faunal, and floral studies are planned. These studies will refine chronologies based on improved biostratigraphies, detailed tuning of lithologic and isotopic data to known changes in Earth's orbit, and linkage to radiometric dates via the paleomagnetic record. With these high-resolution data, refined reconstructions of sediment mass accumulation rates will lead to better understanding of variations in production and preservation of biogenic sediments. Changes in the input of terrigenous sediment components to the ocean will reveal new information about climatic and tectonic influences on continental erosion and explosive volcanism. Detailed studies of organic components, and their nitrogen and carbon isotopic character, along with biotic tracers of productive upwelling systems such as diatom species, will yield insights into nutrient cycling in the region. Analysis of subsurface water masses using isotopic, geochemical, and faunal analyses will help us to understand the role of the South Pacific in the global circuit of matter masses that is thought to influence global climate and biogeochemistry.

Leg 202 has opened a new window into understanding global environmental change, by providing high-quality sediment sequences from a previously unsampled region, by targeting sites that record variations on timescales ranging from decades to tens of millions of years, and by analyzing transects of both depth and latitude. We expect that this strategy will establish the linkages between a broad range of systems and will reveal the role of the southeast Pacific in global climate.

LEG 202 SITE SUMMARIES

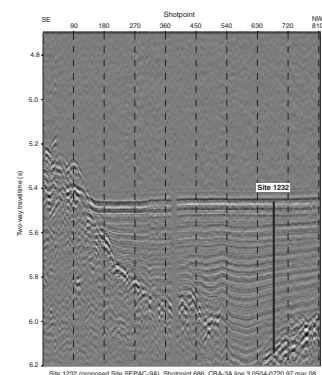
Site 1232

Site 1232 (proposed Site SEPAC-09A) is located in the Chile Basin between the Mocha and Valdivia Fracture Zones ~50-km westward of the Peru-Chile Trench (Fig. F1). The water depth of 4072 m is ideal to monitor the influx of CPDW into the Chile Basin (Fig. F5) and variations in terrigenous sediment transported from southern Chile. Crustal ages are not well defined but are expected to be between 19 and 29 Ma based on limited study of regional seafloor magnetic lineations. The total thickness of the sedimentary section was estimated at 470 m based on site survey seismic profiles that revealed well-stratified, moderately reflective layers in a style characteristic of hemipelagic sediments (Fig. F42).

The primary paleoceanographic objectives at Site 1232 were to recover a nearly continuous sequence of Neogene hemipelagic sediments for paleoceanographic investigations to (1) reconstruct variations in the character of the Antarctic CPDW as it enters the Chile Basin from the south and (2) assess variations in the southernmost reaches of the northward-flowing Peru-Chile Current.

Three holes were drilled at Site 1232 (Table T2) during relatively high swell following a force 8 storm. Hole 1232A was cored with the APC from 0 to 112.5 mbsf and then was deepened with the XCB to 371.3 mbsf. Holes 1232B and 1232C included 10 APC cores to 90.1 mbsf and four APC cores to 33.2 mbsf depth, respectively. A composite section and splice documented nearly complete recovery for the upper 100 mcd.

F42. Seismic profile across Site 1232, p. 117.



The 390.6-mcd-thick (371.3 mbsf) sequence recovered at Site 1232 represents an expanded upper Pleistocene section (<1 Ma) of silty clay (inferred upper parts of turbidites and hemipelagic sediments) interbedded with >800 graded layers of silty sand beds with sharp, sometimes scoured, basal contacts (basal parts of distal turbidites) (Fig. F43). The silty sand layers are marked by high magnetic susceptibility and GRA bulk density, and low chroma (a^* and b^*) and reflectance (L^*) values. Over the entire cored interval, the sandy silt turbidite layers range from a few millimeters to 118 cm in thickness (average = 3 cm) (Fig. F43) and are present throughout the section between silty clay layers that range from a few millimeters to 610 cm in thickness (average = 27 cm). The thickness and frequency of the turbidites decrease downhole: recognized sandy silt intervals account for ~22% of the section from 0 to 20 mbsf, 15% of the section from 20 to 200 mbsf, and 3% of the section from 200 to 250 mbsf. Within both interbedded lithologies, clay minerals and feldspar are common, whereas amphiboles, pyroxenes, mica, and quartz are present in minor amounts, consistent with a source area dominated by andesitic volcanic rocks of the Andes Mountains. A plausible transport path for turbidity currents is via the southernmost extent of the Chile Trench north of Chile Rise, where the trench has relatively little bathymetric expression. Calcium carbonate contents are typically low, less than a few weight percent, although isolated peaks were found with values as high as 27 wt%. The sediments are poor in organic carbon, typically <0.25 wt%. Organic carbon/organic nitrogen ratios indicate dominance of marine organic matter.

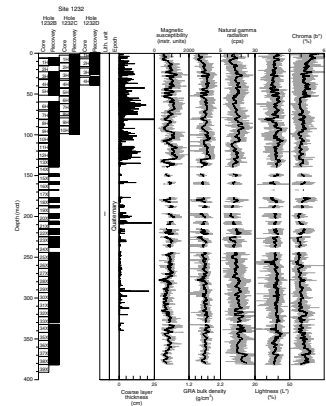
The abundance of calcareous microfossils at Site 1232 is generally low, and their preservation is generally poor to moderate. Diatom abundance and preservation fluctuate significantly and deteriorate noticeably at depths >202 mcd. Reworking of microfossils is apparent in all the fossil groups examined. In particular, freshwater diatoms such as *Aulacoseira granulata* and shallow-water benthic species such as *Eunotia* spp. are abundant in the intervals 43–69 and 193–241 mcd and indicate reworking from continental or nearshore sources. Calcareous nannofossils suggest an age of 0.26 Ma at 143 ± 5 mcd, 0.46 Ma at 259 ± 5 mcd, and <1.7 Ma for the deepest core at 382 mcd.

NRM intensities at Site 1232 were extremely high both before (mean = 1.41 A/m) and after alternating-field (AF) demagnetization (0.21 A/m) at peak fields up to 20 mT. The large drop in remanence intensity after demagnetization is due to the removal of a strong drill string overprint. Aside from drilling disturbance and the drill string overprint, the NRM after demagnetization is characterized by negative inclination (normal polarity) throughout the sequence and therefore is interpreted to represent the Brunhes Chron (0–0.78 Ma).

Results from gas, interstitial water, and sedimentary composition measurements at Site 1232 reflect the influences of organic matter diagenesis and the low biogenic content of sediments at this site. The sediments were moderately gassy, with methane dominating the gas composition throughout.

The seismic reflection profile indicates an unconformity between acoustic basement (which may be lithified sediment) and the turbidite-dominated Pleistocene sequence. Extrapolation of the high late Pleistocene sedimentation rates (>450 m/m.y.) to the unconformity suggests that much of the sediment accumulation here has occurred within the last million years. A similar situation has been described on the Peru continental margin, with a change from carbonate to terrigenous deposition in the late Pleistocene (0.93–0.44 Ma). Whether these dramatic

F43. Core recovery, lithology, age, and physical and chemical data summary, Site 1232, p. 118.



secular changes in sedimentation off western South America can be attributed to changes in tectonics or climate remains a question. On the fine scale, inferred sedimentation rates imply that the turbidite layers observed at Site 1232, which have an average depth spacing of ~30 cm, have an average recurrence time on the order of hundreds of years. Great earthquakes associated with active tectonism of southern Chile, as well as century- to millennial-scale climate changes, may serve as possible triggers for large turbidity flows that transport continental sands and silts to Site 1232. The primary postcruise opportunity at Site 1232 will be to understand this record of turbidity flows and the record of terrigenous sediment components it provides. In addition, it may be possible to extract a paleoceanographic record from the pelagic sediments that are preserved between the turbidite layers, although such a record may be incomplete.

Site 1233

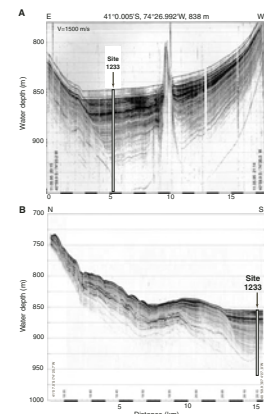
Site 1233 (proposed Site SEPAC-19A) is located 38 km offshore (20 km off the continental shelf) at 838 m water depth in a small forearc basin on the upper continental slope (Fig. F1). Predrilling survey data included high-resolution Parasound profiles and 3.5-kHz profiles that imaged the site to a depth of 110 mbsf (Figs. F44, F45) and 8-m sediment core (GeoB3313-3) that suggested continuous sedimentation at the site at rates of 100 cm/k.y. during the Holocene.

The intent of drilling at Site 1233 was to recover a very high resolution hemipelagic record of upper Quaternary sediments for paleoceanographic investigations to (1) reconstruct millennial- to century-scale changes of climate related to latitudinal shifts of the westerly wind belt, upwelling intensity, and productivity; (2) assess variations in terrigenous sediment components off south-central Chile to reconstruct climate variability on land; (3) reconstruct sea-surface salinity anomalies that may record variations in river runoff or episodes of net glacier retreat in the fjord region of southern Chile; and (4) monitor changes in the signature of AAIW (proxies related to temperature, salinity, nutrients, and oxygen), which ventilates the South Pacific at intermediate depths.

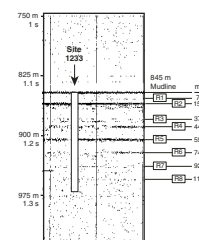
Five APC holes were drilled at Site 1233 (Table T2). Hole 1233A was terminated after the first core was retrieved without a mudline. Hole 1233B provided a good mudline and was cored to 109.5 mbsf. Holes 1233C, 1233D, and 1233E were cored to depths of 116.3, 112.3, and 101.5 mbsf, respectively (Table T2). Seven downhole temperature measurements were taken with the APCT tool, yielding a temperature gradient of ~4.5°C/100 m.

A 136.1-mcd-thick (116.8 mbsf) upper Pleistocene hemipelagic sediment sequence was recovered at Site 1233 (Fig. F46). A composite section and splice based on high-resolution core logging data documented continuous recovery to the bottom of the sequence (Fig. F46). The sediment consists primarily of clay and silty clay with varying amounts of calcareous nannofossils. Interbedded minor lithologies include thin silt-rich layers, which might represent distal turbidites, and five volcanic ash layers that will serve as regional stratigraphic markers. The relative paucity of turbidites in the basin suggests that sediment gravity flows were mostly channeled away from the basin in the extensive system of canyons that characterizes this portion of the Chile margin. Mineral assemblages are consistent with a siliciclastic provenance in both the Andes (relatively rich in feldspar) and the Coastal Range (rela-

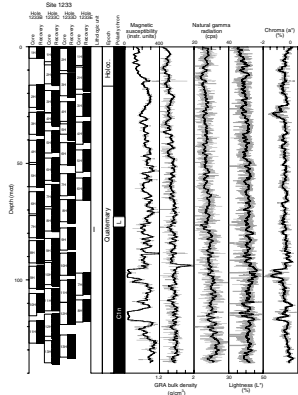
F44. Digital Parasound profile, Site 1233, p. 119.



F45. Analog 3.5-kHz profile acquired during the approach to Site 1233, p. 120.



F46. Core recovery, lithology, age, and physical and chemical data summary, Site 1233, p. 121.



tively rich in quartz) in southern Chile. The quartz/feldspar ratio decreases downhole, indicating a change in provenance favoring Andean sources during older intervals.

Calcium carbonate concentrations range between 1 and 11 wt% (average = 5.4 wt%). Calcium carbonate and TOC contents (range = 0.4–2.5 wt%; average = 0.9 wt%) decrease downhole from the Holocene to the glacial interval, consistent with either significant terrigenous dilution of the biogenic components or downhole diagenesis. C/N ratios of TOC average 5.9, consistent with a marine origin of the organic matter. Preliminary predictive relationships between color reflectance spectra and carbonate and TOC, developed via a multiple linear regression, indicate substantial millennial- to centennial-scale variability in these biogenic components.

Calcareous nannofossils, foraminifers, and diatoms are abundant and well preserved at Site 1233. The presence of *Emiliania huxleyi* to the bottom of Hole 1233B indicates that the entire sequence is younger than 0.26 Ma. The planktonic foraminiferal assemblage, including *Globigerina bulloides* and *Globorotalia inflata*, is typical of eastern boundary settings in the transition from subtropical to the subpolar systems. The benthic foraminiferal assemblage represents 15% to 50% of the total foraminifers and indicates an upper to middle bathyal environment with high carbon fluxes to the seafloor. The diatom flora includes *Chaetoceros* spores, bristles, vegetative cells, and *Thalassiosira* species and reflects intermittent upwelling conditions at Site 1233. Freshwater diatoms, mainly *Aulacoseira granulata*, are in low abundance throughout the core. Silicoflagellates, radiolarians, sponge spicules, and phytoliths are observed in most samples.

NRM intensities at Site 1233 were extremely high before and after AF demagnetization at peak fields up to 25 mT. AF demagnetized inclinations averaged approximately -52° , close to the expected inclination for an axial geocentric dipole (-59°) at this site latitude ($\sim 41^\circ\text{S}$), indicating that the drill string overprint was largely removed. The negative inclinations are consistent with normal polarity, and the entire sequence is interpreted to lie within the Brunhes Chron (0–0.78 Ma). Fine-scale variations in magnetic inclination and declination are consistent from hole to hole, suggesting that a high-fidelity record of paleomagnetic secular variation was recorded. Anomalous magnetic directions and low remanence intensities over a 2-m interval between 65 and 70 mcd in Holes 1233B, 1233C, and 1233D may represent the Laschamp geomagnetic field excursion (~ 41 ka). Normalization of the demagnetized NRM intensity by MST-derived magnetic susceptibility suggests that these sediments may provide high-resolution records of relative geomagnetic paleointensity. These extraordinary records should provide opportunities for high-resolution regional correlation of marine and terrestrial records using paleomagnetic secular variation and, perhaps, global correlation through paleointensity variations. Two intervals with exceptionally low remanence intensity (95–101 and 113–118 mcd) may reflect events of extreme sediment diagenesis.

A preliminary age model was constructed based on the correlation of the magnetic susceptibility of the uppermost 9 mcd to the ^{14}C -dated sediment record of core GeoB 3313-1, recognition of the Laschamp geomagnetic excursion, and tentative constraints provided by correlation of relative paleointensity to similar data from Site 1089 that has been calibrated with oxygen isotope stratigraphy. MARs and LSRs estimated from this age model are 80 g/cm²/k.y. and 110 cm/k.y., respectively, for the Holocene and have maximum values of at least 150 g/cm²/k.y. and

160 cm/k.y., respectively, for much of the last glacial interval (MIS 2–3). Such high MARs and LSRs can be explained by extremely high fluvial sediment discharge in response to glaciation, heavy rainfall associated with the Southern Hemisphere westerly winds, and a dense drainage system in mountainous southern Chile. Prior to the Laschamp excursion, inferred sediment MARs and LSRs were 50 g/cm²/k.y. and 50 cm/k.y., respectively, suggesting that either transport pathways of terrigenous material and/or local syndepositional sediment focusing was different in the older interval. However, no major change in sediment composition accompanied this drastic shift in sedimentation rates.

Gas, fluid, and sediment geochemical profiles are dominated by the influence of organic matter diagenesis, despite the relatively low TOC contents at Site 1233. Sulfate reduction is complete by 5 mcd. Methane, apparently of biogenic origin, is found in high concentrations at depths >20 mcd. The zone of sulfate depletion is marked by a maximum in dissolved barium, possibly from barite dissolution. Dissolved calcium concentrations drop rapidly, consistent with the effects of authigenic mineralization reactions driven by the high alkalinity values. Interstitial water chloride concentrations decrease by >10% over ~120 mcd, indicating the possible presence of gas hydrates.

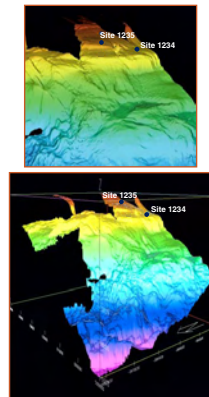
The combination of continuous recovery in a composite section to ~136 mcd, exceptionally high sedimentation rates apparently driven by input of terrigenous silt and clay in a hemipelagic setting, an extraordinary record of paleomagnetic field variations, clear geochemical signatures of organic matter diagenesis and authigenic mineralization, and a rich array of well-preserved biogenic and mineralogical tracers of paleoclimatic utility suggest that Site 1233 will provide unprecedented opportunities for understanding Southern Hemisphere and global climate changes and properties of Earth's magnetic field on scales from millennia to centuries, perhaps even decades.

Site 1234

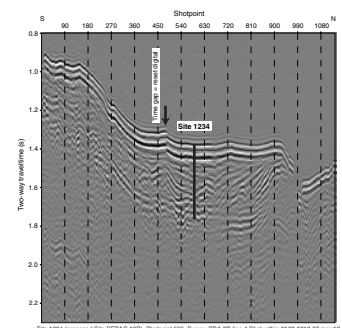
Site 1234 (proposed Site SEPAC-13B) is located ~65 km offshore (5 km off the continental shelf) and 60 km shoreward of the Peru-Chile Trench within the influence of the highly productive coastal upwelling center near Concepción, Chile (Figs. F1, F38). It is positioned on a relatively flat bench in the middle of the continental slope at 1015 m water depth, ~526 m deeper than and 10 km to the southwest of Site 1235 (Figs. F47, F48). We expect that these two sites have been influenced by similar surface water conditions, so major differences in physical, chemical, and paleontological properties can be attributed to depth-related effects. Precruise seismic survey data suggested mostly hemipelagic sedimentation at Site 1234. The uppermost part of the seismic profile shows flat-laying reflectors with undulating but continuous layers farther below, possibly reflecting the original relief of the acoustic basement (Fig. F48).

This site takes advantage of the high sedimentation rates on the continental margin that will allow reconstruction of regional climate and oceanographic variability on millennial to centennial timescales for the late Quaternary. Major objectives were to (1) assess late Quaternary history of productivity and coastal upwelling near Concepción, which is sensitive to regional winds, (2) assess variations in terrigenous sediment components off central Chile to reconstruct climate variability on land, (3) monitor changes in the boundary between oxygen-rich (nutrient poor) AAIW and oxygen-poor (nutrient rich) PCW, and (4) assess late

F47. Swath bathymetry of a Chile margin segment, p. 122.



F48. Seismic profile across Site 1234, p. 123.



Site 1234 (proposed Site SEPAC-13B), Shotpoint 045, Survey CBA-3D line 4 Blue within 2100-0018 97 mar-12

Quaternary variations in paleomagnetic intensities and field directions in the southeast Pacific as a stratigraphic tool for comparison with similar data from the Northern Hemisphere.

Three holes were drilled at Site 1234 (Table T2). Hole 1234A was initiated with a mudline APC core, advanced to 100.3 mbsf, and deepened with XCB coring to the target depth of 205.2 mbsf. Hole 1234B was cored with the APC from the mudline to 93.8 mbsf and deepened with the XCB to 182.4 m. Hole 1234C was cored with the APC to a depth of 79.1 mbsf to target remaining coring gaps. Four downhole temperature measurements were taken with the APCT tool, yielding a temperature gradient of $\sim 4.2^\circ\text{C}/100\text{ m}$. Most cores were affected by expanding gas during recovery. Holes were drilled in liners to relieve gas pressure to the extent possible, and major voids were closed prior to core logging operations.

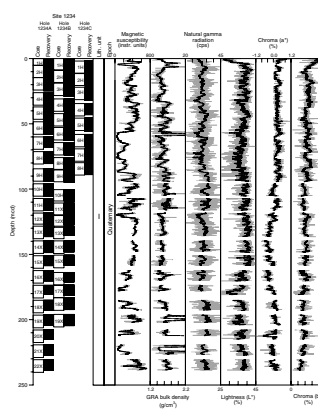
A 239-mcd-thick (203.8 mbsf) upper Quaternary hemipelagic sediment sequence was recovered at Site 1234 (Fig. F49). A composite depth scale and splice based on high-resolution core logging data document complete recovery from 0 to 94.4 mcd and a nearly complete recovery to 240.4 mcd. Sediments consist primarily of homogeneous dark olive-gray to dark gray silty clay and clay. The dominant siliciclastic component provides high magnetic susceptibility and natural gamma radiation (NGR) values. The quartz/feldspar ratio decreases downhole, reflecting a change in the source region of siliciclastic sediment supply as basaltic to andesitic rocks from the Andes are relatively rich in feldspar, whereas the predominantly metamorphic rocks from the Coastal Range province are rich in quartz. Recognizable turbidites in the form of thin silt-rich layers are rare, indicating that major turbidity flows are contained in the extensive channel system that characterizes this steep continental margin. We recovered eight ash layers that may provide useful stratigraphic markers in the region.

Calcium carbonate concentrations are low, ranging from 1 to 12 wt% (average = 3.5 wt%). TOC concentrations are also low, ranging from 0.2 to 3.0 wt% (average = 1.1 wt%). TOC/TN ratios range between 5 and 10, indicating a mostly marine origin of the organic matter, although a positive correlation between C/N and TOC suggests that some contribution of terrigenous organic matter, or selective preservation effects, may contribute to the observed variability. Biogenic material decreases downhole, either indicating dilution of biogenic material with siliciclastic detritus, a decrease in biogenic productivity, or an increase in diagenetic dissolution of biogenic components.

Diatoms are abundant and are dominated by upwelling related taxa. Despite the dominance of the coastal upwelling forms, warm water species are present in higher abundance below 62 mcd, whereas cold-water forms dominate the younger record. Benthic diatoms are present in most of the samples, indicating relatively persistent redeposition from the upper continental margin.

Calcareous nannofossils are abundant and moderately to well preserved, except for the core-catcher samples from the lowermost six cores where recrystallization was significant. The presence of *Emiliana huxleyi* suggests that the base of the cored interval has an age of $<0.26\text{ Ma}$. Planktonic foraminifers are present in all samples, but abundance and preservation vary markedly. The generally good preservation of carbonate fossils in most samples confirms that the relatively low carbonate contents result mostly from dilution by siliciclastic material rather than from dissolution. The benthic foraminiferal assemblage represents 20% to 98% of the total foraminifers and is dominated by species asso-

F49. Core recovery, lithology, age, and physical and chemical data summary, Site 1234, p. 124.



ciated with high carbon fluxes in coastal upwelling regions. Downhole variations are interpreted to reflect shifts in bottom water oxygenation related to either changes in water masses at the seafloor or changes in surface production and the export of organic matter. For example, a distinct pronounced peak in the abundance of *Bolivina* spp. at ~175 to 223 mcd points to an intense episode of seafloor dysoxia.

NRM intensities at Site 1234 were extremely high before and after AF demagnetization at peak fields up to 25 mT. AF demagnetized inclinations averaged approximately -30° , far from the expected inclination for an axial geocentric dipole (-55°) at this site latitude ($\sim 36^\circ\text{S}$), indicating that the drill string overprint was substantial. Patterns of paleosecular variation are apparent and include directional excursions in both inclination and declination in three holes from 21 to 23 mcd, which may represent the Laschamp Excursion (~ 41 ka). If so, average sedimentation rates in the upper 23 mcd are ~ 50 cm/k.y. The basal nannofossil age of <260 ka suggests higher sedimentation rates (average = >100 cm/k.y.) prior to 41 ka. Site 1234 likely records at least the last two late Pleistocene glacial–interglacial cycles at very high resolution.

Gas, fluid, and sediment geochemical profiles are dominated by the influence of organic matter diagenesis, despite the relatively low TOC contents. High amounts of methane and low amounts of ethane indicate that the gas is biogenic in origin. High alkalinity and high concentrations of ammonium and phosphate in interstitial waters also result from organic matter degradation by sulfate reduction and methanogenesis. Dissolved calcium concentrations drop rapidly below the sediment/water interface, consistent with the effects of authigenic mineralization reactions driven by the high alkalinity values. Magnesium/calcium ratios increase to >30 between 17.9 and 40.4 mcd, which is consistent with authigenic precipitation of calcite in shallower sediments. At greater depths, magnesium/calcium ratios decrease to ~ 12 by 230 mcd, indicating that authigenic mineralization reactions such as dolomite formation may take up magnesium deeper in the sediments.

With a nearly complete recovery to ~ 239 mcd, a rich assemblage of biogenic fossils and terrigenous sediment components, promise of an improved paleomagnetic record after further removal of overprints, and sedimentation rates high enough to record millennial-scale climate variability over at least one full (and perhaps several) glacial cycles, and evidence for substantial variations in biogenic production and bottom water properties all suggest that Site 1234 will provide an extraordinary record of Southern Hemisphere climate and biogeochemical changes of the late Quaternary.

Site 1235

Site 1235 (proposed Site SEPAC-14A) is located at a water depth of 489 m on a gently sloping terrace of the upper continental slope ~ 65 km shoreward of the Peru-Chile Trench and ~ 60 km offshore (Figs. F1, F38, F47). This site underlies a highly productive coastal upwelling zone off Chile, 526 m shallower than and 10 km to the northeast of Site 1234. We expect that these two sites have been influenced by similar surface water conditions, so major differences in physical, chemical, and paleontological properties can be attributed to depth-related effects. Predrilling surveys including gravity cores and seismic data point to high hemipelagic sedimentation rates at the site. The upper part of the seismic profile documents well-stratified, flat-lying reflectors. At greater depths, deformed but continuous layers of moderate reflection

appear to smooth the original relief of the acoustic basement, which is likely to be continental crust (Fig. F50).

This site was chosen to take advantage of expected high sedimentation rates to decipher the late Quaternary history of regional continental climate and oceanography on millennial to centennial timescales. Primary goals at Site 1235 were to (1) assess fluctuations in biological productivity and coastal upwelling that is sensitive to regional winds, (2) assess the late Quaternary history of terrigenous sediment components off central Chile to reconstruct climate variability on land, (3) assess variations in the boundary between oxygen-poor GUC water and oxygen-rich AAIW, and (4) monitor centennial- to millennial-scale variations in paleomagnetic intensities and field directions as a stratigraphic tool for comparison with similar data from the Northern Hemisphere.

Three APC holes were drilled at Site 1235 (Table T2). Holes 1235A, 1235B, and 1235C were cored to 181.3, 176.2, and 152.5 mbsf, respectively. A nonmagnetic core barrel, cutting shoe, and flapper valve were deployed here for the first time on Leg 202, resulting in sediment records with substantially less magnetic overprint than those retrieved with regular steel barrels (see Lund et al., this volume). Eight downhole temperature measurements were taken with the APCT tool, yielding a temperature gradient of $\sim 3.8^\circ\text{C}/100\text{ m}$. Most cores were affected by expanding gas during recovery, and one core disintegrated entirely. Holes were drilled in liners to relieve gas pressure to the extent possible, and major voids were closed prior to core logging operations.

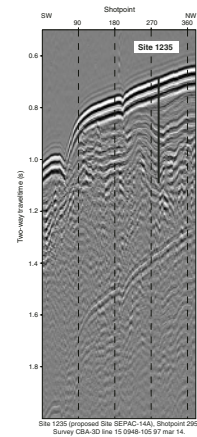
A 215.5-mcd-thick (181.3 mbsf) Pleistocene to Holocene hemipelagic sequence was recovered at Site 1235 (Fig. F51). A composite section and splice, constructed on the basis of high-resolution core logging data, indicated that complete recovery was most likely achieved to ~ 171.45 mcd, although some correlations between holes were problematic, especially at $\sim 45\text{--}49$, $71\text{--}73$, and $126\text{--}128$ mcd.

Sediments consist primarily of homogeneous dark olive-gray to dark gray silty clay and clay with a dominant siliciclastic component and high magnetic susceptibility and NGR values. The silt fraction is dominated by feldspars, with lesser amounts of quartz, pyroxenes, and volcanic glass, consistent with a sediment provenance in both the Andes and the Coastal Range. The large supply of siliciclastic sediment onto the upper continental margin of Central Chile is considered to result mainly from rivers that drain the mountainous regions of the Andes and the Coastal Range.

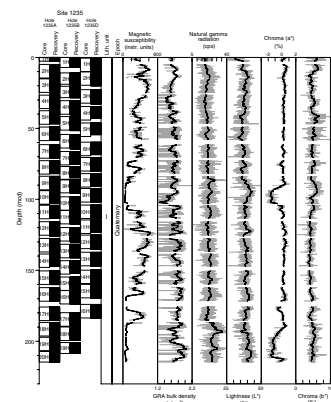
Calcium carbonate concentrations range from 0.3 to 15.5 wt% (average = 2.4 wt%). TOC contents range from 0.4 to 1.5 wt% (average = 0.6 wt%) and are dominated by marine organic matter (TOC/TN ratios of 5 to 9). The relatively low organic carbon and carbonate contents relative to other continental margin settings indicate dilution with siliciclastic material. Organic matter degradation and carbonate dissolution also contribute to the observed variations of these components. Intervals of abundant authigenic carbonate underlie zones of intense burrowing in at least three repetitive sequences. Color reflectance data document the presence of hematite and goethite near the top of these sequences, in each case overlying green sediments (negative a^* values).

Calcareous nannofossils, diatoms, and foraminifers vary from rare to abundant and are typical of a productive coastal upwelling zone. Microfossil preservation is moderate to good in the upper section but deteriorates downhole, especially for the calcareous nannofossils. Reworked benthic diatoms and pre-Pleistocene calcareous nannofossil are fre-

F50. Seismic profile across Site 1235, p. 125.



F51. Core recovery, lithology, age, and physical and chemical data summary, Site 1235, p. 126.



quently present. The planktonic foraminiferal assemblage is typical of the upper Pleistocene Subzone Pt1b, and the continued presence of the calcareous nannofossil species *Emiliania huxleyi* to the bottom of the sequence documents an age younger than 0.26 Ma. Sedimentation rates are at least 80 cm/k.y. The ubiquitous presence of burrows and benthic faunal assemblages does not reveal any episodes of bottom water anoxia. As at Site 1234, the benthic foraminiferal assemblage is dominated by species associated with high carbon fluxes in an oxygen minimum zone environment.

Initial NRM intensities were extremely high, ranging from 0.5 to 2.1 A/m, and were characterized by steep positive inclinations (averaging +79°) associated with a drill string magnetic overprint. AF demagnetization at peak fields up to 25 mT only partially reduced this overprint but revealed discrete intervals of low NRM intensity that are likely associated with substantial reduction diagenesis. The application of the non-magnetic core barrel substantially reduced the viscous magnetic overprint. Paleomagnetic declinations are much less affected by overprints. Coherent patterns of paleomagnetic secular variation in all holes may provide a high-resolution regional stratigraphy at Sites 1234 and 1235.

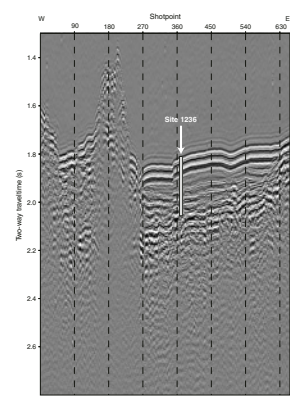
Gas, fluid, and sediment geochemical profiles are dominated by the influence of marine organic matter degradation associated with sulfate reduction and methanogenesis. Sediments contained abundant methane and low amounts of ethane. A decrease in chlorinity with depth at Site 1235, similar to that of Site 1233, indicates the presence of methane hydrates that dissociated either within subsurface sediments or after recovery. Authigenic pyrite and carbonate are present, especially in deeper intervals. Conspicuous carbonate concretions are intermittent downhole. Dissolved calcium concentrations drop rapidly with depth to values <2 mM, consistent with the effects of authigenic carbonate mineralization driven by high alkalinity.

Site 1235 will provide a long sequence of extremely rapidly accumulating sediment for the study of century- to millennial-scale changes in climate, biogeochemistry, and oceanography of subsurface water masses, as well as variations in paleomagnetic declination. Preliminary data on the fossil biota, geochemical composition of interstitial water and sediment, and variations in the terrigenous sediment components lead us to anticipate a rich record of paleoceanographic and paleoclimatic change and chemical diagenesis, as long as the stratigraphic challenges associated with gassy and somewhat disturbed cores can be overcome.

Site 1236

Site 1236 (proposed Site NAZCA-10A) is located at a water depth of 1323 m atop Nazca Ridge, a fossil hotspot track with its modern expression at Easter Island (Fig. F1). The total thickness of sediment at Site 1236 is ~200 m. Seismic data reveal a well-stratified pelagic sequence with strong to moderately reflective layers from the sediment surface to ~120 mbsf. At depths from ~120 to ~200 mbsf, deformed but almost continuous layers of moderate reflection appear to smooth the relief of the acoustic basement (Fig. F52). Based upon a fixed hotspot model and on magnetic anomalies of the surrounding oceanic crust, basement ages are expected to be 30–35 Ma (Fig. F6). The ~20-km-wide plateau occupied by Site 1236 is punctuated by small volcanic spires a few hundred meters high that represent eroded remnants of an archipelago of volcanic islands. About 20 km to the southwest of Site 1236, a flat-

F52. Seismic profile across Site 1236, p. 127.



topped guyot, which is presumably younger than the plateau surface, rises to within 350 m of present sea level. The existence of this relatively well preserved shallow bathymetric feature adjacent to the deeper, more eroded plateau surface suggests multiple episodes of volcanism in the region or the presence of a carbonate reef system that grew atop the volcanic edifice. A tectonic backtrack path on the Nazca plate moves Site 1236 $\sim 20^\circ$ westward, toward the center of the subtropical gyre, by 30 Ma (Fig. F6). Thermal subsidence would predict that the site was at shallower water depths during the early Miocene and, perhaps, above sea level very early in its history.

Today, Site 1236 is situated near the western edge of the northward-flowing Peru-Chile Current in an oligotrophic region of the subtropical gyre and at depths suitable for monitoring intermediate-water chemistry in the open ocean (Figs. F5).

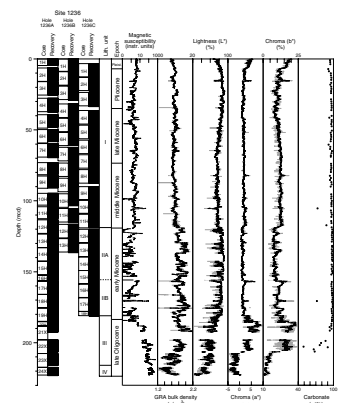
The primary objectives at Site 1236 were to provide a continuous sequence of Neogene and Quaternary sediments to (1) improve on South Pacific Neogene timescales by combining magnetostratigraphy, biostratigraphy, and isotopic stratigraphy, (2) assess climate changes of the subtropical South Pacific focusing on major intervals of changing climate (e.g., the early Miocene intensification of Antarctic glaciation [~ 24 Ma], the middle Miocene climatic optimum [14–15 Ma], the expansion of the East Antarctic Ice Sheet [~ 13 Ma], and the mid-Pliocene intensification of the Northern Hemisphere glaciation [3.1–2.6 Ma]), (3) examine the late Miocene to early Pliocene reorganization in South Pacific surface and intermediate-water circulation in response to the closure of the Isthmus of Panama (10–4 Ma), and (4) reconstruct changes in the boundary between Pacific Deep Water and AAIW on orbital and tectonic timescales.

Three holes were drilled at Site 1236 (Table T2). Hole 1236A was APC-cored to a depth of 173.1 mbsf and advanced with the XCB to a total depth of 207.7 mbsf, where basement was reached. Hole 1236B was piston cored and abandoned at 122.8 mbsf because of mechanical problems. In Hole 1236C, 13 APC cores were recovered to a refusal depth of 167.3 mbsf. The nonmagnetic core barrel assembly was deployed on nearly every second APC core at this and all subsequent sites. Six down-hole temperature measurements were taken with the APCT tool, yielding a temperature gradient of $\sim 3.9^\circ\text{C}/100$ m.

A 223.2-mcd-thick (207.7 mbsf) sequence of Neogene and upper Oligocene (~ 28 Ma) mostly calcareous sediments was recovered at Site 1236 (Fig. F53). A composite section and splice, based on high-resolution core logging data, documented complete stratigraphic recovery to ~ 129.7 mcd (~ 17 –18 Ma). Pelagic sedimentation is prevalent at Site 1236, but gravity flow deposits during the early–middle Miocene and the impact of volcanic evolution of Nazca Ridge during the late Oligocene are also clearly represented. Calcium carbonate concentrations are >90 wt% throughout the section except for the lowermost (Oligocene) interval. TOC content was not measurable with shipboard techniques (<0.2 wt%).

Four major lithologic units are defined at Site 1236. Unit I (0–119.5 mcd) corresponds to the last 17 m.y. and contains primarily pelagic nannofossil ooze. Two isolated layers at depths of ~ 65 and ~ 98 mcd consist mostly of neritic grains and represent waning supply of gravity flows from a nearby carbonate platform during the late Miocene. A minor siliciclastic fraction in the uppermost ~ 40 mcd, corresponding to increased magnetic susceptibility values and containing goethite and hematite according to reflectance spectrometry results, is considered to

F53. Core recovery, lithology, age, and physical and chemical data summary, Site 1236, p. 128.



represent eolian material transported from South America during the Pleistocene and Pliocene. Unit II (119.5–181.0 mcd; ~17 to ~23 Ma) consists mainly of nannofossil ooze (Subunit IIA) and unlithified calcareous mudstone (Subunit IIB), consistent with the presence of a pelagic sedimentary environment at Site 1236 since the late Oligocene. Frequent intercalations of well-sorted nonpelagic calcareous sediment (neritic grains and micrite), which sometimes fine upward, were supplied by gravity flows from nearby carbonate platforms. Micrite, which becomes dominant in Subunit IIB, reflects *in situ* recrystallization of nannofossils.

Allochthonous coarse-grained calcareous sediments in Unit III (181.0–207.7 mcd), including recrystallized larger benthic foraminifers, bryozoan fragments, and some remains and encrustations of red algae, indicate proximity of Site 1236 to a carbonate platform from ~25 to 23 Ma. The presence of glauconite within Unit III sediments is consistent with a shallow-water environment below the storm wave base. Volcaniclastic constituents with relatively high magnetic susceptibility are present through the upper Oligocene, suggesting proximity to volcanic islands at that time. Unit IV (207.7–222.3 mcd; >25 Ma) is a fine-grained chalk with abundant nannofossils and foraminifers overlying basalt (inferred basement), with no evidence for input of nonpelagic material. We infer, based on the presence of authigenic glauconite, a relatively shallow open-ocean environment on the order of hundreds of meters below sea level.

Calcareous nannofossils are generally abundant and moderately to well preserved throughout the interval. Planktonic foraminifers are common to abundant down to ~150 mcd (~20 Ma). Below this depth, foraminiferal abundance decreases and preservation deteriorates markedly. Calcareous nannofossil and planktonic foraminifer biostratigraphies indicate that the upper Pleistocene to upper Oligocene succession is essentially complete. Benthic foraminiferal assemblages document an oligotrophic, pelagic environment from Pliocene to middle Miocene time. Older intervals from the early Miocene and late Oligocene contain higher numbers of buliminids and nodosariids, reflecting shallower water depth and proximity to the oxygen minimum zone. The presence of poorly preserved larger benthic foraminifers, which have modern equivalents that host algal endosymbionts, indicates redeposition from a nearby carbonate platform during the Oligocene and early Miocene. Diatoms are only found close to the two ash layers and indicate either increased diatom production near the time of ash deposition or anomalous preservation as a result of the presence of ash. The presence of benthic and neritic diatoms at 82.3 and 206.7 mcd indicates redeposition from shallow-water environments.

NRM intensities are similar to the magnetic susceptibility profiles and reflect the major lithologic changes at Site 1236. A preliminary magnetostratigraphy was established for the upper 89 mcd (0–14 Ma) based on correlation to the geomagnetic polarity timescale, and this significantly augmented the biostratigraphy and provided a well-constrained chronology for the younger interval.

A long history of oligotrophic conditions with little input of nonbiogenic sediments at Site 1236 resulted in generally low MARs and linear sedimentation rates (LSRs) of <1.6 g/cm²/k.y. and <11 m/m.y., respectively. Winnowing processes may have contributed to the overall low MARs on this bathymetric rise. MARs are overwhelmingly controlled by carbonate MAR throughout the record. Higher rates of 0.6–1.6 g/cm²/k.y. (6–11 m/m.y.) in the lower to middle Miocene (>12 Ma) reflect the

influence of nearby carbonate platforms and/or islands supplying significant amounts of nonpelagic calcareous material and siliciclastic and volcanic constituents. The lowest rates of ~ 0.4 g/cm²/k.y. (~ 4 m/m.y.) are typical for the lower upper Miocene (12–8 Ma) and in the Pleistocene (2–0 Ma). The uppermost Miocene to Pliocene (8–2 Ma, but especially 6–5 Ma) has a broad peak in MARs (0.5–0.9 g/cm²/k.y.) and LSRs (5–9 m/m.y.). Given no detectable changes in fossil preservation, these high MARs likely reflect an interval of increased productivity. Similar events are recorded at other Leg 202 sites (1237, 1238, 1239, and 1241) and at equatorial Pacific sites (846–853) during approximately the same time interval.

Interstitial water chemistry at Site 1236 is consistent with low input of organic matter in an oligotrophic setting. Diagenesis of opal and calcite is minimal, as reflected in silicate, calcium, and magnesium measurements of interstitial waters.

Site 1236 provides an essentially complete Neogene to Quaternary sequence relatively unmodified by burial diagenesis and recovered with the APC to 188 mcd (~ 23 Ma). The tight framework of bio- and magnetostratigraphic age controls together with good preservation of calcareous microfossils extending to the late Oligocene will provide a solid base for detailed studies that aim to reconstruct the long-term history of sea-surface and intermediate-water characteristics and regional climate in the southeast Pacific.

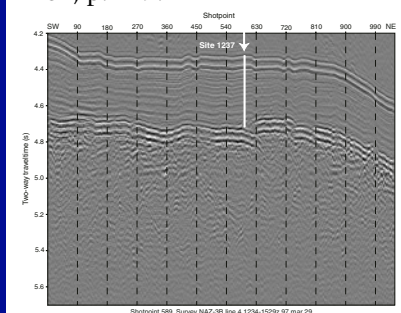
Site 1237

Site 1237 (proposed Site NAZCA-17A) is located at a water depth of 3212 m on a relatively flat bench on the easternmost flank of Nazca Ridge, ~ 140 km off the coast of Peru (Fig. F1). Nazca Ridge, a fossil hotspot track with its modern expression at Easter Island, terminates just outboard of the Peru-Chile Trench, where it is deformed and subducted beneath Peru. About 19 km to the west of Site 1237, an abrupt scarp (probably and active normal fault) rises 600 m to the summit of the ridge. Eastern Nazca Ridge is covered by a thick drape of pelagic sediment to its shallowest reaches. The seismic record reveals well-stratified reflective layers, which clearly drape the underlying bathymetry from the sediment surface to acoustic basement (Fig. F54). The basement age is expected to be between 40 and 45 Ma, based upon a hotspot model and magnetic anomalies of the surrounding oceanic crust. Considering the thermal subsidence over this time span, the site may have been within several hundred meters of sea level in its early history.

The modern water depth of Site 1237 reflects the transition zone between the relatively oxygen-rich (nutrient poor) remnants of CPDW, which enter the Peru Basin as bottom water through the Peru-Chile Trench, and the relatively oxygen-poor (nutrient rich) PCW (Fig. F5). During its early history, the site may have occupied depths of the modern PCW or its paleoequivalent. Today, Site 1237 is situated near the eastern edge of the northward-flowing Peru-Chile Current, close to the productive upwelling system off Peru, and underlies the path of eolian dust that originates in the Atacama Desert of Chile (Fig. F33). Given the tectonic backtrack $\sim 20^\circ$ westward toward the center of the oligotrophic gyre (Fig. F6), and assuming there were no compensating changes in the environment, we expect that accumulation rates of both biogenic and eolian sediments at Site 1237 would have been lower in the past.

The primary objectives at Site 1237 were to provide a continuous and complete sedimentary sequence from the late Cenozoic to (1) improve

F54. Seismic profile across Site 1237, p. 129.

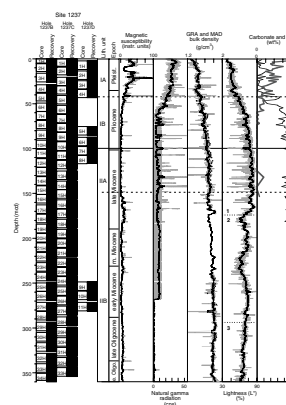


on regional chronological frameworks by combining magnetostratigraphy, biostratigraphy, isotopic stratigraphy, and orbital tuning methods; (2) assess climate and biogeochemical changes of the subtropical South Pacific, focusing on major intervals of changing global climate, such as the early Miocene intensification of Antarctic glaciation (~24 Ma), the middle Miocene climatic optimum (14–15 Ma), the expansion of the East Antarctic Ice Sheet (~13 Ma), the mid-Pliocene intensification of the Northern Hemisphere glaciation (3.1–2.6 Ma), and the transition from early Pleistocene climate cycles dominated by ~41-k.y. rhythms to those of the late Pleistocene that are dominated by ~100-k.y. rhythms (~0.9 Ma); (3) examine the impact of tectonic events on regional climate, productivity, biogeochemical cycles, and ocean circulation, including the opening of Drake Passage (~25 Ma), the major uplift of the Andes (probably within the past 15 m.y.), and the closure of the Isthmus of Panama (10–4 Ma); and (4) reconstruct changes in the boundary between PCW and Circumpolar Deep Water on orbital and tectonic timescales.

Four APC holes were drilled at Site 1237 (Table T2). Hole 1237A was terminated after retrieving the first core without a mudline. Hole 1237B recovered the mudline, and piston coring advanced until refusal at 317.4 mbsf. This represented the deepest penetration with the APC since Leg 162 and one of the five deepest APC penetrations in ODP history. Hole 1237C was cored to refusal at 315.3 mbsf. Hole 1237D was spot-cored to cover coring gaps left in the previous holes in four intervals to a total depth of 281.1 mbsf. The nonmagnetic core barrel was used on approximately every second APC core. Ten downhole temperature measurements were taken with the APCT tool, yielding a temperature gradient of ~3.1°C/100 m.

A 360.6-mcd-thick (317.4 mbsf) Oligocene (~31 Ma) to Holocene pelagic sediment sequence was recovered at Site 1237 (Fig. F55). A composite depth section and splice, based on high-resolution core logging data, document complete recovery for the entire sequence. The sequence was divided into two major lithologic units, and each unit was divided into two subunits (Fig. F55). The upper ~100 mcd of the sequence (Unit I) reflects pelagic sedimentation with significant terrigenous (probably mostly eolian) and siliceous microfossil components. In Subunit IA (0–41 mcd), calcium carbonate concentrations are <50 wt% (and often just a few percent), and TOC contents are relatively high for an open-ocean setting (0.3–1.9 wt%). The sediment gradually changes downhole from nannofossil-bearing (silty) clay to nannofossil ooze in Subunit IB (41–100 mcd). Below ~100 mcd (Unit II), the sedimentary sequence is dominated by nannofossil ooze, calcium carbonate values are >90 wt%, and TOC values fall below detection limits (<0.2 wt%). Micrite contents increase at depths >148 mcd (Subunit IIB) and are likely associated with recrystallization of calcareous nannofossils. A marked color change from more greenish younger sediment to reddish older sediment containing goethite and hematite occurs at ~164 mcd (8–9 Ma). The abrupt color change appears to result from diagenetic reduction processes or analytical detection problems (i.e., matrix effects) rather than from a possible change in the primary signal of dust source areas, based on evidence from Site 1236 (1500 km southwest of Site 1237 and farther from the probably source region), where the reddish color signal persists into the Pleistocene interval. At approximately the depth where the color change occurs, discrete ash layers and dispersed ash begin to appear in the sediment. Fifty-five ash layers were deposited during the last ~9 m.y. The Pliocene to Pleistocene interval contains sig-

F55. Core recovery, lithology, age, and physical and chemical data summary, Site 1237, p. 130.



nificant amounts of both terrigenous material and siliceous microfossils.

Calcareous nannofossils and foraminifers are generally abundant or common and well to moderately well preserved throughout, indicating that a complete late Pleistocene to late Oligocene succession was recovered. Calcareous nannofossils at the base of the hole indicate an age of <31.5 Ma. Marked changes in the relative proportions of benthic foraminiferal species within the Pleistocene to late Pliocene assemblage indicate variations in carbon fluxes at the seafloor that are probably related to temporal and spatial fluctuations of the coastal upwelling system. At greater ages, the benthic foraminiferal assemblage is consistent with an oligotrophic, pelagic environment. Diatoms are abundant and are usually well preserved from 0 to 60 mcd, but abundance decreases and preservation deteriorates at greater depths, and diatoms are essentially absent at depths >174 mcd. Diatoms provide additional biostratigraphic control down to ~136.7 mcd (7 Ma). The diatom assemblage from 0 to 60 mcd is typical of a coastal upwelling zone on a continental margin. At greater depths, upwelling forms are present only occasionally with some oceanic forms.

The paleomagnetic stratigraphy at Site 1237 is excellent with clear definitions of all chrons and subchrons over the last 5 m.y. and from 7 to 13 Ma. Even fine-scale features and short polarity subchrons, such as the "Cobb Mountain Event" within the Matuyama Chron, may be present. Based on shipboard data, the polarity assignments for the interval from 5 to 7 Ma and for the lowermost part of the sequence between 13 and 31 Ma are uncertain because the polarity sequence allows for several possible interpretations.

Total MARs and LSRs range between 0.6 and 2.5 g/cm²/k.y. and between 5 and 23 m/m.y., respectively. Before 8 Ma (>150 mcd), the rates are generally lower (<1.2 g/cm²/k.y. and <9 m/m.y., respectively) and driven by the carbonate MAR, as is typical for oligotrophic settings far from the continents. Between 8 and 4 Ma, MARs are higher and reach maximum values at 6–5 Ma, most likely associated with anomalously high production of carbonate-secreting plankton. The enhanced rain of organic carbon that follows from high productivity would also support the hypothesis of a diagenetic boundary that reduced the reddish oxides at <150 mcd. The Miocene to early Pliocene biogenic bloom was also found at Site 1236, as well as in the equatorial Pacific (6.7–4.5 Ma). At ages <5 Ma, carbonate MARs decreased gradually at Site 1237 and reached minimum values during the last 2 m.y.

Noncarbonate accumulation rates gradually increased from 12 Ma to the Holocene, constituting about half of the total MAR at ~3 Ma and dominating the total MAR during late Pliocene and Pleistocene. This trend represents the tectonic drift of the Nazca plate eastward toward both the eolian dust source in the Atacama Desert and the region of coastal upwelling. Ash layers become more frequent after ~9 Ma and may record the onset of intense volcanism and accompanying tectonic uplift of the Andes. If so, the topographic barrier of an early mountain range would have enhanced the steering of westerly and trade winds along the coast, resulting in stronger meridional flow, enhanced eolian transport, coastal upwelling, and biogenic productivity within the eastern boundary current.

Interstitial water chemistry reflects minor influence from organic matter diagenesis, a limited degree of biogenic opal dissolution, and a minor signature of biogenic calcite diagenesis. Dissolved silicate con-

centrations have highest values in the depth range where diatoms are reported to have the best preservation and abundance.

Site 1237 provides a complete upper Paleogene to Neogene sequence relatively unmodified by burial diagenesis and fully recovered with the APC. Good preservation of calcareous microfossils to the base of the Oligocene and the tight framework of bio- and magnetostratigraphic age controls will provide an excellent stratigraphic reference section for the South Pacific, with opportunities for further refinement based on an orbitally tuned timescale. Detailed studies will aim to reconstruct the long-term history of Andean uplift and continental climate as well as the evolution of upwelling, biota, biogeochemistry, and sea-surface and intermediate-water characteristics in the southeast Pacific.

Site 1238

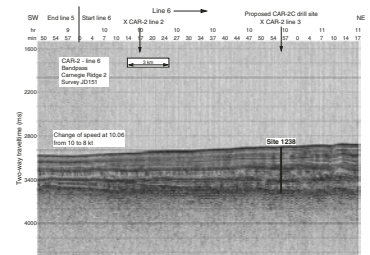
Site 1238 (proposed Site CAR-2C) is located ~200 km off the coast of Ecuador on the southern flank of Carnegie Ridge at 2203 m water depth (Fig. F1). The region is draped with pelagic sediment ~400–500 m thick on a bench that slopes gently to the south (Fig. F56). Basement at Site 1238 likely consists of basalt formed at the Galapagos hotspot at ~11–13 Ma. A tectonic backtrack path on the Nazca plate moves Site 1238 ~600 km westward and slightly to the south relative to South America, probably to shallow water depths by 10–12 Ma (Fig. F6).

Today, Site 1238 is situated under the eastern reaches of the equatorial cool tongue, in an open-ocean upwelling system near the equator. The nutrient-rich Equatorial Undercurrent (EUC) supplies waters that upwell here and along the coast of Peru and Ecuador, driving exceptionally high primary productivity. Sediments at the site are likely to record changes in upwelling and biological production, as well as long-term changes in upper-ocean temperature and pycnocline depth. The modern water depth is appropriate to monitor PCW south of Carnegie Ridge, roughly at the sill depth of Panama Basin (Fig. F5).

The primary objectives at Site 1238 were to provide a continuous sedimentary sequence of Neogene age to (1) assess the history of near-surface water masses, including the eastern reaches of the equatorial cold tongue, (2) assess changes in biogeochemistry and biota that are linked to variations in nutrients, productivity, and fluxes of organic matter and biogenic sediments to the seafloor, (3) monitor temporal and vertical fluctuations of PCW, (4) assess oceanographic changes that are related to the closure of the Isthmus of Panama, and (5) record changes in the occurrence and frequency of volcanic ashes, which might be associated with active tectonic phases of the northern Andes.

Three holes were drilled at Site 1238 (Table T2). Hole 1238A was cored with the APC to 204.5 mbsf and then deepened with the XCB to refusal at 430.6 mbsf. Holes 1238B and 1238C were APC cored to 201.0 and 167.5 mbsf, respectively, to cover coring gaps. The nonmagnetic core barrel was used on approximately every second APC core. Hole 1238A was logged using the triple combo tool string with the Lamont Multi-Sensor Spectral Gamma Ray Tool (MGT) on top, and then by the FMS-sonic tool string. Downhole logging operations experienced smooth borehole conditions and calm seas (peak heave of <2 m), and as a result the data were of excellent quality from the density, porosity, and FMS tools that require good borehole contact. Six downhole temperature measurements were taken with the APCT tool, yielding an anomalously high temperature gradient of ~12.7°C/100 m.

F56. Seismic profile across Site 1238, p. 131.



A 468.2-mcd-thick (430.6 mbsf) sequence of middle Miocene (~12 Ma) to Holocene pelagic sediment was recovered at Site 1238 (Fig. F57). Based on high-resolution core logging data, a composite section and splice documented complete recovery of the section cored with the APC to a depth of 225.4 mcd. XCB cores from Hole 1238A were appended onto the mcd scale, using a 10% growth rate of mcd relative to mbsf. The dominant lithologies at Site 1238 are diatom nannofossil ooze and nannofossil diatom ooze, reflecting primarily biogenic sedimentation in a moderate- to high-productivity pelagic setting.

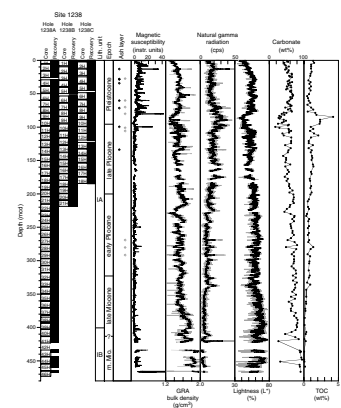
Calcium carbonate contents range between 17 and 94 wt% and generally increase with depth, but with substantial variability. TOC contents range between 0.1 and 4.3 wt%, and vary inversely to calcium carbonate. Consistently low TOC/TN ratios (3.4–11.8) indicate the dominant marine origin of organic matter. Color and lithologic banding is pervasive on a scale of meters (10⁴ to 10⁵ yr, based on shipboard age models) and provides evidence for regional variability associated with Earth's orbital cycles. Similar to the core logging data, the downhole logs document cyclic variations in sediment properties on the scale of meters that reflect alternations between carbonate- and opal-rich sediments. The downhole logs reveal that uranium concentration predominantly drives variations in natural gamma measured in core logs, and both properties are well correlated with TOC. Uranium variations likely reflect changes in sedimentary redox conditions in response to fluxes of organic matter to the seafloor, meaning that the primary lithologic variations at Site 1238 are probably driven by changing productivity of surface waters.

One lithologic unit, divided into two subunits, was defined at Site 1238. Subunit IA (0–403 mcd) contains bioturbated nannofossil ooze, diatom nannofossil ooze, and nannofossil diatom ooze with varying abundance of clay and foraminifers. High productivity during this latest Miocene to Pliocene interval is indicated by high concentrations of diatoms, organic carbon, and organic pigments in the sediment. An anomalous event of low calcium carbonate and high TOC and U contents occurs from 85 to 104 mcd (~1.7–2.0 Ma). Similar coeval events are found at Sites 1239 and 1240, and at other equatorial sites (e.g., 846 and 847), they are associated with high accumulations of opal. Several ash layers occur within the upper ~300 m (<5 Ma), including the regionally correlative ash layer L (~230 ka). The frequency of ash layers increased during the past 3 m.y. and may represent a phase of intensified volcanism in the northern Andes.

Subunit IB (~403–467 mcd), the base of the recovered sequence, is characterized by partially lithified diatom and nannofossil oozes interbedded with chalk and occasional chert horizons. Increasing lithification is documented by increases in bulk density and decreases in porosity. The presence of chert and micrite indicates significant opal and carbonate diagenesis, respectively, perhaps driven by the relatively high heat flow at Site 1238.

Calcareous nannofossils are generally abundant, and planktonic and benthic foraminifers are common to abundant, with good to moderate preservation throughout the section, except in the lower Pleistocene and middle Miocene. Diatoms are common to abundant, except at depths >430 mcd (~9 Ma), where diatoms are essentially barren. This absence of diatoms at depth is probably due to opal diagenesis and chert formation. The various microfossil groups provide a well-constrained biostratigraphy. The lower Pliocene–upper Miocene section contains a minor component of reworked older microfossils. Calcareous

F57. Core recovery, lithology, age, and physical and chemical data summary, Site 1238, p. 132.



nannofossils indicate a basal age of 10.4–11.6 Ma. However, considering possible reworking of that indicator, and considering a planktonic foraminifer datum (11.7 Ma) at 423–437 mcd, a hiatus may be present at ~420 mcd, spanning the interval of ≥ 12 Ma to ~8 Ma. Paleomagnetic measurements were compromised by drill string overprints, as well as diagenesis of magnetic minerals, and thus did not provide useful information for age control.

MARs and LSR are low at ages >8 Ma (<0.4 g/cm²/k.y. and <5 m/m.y, respectively), although the lack of biostratigraphic datums precludes a detailed assessment in the deepest 40 mcd. A broad peak in MAR and LSR values is indicated between 6 and 3 Ma (lower part of Subunit IA), with maximum values of 5 g/cm²/k.y. and 70 m/m.y., respectively. At ages >4 Ma, the total MAR values are dominated by carbonate MARs. In the interval 0–4 Ma, the noncarbonate MARs account for about half of the total MAR. Peak noncarbonate MAR occurs at 3–4 Ma, somewhat earlier than the peak carbonate MAR at 4–5 Ma.

Moderate amounts of biogenic gas, mostly methane but also traces of ethane, result from the limited effects of methanogenesis at this site. Chemical gradients in the interstitial waters reflect the influence of organic matter oxidation by sulfate reduction, although not to complete sulfate depletion. As a result, hydrogen sulfide was present. Silicate increases to >1800 μ M by ~350 mcd, indicating temperature control of the solubility of biogenic opal. At greater depths, sharp decreases in silicate concentrations are consistent with chert formation.

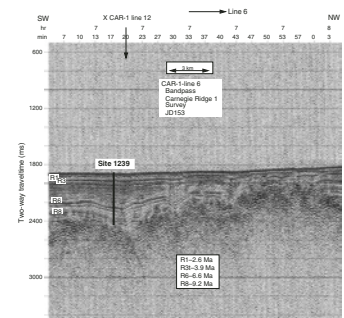
With the combination of a complete composite section and a spliced record through the APC interval, excellent logging data to place XCB cores into a true depth framework, and moderately high sedimentation rates, Site 1238 will provide excellent opportunities for high-resolution studies of Neogene climate and biogeochemical change. A well-constrained age model provides great potential for the study of near-surface water masses in the eastern reaches of the equatorial cold tongue, including processes of upwelling and paleoproductivity off Ecuador. A well-preserved benthic fauna will facilitate study of deepwater masses. Volcanic ashes are present, which opens opportunities for tephrochronology and for establishing the history of major volcanic events in the northern Andes.

Site 1239

Site 1239 (proposed Site CAR-1C) is located ~120 km off the coast of Ecuador near the eastern crest of Carnegie Ridge at a water depth of 1414 m (Fig. F1). Just to the east, Carnegie Ridge slopes downward into the Peru-Chile Trench. To the north, steep basaltic flanks of Carnegie Ridge are mostly bare rock, so some downslope transport of sediment is possible. Seismic profiles reveal stratified reflective sediments that fill rough basement lows and drape the remaining basement topography to form a bench that slopes gently to the south (Fig. F58). Basement at Site 1239 likely consists of basalt formed at the Galapagos hotspot at 15–18 Ma. The tectonic backtrack path on the Nazca plate moves Site 1239 ~600 km westward over this time, almost parallel to the equator. Thus, the site resided within the highly productive and climatically sensitive region south of the equator throughout its history.

Today, Site 1239 is situated under the eastern reaches of the equatorial cold tongue, in an open-ocean upwelling system near the equator. The site is close to the equatorial front that separates cool, relatively high salinity surface waters south of the equator from the warm, low-

F58. Seismic profile across Site 1239, p. 133.



salinity waters of Gulf of Panama. The EUC supplies the nutrient-rich upwelling waters that fuel high surface productivity, although nitrate and phosphate are not fully utilized by the phytoplankton, and primary productivity here is ~25% lower than it is 120 km to the south at Site 1238.

The modern water depth of Site 1239 is within the range of PCW south of Carnegie Ridge, but shallow enough that some mixing with remnants of AAIW can be detected here, especially by its relatively low salinity (Fig. F5). Thermal subsidence would predict that the site was at shallower water depths during the Miocene and perhaps above sea level very early in its history.

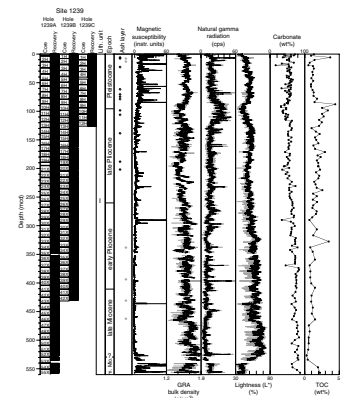
The primary objectives at Site 1239 were to provide a continuous sedimentary sequence of Neogene age (as old as 11–12 Ma) to (1) assess the history of near-surface water masses, including the eastern reaches of the equatorial cold tongue, upwelling, and paleoproductivity, (2) monitor temporal and vertical fluctuations of intermediate water masses near water depths of 1400 m and even shallower during its early history, (3) assess oceanographic changes that are related to the closure of the Isthmus of Panama, and (4) monitor changes in the occurrence and frequency of volcanic ashes, which might be associated with active tectonic phases of the northern Andes.

Three holes were drilled at Site 1239 (Table T2). Hole 1239A was cored with the APC to 174.4 mbsf and then deepened with the XCB to 515.4 mbsf, where the last core contacted acoustic basement. This hole was logged with the triple combo and the FMS-sonic tool strings. Hole 1239B was drilled with the APC to 171.3 mbsf and extended to 398.7 mbsf with the XCB. Hole 1239C was APC cored to 117.3 mbsf with the objective to fill stratigraphic gaps left in the APC-cored intervals of the first two holes. The nonmagnetic core barrel was used on approximately every second APC core. Five downhole temperature measurements taken with the APCT tool indicated a thermal gradient of ~9.4°C/100 m at Site 1239.

A 560.7-mcd-thick (515.4 mbsf) sequence of Miocene (~15 Ma) to Pleistocene pelagic sediments was recovered at Site 1239 (Fig. F59). The composite section constructed using cores from the three APC holes documented complete recovery of the upper 188.9 mcd of the sediment section. Density and NGR records from borehole and core logging data (including the XCB-cored interval of Hole 1239A) exhibit strong correlation of meter-scale variability and allowed construction of an *eld* scale for the XCB-cored intervals. The recovered sediments are dominated by foraminifer and nannofossil ooze with varying amounts of diatoms, clay, and micrite. Siliciclastic components include clay minerals and lesser amounts of feldspars and biotite.

Carbonate contents range between 16 and 87 wt%, and TOC contents are relatively high (up to 3.7 wt%) (Fig. F59). Almost the entire sequence is characterized by meter-scale cyclic changes in color reflectance (particularly *L**) and bulk density that likely reflect changes in relative proportions of biogenic opal and carbonate. Preliminary evaluation suggests that these features are related to the Earth's orbital cycles on the scale of 10⁴ to 10⁵ yr. Color banding on the FMS downhole logging images occurs on the same scale, which clearly documents the potential for developing an orbitally tuned timescale for this site. High sedimentation rates and meter-scale rhythmic changes in density and resistivity are encountered in the upper Miocene to Pliocene interval and are interpreted to reflect orbital-scale changes in carbonate vs. biogenic opal in the sediment. The downhole logs reveal that uranium

F59. Core recovery, lithology, age, and physical and chemical data summary, Site 1239, p. 134.



concentration predominantly drives variations in natural gamma measured in core logs, and both properties are well correlated with TOC. Uranium variations likely reflect changes in sedimentary redox conditions in response to fluxes of organic matter to the seafloor, meaning that the primary lithologic variations at Site 1239 are probably driven by changing productivity of surface waters. Volcanic ash deposition began in the late Miocene to early Pliocene (~5-4 Ma) and increased in frequency over the last 3 m.y. The magnetic susceptibility signal increases in both mean values and amplitude of high-frequency fluctuations within the interval representing the last ~2.5 m.y. (0-140 mcd), suggesting pronounced changes in the relative supplies of terrigenous and biogenic material.

Calcareous nannofossils are abundant and well preserved within the top ~100 mcd, but both abundance and preservation decline slightly below this interval. Planktonic foraminifers are common within the top ~100 mcd but decrease in abundance rapidly at greater depths. Diatoms are also present throughout the sedimentary section although, in comparison to Site 1238, their abundance is relatively low in the Holocene to middle Pleistocene and lower Pliocene to uppermost Miocene intervals. A well-constrained biostratigraphy was obtained from all three microfossil groups.

A major hiatus was identified at ~530 mcd, encompassing the interval from ~8 to ~15 Ma. MARs and LSRs display a broad peak from ~8 Ma to the present, with maximum values (~8 g/cm²/k.y. and ~100 m/m.y., respectively) between ~4 and 3 Ma. The generally high sediment accumulation rates between ~6 and ~1 Ma, high concentrations of diatoms, nannofossils, and TOC, and the fossil assemblages and abundances at Site 1239 reflect a moderate- to high-productivity pelagic environment, similar to that at Site 1238. Near and below the hiatus at ~530 mcd (~8 to ~15 Ma), MARs and LSRs are presumably very low but cannot be estimated accurately because of the uncertain age control.

Chemical gradients within interstitial water reflect the influence of organic matter oxidation, the dissolution of biogenic silica and its reprecipitation in authigenic phases, the effects of authigenic calcite precipitation, and the diffusive influence of basalt alteration processes. Sulfate is completely consumed by ~71 mcd, coincident with an increase in methane, and near an interval of high organic carbon contents that marks the final phase of a late Pliocene biogenic bloom. Authigenic mineral precipitation is reflected by increased amounts of micrite within the sediments at depths >100 mcd and a decrease in calcium concentrations to minimum values at ~75 mcd. As at Site 1238, the increase in dissolved silicate with increasing depth reflects enhanced dissolution of biogenic opal that is controlled by the anomalously high temperature gradient at Site 1239.

Site 1239 combines a complete composite section through the APC interval of 189 mcd, double XCB coring that may document complete recovery to basement, and excellent logging data to place the deeper APC cores and the XCB cores into a true depth framework. Moderately high sedimentation rates combined with observations of rhythmic shifts in sediment composition that probably represent orbital-scale variability, and a rich array of well to moderately preserved biogenic tracers offer opportunities for high-resolution studies of late Neogene changes in equatorial East Pacific oceanography and biogeochemical cycles. Volcanic ashes present an opportunity for tephrochronology and for establishing the history of major volcanic events in the northern Andes.

Site 1240

Site 1240 (proposed Site PAN-2A) is located at 2921 m water depth in the southern Panama Basin (Fig. F1). The site is in a small east-west-trending trough of basaltic crust (Fig. F60) formed at the Cocos-Nazca spreading center ~3 m.y. ago. The pelagic sediment cover at Site 1240 drapes the abyssal hills, with a slight thickening of the section within the valleys. Total sediment thickness was estimated at 250–280 m based on seismic survey data (Fig. F61). The tectonic backtrack path of Site 1240 over the past 3 m.y. moves the site from its current position (~2 km north of the equator) ~40 km to the south and 200 km to the west (Fig. F6). Thus, the site persisted below the equatorial upwelling belt during its Pleistocene to Pliocene history.

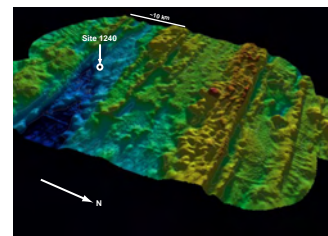
Today, equatorial upwelling driven by southeasterly trade winds is strong over Site 1240, especially during the Southern Hemisphere winter. The nutrient-rich EUC serves as primary source of upwelled waters that maintain a high productivity, although modern productivity is 12% to 40% lower than it is to the east at Sites 1238 and 1239. The surface-ocean properties of the eastern equatorial Pacific are sensitive to interannual to decadal variability such as those of the well-known El Niño Southern Oscillation (ENSO) events, as well as to longer-term changes associated with the Pleistocene ice ages. Modern deep waters at Site 1240 derive from mid-depth waters that enter the Panama Basin from the north and south through passages above sill depths of ~2000–2500 m (Fig. F5). Panama Basin deep waters are depleted in oxygen and ¹³C and enriched in nutrients relative to waters at equivalent depths outside the basin, because of high organic carbon flux and in situ oxidation of ¹³C-depleted organic matter.

The primary objectives at Site 1240 were to provide a continuous sedimentary sequence of upper Neogene sediment to (1) assess variability of upper-ocean processes, including equatorial upwelling and productivity, as well as changes in upper-ocean temperature and pycnocline depth at millennial to orbital timescales and (2) monitor changes in the signature of Panama Basin deep water that combine global, regional, and local effects.

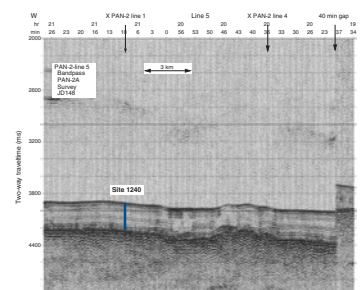
At Site 1240, four APC holes were cored to 253.0, 248.2, 80.2, and 31.7 mbsf, with the objective to recover a complete stratigraphic sequence (Table T2). The nonmagnetic core barrel was used on approximately every second APC core. APCT downhole temperature measurements yielded a low average thermal gradient of 2.6°C/100 m, about half the normal gradient for sediments above oceanic crust.

A 282.9-mcd-thick (253.0 mbsf) sequence of Pliocene (~2.8 Ma) to Holocene pelagic sediments was recovered at Site 1240 (Fig. F62). A composite depth scale and splice document complete recovery to the bottom of the sequence. Sediments consist mostly of nannofossil ooze with varying amounts of diatoms. Siliciclastic components, primarily clay, are rare. A single lithostratigraphic unit was defined and subdivided into three subunits. Subunit IA (0–142.2 mcd) and IC (206.4–282.93) are very similar and primarily consist of nannofossil ooze with TOC contents of <1.5 wt% and carbonate concentrations ranging between 40 and 80 wt%. Subunit IB (142.2–206.4 mcd; ~1.7–2.0 Ma) has lower carbonate contents (20–50 wt%) and is enriched in diatoms, siliciclastic components and TOC (1.1–3.1 wt%). A similar event was recorded at Sites 1238 and 1239, as well as at Leg 138 Sites 846 and 847, which span a modern depth range from ~1400 to ~3300 m. Color banding is frequently present throughout Subunit IB. The change in the rela-

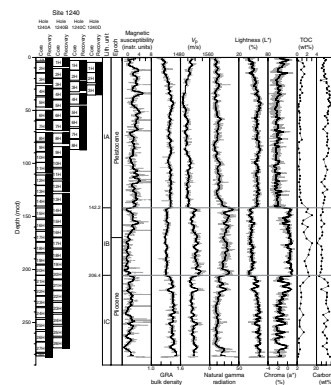
F60. Swath bathymetry of a Panama Basin segment, p. 135.



F61. Seismic profile across Site 1240, p. 136.



F62. Core recovery, lithology, age, and physical and chemical data summary, Site 1240, p. 137.



tive supply of biogenic opal, carbonate, and TOC is clearly documented in the core logging data, with distinctly lower values in bulk density and lightness (L^*) and higher reddish hue ($a^* > 0$) and NGR values (Fig. F62). These records separate Subunit IB by sharp transitions from Subunits IA and IC. Downhole logs at Sites 1238 and 1239 revealed that high NGR is driven by high uranium content, a probably redox signal associated with enhanced carbon flux. Eight ash layers were recorded at Site 1240. Grain compositions of most of the ash layers can be associated with volcanism from northern South America. However, some ash layers containing brown volcanic glass indicate that Central America is a possible source region. In addition, the presence of an ash layer fully composed of brown glass (~268 mcd; ~2.5 Ma) may indicate a different source such as the Galapagos archipelago, which was nearby at the time, based on a tectonic backtrack.

Calcareous nannofossils are generally abundant and well preserved at Site 1240, but preservation declines between 20 and 46 mcd (0.2–0.5 Ma) and >120 mcd (>1.4 Ma). Foraminifers are common, with moderate to good preservation, except between 163 and 194 mcd (1.7–1.9 Ma). Diatoms are common throughout the section and are very abundant but severely fragmented in the upper portions of Subunit IB. Persistent reworking of late Miocene microfossils is noted throughout the sequence. A well-constrained biostratigraphy was obtained from calcareous microfossils and diatoms. The paleomagnetic record provided additional age control points through the Gauss/Matuyama boundary that are consistent with the biostratigraphic datums.

MARs and LSRs vary between 3 and 8 g/cm²/k.y. and 70–160 m/m.y., respectively. The highest MARs occur in upper Pliocene Subunit IB (2.0–1.7 Ma), and the lowest MARs are estimated for the last 1 m.y. High TOC contents and MARs as well as a high abundance of diatoms suggest a late Pliocene interval of increased productivity between ~1.7 and 2.0 Ma, perhaps associated with enhanced equatorial upwelling and intensified atmospheric and oceanic circulation.

Very low amounts of biogenic methane and ethane were detected. Pore water chemical gradients reflect the influence of organic matter oxidation and sulfate reduction to values about one-half that of seawater. Fluid flows of relatively unaltered seawater in the underlying basement affect pore waters in the deeper section, for example with return to relatively high concentrations of sulfate and calcium at depths >210 mcd. Pore water silicate increases to generally high values of >1000 mM but never reaches the values observed at Sites 1238 and 1239, where downhole temperatures were significantly higher.

Site 1240 provides a continuous sedimentary sequence of upper Neogene sediment to assess variability of upper-ocean processes, including equatorial upwelling, at millennial to orbital timescales. Sedimentation rates at this site are clearly high enough to record millennial scale variability, and the record is continuous as far back as ~2.8 Ma, encompassing the Pliocene–Pleistocene interval associated with Northern Hemisphere glaciation. The major changes in lithology at this setting of equatorial divergence are between sediments rich in calcareous nannofossils and those rich in diatoms and organic carbon, consistent with control by variations in upwelling and productivity.

Site 1241

Site 1241 (proposed Site COC-2A) is located on a gently sloping sediment-covered ramp on the north flank of Cocos Ridge at a water depth

of 2027 m in the Guatemala Basin (Fig. F1). Seismic survey data document a ~400-m-thick sedimentary section (Fig. F63). The underlying crust formed at the Galapagos hotspot ~11–13 m.y. ago. A tectonic backtrack path on the Cocos plate moves Site 1241 southward and slightly to the west relative to South America.

Today, Site 1241 is situated under the warm, relatively low salinity surface waters of the Panama Basin. Nutrients at the sea surface are low, and biological productivity is substantially lower than at the equator. The site is likely to record changes in upwelling and biological productivity, from higher values early in its history (when it was close to the equator and at relatively shallow depths) to relatively low values at present. Furthermore, Site 1241 is expected to provide a record of surface water salinity reduction that occurred in response to the closure of the Isthmus of Panama, as well as shorter fluctuations associated with variable rainfall under the intertropical convergence.

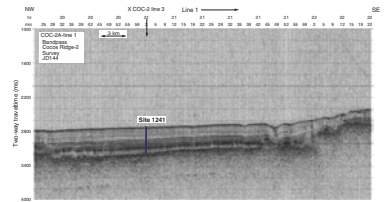
The water depth of Site 1241 is ideal to monitor changes in PCW that originates in the North Pacific and is relatively depleted in oxygen and enriched in nutrients (Fig. F5). Today, PCW enters the Guatemala Basin through fracture zones in the East Pacific Rise above 3000 m water depth (sill depth). Thermal subsidence would predict that the site was at shallower water depths during late Miocene time, possibly monitoring intermediate waters.

The primary objectives at Site 1241 were to provide a continuous sedimentary sequence over the Neogene to (1) assess variability of upper-ocean processes, including the development of Atlantic to Pacific salinity contrast associated with the closure of the Isthmus of Panama and other late Neogene climate changes, (2) reconstruct changes in the signature of PCW, (3) monitor late Neogene changes in carbonate dissolution at the upper reaches of the lysocline depth, including processes that are associated with the phenomenon of the Miocene carbonate crash, and (4) provide a history of explosive volcanism in Mesoamerica, as reflected in ash layers.

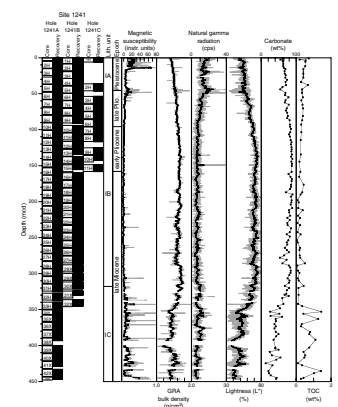
At Site 1241, three holes were cored with the APC to 314.2, 259.4, and 143.5 mbsf (Table T2). The nonmagnetic core barrel was used on approximately every second APC core. Holes 1241A and 1241B were advanced with the XCB to 394.4 and 307.6 mbsf, respectively. Several short intervals were drilled without coring in Holes 1241B and 1241C to adjust the coring depth and optimize stratigraphic overlap. Hole 1241B was logged with the triple combo, including the MGT and the FMS-sonic tool strings. Downhole temperature measurements taken with the APCT tool indicated a low thermal gradient of ~2.7°C/100 m.

A 447.8-mcd-thick (399.4 mbsf) upper Miocene (~12 Ma) to Holocene pelagic sediment sequence was recovered at Site 1241 (Fig. F64). Based on high-resolution core logging data, a composite section and splice documented complete recovery of the upper 303.1 mcd. XCB cores from Hole 1241A and 1241B were appended onto the mcd scale using a 13% growth rate of mcd relative to mbsf. The recovered sediments are dominated by nannofossil ooze with varying amounts of foraminifers, diatoms, clay, micrite, and volcanic glass. Increases in biogenic silica are reflected by decreases in bulk density. Color reflectance data (lightness L^*) correlate well with changes in carbonate contents ($R^2 = 0.8$) and increases in magnetic susceptibility data are associated with increases in clay. Almost the entire sequence is characterized by meter-scale cyclic changes in color reflectance (particularly L^*) and bulk density. Downhole logging also provided evidence for high-frequency variability in density and resistivity throughout the sequence from 82 (the

F63. Seismic profile across Site 1241, p. 138.



F64. Core recovery, lithology, age, and physical and chemical data summary, Site 1241, p. 139.



shallowest logging depth) to 395 mbsf. Color banding on the FMS images occurs on the same scale. These variations in the cores and logs are interpreted to reflect orbital-scale changes in carbonate relative to biogenic opal in the sediment.

One lithologic unit is defined and divided into three subunits on the basis of changes in sediment composition and associated changes in core logging data (Fig. F64). Subunit IA (0 to ~52 mcd; 0–2 Ma) is marked by moderate carbonate concentrations of 55–75 wt%, high amounts of foraminifers, and low amounts of biogenic opal. Clay content and magnetic susceptibility values are higher from 0 to 15 mcd. Subunit IB (52–318 mcd; 2–9 Ma) is characterized by generally high carbonate concentrations. Carbonate concentrations increase in Subunit IB (52–120 mcd; 2–4.5 Ma) to ~85 wt% as nannofossil abundance increases and foraminifer abundance decreases. As a result, NGR and magnetic susceptibility decrease and color reflectance (L^*) increases, reflecting an increasing carbonate/clay ratio. The lower part of Subunit IB (120–318 mcd; ~4.5–9 Ma) is remarkably homogeneous with high carbonate concentrations (~70–90 wt%) reflecting high abundance of nannofossils, moderate amounts of biogenic opal, and low abundance of siliciclastic grains. Subunit IC (318–447 mcd; 9–12 Ma) is characterized by reduced carbonate concentrations (~40 wt%) and increased abundance of diatoms, organic carbon, siliciclastic grains, and volcanic glass.

Calcareous nannofossils are abundant and generally well to moderately well preserved throughout the sequence. Of taxonomic interest is the observation of a new transitional form between *Discoaster bellus* and *Discoaster berggrenii* at the site. This new form fills in the missing link between the two species and has implications for biostratigraphy and evolutionary studies. Planktonic foraminifers are abundant to common in the interval from 0 to 217 mcd and generally rare at depths >217 mcd (~6.4 Ma). The percentage of benthic foraminifers relative to total foraminifers is low (~1%) in the upper interval but high (~99%) in the lower interval. Diatoms are rare to few and poorly preserved in the upper 184 mcd of the sequence. Diatom abundance increases and preservation improves below ~195 mcd (~6 Ma).

The biostratigraphies of the three planktonic microfossil groups document a continuous sequence of the early late Miocene through the late Pleistocene. Calcareous nannofossils and planktonic foraminifers constrain the basal age of the site at ~11.2–11.6 Ma. The uppermost part of the sequence might be affected by a hiatus (or anomalously low sedimentation rates) during the interval from 0 to 0.46 m.y. as indicated by the absence of the calcareous nannofossils *Emiliana huxleyi* and *Pseudemiliana lacunosa*. In contrast, the last occurrence datum of the planktonic foraminifer *Globigerinoides ruber* (pink) between 2.35 and 3.86 mcd indicates an age younger than 0.12 Ma for the overlying interval and suggests that sedimentation was continuous at least for the late Pleistocene and possibly to the Holocene. Paleomagnetism provided a magnetic stratigraphy for the upper 15 mcd indicating that the Brunhes/Matuyama and the upper and lower Jaramillo boundaries are clearly recognizable from both inclination and declination records. Little NRM was left below that interval.

Lithology as well as fossil assemblages and abundances at Site 1241 reflect the influence of the equatorial high productivity belt, the Miocene to Holocene path of the site away from the equator toward its modern more northeasterly position at ~6°N, and the vicinity of volcanic islands in the early history of the site. MARs and LSRs are 1–6 g/cm²/k.y. and 18–60 m/m.y., respectively. The rates reflect mainly the

variations in carbonate MARs and also show a clear trend of decreasing noncarbonate MARs with time. A relative peak in MARs is indicated at 9–10 Ma, when a significant opal and TOC component amplified the carbonate MAR. This interval corresponds to the time of the carbonate crash (~8.6–11.2 Ma), characterized by low carbonate accumulation rates and poor preservation of calcareous microfossils. Although Site 1241 was located well above the CCD during the middle Miocene, the preservation of calcareous nannofossils, planktonic foraminifers, and even benthic foraminifers was strongly affected by carbonate dissolution. The increase in biogenic opal (including laminated diatom oozes), organic carbon, and MARs at depths >320 mcd reflects high surface productivity and enhanced organic carbon rain when the site was near the equator early in its history.

At ages <6 Ma, MARs and LSRs decrease gradually to minimum values during the last 1 m.y. Considering the backtrack of Site 1241, this continuous decline probably reflects the slow drift away from the more productive equator and subsidence to greater water depths, where carbonate dissolution increases. The main peaks in MARs and LSRs occur at ~7–6 Ma and are mainly driven by the accumulation of calcareous nannofossils; however, micrite also doubles (to ~15%) in this interval, reflecting recrystallization. A high carbonate MAR was found for approximately the same time interval at Sites 1236 (~21°S) and 1237 (16°S) as well as in the equatorial Pacific at Sites 848–853 and is often referred to as the late Miocene to early Pliocene biogenic bloom.

Abundant clay and volcanic glass in the lower upper Miocene interval (Subunit IC) points to an enhanced supply of siliciclastic material, possibly from a former island of Cocos Ridge. The early history of Site 1241 is marked by several ash layers enriched in brown glass and mafic minerals as well as black lapilli-sized scoria, which may reflect the volcanic activity of the nearby Galapagos hotspot. The interval of 0–6 Ma, and especially 0–2.5 Ma, is marked by ash layers enriched in clear glasses, possibly originating from Central America.

Chemical gradients in interstitial water at Site 1241 reflect the limited influence of organic matter oxidation, the dissolution of biogenic silica driven by the relatively low thermal gradient, and biogenic calcite recrystallization. Many of the profiles are consistent with a flow of relatively unaltered seawater in the underlying oceanic crust, but the lack of major change in composition makes this more difficult to assess than at Site 1240. Methanogenesis at this site is limited by the persistence of dissolved sulfate and the low organic carbon contents ranging between 0.1 and 1.4 wt%.

Site 1241 recovered a complete 303-m-long composite section with the APC and a double XCB-cored interval that may be correlated and spliced later using downhole logs. An opportunity arises here to study changes in biogeochemical cycles and oceanography associated with the Miocene to Pliocene closure history of the Isthmus of Panama and the Miocene carbonate crash. Sedimentation rates of 18–60 m/m.y., combined with observations of rhythmic shifts in sediment composition that probably represent orbital-scale variability, offer the opportunity to integrate an excellent framework of biostratigraphy into an orbitally tuned isotope stratigraphy. Volcanic ashes present an opportunity for tephrochronology and the study of linkages between major ash layers from the Caribbean and Pacific to establish the history of major volcanic events in Central America.

Site 1242

Site 1242 (proposed Site COC-4A) is located at 1364 m water depth in a shallow graben within the intersection between Cocos Ridge and the Mesoamerican Trench (Fig. F1). The sediment cover at Site 1242 is ~460 m thick and fills a subsiding basin. The basin geometry is complex, however, and is clearly affected by faulting (Fig. F65). The crust underlying the site was probably formed at the Galapagos hotspot ~15–16 m.y. ago. A tectonic backtrack path on the Cocos plate moves Site 1242 southward and to the west, placing it close to the equator and near the ancestral Galapagos hotspot early in its history (Fig. F6).

The present location of Site 1242 within the pool of warm, low-salinity surface waters north of Panama Basin is strongly influenced by heavy rainfall under the ITCZ. Nutrients at the sea surface are low, and biological productivity is relatively low for a continental margin setting.

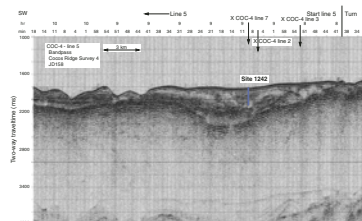
The bottom water mass at Site 1242 is associated with the lower reaches of an anomalously thick oxygen minimum zone between PCW and remnants of NPIW. These waters of North Pacific origin are relatively depleted in oxygen and enriched in nutrients. The region has one of the deepest and strongest oxygen minimum zones in the world and is, thus, an important site for denitrification. Given the relatively shallow depth of Site 1242 above the regional lysocline, variations in carbonate dissolution should be controlled by the flux rates of carbonate vs. organic carbon and subsequent organic carbon degradation within the sediments.

The primary objectives at Site 1242 were to provide a continuous sedimentary sequence of Pliocene to Holocene age to (1) assess variability of upper-ocean processes at high time resolution, including variations in the Atlantic to Pacific salinity contrast and climate-related dynamics of the ITCZ, (2) study long-term changes associated with denitrification in low-oxygen subsurface water masses, and (3) reconstruct changes in ventilation and nutrients in the transition zone between PCW and NPIW.

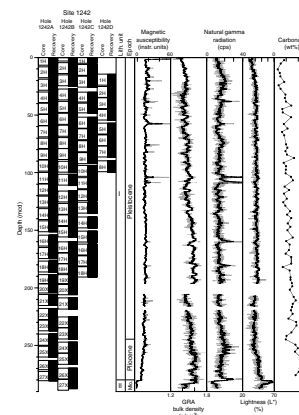
We drilled four holes at Site 1242 with APC penetration depths of 176.0, 169.9, 166.5, and 91.5 mbsf (Table T2). The nonmagnetic core barrel was used on approximately every second APC core. Holes 1242A and 1242B were advanced with the XCB to 250.8 and 256.0 mbsf, respectively. Downhole temperature measurements indicated an anomalously high thermal gradient of ~20°C/100 m.

A 288.9-mcd-thick (256.0 mbsf) middle Miocene to Holocene sequence was recovered at Site 1242 (Fig. F66). A composite depth scale and a splice document complete recovery for the upper 196.4 mcd. A major hiatus at ~280 mcd encompasses the interval from ~2.5 to 13 Ma. The sequence was subdivided into two lithologic units, Unit I (0–281 mcd) above the hiatus and Unit II (281–287 mcd) below the hiatus. Unit I consists of fine-grained, homogeneous hemipelagic sediments. Core logging data vary significantly on decimeter to meter scales throughout this sequence, indicating changes in the relative supplies of terrigenous and biogenic material to Site 1242. These changes likely reflect millennial to orbital scale changes in productivity and/or climate. Siliciclastic material is the dominant sediment component and gradually decreases downhole except for the top 20 mcd, where it increases downhole. TOC decreases downhole in the top 10 mcd, from 3.5 to 2.2 wt%, and then also decreases gradually downhole to ~1.4 wt% at depths >150 mcd. Calcium carbonate concentrations increase gradually

F65. Seismic profile across Site 1242, p. 140.



F66. Core recovery, lithology, age, and physical and chemical data summary, Site 1242, p. 141.



downhole from values <20 wt% in the top 40 mcd to values >35% in the interval 250–280 mcd.

Unit II, representing the middle Miocene sediments below the hiatus, consists of diatom-bearing nannofossil ooze. The southward tectonic backtrack path of Site 1242 and the relatively high abundance of siliceous microfossils suggests that the site was close to the equatorial upwelling and high productivity belt in its early history.

Calcareous nannofossils are relatively rare and moderately preserved at Site 1242. Planktonic foraminifers are abundant to common in the upper ~70 m, but abundance decreases markedly downhole. Planktonic foraminifers are rare from 269 to 277 mcd, just below the major unconformity. Preservation is moderate to good in the upper 99 mcd but deteriorates markedly below this depth. Diatoms are generally rare at Site 1242, with higher abundance from ~208 to 215 mcd and below the hiatus. The combination of biostratigraphic markers yields a relatively well constrained age model over the past 2.5 m.y. Shipboard paleomagnetic measurements showed promise of a detailed stratigraphy based on geomagnetic paleointensity and declination variations; however, these results were limited by time constraints at the end of the cruise.

Ash layers are most frequent between 30 and 120 mcd and between 160 and 210 mcd, suggesting intervals of increased volcanic activity from ~0.4 to 1.1 Ma and from ~1.3 to 1.6 Ma. Clear platy and vesicular glass and intermediate accessory mineral compositions suggest an andesitic volcanic source, most likely in Central America.

MARs and LSRs are generally high above the hiatus (<2.4 Ma), with maximum values of 13 g/cm²/k.y. and 165 m/m.y., respectively. Non-carbonate MARs are two to three times higher than carbonate MARs in this interval. MARs and LSRs display a broad peak over the upper Pliocene to Pleistocene sequence, with maximum rates between 1.6 and 1.2 Ma. Carbonate accumulation rates are thus highest in the lower Pleistocene and lower in the Pliocene and upper Pleistocene to Holocene interval. The observed changes in sediment composition and MAR may reflect vertical tectonic movements associated with the subduction of Cocos Ridge under Central America during the past few million years, which may result in focusing of terrigenous material and environmental changes affecting both continental rainfall and marine productivity.

Chemical gradients in the interstitial waters at Site 1242 reflect the influence of organic matter oxidation by sulfate reduction, authigenic mineralization, the dissolution of biogenic silica, and the diffusive influence of basalt alteration reactions at greater depth.

Site 1242 provides a continuous sedimentary sequence of Pliocene to modern sediments to assess variability of upper-ocean and subsurface water mass processes at high resolution. The relatively high sedimentation rates of up to 138 m/m.y. and an abundant fossil record suggest that this site will provide an excellent history of climate and geochemical changes near the ITCZ.

REFERENCES

- Alpers, C., and Brimhall, G., 1988. Middle Miocene climate change in the Atacama Desert, northern Chile: evidence from supergene mineralization at La Escondida. *Geol. Soc. Am. Bull.*, 100:1640–1656.
- Barker, P.F., and Burrell, J., 1977. The opening of Drake Passage. *Mar. Geol.*, 25:15–24.
- Beaufort, L., Garidel-Thoron, T., Mix, A.C., and Pisias, N.G., 2001. ENSO-like forcing on oceanic primary production during the late Pleistocene. *Science*, 293:2440–2444.
- Behl, R.J., and Kennett, J.P., 1996. Brief interstadial events in the Santa Barbara Basin, NE Pacific, during the last 60 kyr. *Nature*, 379:243–246.
- Behrenfeld, M.J., Randerson, J.T., McClain, C.R., Feldman, G.C., Los, S.O., Tucker, C.J., Falkowski, P.G., Field, C.B., Frouin, R., Esaias, W.E., Kolber, D.D., and Pollack, N.H., 2001. Biospheric primary production during and ENSO transition. *Science*, 291:2594–2597.
- Bender, M.L., Malize, B., Orcharto, J., Sowers, T., and Jouzel, J., 1999. High precision correlations of Greenland and Antarctic ice core records over the last 100 kyr, in mechanisms of millennial scale global climate change. In Clark, P.U., Webb, R.S., and Keigwin, L.D. (Eds.), *Mechanisms of Global Climate Change at Millennial Time Scales*. Geophys. Monogr., Am. Geophys. Union, 112:149–164.
- Berger, W.H., and Jansen, E., 1994. Mid-Pleistocene climate shift: the Nansen connection. In Johannessen, O.M., Muensch, R.D., and Overland, J.E. (Eds.), *The Role of the Polar Oceans in Shaping the Global Environment*. Geophys. Monogr., Am. Geophys. Union, 85:295–311.
- Berger, W.H., Lange, C.B., and Weinheimer, A., 1997. Silica depletion of the thermocline in the eastern North Pacific during glacial conditions: clues from Ocean Drilling Program Site 893, Santa Barbara Basin, California. *Geology*, 25:619–622.
- Berger, W.H., and Wefer, G., 1996. Central themes of South Atlantic circulation. In Wefer, G., Berger, W.H., Siedler, G., Webb, D.J. (Eds.), *The South Atlantic: Present and Past Circulation*: Berlin (Springer-Verlag), 1–11.
- Berggren, W.A., and Hollister, C.D., 1974. Paleogeography, paleobiogeography, and the history of circulation of the Atlantic Ocean. In Hay, W.W. (Ed.), *Studies in Paleooceanography*. Spec. Publ.—Soc. Econ. Paleontol. Mineral., 20:126–186.
- Blunier, T., Chappellaz, J., Schwander, J., Dällenbach, A., Stauffer, B., Stocker, T.F., Raynaud, D., Jouzel, J., Clausen, H.B., Hammer, C.U., and Johnson, S.J., 1998. Asynchrony of Antarctic and Greenland climate change during the last glacial period. *Nature*, 394:739–743.
- Blunier, T., Schwander, J., Stauffer, B., Stocker, T., Dällenbach, A., Indermühle, A., Tschumi, J., Chappellaz, J., Raynaud, D., and Barnola, J.M., 1997. Timing of the Antarctic Cold Reversal and the atmospheric CO₂ increase with respect to the Younger Dryas event. *Geophys. Res. Lett.*, 24:2683–2686.
- Bond, G., Kromer, B., Beer, J., Muscheler, R., Evans, M.N., Showers, W., Hoffmann, S., Lotti-Bond, R., Hajdas, I., and Bonani, G., 2001. Persistent solar influence on North Atlantic climate during the Holocene. *Science*, 294:2130–2136.
- Bond, G., Showers, W., Cheseby, M., Lotti, R., Almasi, P., deMenocal, P., Priore, P., Cullen, H., Hajda, I., and Bonani, G., 1997. A pervasive millennial-scale cycle in North Atlantic Holocene and glacial climates. *Science*, 278:1257–1266.
- Broecker, W.S., 1991. The great ocean conveyor. *Oceanography*, 4:79–89.
- , 1998. Paleocean circulation during the last deglaciation: a bipolar seesaw? *Paleoceanography*, 13:119–121.
- Broecker, W.S., Bond, G., Klas, M., Bonani, G., and Wolfli, W., 1990. A salt oscillator in the glacial Atlantic? 1. The concept. *Paleoceanography*, 5:469–477.
- Broecker, W.S., and Peng, T.-H., 1982. *Tracers in the Sea*: Palisades NY (Lamont-Doherty Geol. Observ.).

- Bryden, H.L., and Brady, E.C., 1985. Diagnostic model of the three-dimensional circulation in the upper Equatorial Pacific Ocean. *J. Phys. Oceanogr.*, 15:1255–1273.
- Cande, S.C., and Kent, D.V., 1995. Revised calibration of the geomagnetic polarity timescale for the Late Cretaceous and Cenozoic. *J. Geophys. Res.*, 100:6093–6095.
- Cande, S.C., and Leslie, R.B., 1986. Late Cenozoic tectonics of the southern Chile Trench. *J. Geophys. Res.*, 91:471–496.
- Cande, S.C., Leslie, R.B., Parra, J.C., and Hobart, M., 1987. Interaction between the Chile Ridge and Chile Trench: geophysical and geothermal evidence. *J. Geophys. Res.*, 92:495–520.
- Cane, M., and Clement, A.C., 1999. A role for the tropical Pacific coupled ocean-atmosphere system on Milankovitch and millennial timescales, Part II: global impacts. In Clark, P.U., Webb, R.S., and Keigwin, L.D. (Eds.), *Mechanisms of Global Climate Change at Millennial Time Scales*. Geophys. Monogr., Am. Geophys. Union, 112:373–383.
- Cannariato, K.G., Kennett, J.P., and Behl, R.J., 1999. Biotic response to late Quaternary rapid climate switches in Santa Barbara Basin: ecological and evolutionary implications. *Geology*, 27:63–66.
- Charles, C.D., Lynch-Stieglitz, J., Ninnemann, U.S., and Fairbanks, R.G., 1996. Climate connections between the hemispheres revealed by deep sea sediment core/ice core correlations. *Earth Planet. Sci. Lett.*, 142:19–27.
- Clark, C.D., Knight, J.K., and Gray, J.T., 2000. Geomorphological reconstruction of the Labrador sector of the Laurentide ice sheet. *Quat. Sci. Rev.*, 19:1343–1366.
- Clark, P.U., and Pollard, D., 1998. Origin of the middle Pleistocene transition by ice sheet erosion of regolith. *Paleoceanography*, 13:1–9.
- Claypool, G.E., and Kvenvolden, K.A., 1983. Methane and other hydrocarbon gases in marine sediment. *Annu. Rev. Earth Planet. Sci.*, 11:299–327.
- Clement, A.C., Seager, R., and Cane, M.A., 1999. Orbital controls on the El Niño/Southern Oscillation and the tropical climate. *Paleoceanography*, 14:441–456.
- Codispoti, L.A., and Christensen, J.P., 1985. Nitrification, denitrification and nitrous oxide cycling in the eastern tropical South Pacific Ocean. *Mar. Chem.*, 16:277–300.
- Collins, L.S., Coates, A.G., Berggren, W.A., Aubry, M.-P., and Zhang, J., 1996. The late Miocene Panama isthmian strait. *Geology*, 24:687–690.
- Cox, A., and Engebretson, D., 1985. Changes in motion of the Pacific plate at 5 Myr BP. *Nature*, 313:472–474.
- Crowley, T.J., Kim, K.-Y., Mengel, J.G., and Short, D.A., 1992. Modeling 100,000-year climate fluctuations in pre-Pleistocene time series. *Science*, 255:705–707.
- Curry, W.B., Shackleton, N.J., Richter, C., et al., 1995. *Proc. ODP, Init. Repts.*, 154: College Station, TX (Ocean Drilling Program).
- DeMets, C., Gordon, R.G., Argus, D.F., and Stein, S., 1990. Current plate motions. *Geophys. J. Int.*, 101:425–478.
- Dengo, G., 1985. Tectonic setting for the Pacific margin from southern Mexico to northwestern Columbia. In Naim, A.E., Stehli, F.G., and Uyeda, S. (Eds.), *The Pacific Ocean: The Ocean Basins and Margins*, 7A: New York (Plenum Press), 123–180.
- Denton, G.H., Heusser, C.J., Lowell, T.V., Moreno, P.J., Andersen, B.G., Heusser, L.E., Schlüchter, C., and Marchant, D.R., 1999. Interhemispheric linkage of paleoclimate during the last glaciation. *Geografiska Annaler*, 81A:107–153.
- Detrick, R.S., and Crough, S.T., 1978. Island subsidence, hot spots, and lithospheric thinning. *J. Geophys. Res.*, 83:1236–1244.
- Driscoll, N.W., and Haug, G.H., 1998. A short circuit in thermohaline circulation: a cause for northern hemisphere glaciation? *Science*, 282:436–438.
- Duque-Caro, H., 1990. Neogene stratigraphy, paleoceanography and paleobiogeography in northwest South America and the evolution of the Panama Seaway. *Palaeogeogr., Palaeoclimatol., Palaeoecol.*, 77:203–234.
- Farrell, J.W., Pedersen, T.F., Calvert, S.E., and Nielsen, B., 1995a. Glacial–interglacial changes in nutrient utilization in the equatorial Pacific Ocean. *Nature*, 377:515–517.

- Farrell, J.W., Raffi, I., Janecek, T.C., Murray, D.W., Levitan, M., Dadey, K.A., Emeis, K.-C., Lyle, M., Flores, J.-A., and Hovan, S., 1995b. Late Neogene sedimentation patterns in the eastern equatorial Pacific. *In* Pisias, N.G., Mayer, L.A., Janecek, T.R., Palmer-Julson, A., and van Andel, T.H. (Eds.), *Proc. ODP, Sci. Results*, 138: College Station, TX (Ocean Drilling Program), 717–756.
- Feldberg, M.J., and Mix, A.C., 2002. Sea-surface temperature estimates in the Southeast Pacific based on planktonic foraminiferal species: modern calibration and last glacial maximum. *Mar. Micropaleontol.*, 44:1–29.
- Frakes, L.A., 1979. *Climate Throughout Geological Time*: New York (Elsevier).
- Ganeshram, R.S., Pedersen, T.F., Calvert, S.E., and Murray, J.W., 1995. Large changes in oceanic nutrient inventories from glacial to interglacial periods. *Nature*, 376:755–758.
- Gildor, H., and Tziperman, E., 2001. Sea ice as the glacial cycles' climate switch: role of seasonal and orbital forcing. *Paleoceanography*, 15:605–615.
- Gordon, A.I., 1986. Interocean exchange of thermocline water. *J. Geophys. Res.*, 91:5037–5046.
- Gregory-Wodzicki, K.M., 2000. Uplift history of the central and northern Andes: a review. *Geol. Soc. Am. Bull.*, 112:1091–1105.
- Groottes, P.M., Stuvier, M., White, J.W.C., Johnsen, S., and Jouzel, J., 1993. Comparison of oxygen isotope records from the GISP2 and GRIP Greenland ice cores. *Nature*, 366:552–554.
- Harris, S.E., and Mix, A.C., 1999. Pleistocene precipitation balance in the Amazon Basin recorded in deep-sea sediments. *Quat. Res.*, 51:14–26.
- , 2002. Climate and tectonic influences on continental erosion in tropical South America, 0–13 Ma. *Geology*, 30:447–450.
- Hartley, A., and Chong, G., 2002. Late Pliocene age for the Atacama Desert: implications for the desertification of western South America. *Geology*, 30:43–46.
- Haug, G.H., and Tiedemann, R., 1998. Effect of the formation of the Isthmus of Panama on Atlantic Ocean thermohaline circulation. *Nature*, 393:673–676.
- Haug, G.H., Tiedemann, R., Zahn, R., and Ravelo, A.C., 2001. Role of Panama uplift on oceanic freshwater balance. *Geology*, 29:207–210.
- Hay, W.W., 1996. Tectonics and climate. *Geol. Rundsch.*, 85:409–437.
- Hebbeln, D., Marchant, M., and Wefer, G., 2002. Paleoproductivity in the southern Peru-Chile Current through the last 33000 yr. *Mar. Geol.*, 186:487–504.
- Hebbeln, D., Wefer, G., Baltazar, M., Beese, D., Bendtsen, J., Butzin, M., Daneri, G., Dellarossa, V., Diekamp, V., Dittert, N., Donner, B., Giese, M., Glud, R., Gundersen, J., Haese, R., and Hensen, C., 1995. Report and preliminary results of SONNE-Cruise SO 102, Valparaiso–Valparaiso, 95. *Berichte aus dem Fachbereich Geowissenschaften der Universität Bremen*, 68: Bremen, Germany (Geowissenschaften der Universität Bremen), 1–134.
- Hendy, I.L., and Kennett, J.P., 1999. Latest Quaternary North Pacific surface water responses imply atmosphere-driven climate instability. *Geology*, 27:291–294.
- , 2000a. Dansgaard-Oeschger cycles and the California current system: planktonic foraminiferal response to rapid climate change in Santa Barbara Basin, Ocean Drilling Program Hole 893A. *Paleoceanography*, 15:30–42.
- , 2000b. Stable isotope stratigraphy and paleoceanography of the last 170 k.y.: Site 1014, Tanner Basin, California. *In* Lyle, M., Koizumi, I., Richter, C., and Moore, T.C. (Eds.), *Proc. ODP, Sci. Results*, 167: College Station, TX (Ocean Drilling Program), 129–140.
- Herron, E.M., Cande, S.C., and Hall, B.R., 1981. An active spreading center collides with a subduction zone: a geophysical survey of the Chile margin triple junction. *Mem.—Geol. Soc. Am.*, 154:683–701.
- Heusser, L.E., Heusser, C.J., Kleczkowski, A., and Crowhurst, S., 1999. A 50,000-yr pollen record from Chile of South American millennial-scale climate instability during the last glaciation. *Quat. Res.*, 52:154–158.

- Hey, R., Johnson, G.L., and Lowrie, A., 1977. Recent plate motions in the Galapagos area. *Geol. Soc. Am. Bull.*, 88:1385–1403.
- Hooghiemstra, H., and Ran, E.T.H., 1994. Late Pliocene–Pleistocene high resolution pollen sequence of Colombia: an overview of climate change. *Quat. Intern.*, 21:63–80.
- Hovan, S.A., 1995. Late Cenozoic atmospheric circulation intensity and climatic history recorded by eolian deposition in the eastern equatorial Pacific Ocean, Leg 138. In Pisias, N.G., Mayer, L.A., Janecek, T.R., Palmer-Julson, A., and van Andel, T.H. (Eds.), *Proc. ODP, Sci. Results*, 138: College Station, TX (Ocean Drilling Program), 615–625.
- Imbrie, J., Boyle, E.A., Clemens, S.C., Duffy, A., Howard, W.R., Kukla, G., Kutzbach, J., Martinson, D.G., McIntyre, A., Mix, A.C., Molfino, B., Morley, J.J., Peterson, L.C., Pisias, N.G., Prell, W.L., Raymo, M.E., Shackleton, N.J., and Toggweiler, J.R., 1993. On the structure and origin of major glaciation cycles, 2. The 100,000-year cycle. *Paleoceanography*, 8:698–736.
- Imbrie, J., McIntyre, A., and Mix, A., 1989. Oceanic response to orbital forcing in the late Quaternary: observational and experimental strategies. In Berger, A., Schneider, S., and Duplessy, J.C. (Eds.), *Climate and Geo-Sciences*: Dordrecht (Kluwer Academic), 121–164.
- Jasper, J.P., Hayes, J.M., Mix, A.C., and Pahl, F.G., 1994. Photosynthetic ^{13}C fractionation and estimated CO_2 levels in the central equatorial Pacific over the last 255,000 years. *Paleoceanography*, 9:781–798.
- Jousaume, S., Sadourny, R., and Vignal, C., 1986. Origin of precipitating water in a numerical simulation of the July climate. *Ocean-Air Interact.*, 1:43–56.
- Kennett, J.P., and Ingram, B.L., 1995. A 20,000-year record of ocean circulation and climate change from the Santa Barbara Basin. *Nature*, 377:510–513.
- Kim, J., Schneider, R.R., Hebbeln, D., Müller, P.J., and Wefer, G., 2002. Alkenone-derived high-resolution sea surface temperature reconstruction in the eastern South Pacific off mid-latitude Chile over the past 33 kyr. *Quat. Sci. Rev.*, 21:2085–2097.
- Kroopnick, P., 1985. The distribution of ^{13}C of ΣCO_2 in the world oceans. *Deep-Sea Res. Part A*, 32:57–84.
- Labeyrie, L., and Elliot, M., 1999. Abrupt climatic changes—causes and consequences: an introduction. In Abrantes, F., and Mix, A. (Eds.), *Reconstructing Ocean History, a Window into the Future*: New York (Kluwer), 73–82.
- Lamy, F., Hebbeln, D., Röhl, U., and Wefer, G., 2001. Holocene rainfall variability in southern Chile: a marine record of latitudinal shifts of the southern Westerlies. *Earth Planet. Sci. Lett.*, 185:369–382.
- Lamy, F., Hebbeln, D., and Wefer, G., 1998. Terrigenous sediment supply along the Chilean continental margin: modern regional patterns of texture and composition. *Geol. Rundsch.*, 87:477–494.
- , 1999. High-resolution marine record of climatic change in mid-latitude Chile during the last 28,000 years based on terrigenous sediment parameters. *Quat. Res.*, 51:83–93.
- Lamy, F., Klump, J., Hebbeln, D., and Wefer, G., 2000. Late Quaternary rapid climate change in northern Chile. *Terra Nova*, 12:8–13.
- Lamy, F., Rühlemann, C., Hebbeln, D., and Wefer, G., 2002. High- and low-latitude climate control on the position of the southern Peru-Chile Current during the Holocene. *Paleoceanography*, 17:10.1029/2001PA000727.
- Lea, D.W., Pak, D.K., and Spero, H.J., 2000. Climate impact of late Quaternary equatorial Pacific sea surface temperature variations. *Science*, 289:1719–1724.
- Lenters, J.D., Cook, K.H., and Ringler, T.D., 1995. Comments on “On the influence of the Andes on the general circulation of the Southern Hemisphere.” *J. Clim.*, 8:2113–2115.

- Levitus, S., Conkright, M.E., Reid, J.L., Najjar, R.G., and Mantyla, N.A., 1993. Distribution of nitrate, phosphate, and silicate in the world oceans. *Prog. Oceanogr.*, 31:245–273.
- Liu, Z., and Huang, B., 2000. Cause of tropical Pacific warming trend. *Geophys. Res. Lett.*, 27:1935–1938.
- Lonsdale, P., 1976. Abyssal circulation of the southeastern Pacific and some geological implications. *J. Geophys. Res.*, 81:1163–1176.
- Lonsdale, P., and Klitgord, K.D., 1978. Structure and tectonic history of the eastern Panama Basin. *Geol. Soc. Am. Bull.*, 89:981–999.
- Loubere, P., 2000. Marine control of biological production in the eastern equatorial Pacific Ocean. *Nature*, 406:497–500.
- Lowell, T.V., Heusser, C.J., Andersen, B.G., Moreno, P.I., Hauser, A., Heusser, L.E., Schlüchter, C., Marchant, D.R., and Denton, G.H., 1995. Interhemispheric correlation of late Pleistocene glacial events. *Science*, 269:1541–1549.
- Lund, D.C., and Mix, A.C., 1998. Millennial-scale deep water oscillations: reflections of the North Atlantic in the deep Pacific from 10 to 60 ka. *Paleoceanography*: 13:10–19.
- Lyle, M., Dadey, K.A., and Farrell, J.W., 1995. The late Miocene (11–8 Ma) eastern Pacific carbonate crash: evidence for reorganization of deep-water circulation by the closure of the Panama Gateway. In Pisias, N.G., Mayer, L.A., Janecek, T.R., Palmer-Julson, A., and van Andel, T.H. (Eds.), *Proc. ODP, Sci. Results*, 138: College Station, TX (Ocean Drilling Program), 821–838.
- Lyle, M., Liberty, L., Mix, A., Pisias, N., Goldfinger, C., Hulett, D., and Janik, A., 2000. *Site Survey Data Package 5: Site Surveys for ODP Leg 201 from the NEMO-3 Cruise, in Support of Proposal 465: Southeast Pacific Paleocceanographic Transects*. CGISS Tech. Rept., 2000-06. Boise ID (Boise State Univ.).
- Lyle, M., Murray, D.W., Finney, B.P., Dymond, J., Robbins, J.M., and Brooksforce, K., 1988. The record of late Pleistocene biogenic sedimentation in the eastern tropical Pacific Ocean. *Paleoceanography*, 3:39–59.
- Maasch, K.A., and Saltzman, B., 1990. A low-order dynamical model of global climatic variability over the full Pleistocene. *J. Geophys. Res.*, 95:1955–1963.
- MacAyeal, D., 1993. Binge/purge oscillations of the Laurentide ice sheet as a cause of the North Atlantic's Heinrich events. *Paleoceanography*, 8:775–784.
- Magaña, V., Amador, J.A., and Medina, S., 1999. The midsummer drought over Mexico and Central America. *J. Clim.*, 12:1577–1588.
- Martinez-Pardo, R., 1990. Major Neogene events of the southeastern Pacific: the Chilean and Peruvian record. *Palaeogeogr., Palaeoclimatol., Palaeoecol.*, 77:263–278.
- McIntyre, A., and Molino, B., 1996. Forcing of Atlantic equatorial and subpolar millennial cycles by precession. *Science*, 274:1867–1870.
- McIntyre, A., Ruddiman, W.F., Karlin, K., and Mix, A.C., 1989. Surface water response of the equatorial Atlantic Ocean to orbital forcing. *Paleoceanography*, 4:19–55.
- Mikolajewicz, U., and Crowley, T.J., 1997. Response of a coupled ocean/energy balance model to restricted flow through the Central American isthmus. *Paleoceanography*, 12:429–441.
- Mikolajewicz, U., Crowley, T.J., Schiller, A., and Voss, R., 1997. Modelling teleconnections between the North Atlantic and North Pacific during the Younger Dryas. *Nature*, 387:384–387.
- Mikolajewicz, U., Maier-Reimer, E., Crowley, T.J., and Kim, K.-Y., 1993. Effect of Drake and Panamanian gateways on the circulation of an ocean model. *Paleoceanography*, 8:409–426.
- Mix, A.C., 1989. Influence of productivity variations on long-term atmospheric CO₂. *Nature*, 337:541–544.
- Mix, A.C., Le, J., and Shackleton, N.J., 1995. Benthic foraminiferal stable isotope stratigraphy of Site 846: 0–1.8 Ma. In Pisias, N.G., Mayer, L.A., Janecek, T.R., Palmer-Julson, A., and van Andel, T.H. (Eds.), *Proc. ODP, Sci. Results*, 138: College Station, TX (Ocean Drilling Program), 839–854.

- Mix, A.C., Lund, D.C., Pisias, N.G., Bodén, P., Bornmalm, L., Lyle, M., and Pike, J., 1999a. Rapid climate oscillations in the northeast Pacific during the last deglaciation reflect Northern and Southern Hemisphere sources. *In* Webb, R.S., Clark, P.U., and Keigwin, L. (Eds.), *Mechanisms of Millennial-Scale Global Climate Change*. Geophys. Monogr., Am. Geophys. Union, 112:127–148.
- Mix, A.C., Morey, A.E., Pisias, N.G., and Hostetler, S., 1999b. Foraminiferal faunal estimates of paleotemperatures: circumventing the no-analog problems yields cool ice-age tropics. *Paleoceanography*, 14:350–359.
- Mix, A.C., Pisias, N.G., Goldfinger, C., Lyle, M., Liberty, L., Janik, A., Hebbeln, D., Wefer, G., and Lamy, F., 2000. *Southeast Pacific Paleoceanographic Transects, Site Survey Data Package 4: NEMO Expedition, Leg III, R/V Melville, May–June 2000*: Corvallis (Oregon State Univ.).
- Mix, A.C., Pisias, N.G., Goldfinger, C., West, B., Mayer, L.A., and Bloomer, S.F., 1997. *Southeast Pacific Paleoceanographic Transects, Site Survey Data Package 2: Genesis Leg III, R/V Roger Revelle, Feb.–Apr. 1997*. Corvallis (Oregon State Univ.).
- Mix, A.C., Pisias, N.G., Zahn, R., Rugh, W., Lopez, C., and Nelson, K., 1991. Carbon 13 in Pacific deep and intermediate waters, 0–370 ka: implications for ocean circulation and Pleistocene CO₂. *Paleoceanography*, 6:205–226.
- Molina-Cruz, A., 1977. The relation of the southern trade winds to upwelling processes during the last 75,000 years. *Quat. Res.*, 8:324–339.
- Moreno, P.I., Jacobson, G.L., Lowell, T.V., and Denton, G.H., 2001. Interhemispheric climate links revealed by a late-glacial cooling episode in southern Chile. *Nature*, 409:804–808.
- Muller R.A., and MacDonald, G.J., 1997. Glacial cycles and astronomical forcing. *Science*, 277:215–218.
- Ninkovich, D., and Shackleton, N.J., 1975. Distribution, stratigraphic position and age of ash layer “L,” in the Panama Basin region. *Earth Planet. Sci. Lett.*, 27:20–34.
- Ninnemann, U.S., and Charles, C.D., 1997. Regional differences in Quaternary subantarctic nutrient cycling: link to intermediate and deep water ventilation. *Paleoceanography*, 12:560–567.
- Ocean Climate Laboratory, 1999. *World Ocean Atlas 1998 (WOA98)* [CD-ROM]. Available from: National Climatic Data Center, Asheville NC 28801-5001, USA.
- Oppo, D.W., and Fairbanks, R.G., 1989. Carbon isotope composition of tropical surface water during the past 22,000 years. *Paleoceanography*, 4:333–351.
- Oyun, S., Elderfield, H., and Klinkhammer, G.P., 1995. Strontium isotopes in pore waters of east equatorial Pacific sediments: indicators of seawater advection through oceanic crust and sediments. *In* Pisias, N.G., Mayer, L.A., Janecek, T.R., Palmer-Julson, A., and van Andel, T.H. (Eds.), *Proc. ODP, Sci. Results*, 138: College Station, TX (Ocean Drilling Program), 813–819.
- Parsons, B., and Sclater, J.G., 1977. An analysis of the variation of ocean floor bathymetry and heat flow with age. *J. Geophys. Res.*, 82:803–827.
- Pickard, G.L., and Emery, W.J., 1990. *Descriptive Physical Oceanography: An Introduction* (5th ed.): New York (Pergamon).
- Pisias, N.G., Mayer, L.A., and Mix, A.C., 1995. Paleoceanography of the eastern equatorial Pacific during the Neogene: synthesis of Leg 138 drilling results. *In* Pisias, N.G., Mayer, L.A., Janecek, T.R., Palmer-Julson, A., and van Andel, T.H. (Eds.), *Proc. ODP, Sci. Results*, 138: College Station, TX (Ocean Drilling Program), 5–21.
- Pisias, N.G., and Mix, A.C., 1997. Spatial and temporal oceanographic variability of the eastern equatorial Pacific during the late Pleistocene: evidence from radiolaria microfossils. *Paleoceanography*, 12:381–393.
- Pisias, N.G., and Moore, T.C., Jr., 1981. The evolution of Pleistocene climate: a time series approach. *Earth Planet. Sci. Lett.*, 52:450–458.
- Pye, K., 1987. *Aeolian Dust and Dust Deposits*: London (Academic Press).
- Rahmstorf, S., 1995. Bifurcations of the Atlantic thermohaline circulation in response to changes in the hydrological cycle. *Nature*, 378:145–150.

- Reid, J.L., 1973. Transpacific hydrographic sections at lats. 43 degrees S and 28 degrees S: the SCORPIO Expedition III. Upper water and a note on southward flow at mid depth. *Deep-Sea Res.*, 20:39–50.
- Rodbell, D.T., Seltzer, G.O., Andreson, D.M., Abbott, M.A., Enfield, D.B., and Newman J.H., 1999. An ~15,000 year record of El Niño-driven alluviation in southwestern Ecuador. *Science*, 283:516–520.
- Roth, J.M., Droxler, A.W., and Kameo, K., 2000. The Caribbean carbonate crash at the middle to late Miocene transition: linkage to the establishment of the modern global ocean conveyor. In Leckie, R.M., Sigurdsson, H., Acton, G.D., and Draper, G. (Eds.), *Proc. ODP, Sci. Results*, 165: College Station, TX (Ocean Drilling Program), 249–273.
- Ruddiman, W.F., and Raymo, M.E., 1988. Northern hemisphere climatic regimes during the past 3 Ma: possible tectonic connections. *Philos. Trans. R. Soc. London B*, 318:411–430.
- Stoner, J.S., Laj, J.E.T., Channell, J.E.T., and Kissel, C., 2002. South Atlantic (SAPIS) and North Atlantic (NAPIS) geomagnetic paleointensity stacks (0–80 ka): implications for inter-hemispheric correlation. *Quat. Sci. Rev.*, 21:1142–1151.
- Strub, P.T., Mesias, J.M., Montecino, V., Rutllant, J., and Salinas, S., 1998. Coastal ocean circulation off western South America. In Robinson, A.R., and Brink, K.H. (Eds.), *The Sea* (Vol. 11): *Coastal Oceans*: New York (Wiley), 273–313.
- Talley, L.D., 1993. Distribution and formation of North Pacific intermediate water. *J. Phys. Oceanogr.*, 23:517–537.
- Thompson, L.G., Davis, M.E., Mosley-Thompson, E., Sowers, T.A., Henderson, K.A., Zagorodnov, V.S., Lin, P.N., Mikhailenko, V.N., Campen, R.K., Bolzan, J.F., Cole-Dai, J., and Francou, B., 1998. A 25,000-year tropical climate history from Bolivian ice cores. *Science*, 282:1858–1864.
- Toggweiler, J.R., Dixon, K., and Broecker, W.S., 1991. The Peru upwelling and the ventilation of the South Pacific thermocline. *J. Geophys. Res.*, 96:20467–20497.
- Toggweiler, J.R., and Samuels, B., 1993. Is the magnitude of the deep outflow from the Atlantic Ocean actually governed by Southern Hemisphere winds? In Heimann, M. (Ed.), *The Global Carbon Cycle*: Berlin (Springer-Verlag), 303–331.
- Tsuchiya, M., and Talley, L.D., 1998. A Pacific hydrographic section at 88°W: water-property distribution. *J. Geophys. Res.*, 103:12899–12918.
- van der Hammen, T., Werner, J.H., and Van Dommelen, H., 1973. Palynological record of the upheaval of the Northern Andes: a study of the Pliocene and lower Quaternary of the Colombian Eastern Cordillera and the early evolution of its High-Andean biota. *Rev. Palaeobot. Palynol.*, 16:1–122.
- Wiedicke-Hombach, M., and Shipboard Scientific Party, 2002. *Cruise Report Sonne SO 161/5 (Subduction Processes of Chile)-Geology-Geochemistry-Heatflow*. Archive Number 11241/02, March 2002.
- Wunsch, C., Hu, D.X., and Grant, B., 1983. Mass, heat, salt, and nutrient fluxes in the South Pacific Ocean. *J. Phys. Oceanogr.*, 13:725–753.
- Wyrski, K., 1962. The oxygen minimum in relation to ocean circulation. *Deep-Sea Res.*, 9:11–23.
- , 1981. An estimate of equatorial upwelling in the Pacific. *J. Phys. Oceanogr.*, 11:1205–1214.
- Zachos, J.C., Pagani, M., Sloan, L., Thomas, E., and Billups, K., 2001. Trends, rhythms, and aberrations in global climate 65 Ma to present. *Science*, 292:686–693.
- Zaucker, F., Stocker, T.F., and Broecker, W.S., 1994. Atmospheric freshwater fluxes and their effect on the global thermohaline circulation. *J. Geophys. Res.*, 99:12443–12457.

Figure F1. Leg 202 drill sites span a broad latitudinal range from southern Chile to Central America. Site 1232 is in the Chile Basin; Sites 1233–1235 are on the Chile margin; Sites 1236 and 1237 are on Nazca Ridge; Sites 1238 and 1239 are on Carnegie Ridge; Site 1240 is in the Panama Basin; and Sites 1241 and 1242 are on Cocos Ridge.

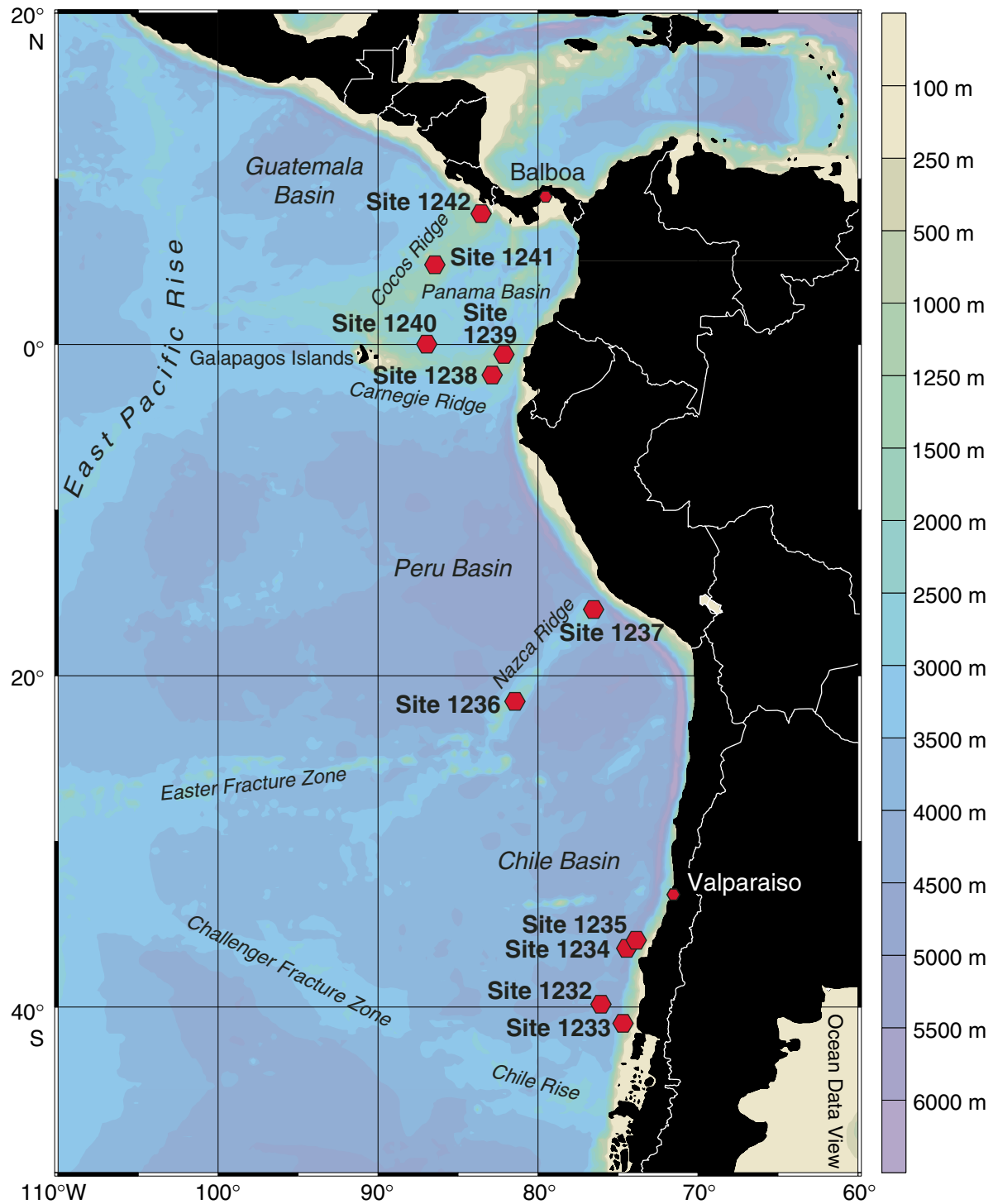


Figure F2. Summary stratigraphic columns document cored intervals, ages, and water depths at Sites 1232–1242. B. = Basin.

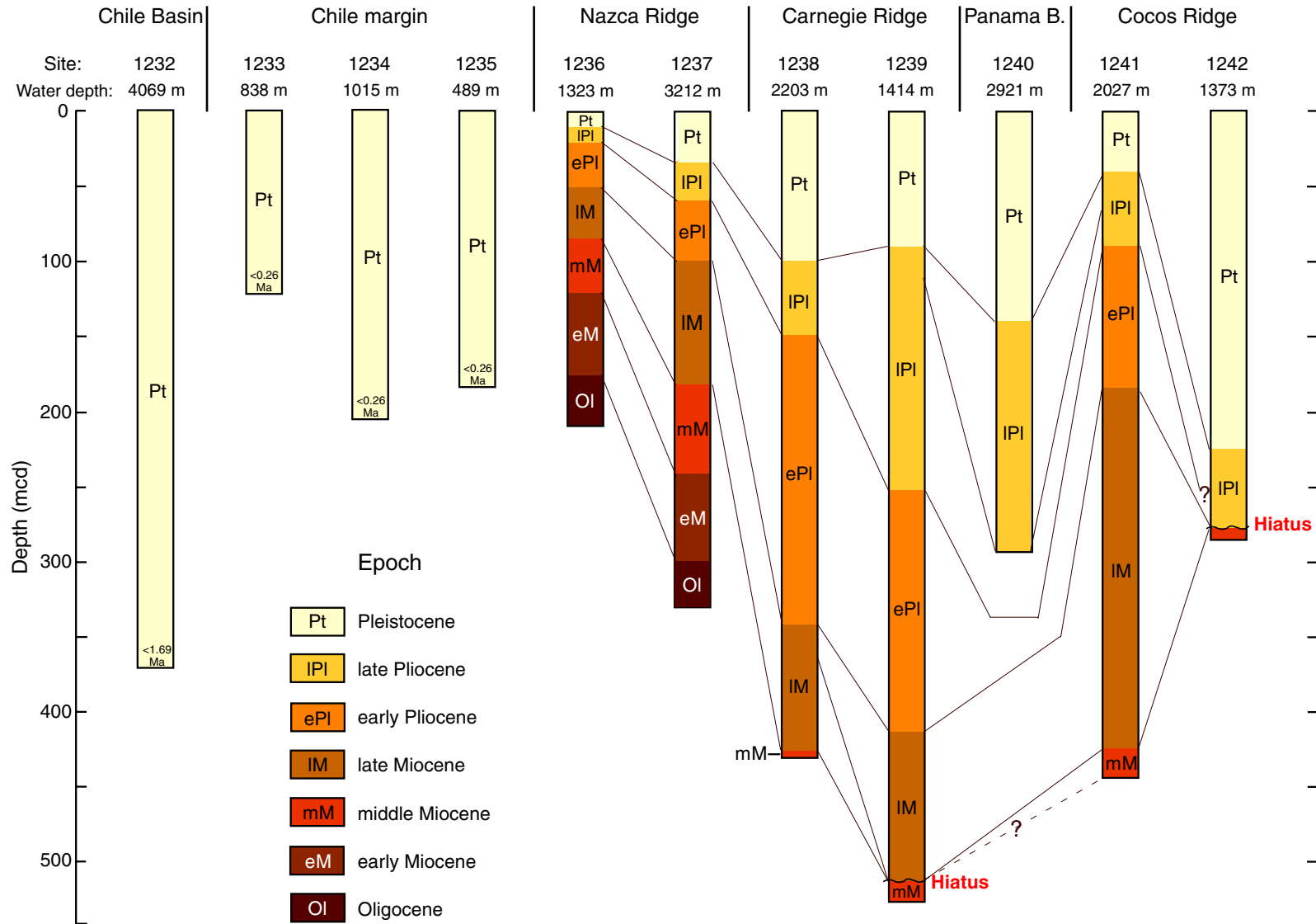


Figure F3. Schematic of upper-ocean currents off the west coast of South America. NECC = North Equatorial Countercurrent, EUC = Equatorial Undercurrent, CC = Coastal Current, GUC = Gunther Undercurrent.

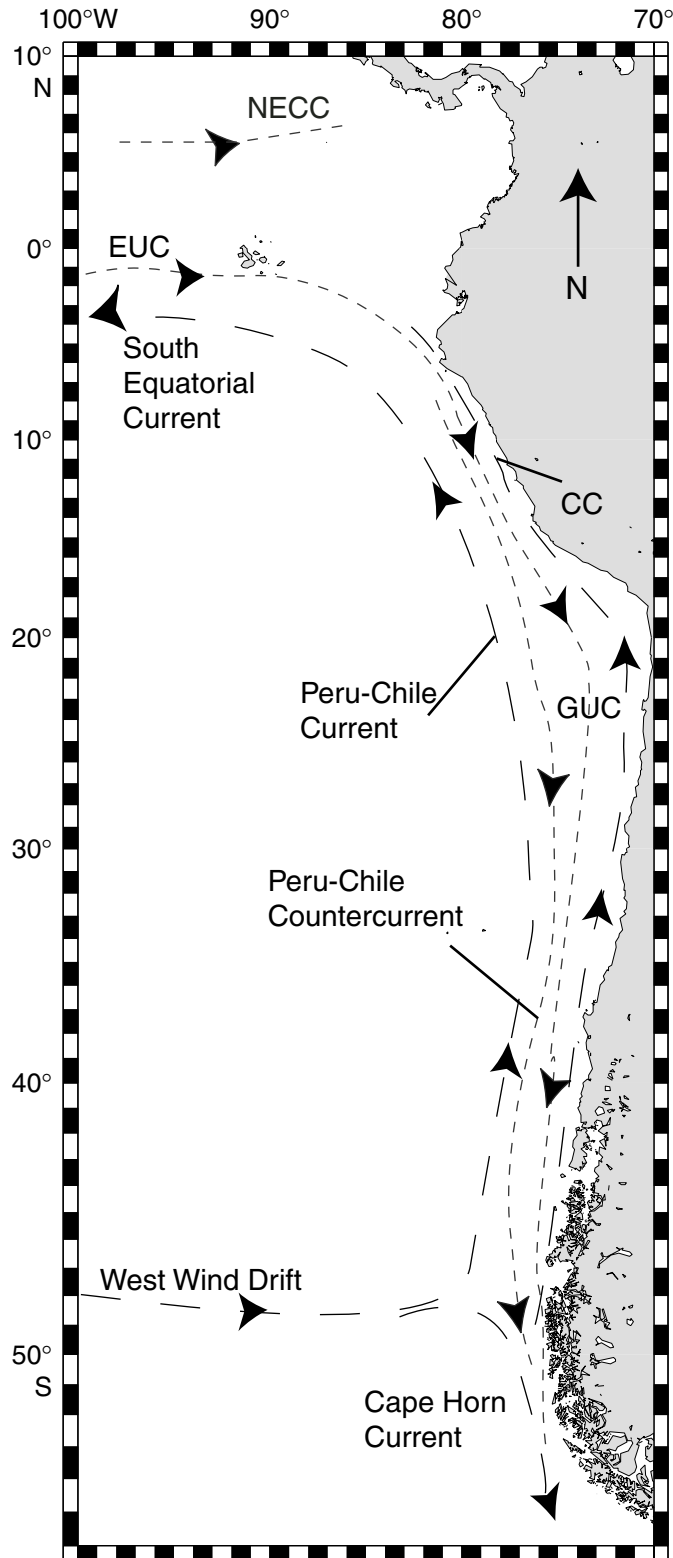


Figure F4. Site locations on modern annual average values of (A) sea-surface temperature ($^{\circ}\text{C}$), (B) sea-surface phosphate (μM), and (C) sea-surface salinity. (Continued on next two pages.)

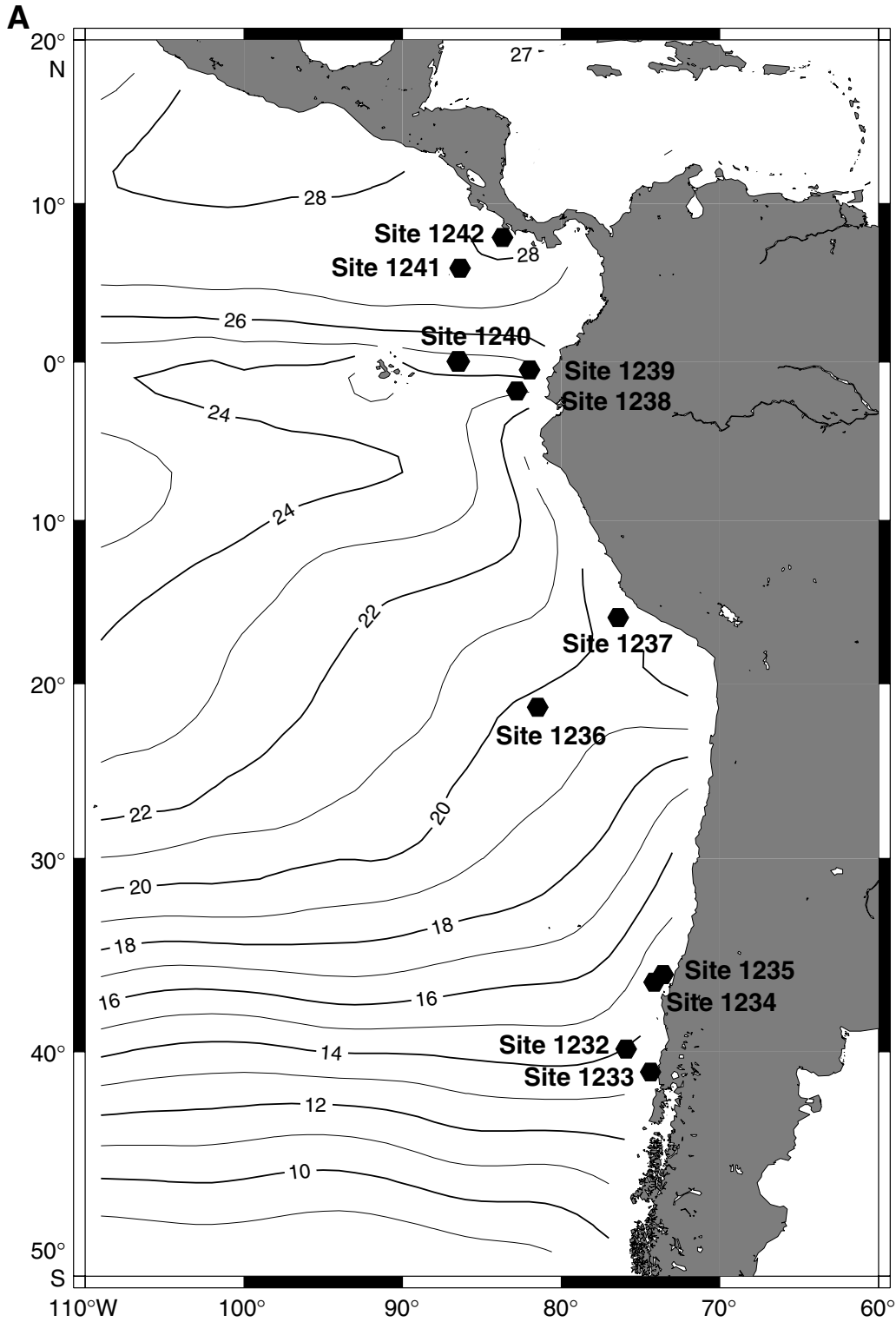


Figure F4 (continued).

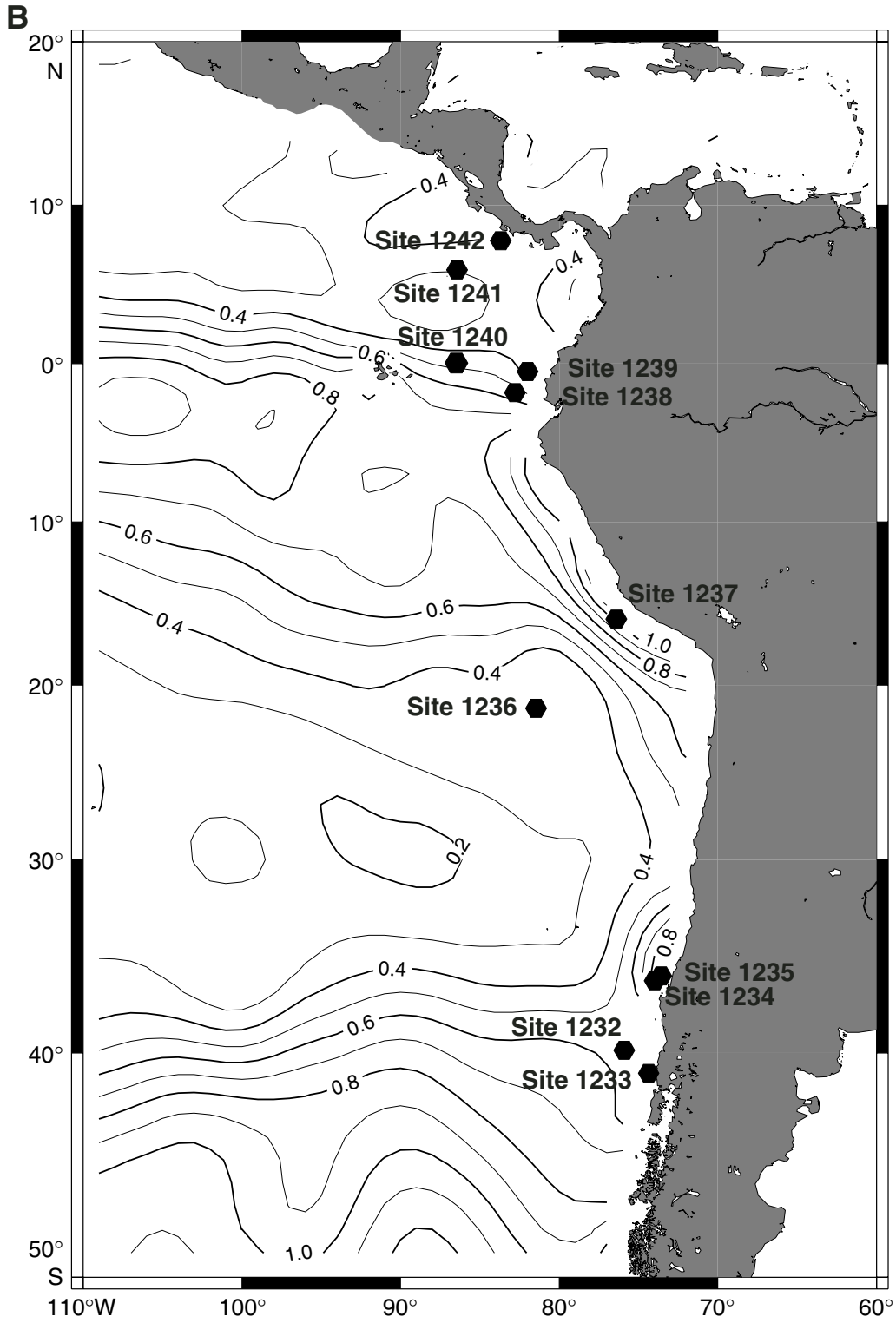


Figure F4 (continued).

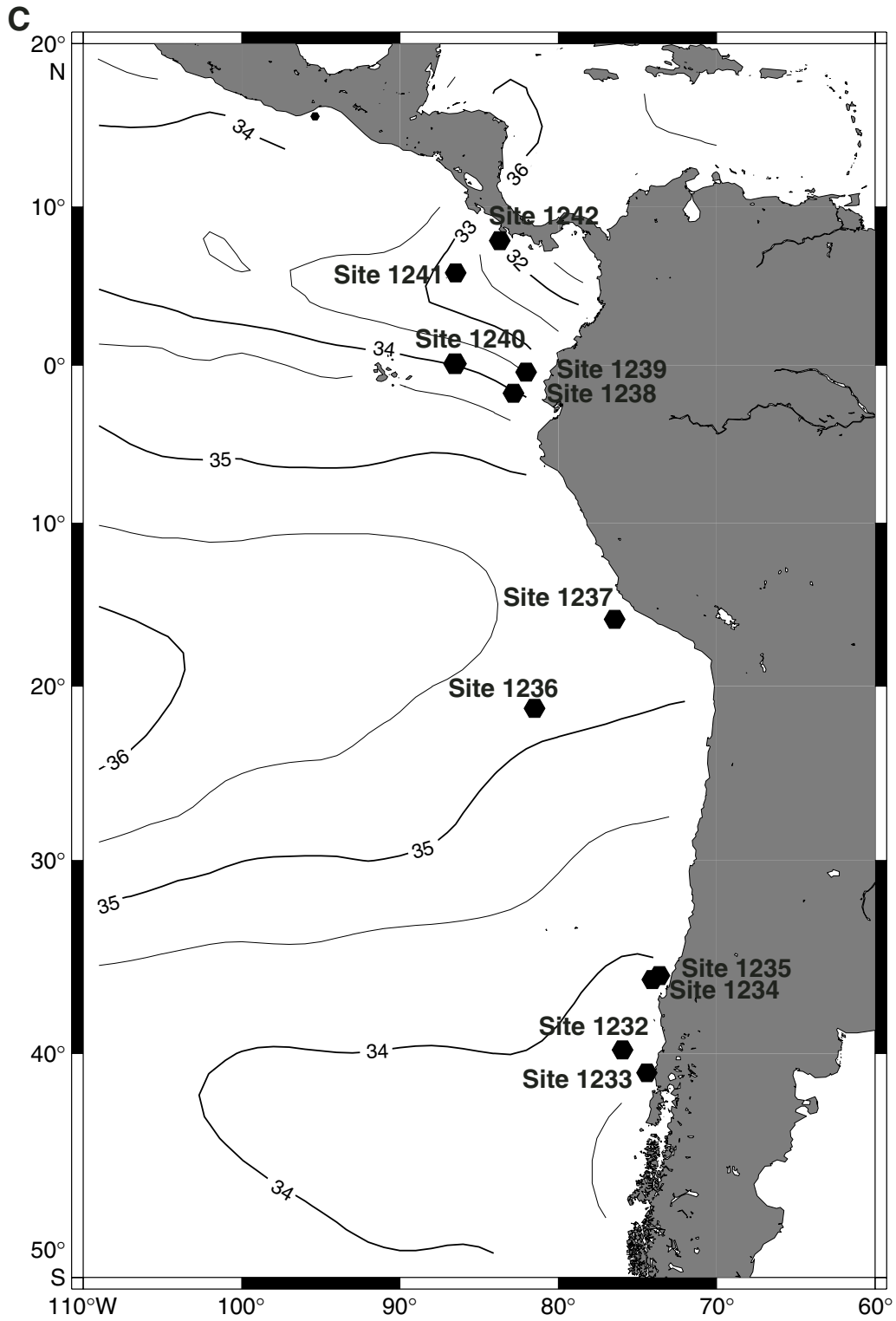


Figure F5. Cross section of subsurface water masses in a transect through the drilling sites, characterized by (A) dissolved oxygen, (B) dissolved phosphate, and (C) salinity. AAIW = Antarctic Intermediate Water, NPIW = North Pacific Intermediate Water, PCW = Pacific Central Water, GUC = Gunther Undercurrent, CPDW = Circumpolar Deep Water.

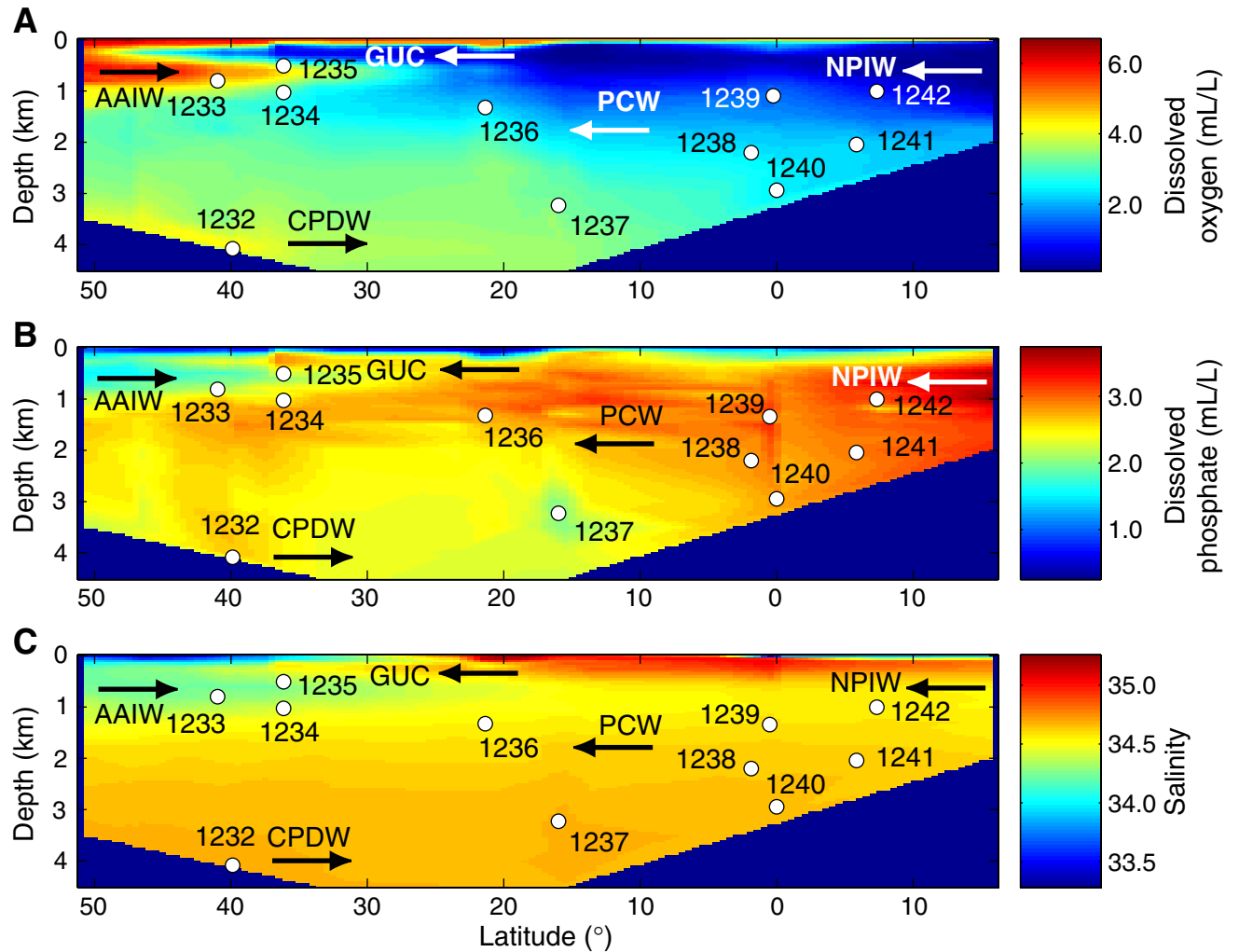


Figure F6. Plate tectonic backtrack of Leg 202 drill sites. Large circles = the modern location, and successive circles = the backtrack position relative to South America at 1-m.y. intervals. Number at the end of each backtrack path = oldest age of recovered sediment at each site in millions of years.

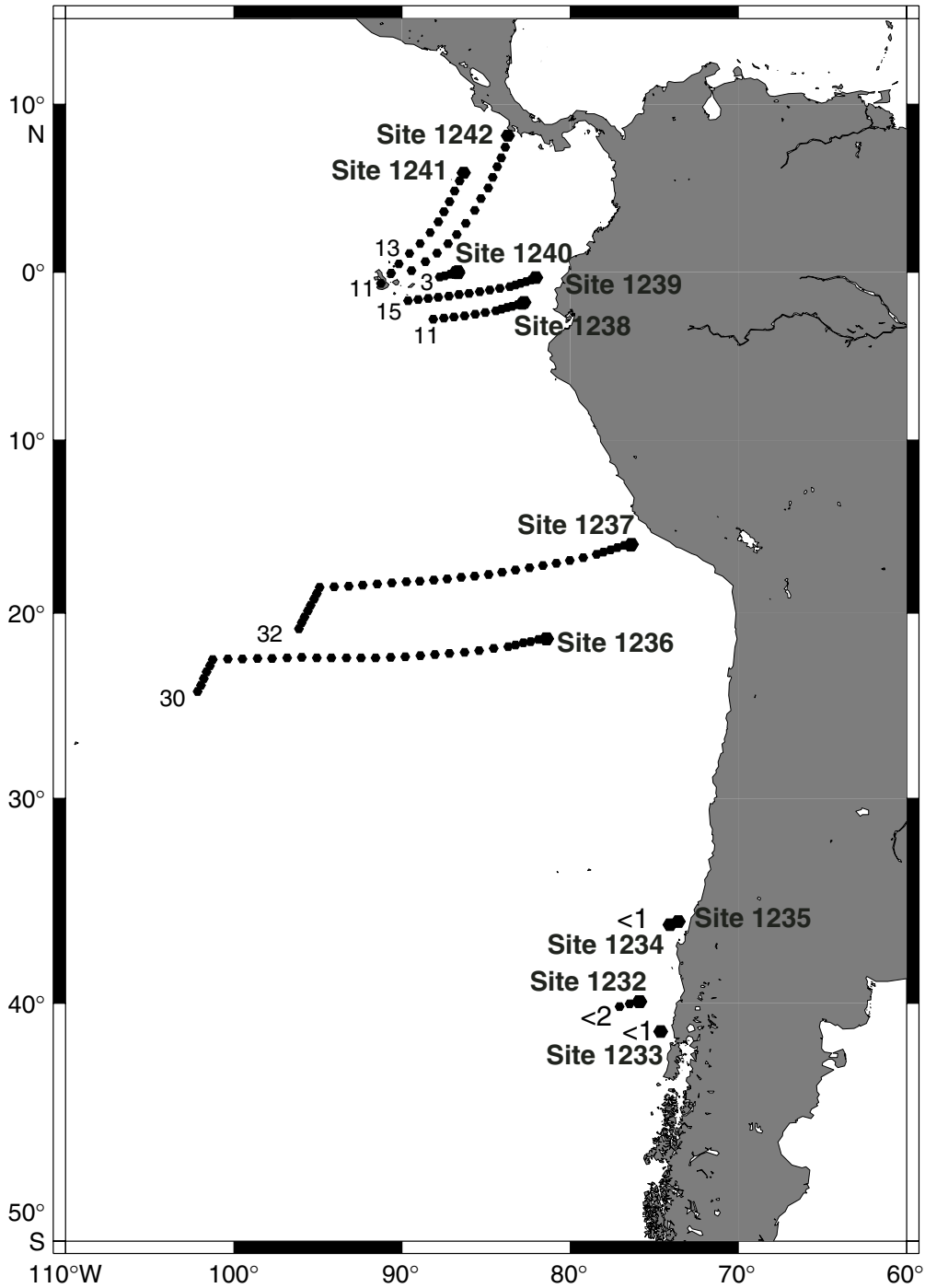


Figure F7. Core-log integration. Pervasive meter-scale rhythmic variations were observed in borehole resistivity and core density logs at Sites 1238, 1239, and 1241. Such variability is likely associated with fluctuations in the fractions of carbonate and biogenic opal in the sediments. The Formation MicroScanner (FMS) image of the borehole at Site 1241 is shown to the right of the 64-button average (5-point smoothing) in red. The similarity of the smoothed FMS and the lower-resolution gamma ray attenuation (GRA) bulk density record (blue) in cores from Hole 1241B suggests that borehole logs will provide a relatively continuous proxy record of lithologic variability and will provide for detailed integration of depth scales between the borehole and core logs. eld in mbsf = equivalent logging depth in meters below seafloor.

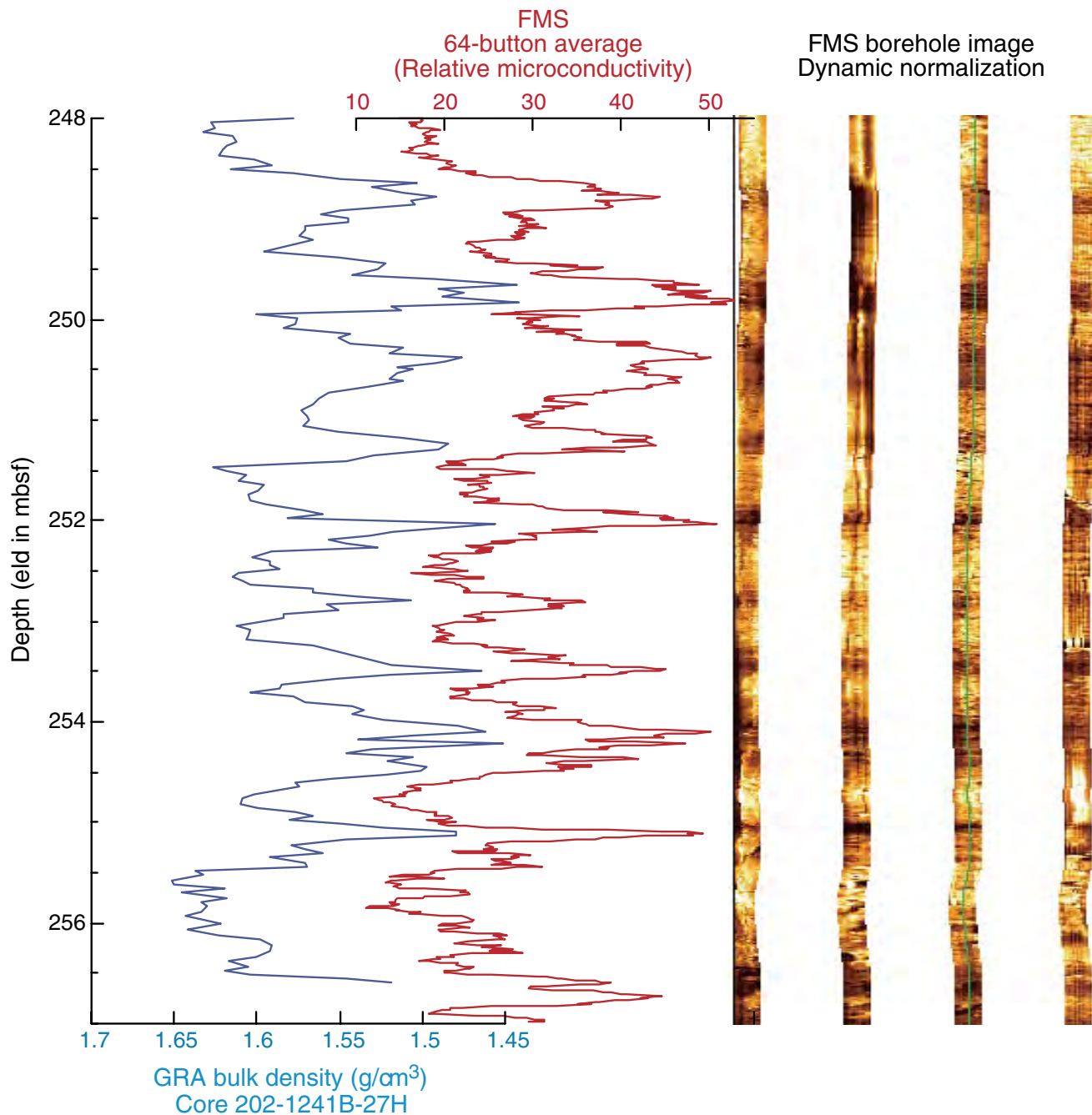


Figure F8. Comparison of Site 1238 natural gamma radiation (NGR) data from core (multisensor track [MST]-NGR) and downhole (Hostile Environment Natural Gamma Ray Sonde–standard gamma radiation [HSGR] and Multi-Sensor Spectral Gamma Ray Tool [MGT]) measurements. Data from cores and downhole tools correlated very well at (A) the meter scale throughout and (B, C) the submeter scale over most intervals.

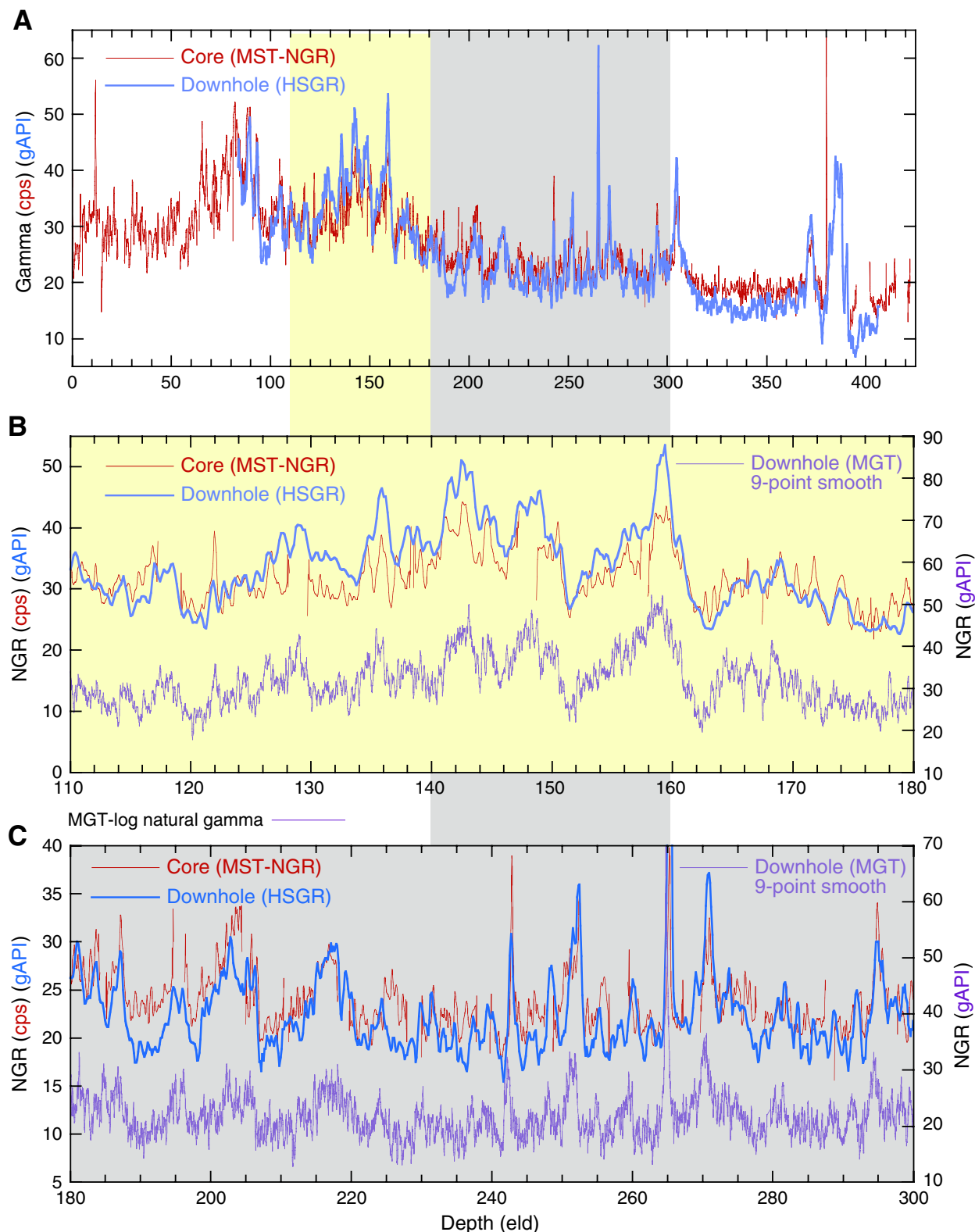


Figure F9. Comparison of gamma ray attenuation (GRA) bulk density data from core logging and downhole logging density. Note the excellent correlation of variations in magnitude and depth at meter scale. Minor discrepancies at the submeter scale may be the result of core disturbance or borehole irregularities.

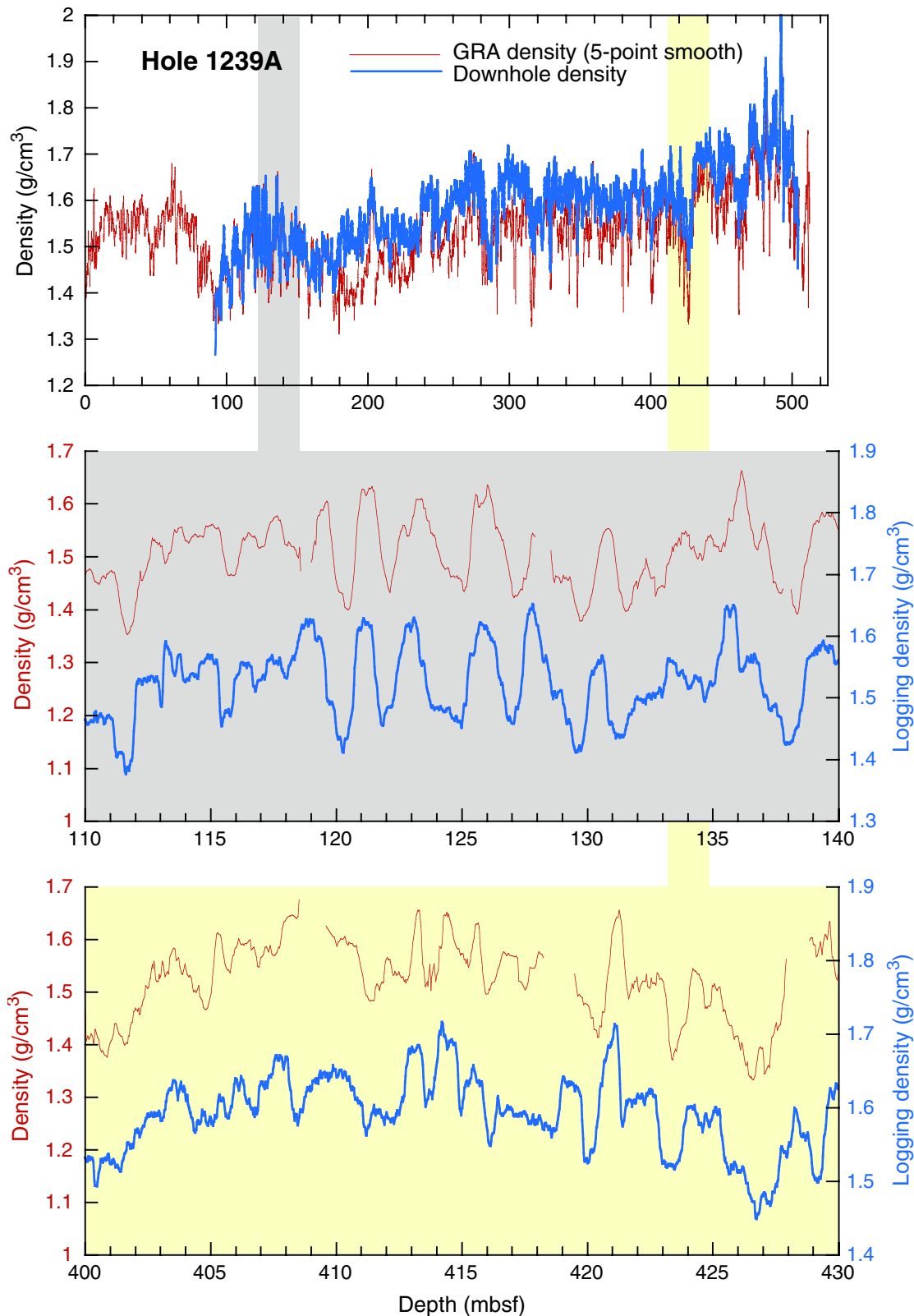


Figure F10. Relative changes in apparent depth offsets (in the mcd scale) of sequential cores vs. time of coring operation compare well with predictions of tidal sea level oscillations at Site 1240.

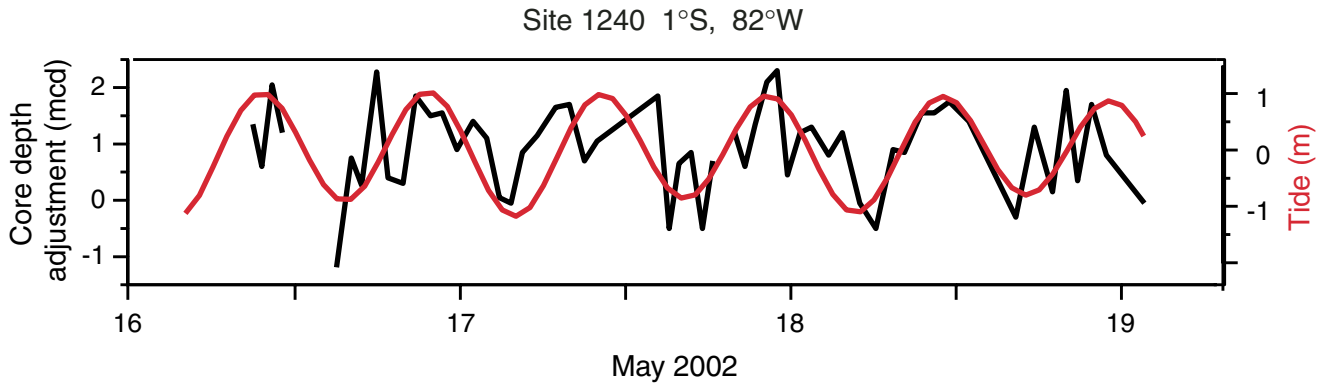


Figure F11. Reflectance spectroscopy–derived calcium carbonate and total organic carbon (TOC) contents compared to directly measured quantities at Site 1237.

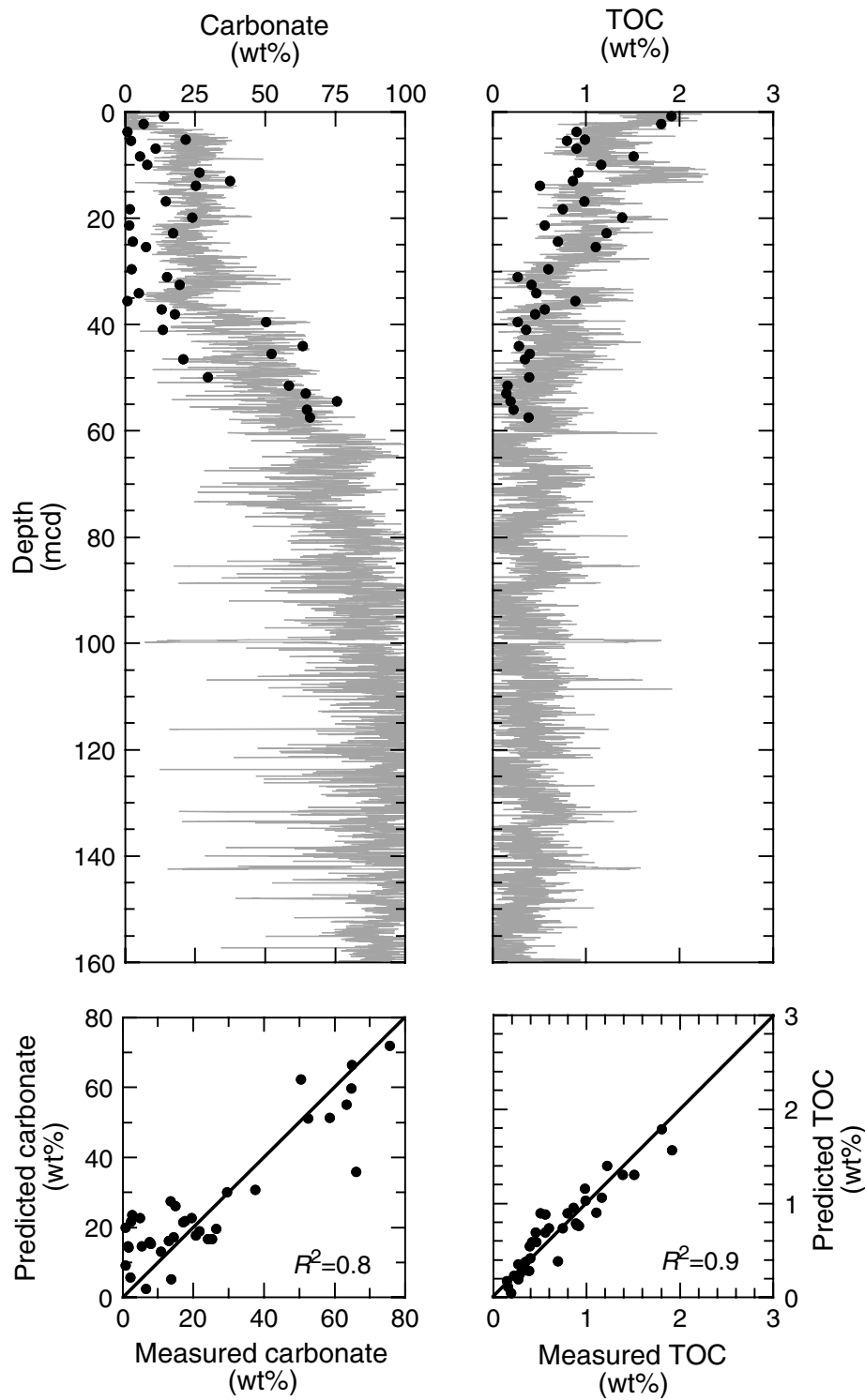


Figure F12. Paleomagnetic secular variation (PSV) at Site 1233, illustrating replication of declination variability in different holes and the assembly of a spliced PSV record with named events from 0 to 30 mcd.

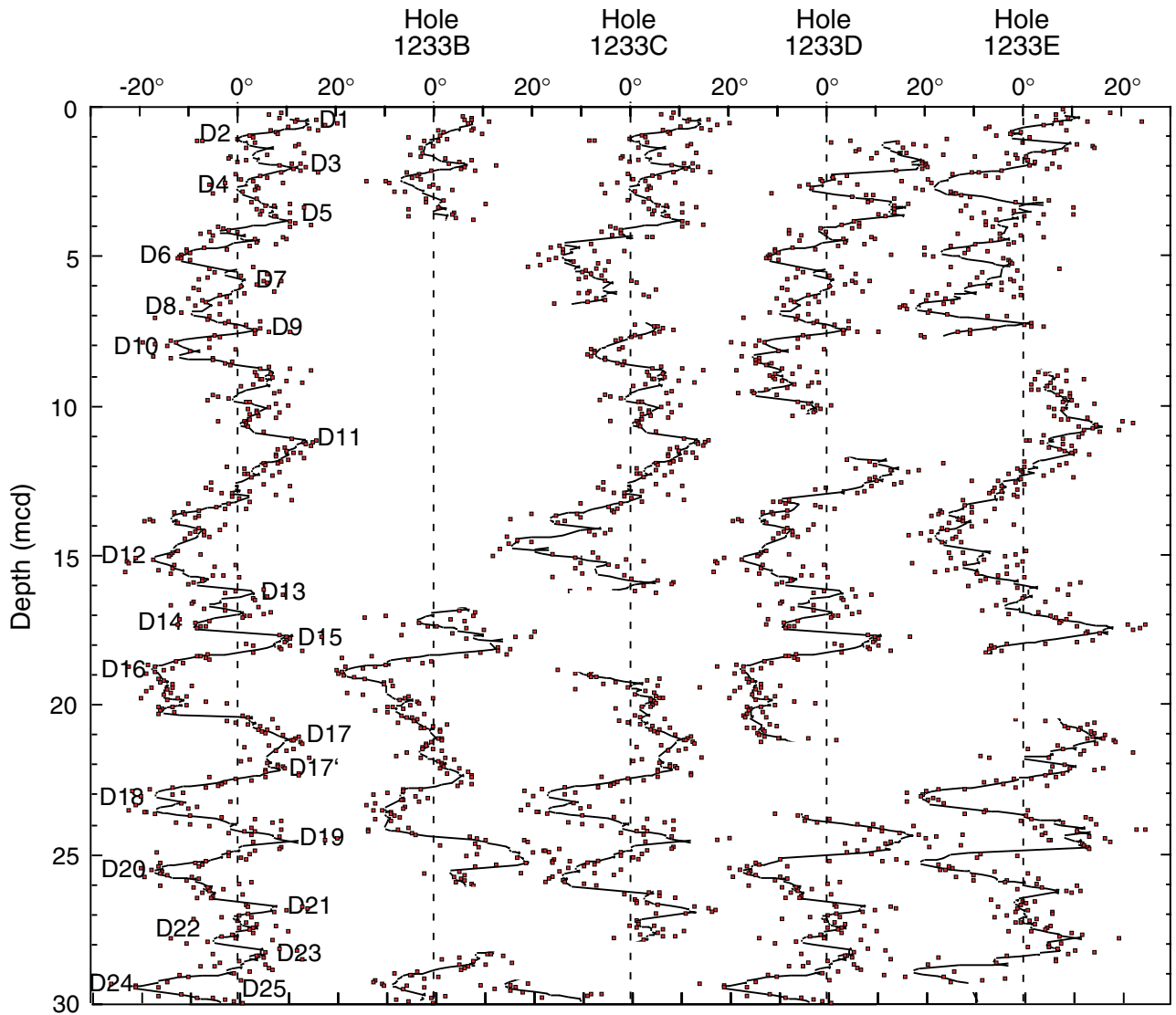


Figure F13. Paleomagnetic secular variation (PSV) at Site 1234, illustrating replication of declination variability in different holes, and the assembly of a spliced PSV record, with named events from 0 to 15 mcd.

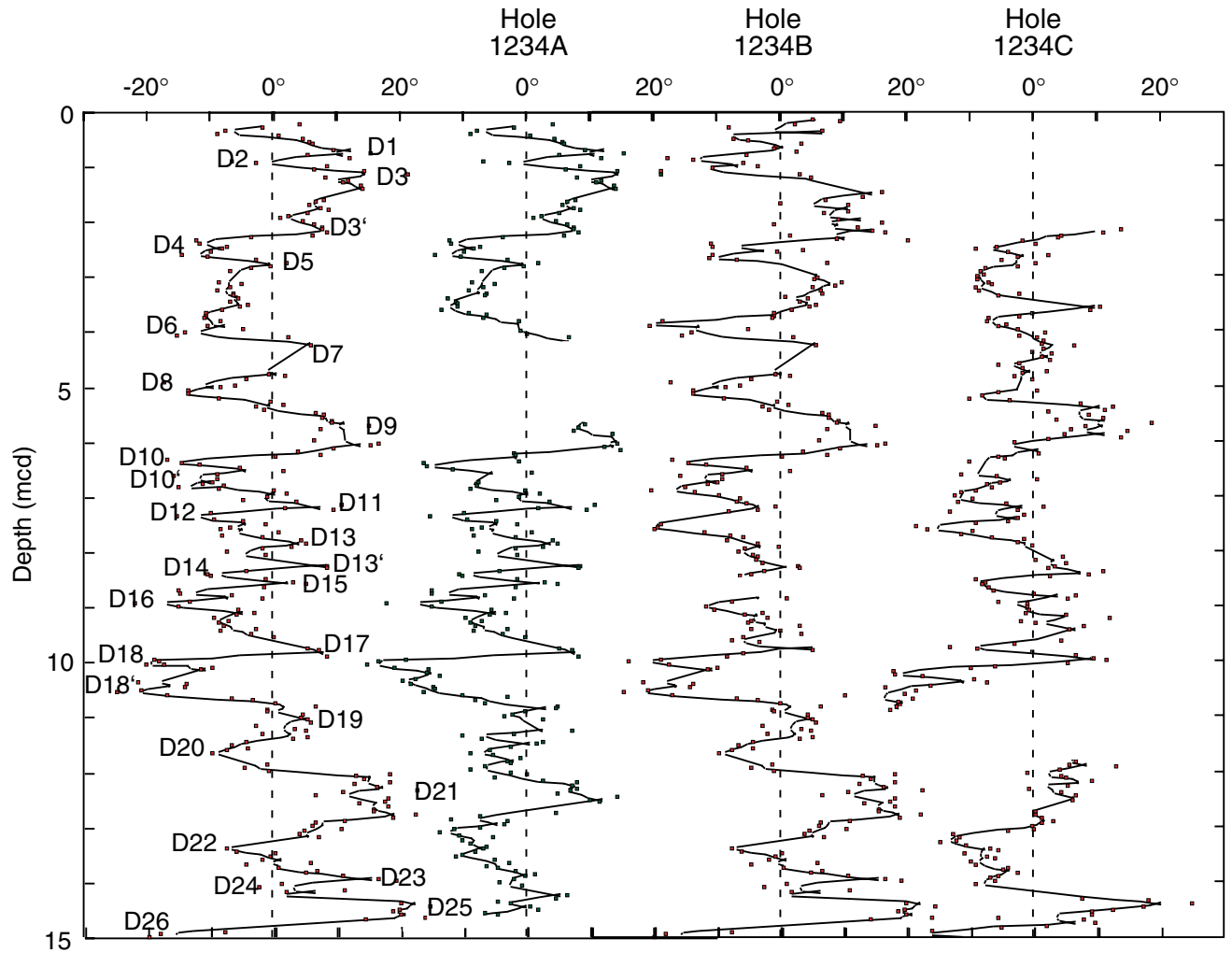


Figure F14. Variations in paleomagnetic declination (top), inclination (middle), and normalized relative paleointensity (bottom) from 0 to 136 mcd at Chile margin Site 1233 (inferred ~0–140 ka). Note the inferred Laschamp Excursion (~41 ka) near 68 mcd, which implies an average sedimentation rate of nearly 170 cm/k.y. from the core top to this level. PSV = paleomagnetic secular variation, BP = before present. Big D = interval of anomalously high declination.

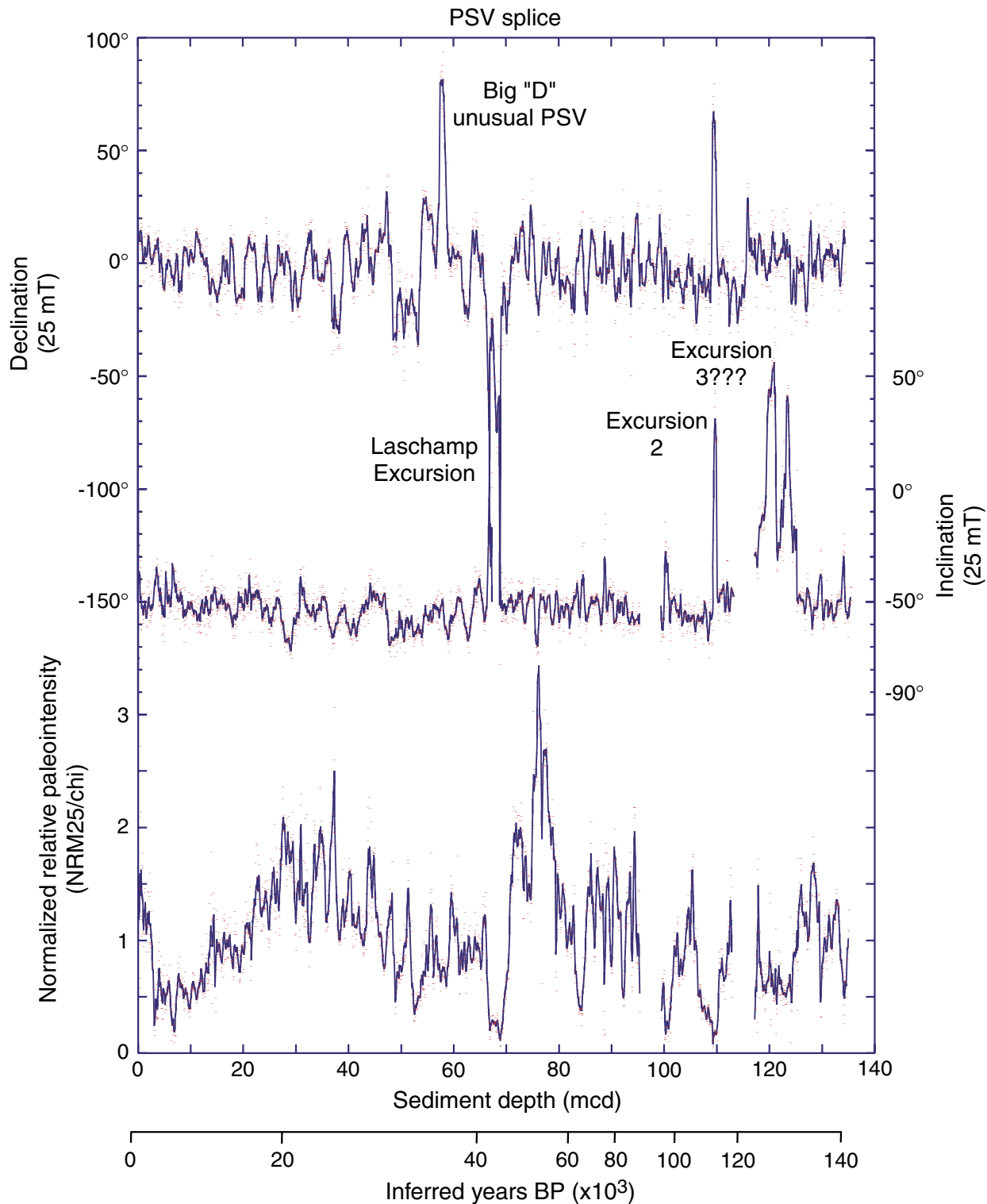


Figure F15. Variations in paleomagnetic declination (top), inclination (middle), and normalized relative paleointensity (bottom) from 15 to 65 mcd at Chile margin Site 1233 (inferred ~11–40 ka). Note the well-defined rhythmic variations in all parameters. PSV = paleomagnetic secular variation, BP = before present.

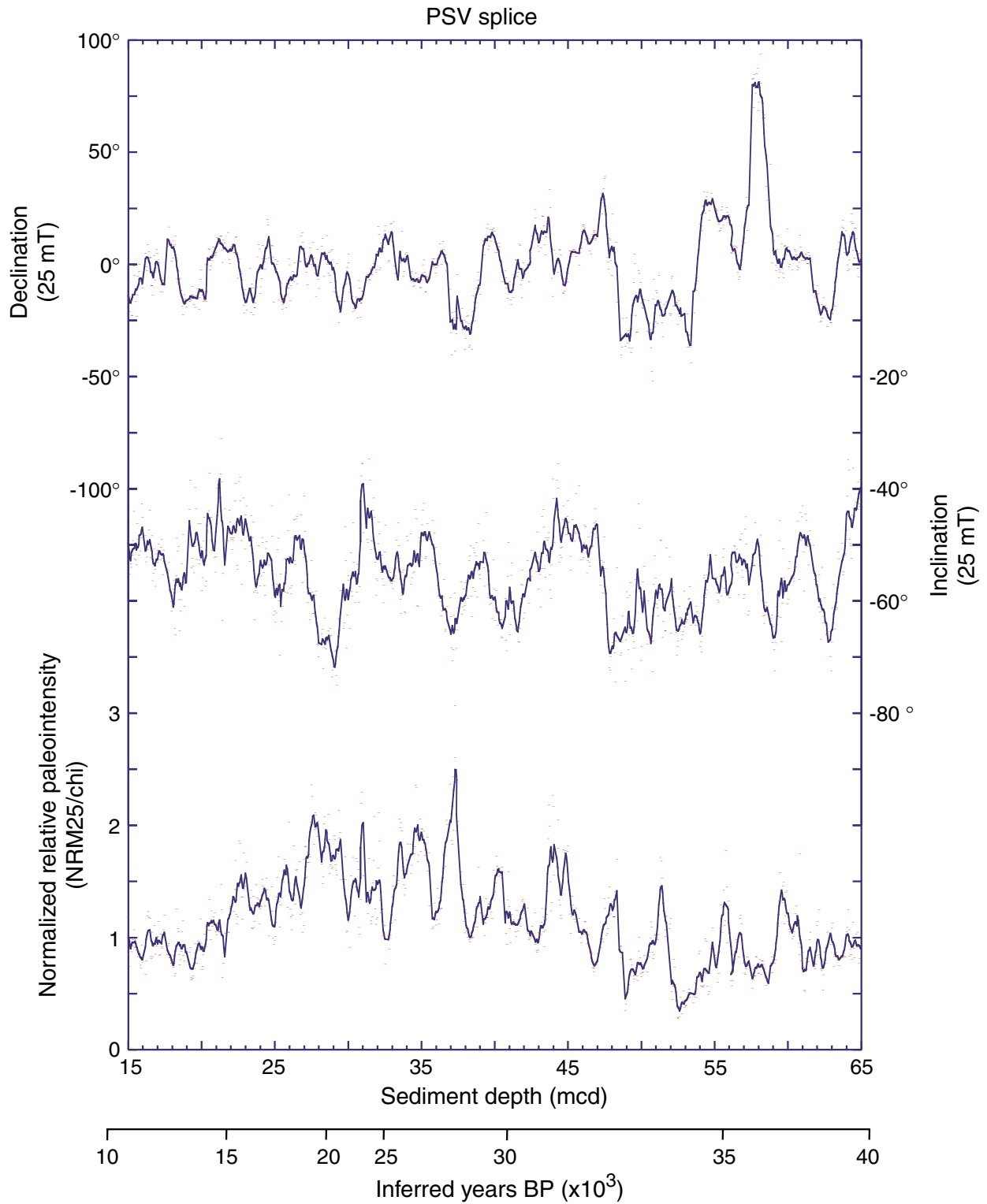


Figure F16. Comparison of paleomagnetic inclination, declination, and normalized relative paleointensity at Sites 1233 and 1234. PSV = paleomagnetic secular variation. Big D = interval of anomalously high declination. Big D = interval of anomalously high declination.

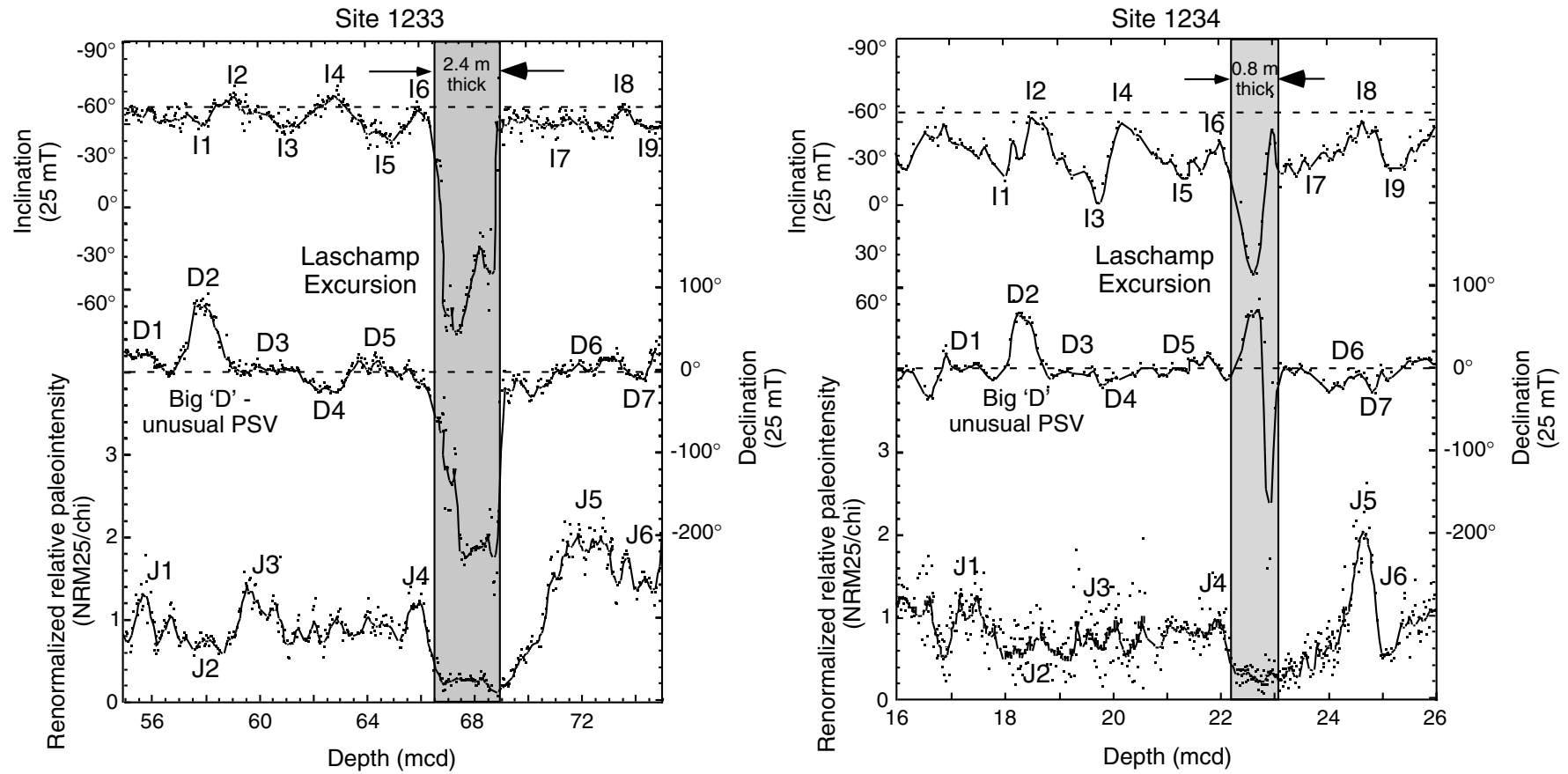


Figure F17. Age models for Leg 202 sites. FO = first occurrence, LO = last occurrence. AMS = accelerator mass spectrometry. (Continued on next page.)

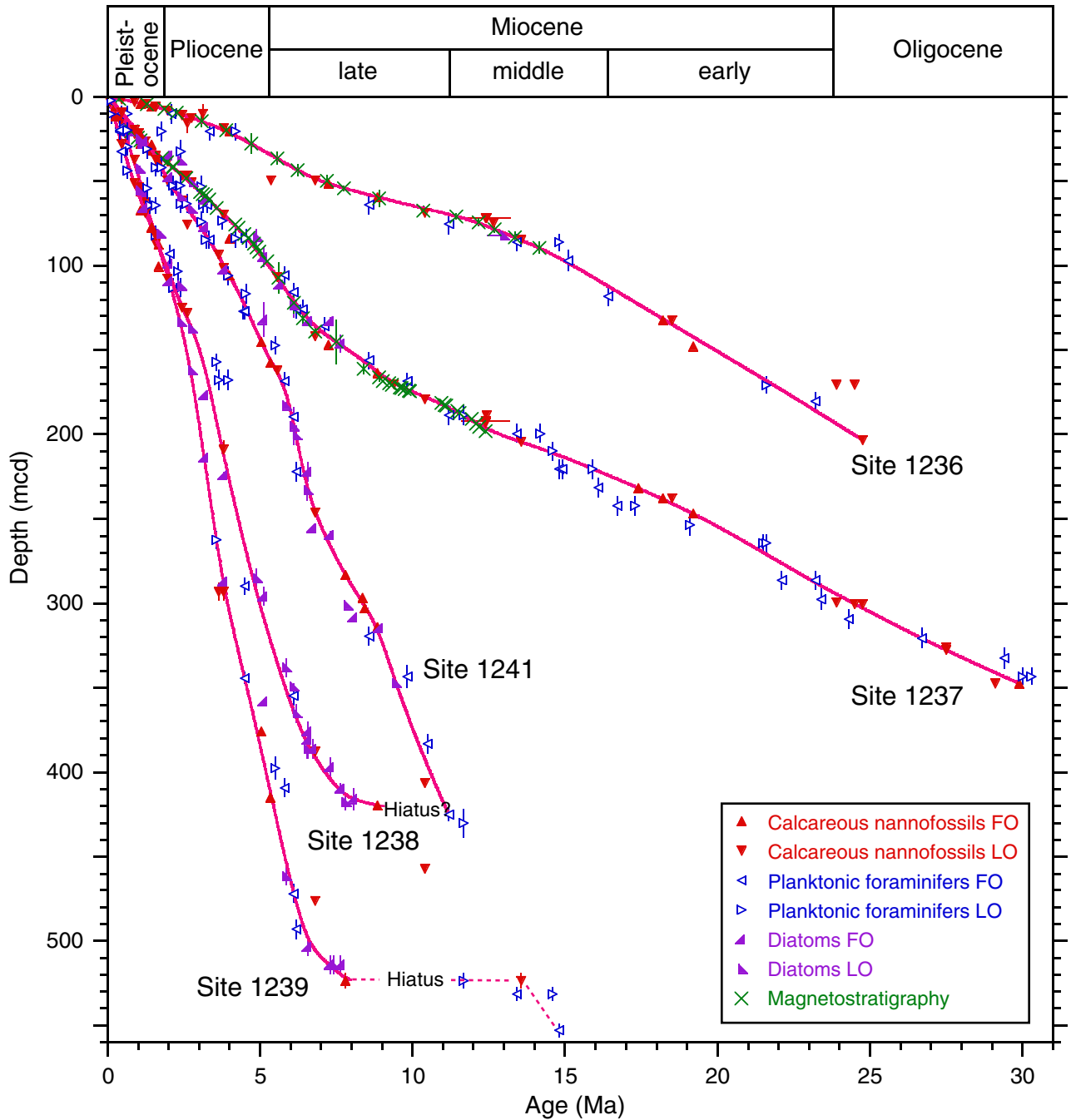


Figure F17 (continued).

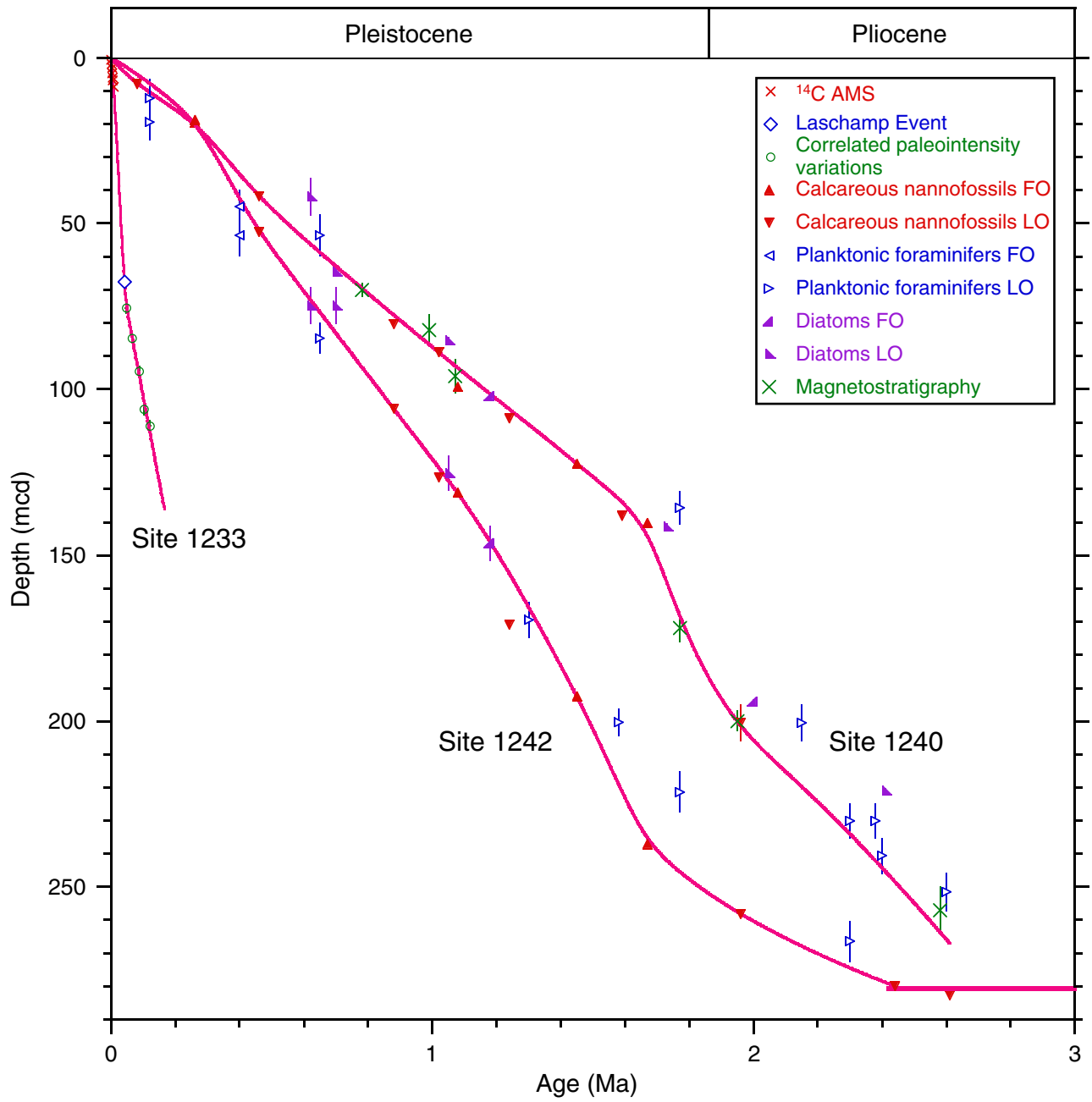


Figure F18. Linear sedimentation rates (LSRs) and total mass accumulation rates (MARs) at Leg 202 sites averaged at (A) 1.0-m.y. intervals for longer records, (B) 0.4-m.y. intervals for shorter records, and (C) 10-k.y. intervals for ultra-high-resolution records.

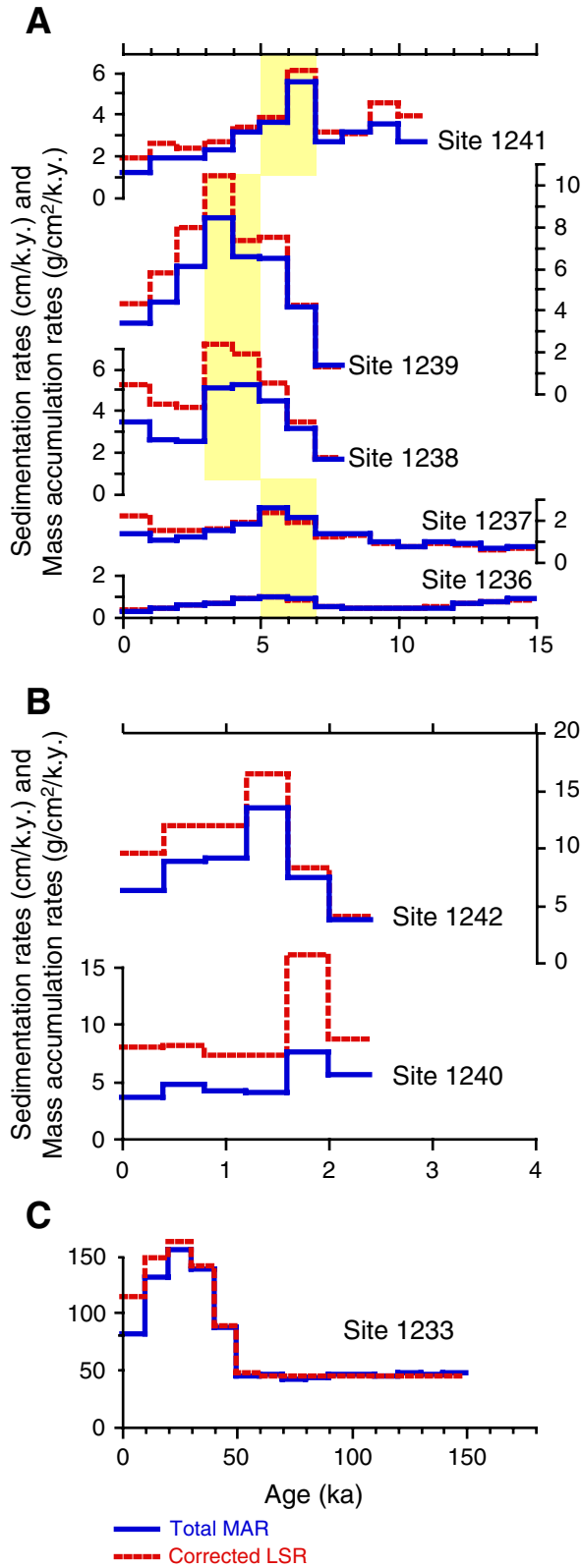


Figure F19. Cyclic variation in gamma ray attenuation (GRA) density at Site 1237. **A.** Fluctuations in GRA density between 60 and 80 mcd (red curve) and the Gaussian weighted smooth (blue curve). The detrended record (green) represents the difference between blue and red records and was used in spectral analysis. Ages and depths of magnetic reversal boundaries are indicated as well as intervals of major changes in sedimentation rates. **B.** Results from spectral analyses. Cycle lengths are given in meters. Considering the sedimentation rates shown in A, cycles of 0.35–0.43 m reflect precession cycles (22 k.y.) and cycles of 0.74–0.98 m are related to obliquity cycles (41 k.y.).

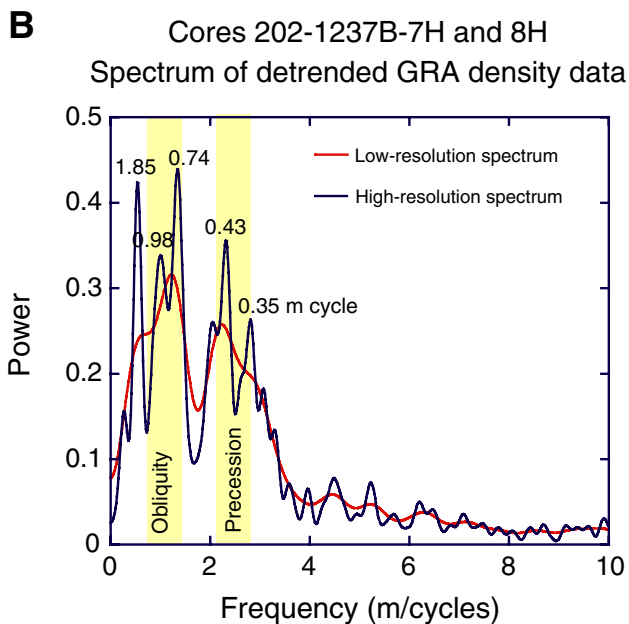
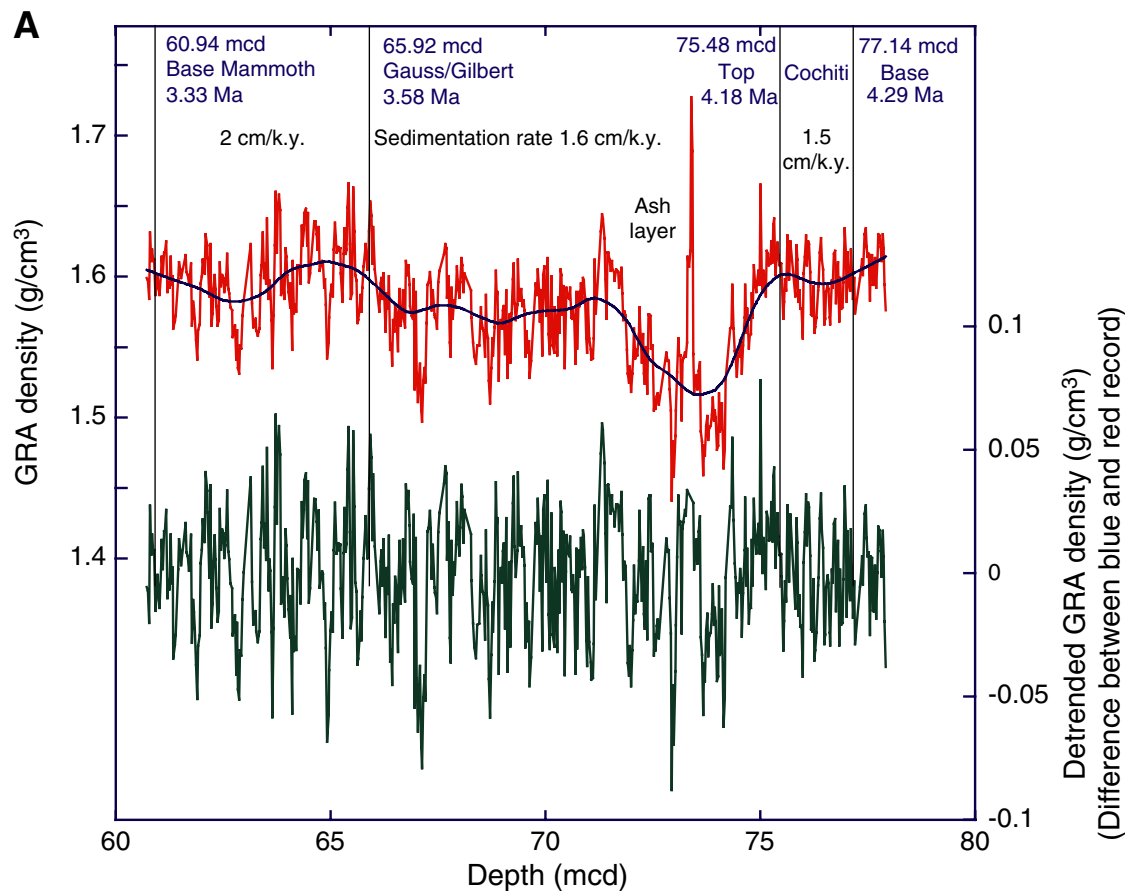


Figure F20. Carbonate (solid lines) and noncarbonate (dashed lines) mass accumulation rates at (A, B) Leg 202 sites and (C) selected Leg 138 sites. Averaged time intervals are 1 m.y. in (A) and (C) and 0.4 m.y. in (B).

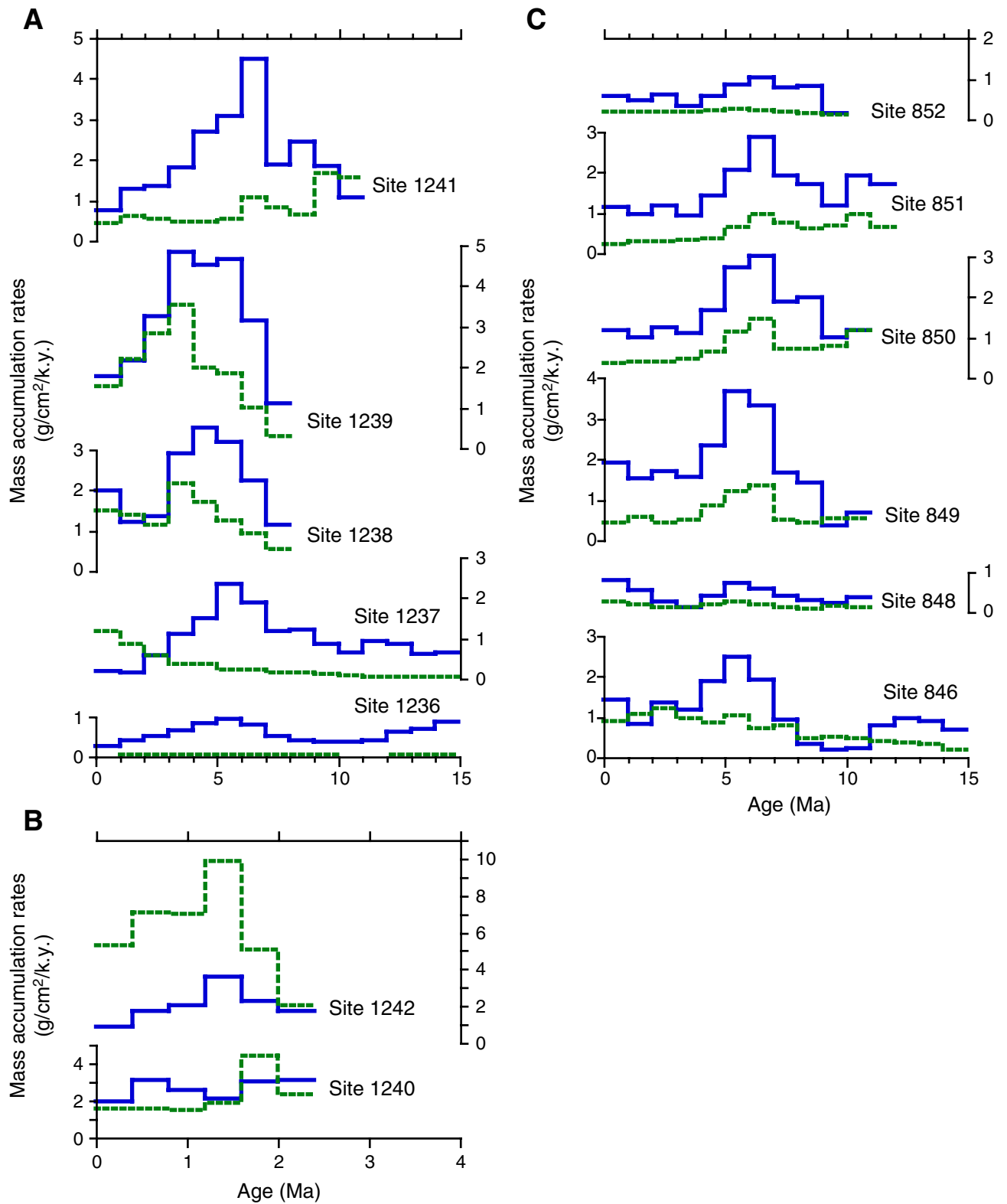


Figure F21. Biogenic opal and terrigenous sediment mass accumulation rates (MARs) as components of the noncarbonate MAR at (A) selected Leg 138 sites and (B) Site 1237, for which total organic carbon (TOC) MAR is also plotted. Note that opal and TOC MARs are plotted at a different scale (on right) than noncarbonate and terrigenous MAR (on left) in (B).

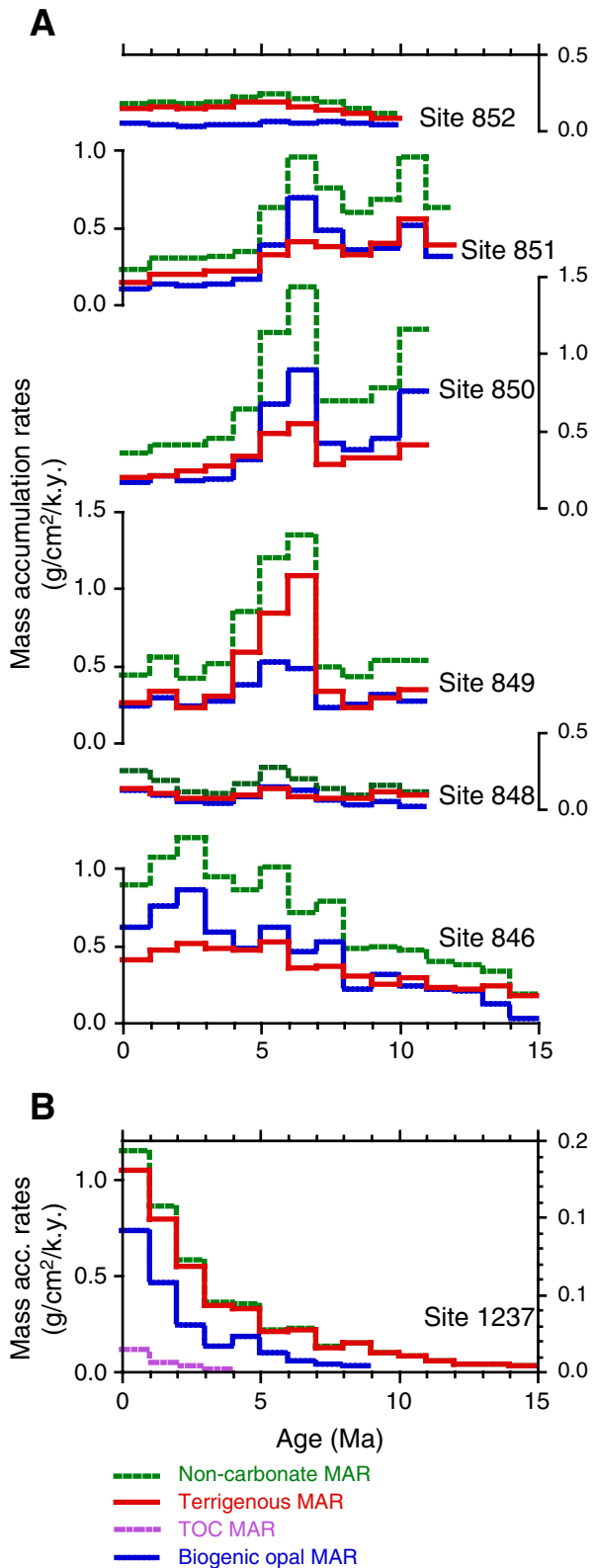


Figure F22. Modern annual-average properties of the upper ocean at paleolocations of Site 1236, based on plate tectonic backtracking and an assumption of no temporal changes in regional oceanic properties. Atlas data on physical and chemical properties are from WOA98 (Ocean Climate Laboratory, 1999). Primary productivity (PP) is from satellite measurements of sea-surface color (Behrenfeld et al., 2001). Pycnocline depth is calculated to the nearest 5 m, based on the shallowest maximum in the vertical density gradient. Symbols are average values extracted from the nearest 1° latitude-longitude box in each atlas. Lines = smoothed trends of each property along the backtrack path. SST = sea-surface temperature, SSS = sea-surface salinity.

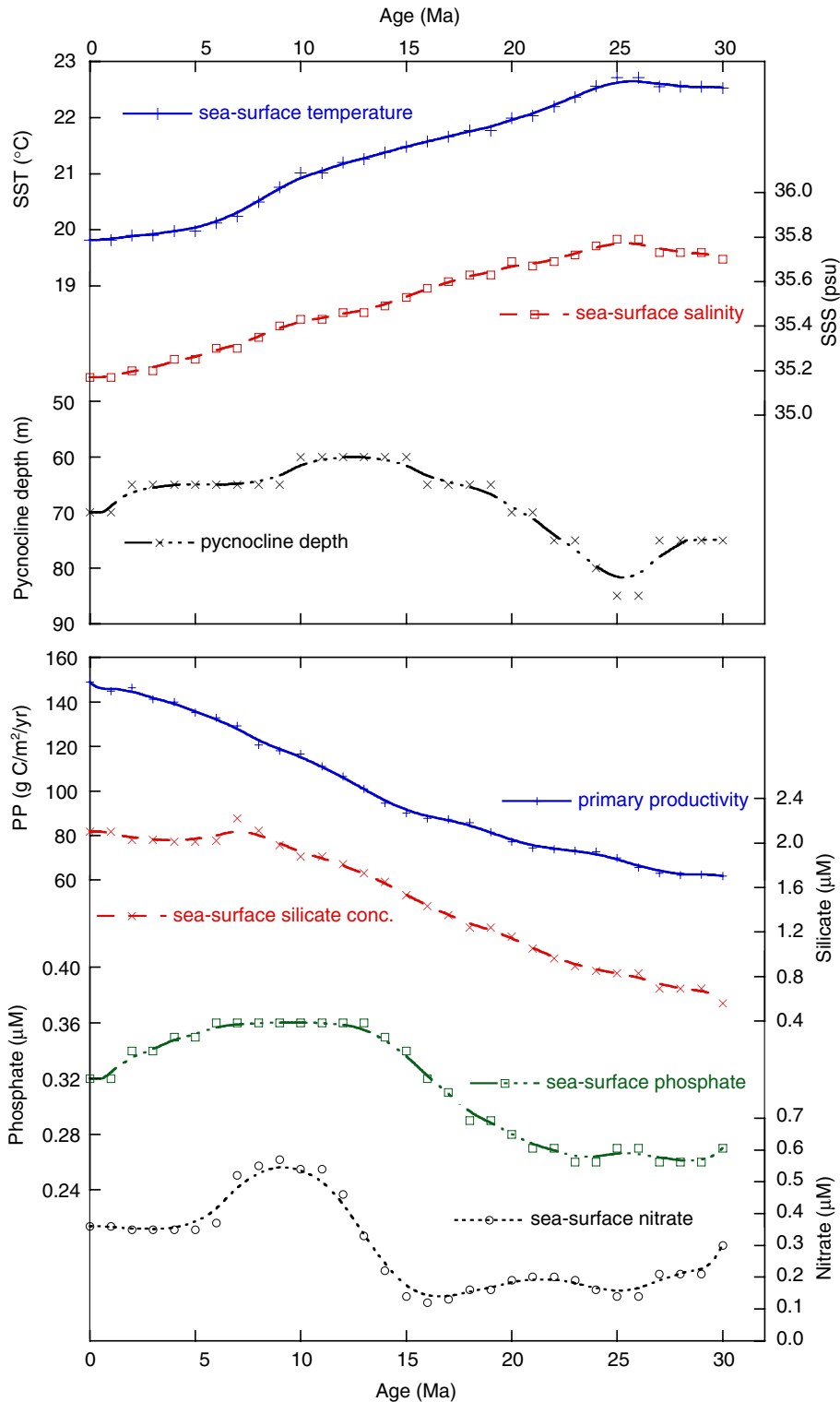


Figure F23. Modern annual average properties of the upper ocean at paleolocations of Site 1237, based on plate tectonic backtracking and an assumption of no temporal changes in regional oceanic properties. Atlas data on physical and chemical properties are from WOA98 (Ocean Climate Laboratory, 1999). Primary productivity (PP) is from satellite measurements of sea-surface color (Behrenfeld et al., 2001). Pycnocline depth is calculated to the nearest 5 m, based on the shallowest maximum in the vertical density gradient. Symbols are average values extracted from the nearest 1° latitude-longitude box in each atlas. Lines = smoothed trends of each property along the backtrack path. SST = sea-surface temperature, SSS = sea-surface salinity.

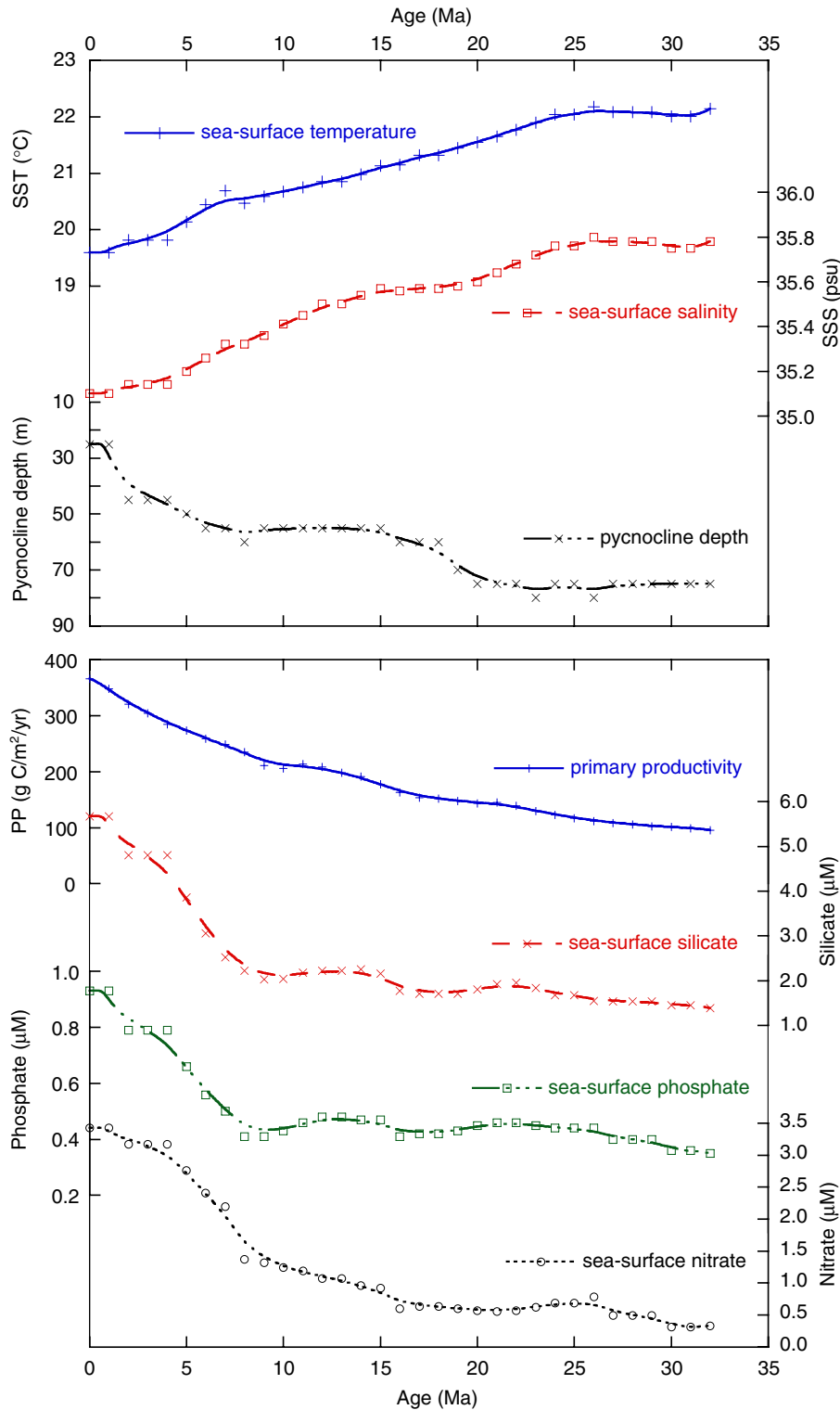


Figure F24. Modern annual-average properties of the upper ocean at paleolocations of Site 1239, based on plate tectonic backtracking and an assumption of no temporal changes in regional oceanic properties. Atlas data on physical and chemical properties are from WOA98 (Ocean Climate Laboratory, 1999). Primary productivity (PP) is from satellite measurements of sea-surface color (Behrenfeld et al., 2001). Pycnocline depth is calculated to the nearest 5 m, based on the shallowest maximum in the vertical density gradient. Symbols are average values extracted from the nearest 1° latitude-longitude box in each atlas. Lines = smoothed trends of each property along the backtrack path. SST = sea-surface temperature, SSS = sea-surface salinity.

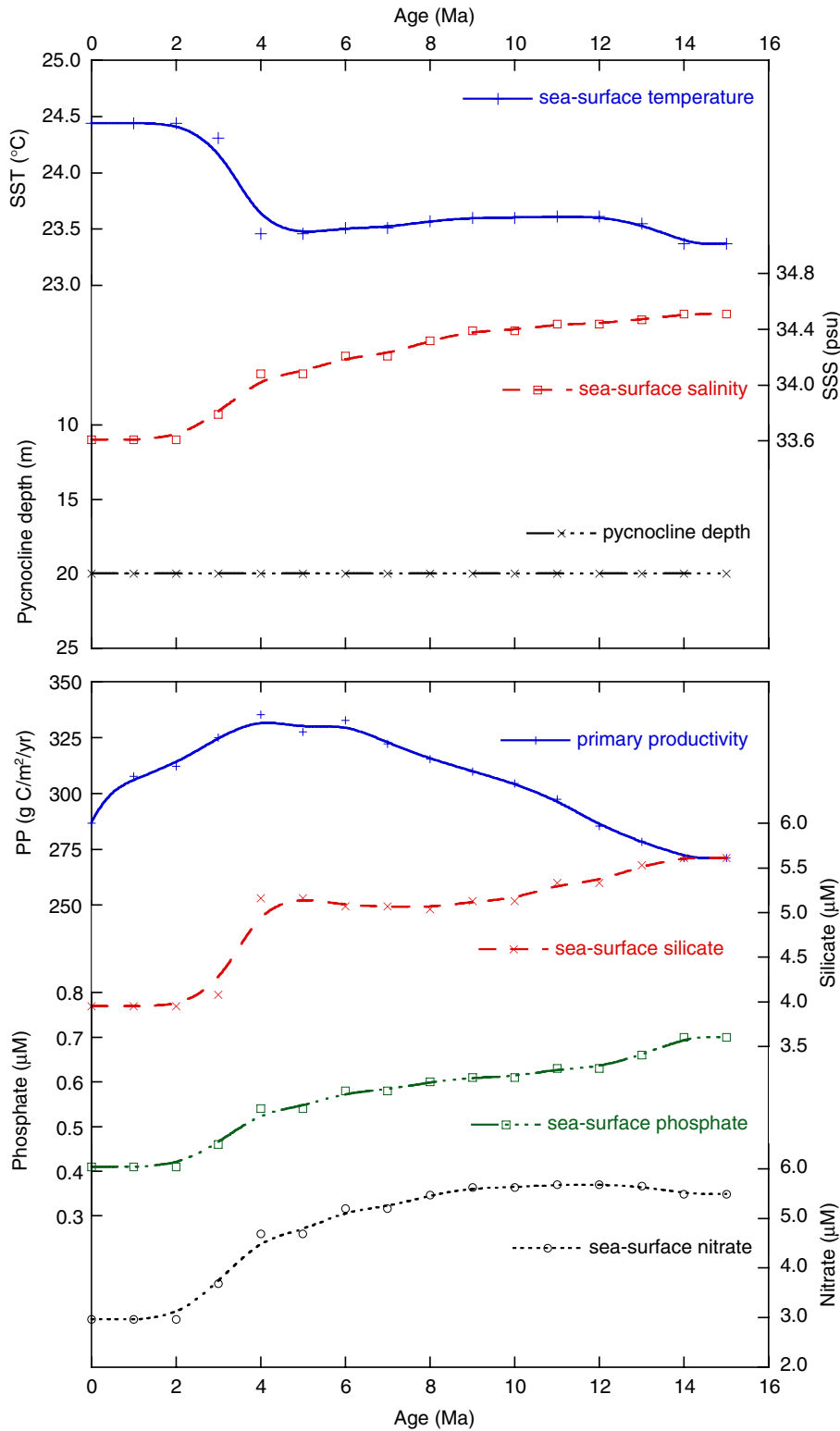


Figure F25. Modern annual-average properties of the upper ocean at paleolocations of Site 1238, based on plate tectonic backtracking and an assumption of no temporal changes in regional oceanic properties. Atlas data on physical and chemical properties are from WOA98 (Ocean Climate Laboratory, 1999). Primary productivity (PP) is from satellite measurements of sea-surface color (Behrenfeld et al., 2001). Pycnocline depth is calculated to the nearest 5 m, based on the shallowest maximum in the vertical density gradient. Symbols are average values extracted from the nearest 1° latitude-longitude box in each atlas. Lines = smoothed trends of each property along the backtrack path. SST = sea-surface temperature, SSS = sea-surface salinity.

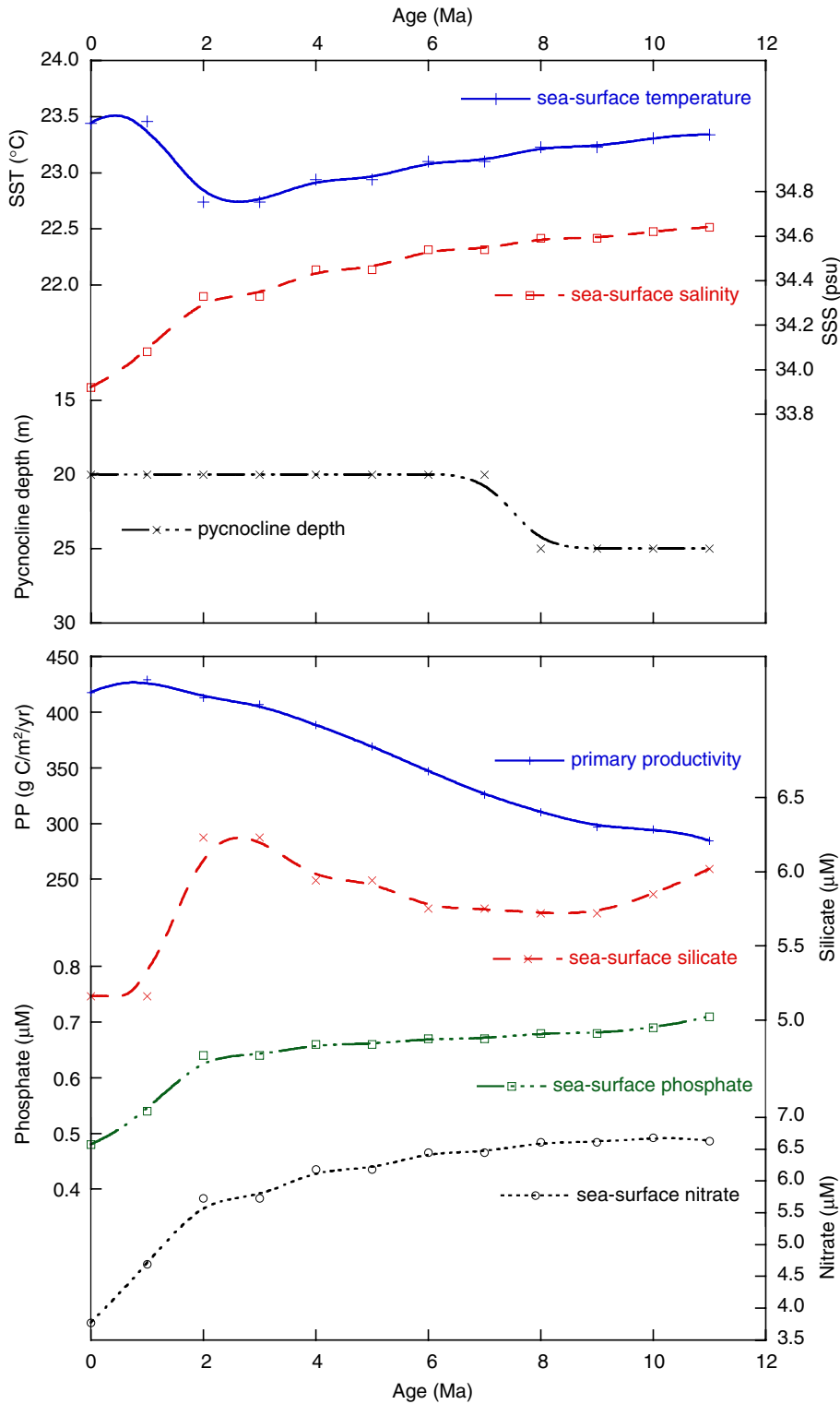


Figure F26. Modern annual-average properties of the upper ocean at paleolocations of Site 1241, based on plate tectonic backtracking and an assumption of no temporal changes in regional oceanic properties. Atlas data on physical and chemical properties are from WOA98 (Ocean Climate Laboratory, 1999). Primary productivity (PP) is from satellite measurements of sea-surface color (Behrenfeld et al., 2001). Pycnocline depth is calculated to the nearest 5 m, based on the shallowest maximum in the vertical density gradient. Symbols are average values extracted from the nearest 1° latitude-longitude box in each atlas. Lines = smoothed trends of each property along the backtrack path. SST = sea-surface temperature, SSS = sea-surface salinity.

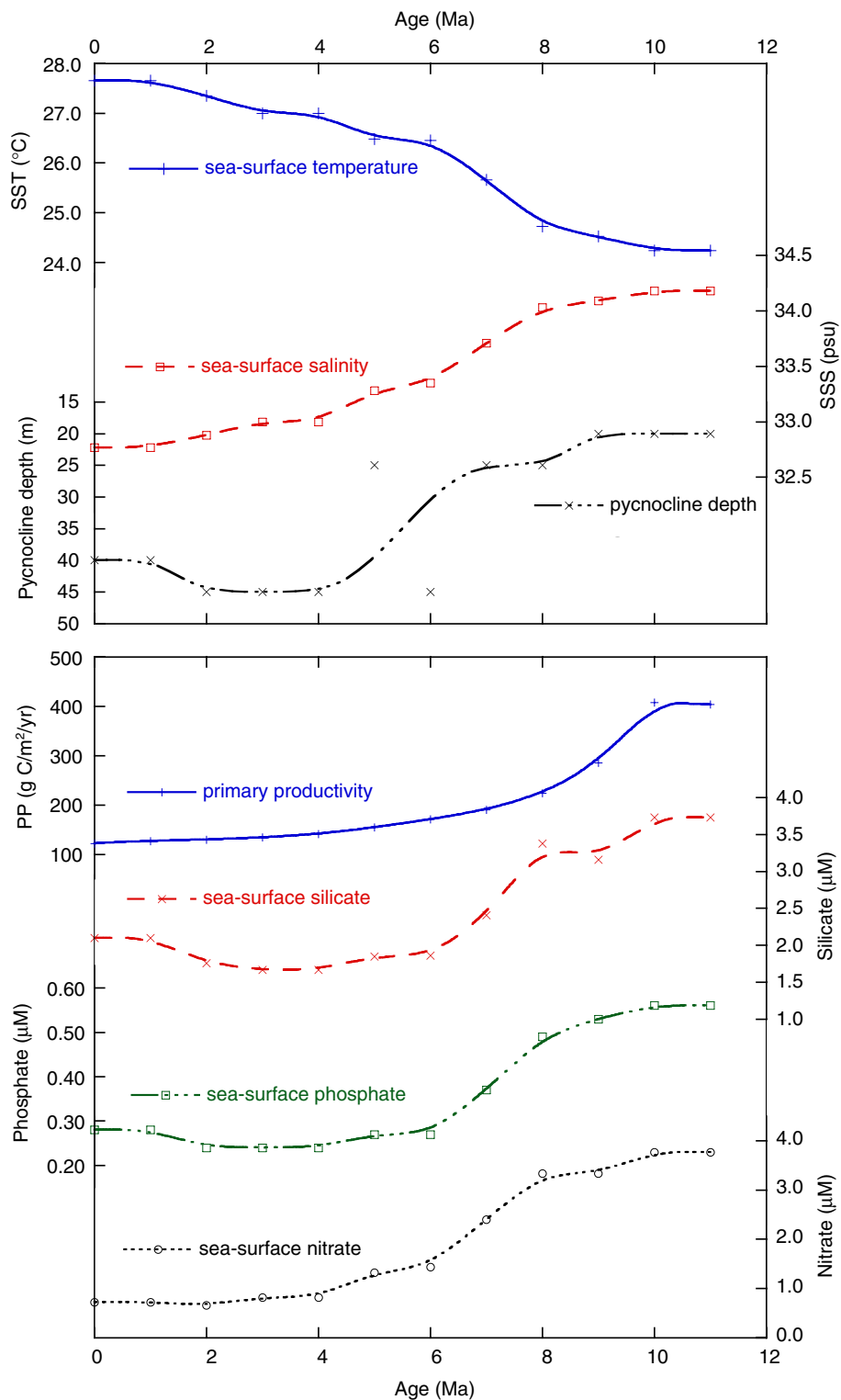


Figure F27. Interstitial sulfate concentrations vs. depth. **A.** All sites. **B.** Sites with complete sulfate reduction, upper 100 mcd. Values below detection limits (typically 1 mM) are plotted at zero.

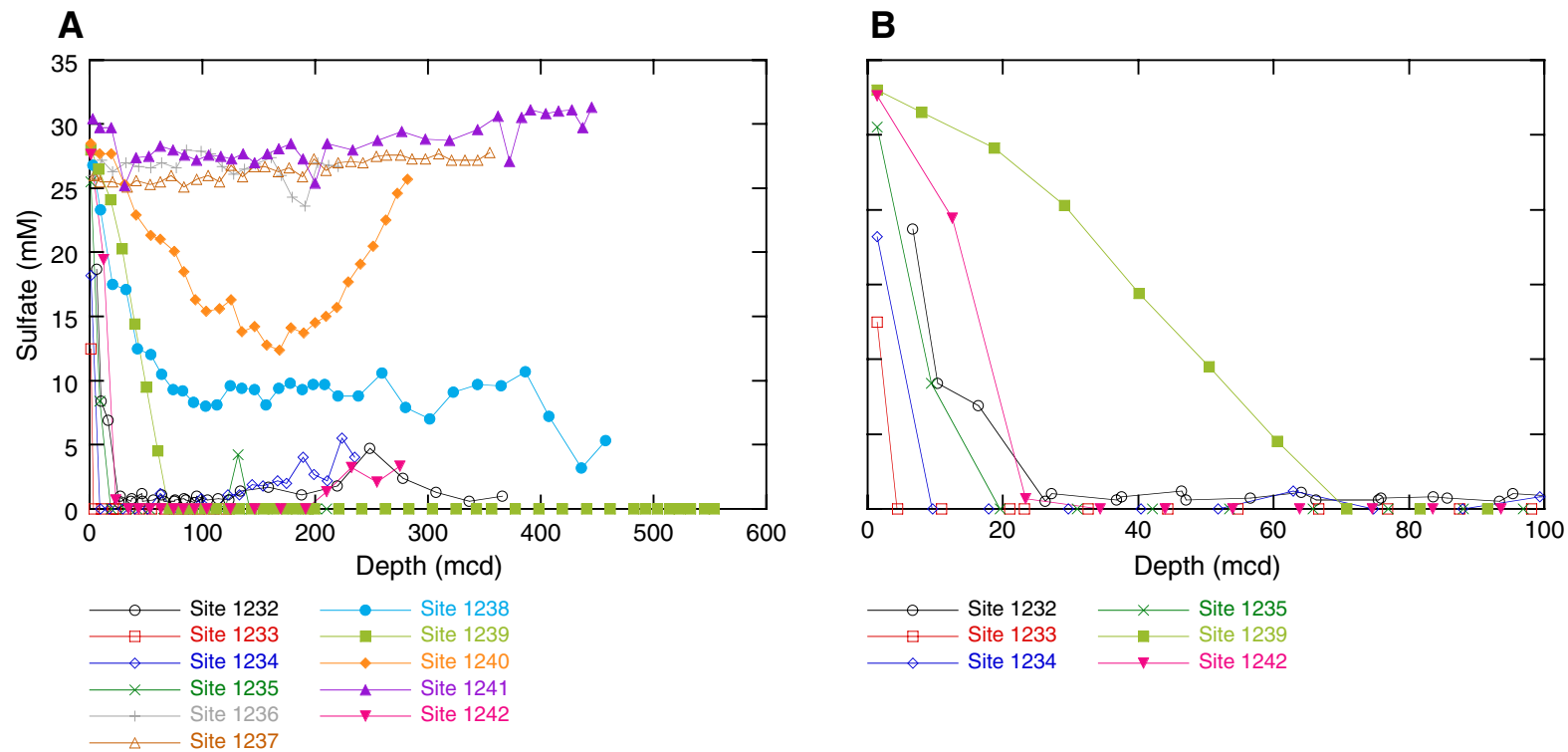


Figure F28. Total nitrogen (TN) vs. total organic carbon (TOC) concentrations in sediments from all Leg 202 sites.

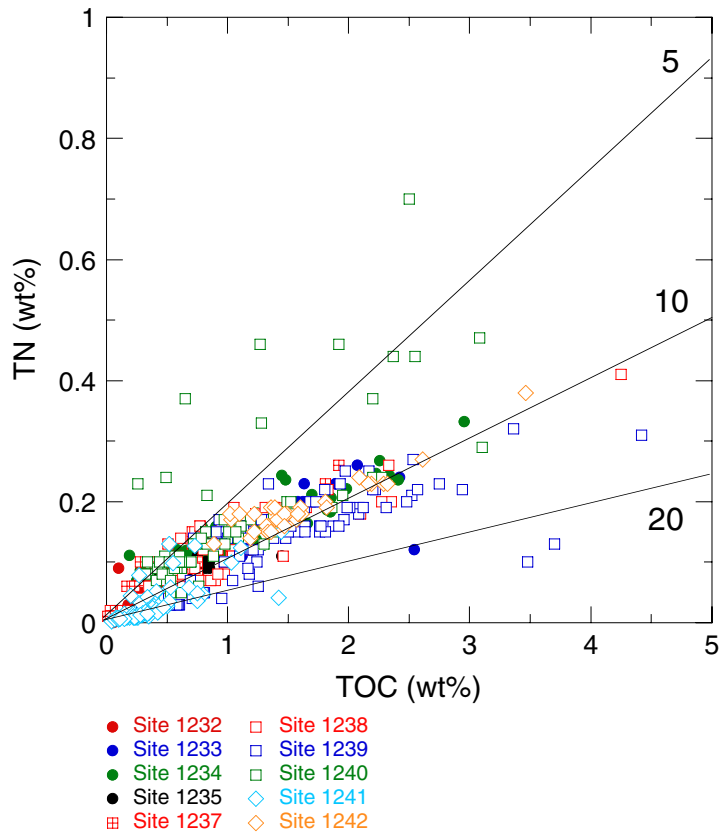


Figure F29. Total organic carbon/total nitrogen (TOC/TN) ratios vs. TOC concentrations in sediments from all ODP Leg 202 sites.

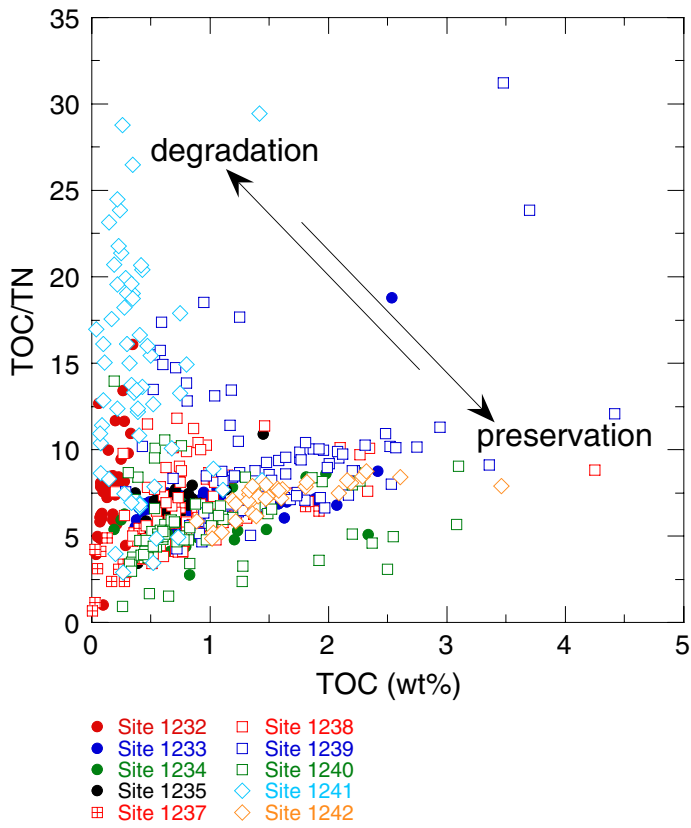


Figure F30. Interstitial calcium and magnesium/calcium profiles vs. depth. **A, C.** Calcium and magnesium/calcium profiles for sites with limited to moderate sulfate reduction. **B, D.** Calcium and magnesium/calcium profiles for sites with complete sulfate reduction. Note that the vertical scale changes from C to D.

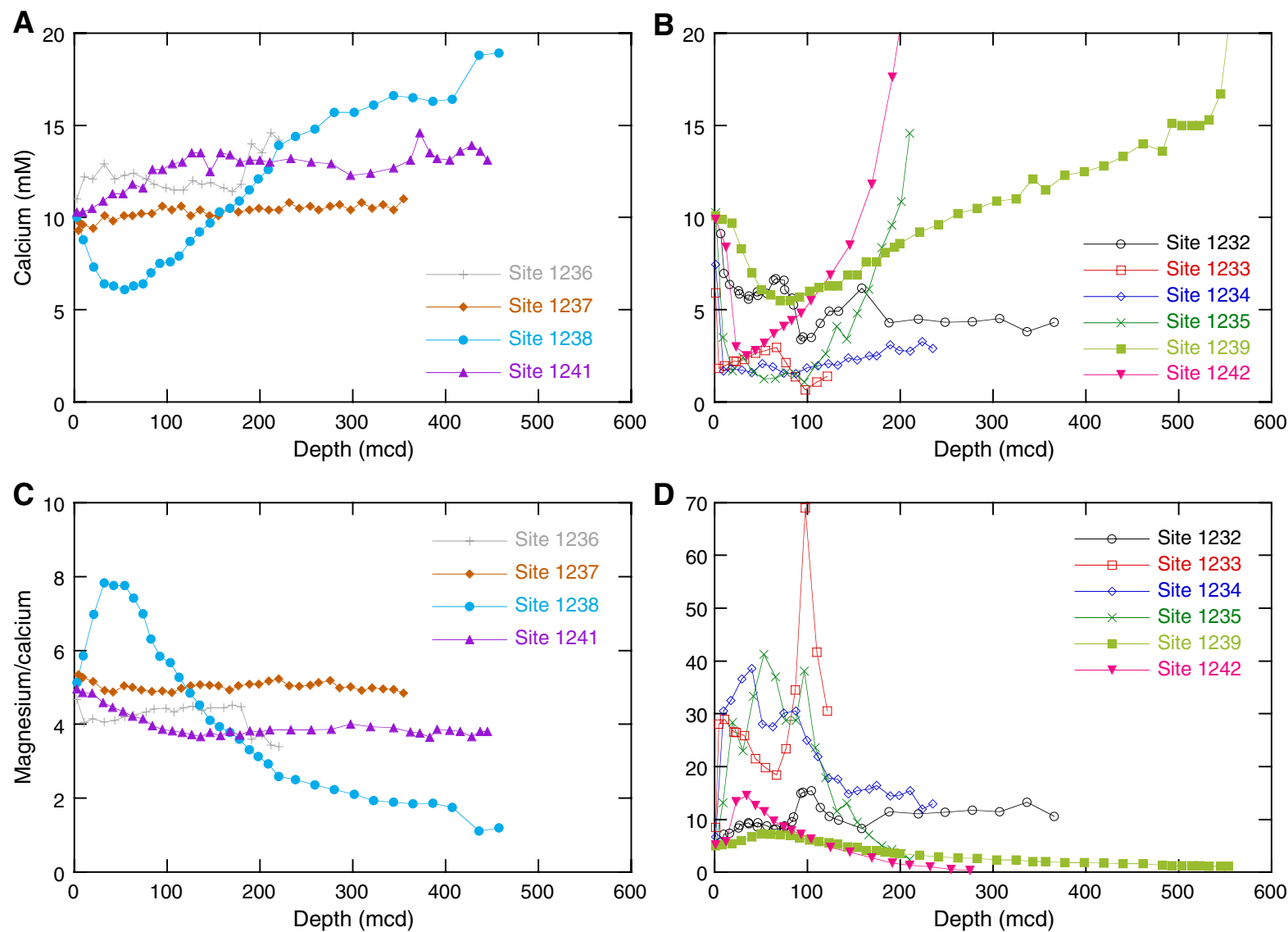


Figure F31. Interstitial chloride vs. depth for Chile margin sites (1233, 1234, and 1235).

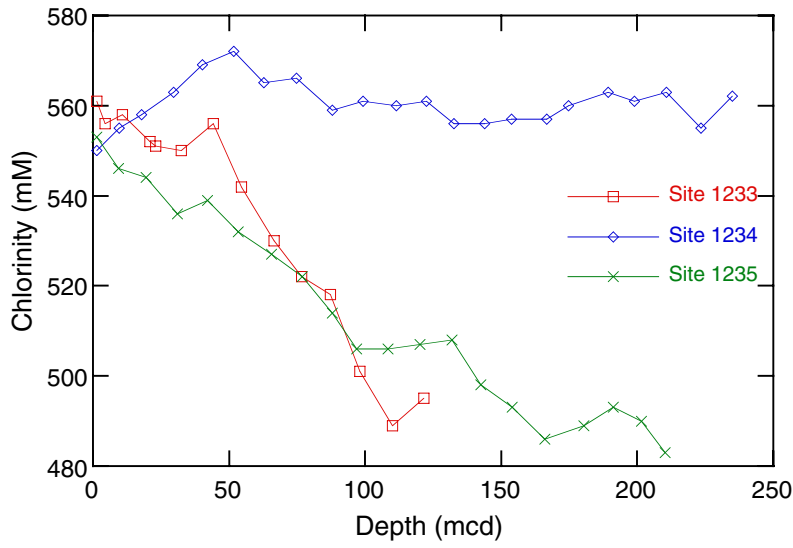


Figure F32. Interstitial profiles of sulfate, alkalinity, phosphate, and ammonium vs. depth for Panama Basin Site 1240.

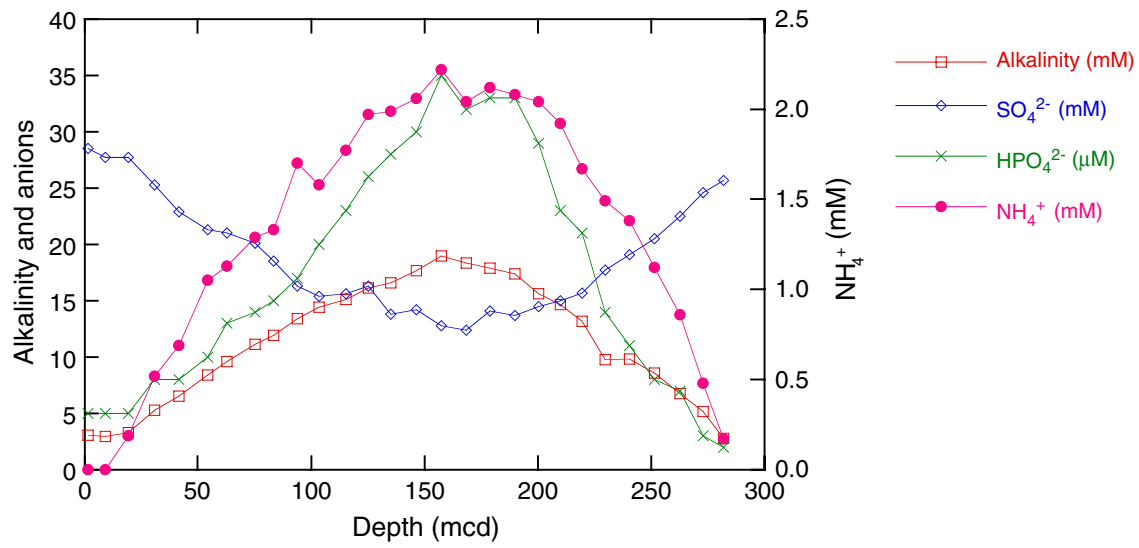


Figure F33. A. Quartz distribution in surface sediments of the subtropical southeast Pacific, expressed as weight percentage (carbonate- and opal-free basis, reproduced from Molina-Cruz, 1977). Arrows indicate trade winds. Sites 1236, 1237, 1238, and 1239 are shown with their plate tectonic backtracks. **B.** Siliciclastic accumulation rates and hematite peak height at Sites 1236 and 1237. The accumulation rates of siliciclastics were estimated as $(100\% - \text{wt}\% \text{ CaCO}_3 - \text{wt}\% \text{ organic matter} - \text{wt}\% \text{ biogenic opal}) \times \text{sedimentation rate} \times \text{dry bulk density}$. The shipboard magnetostratigraphy and biostratigraphy were used to calculate sedimentation rates that were smoothed to avoid overinterpretations of the preliminary age model. Siliciclastic accumulation rates at Site 1237 are used as a proxy for dust flux. The hematite peak height is derived from color reflectance spectra and serves as a proxy for changing concentrations of hematite. MAR = mass accumulation rate.

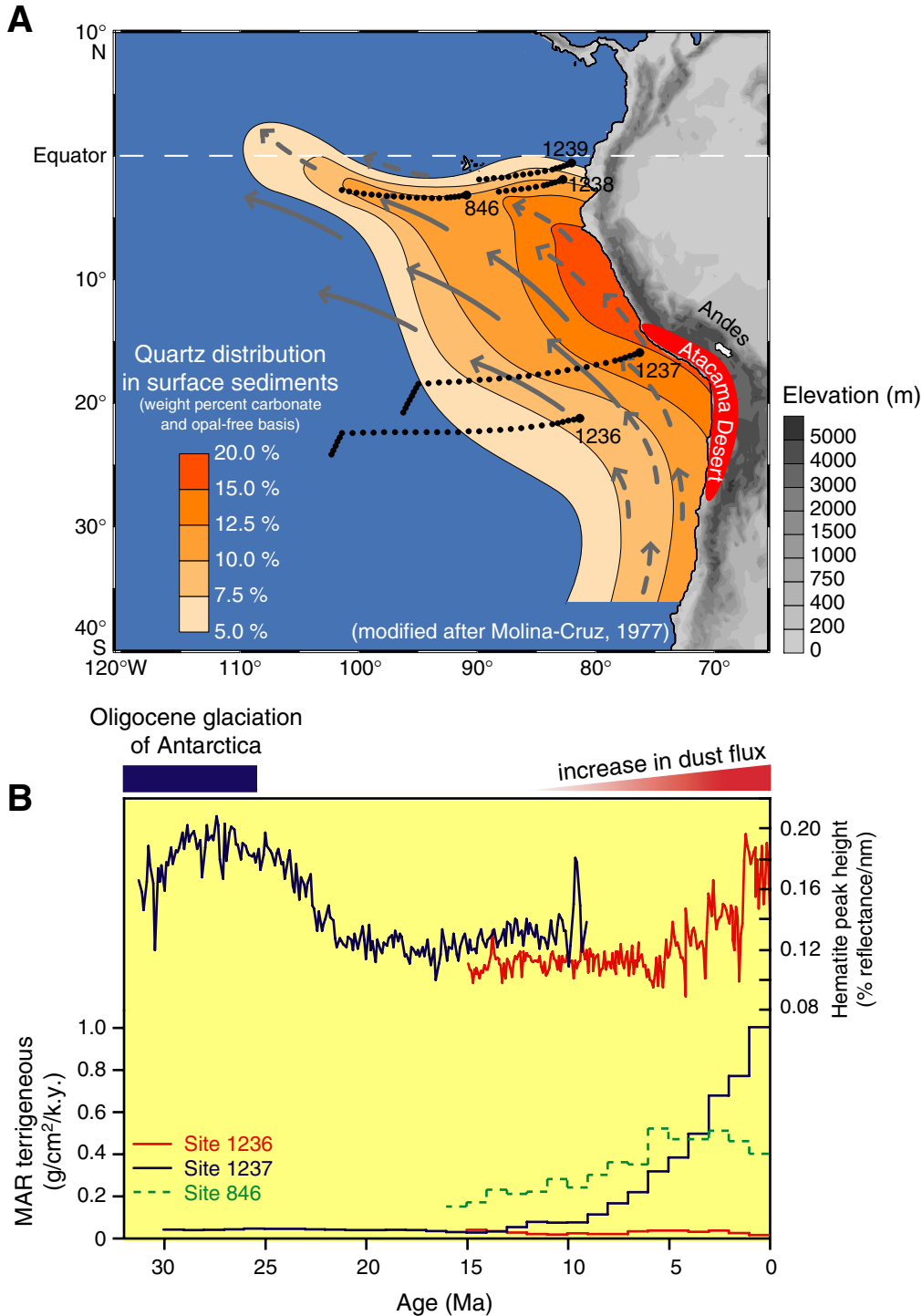


Figure F34. A. Mean calcium carbonate accumulation rates vs. age for sites from Legs 138 and 202. Shaded time intervals mark maxima in carbonate accumulation rates. B. Annual chlorophyll-a concentrations (in milligrams per cubic meter) (see seawifs.gsfc.nasa.gov), site locations, and tectonic backtrack (Pisias et al., 1995). Red dots = paleoposition of sites from ~4 to 8 Ma.

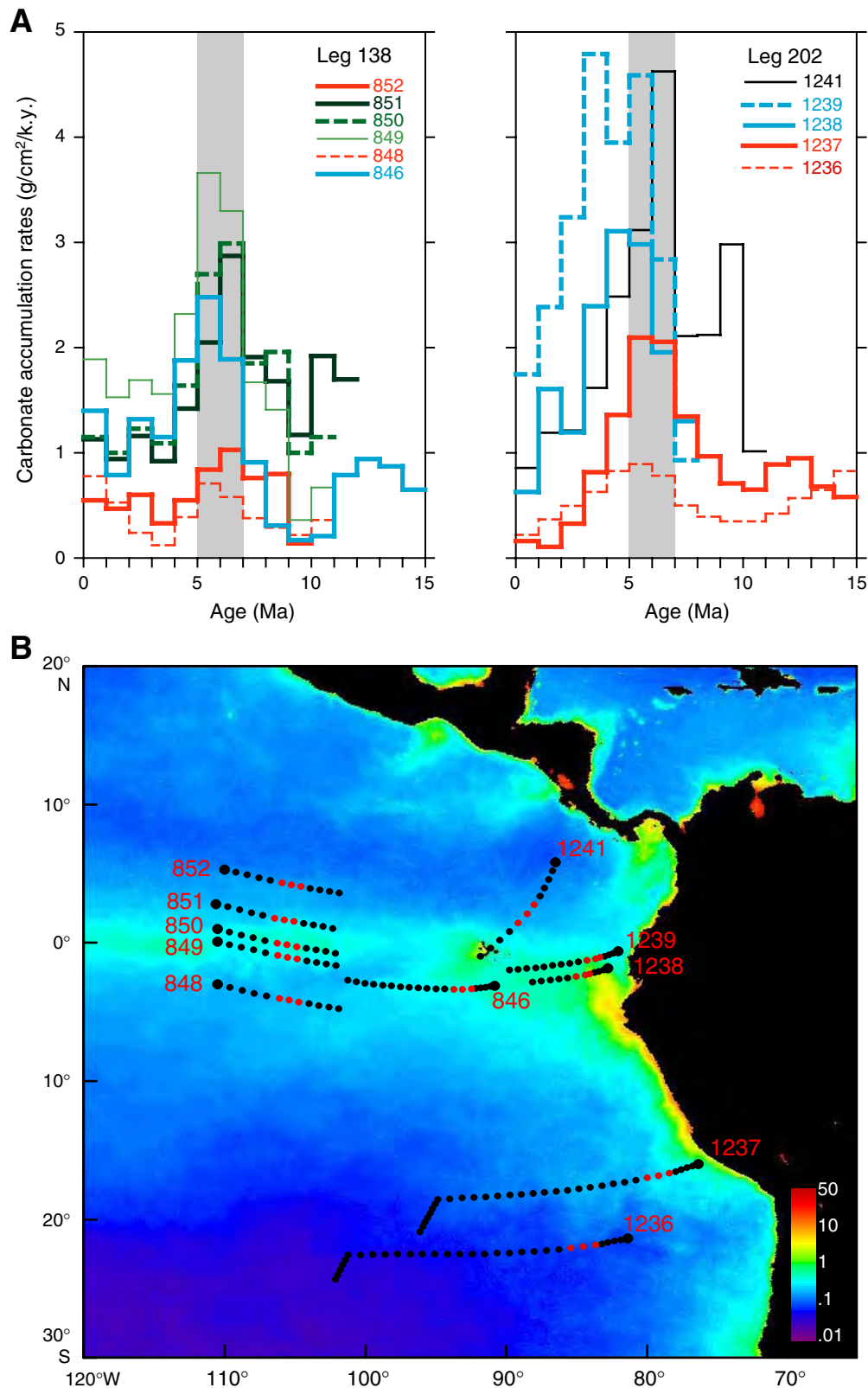


Figure F35. Ash frequency for Sites 1237–1242 was calculated as first derivative of the cumulative number of ash horizons plotted vs. age. Red lines = volcanic ash frequency, green bars = thickness of each ash layer.

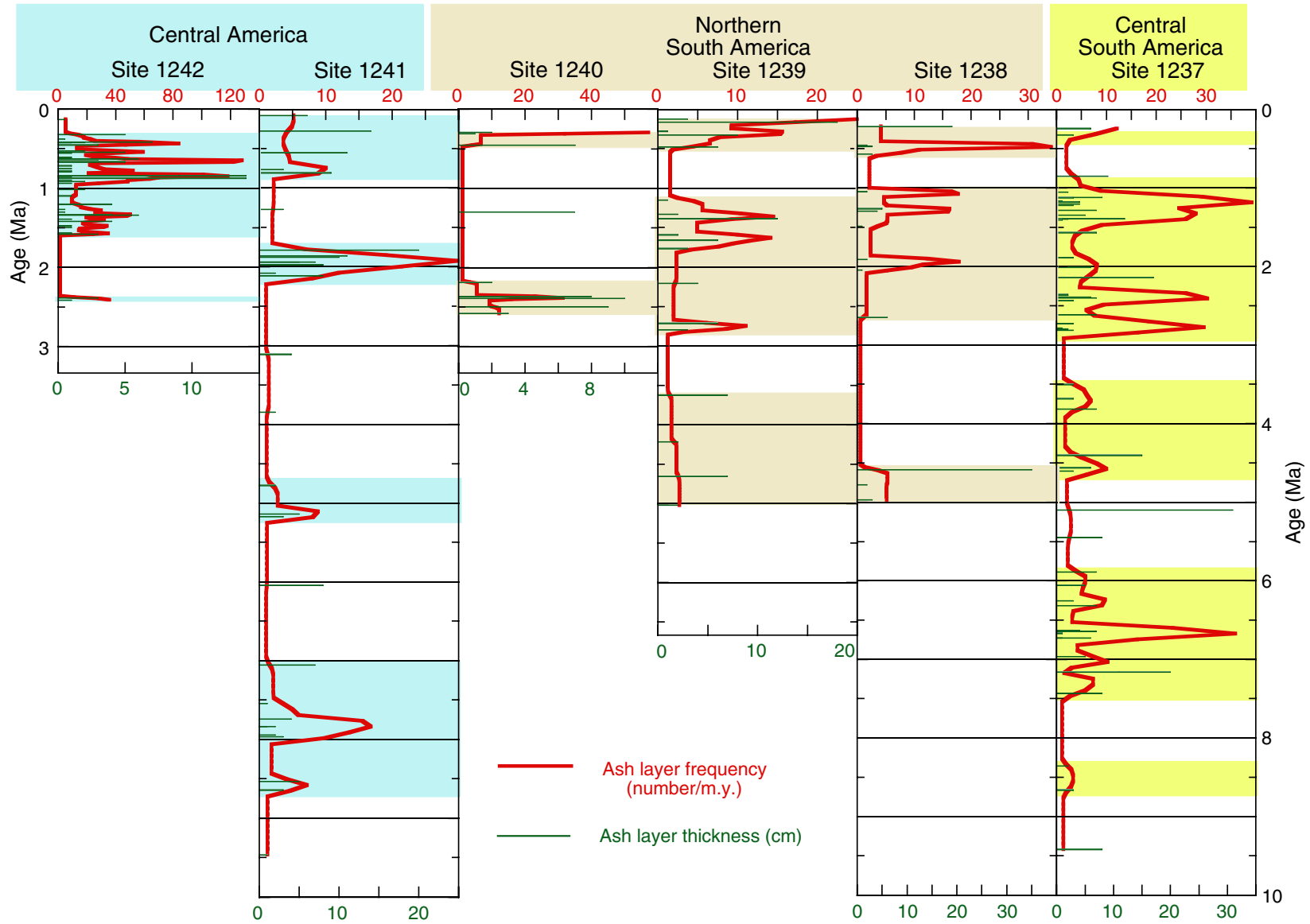


Figure F36. Calcium carbonate concentration, foraminifer abundance (R = rare, F = few, C = common, A = abundant) and preservation (P = poor, M = moderate, G = good), benthic foraminifer percentage, and total organic carbon concentration at Site 1241. The orange box indicates the time interval of the Miocene carbonate crash observed in the eastern equatorial Pacific.

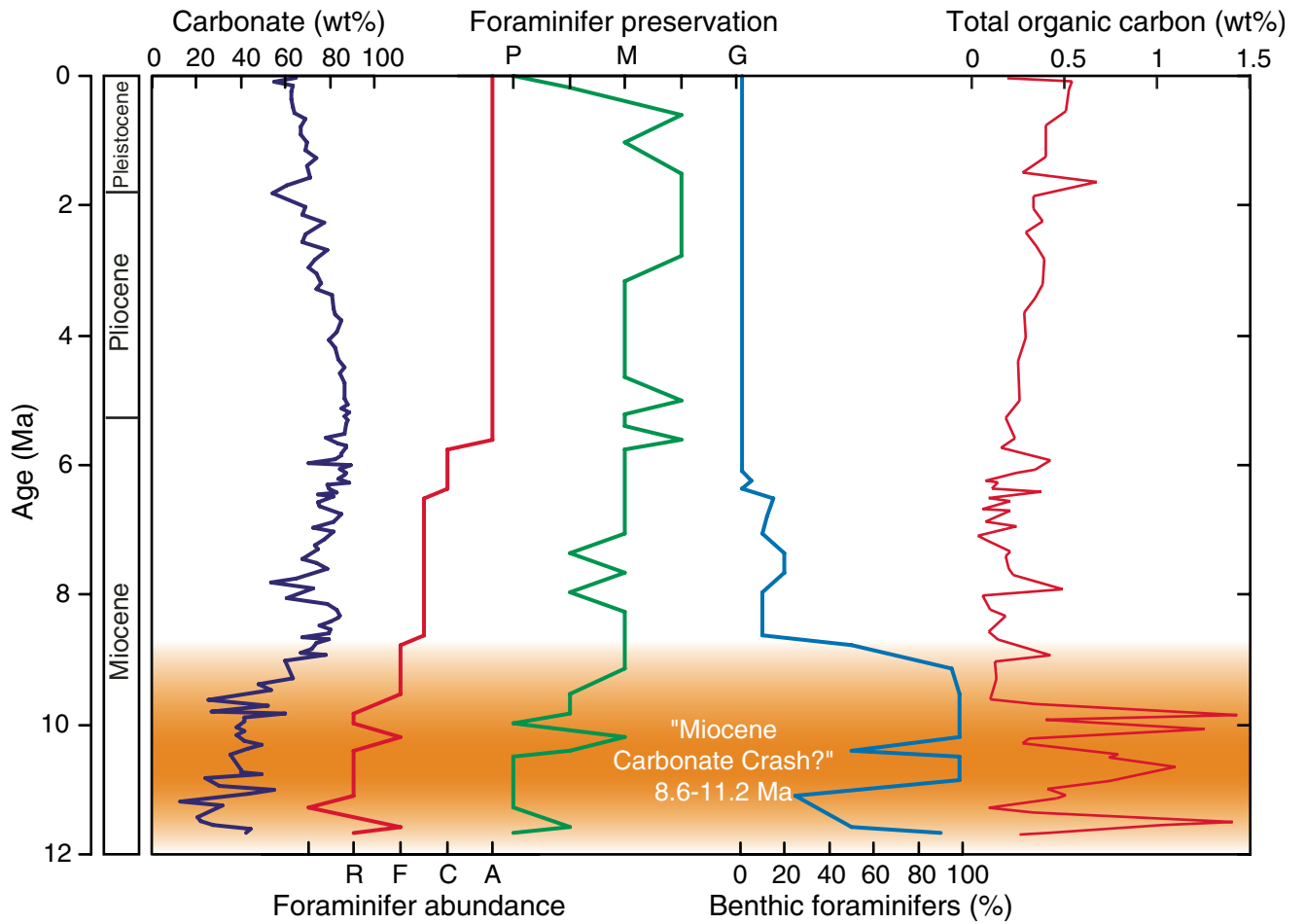


Figure F37. Evolutive spectra of the lightness parameter L^* at Site 1239 (which tends to mimic calcium carbonate content of the sediments) using preliminary shipboard age models. Warm colors indicate greater concentrations of variance within a frequency band.

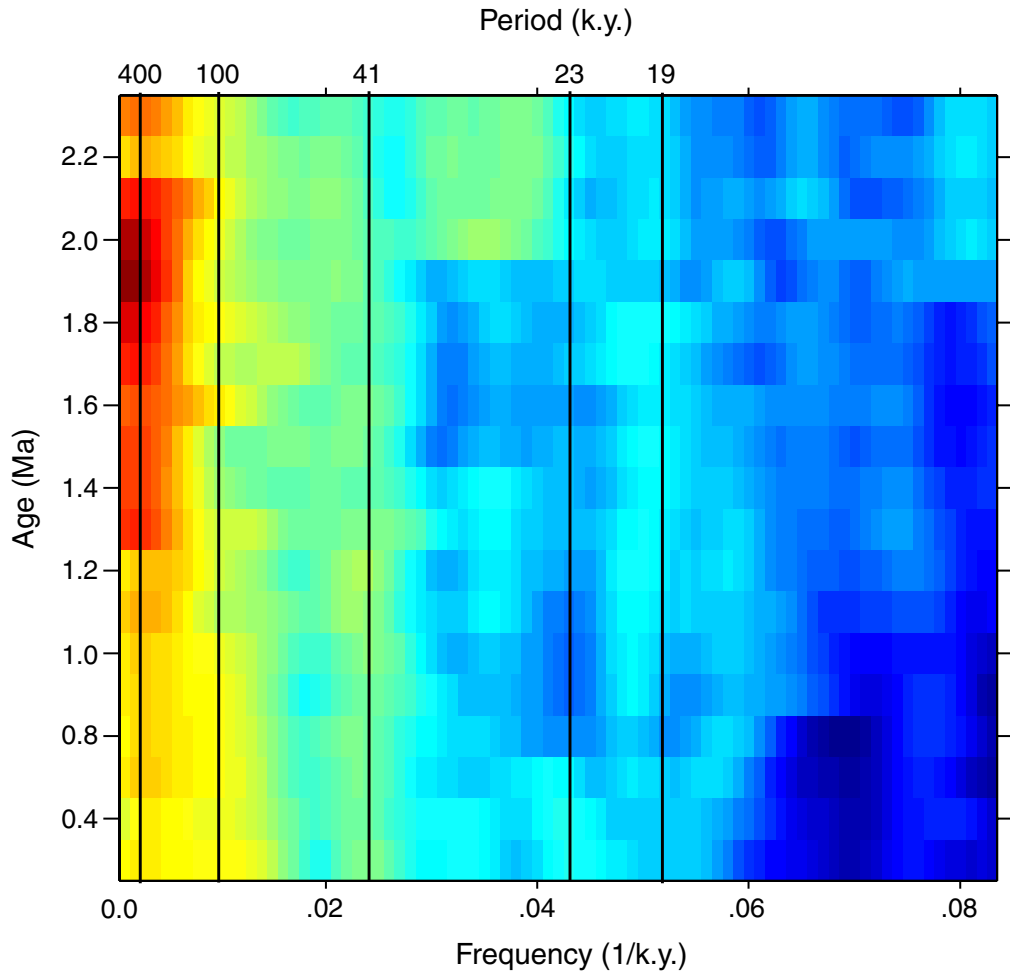


Figure F38. Sites 1232–1235 are located at the southernmost reaches of the Peru-Chile Current system, in the transition between the subtropical and subpolar gyres. **A.** Contours of annual mean surface water temperatures in degrees Celsius. Arrows indicate surface water currents. ACC = Antarctic Circumpolar Current, PCC = Peru-Chile Current, PCCC = Peru-Chile Countercurrent, CFW = Chilean Fjord Water, CC = Coastal Current. **B.** Salinity contours showing influx of Chilean Fjord Water (CFW). Site 1233 is best located to monitor low-salinity surface waters that advect northward, a measure of the strength or location of the westerly winds. Sites 1234 and 1235 are located to the north, within the eastern boundary current setting, in an upwelling center off of Concepción.

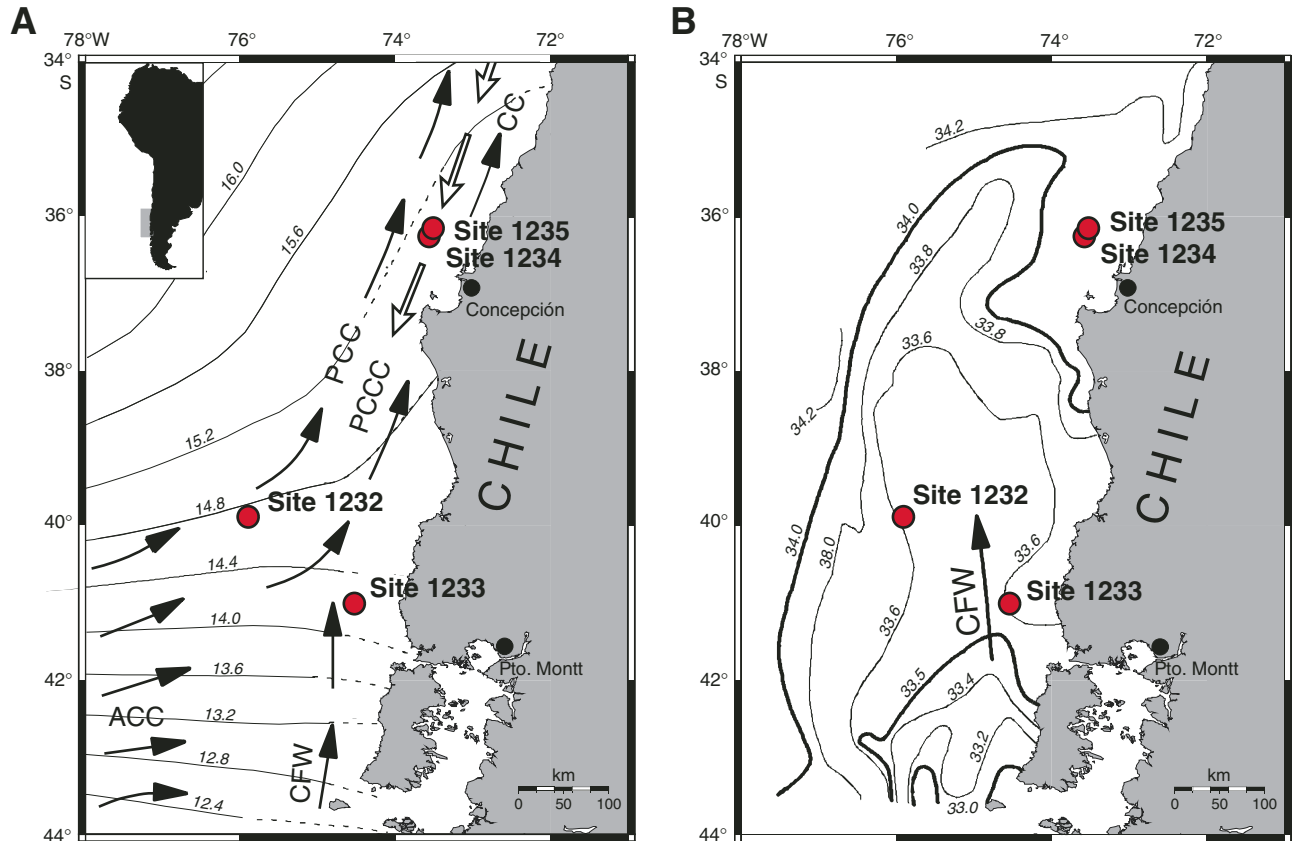


Figure F39. Locations of Sites 1233–1235 on subsurface oxygen contours. Circles mark the current site locations relative to the oxygen-poor Gunther Undercurrent (GUC) and the relatively oxygen-rich Antarctic Intermediate Water (AAIW). Vertical bars on the sites indicate the likely effect of last glacial maximum sea level fall of ~130 m on the position of the sites relative to the sea surface. PCW = Pacific Central Water.

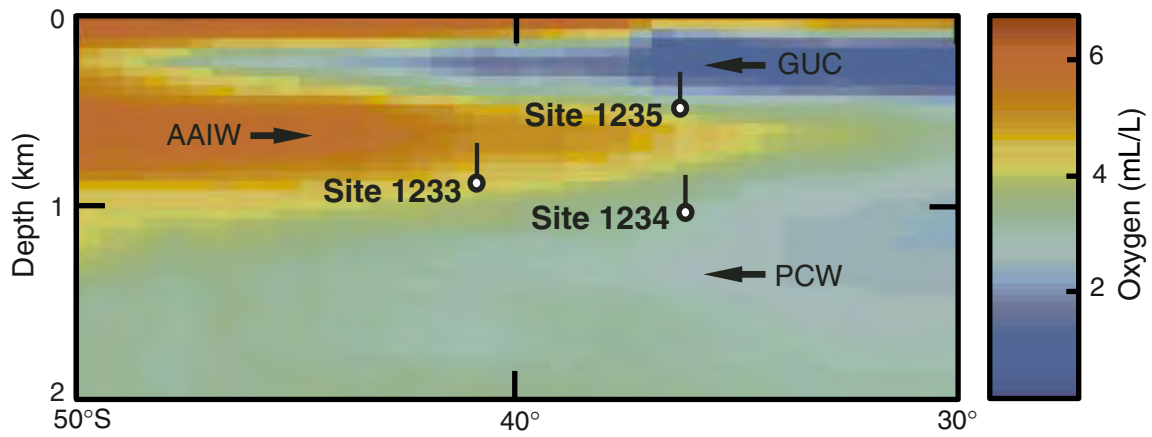


Figure F40. Shipboard correlation of Sites 1233, 1234, and 1235 based on biostratigraphic (<260 ka for all sites) and magnetostratigraphic (e.g., location of Laschamp Event at ~41 ka) evidence as well as long-term patterns in magnetic susceptibility, total organic carbon (C_{org}), and calcium carbonate concentrations. These data indicate that all three sites will contain viable records of century- to millennial-scale climate change.

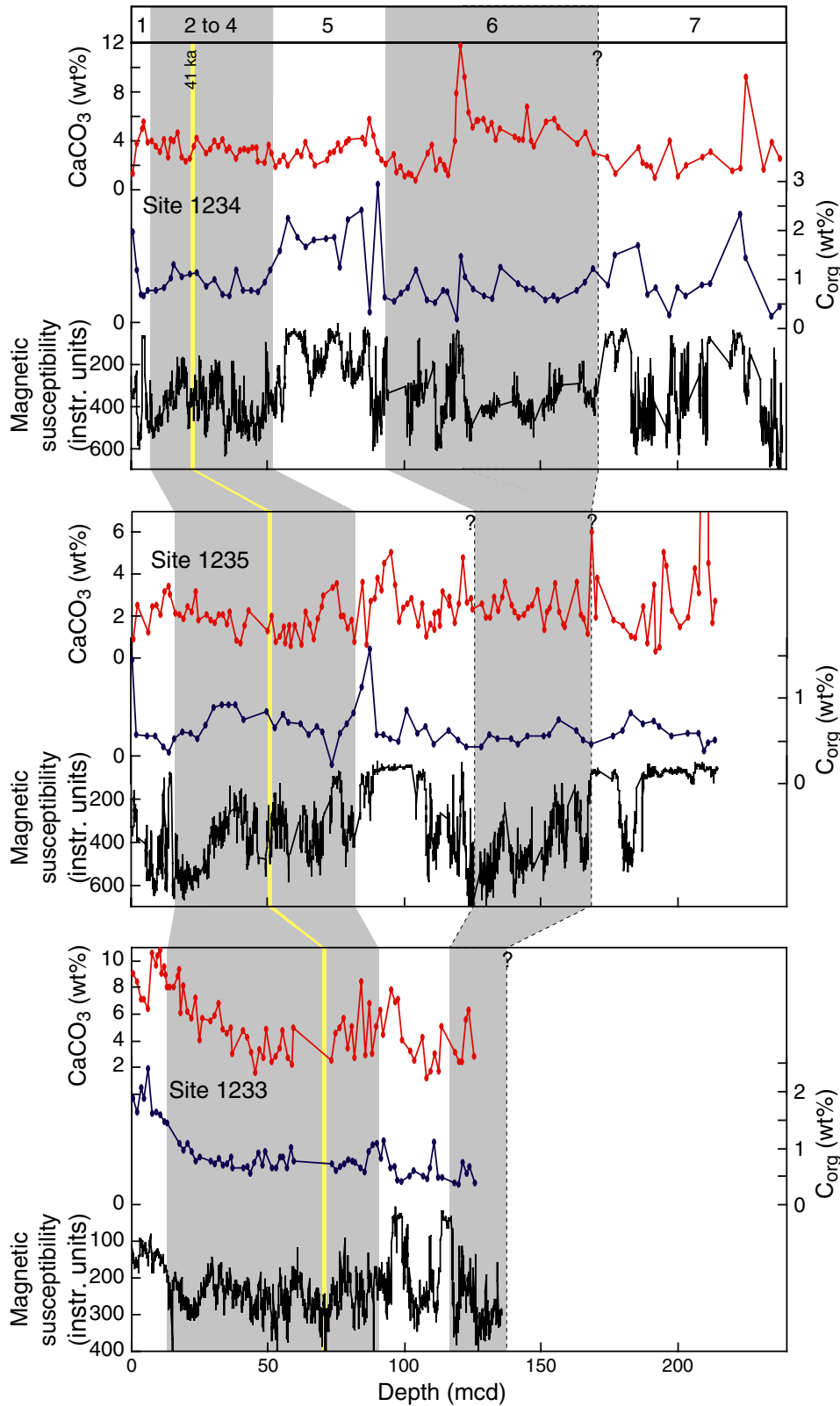


Figure F41. Millennial-scale variability at Site 1233. Magnetic susceptibility and diatom abundance plotted on a preliminary age scale for the interval 0 to 45 ka. The age scale is based on Holocene age control points derived from a correlation of the magnetic susceptibility records between Site 1233 and AMS-¹⁴C dated core GeoB 3313-1 (Lamy et al., 2001) and the location of the Laschamp Event. All ages are calendar years BP and are linearly interpolated between the dates. The data are compared to the GISP2 ice core in Greenland (Grootes et al., 1993) and the Byrd ice core in Antarctica (Bender et al., 1999). SMOW = oxygen isotopic composition of standard mean ocean water. D = dominant, A = abundant, C = common.

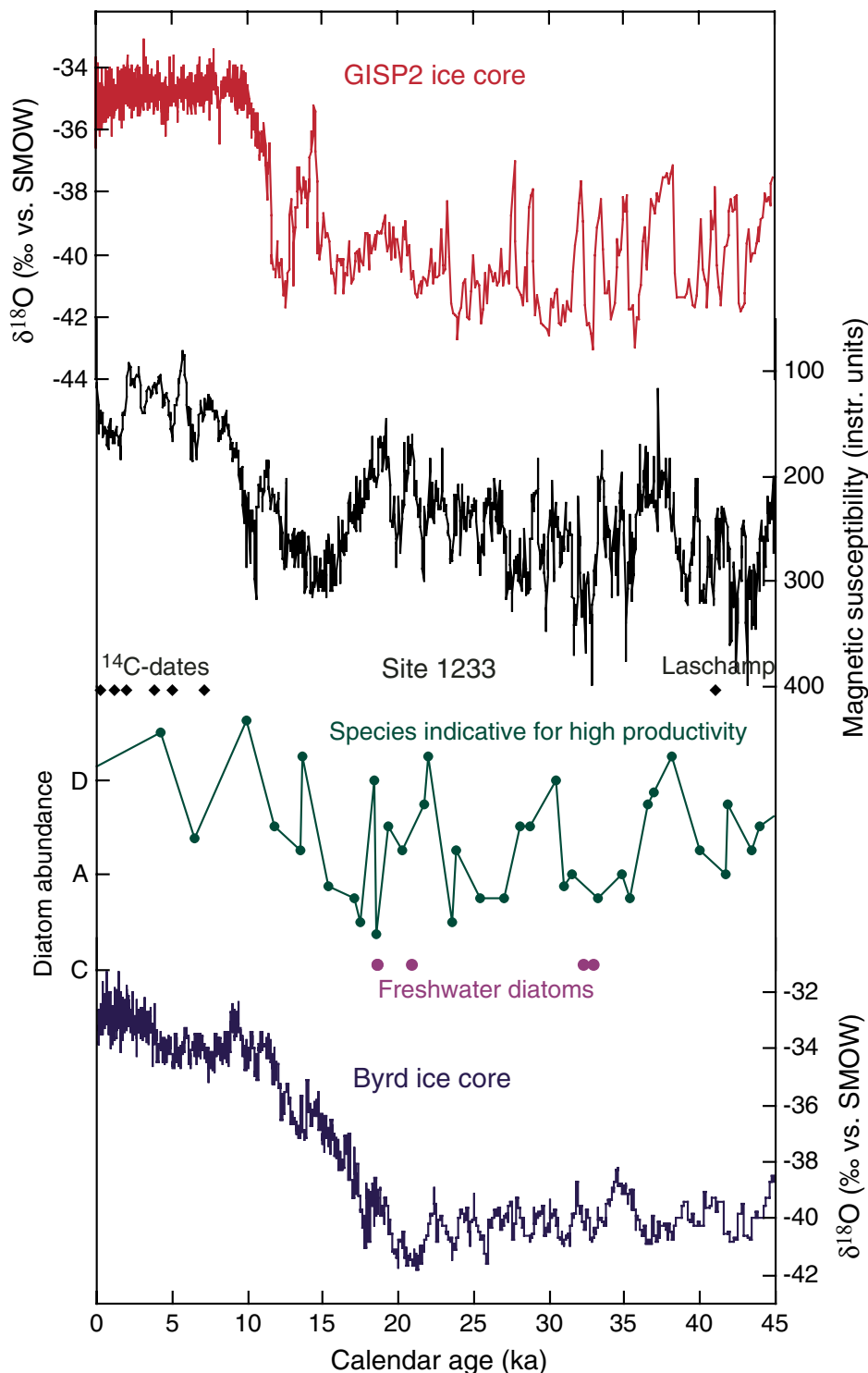
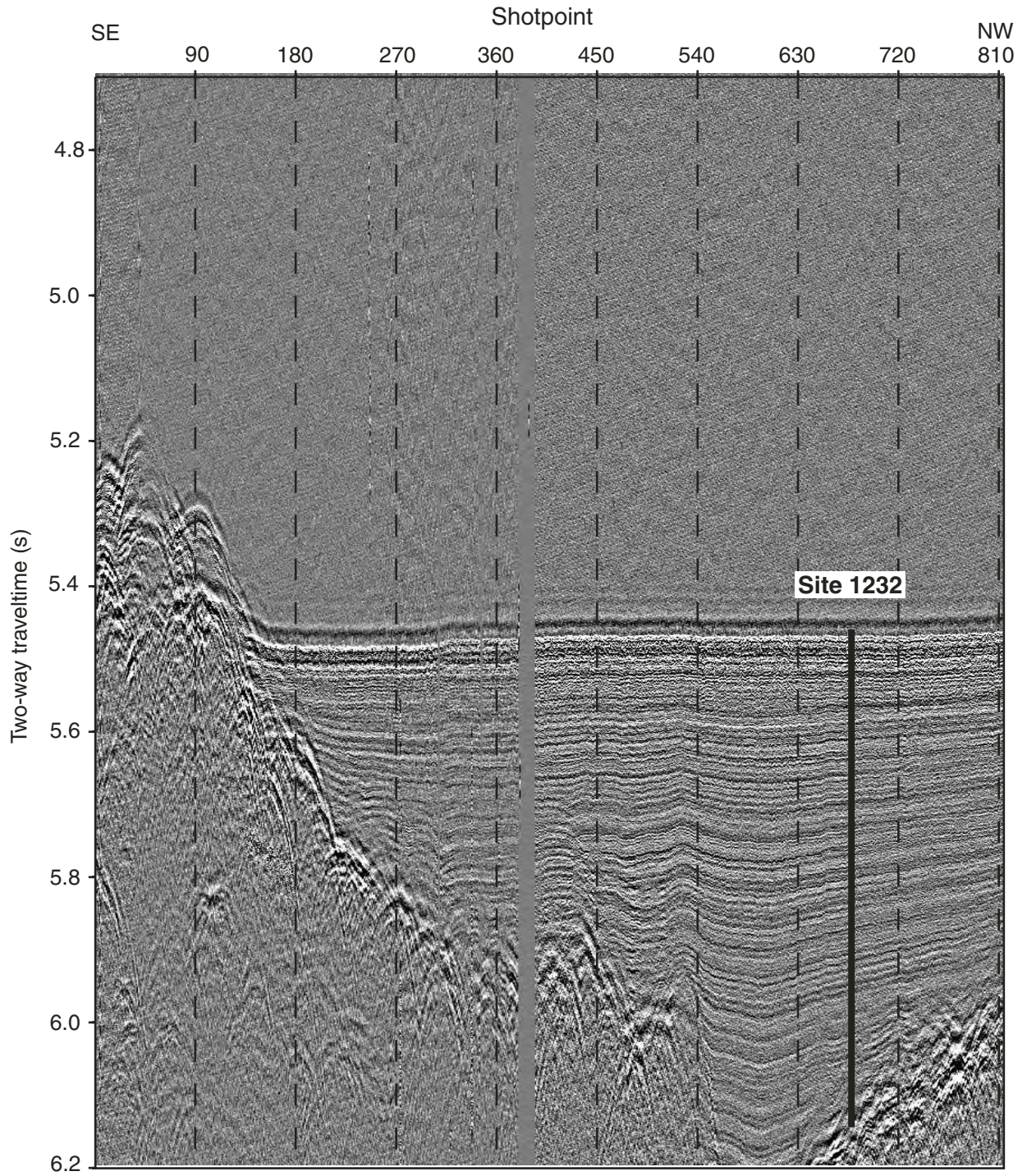


Figure F42. Seismic profile across Site 1232 (Mix et al., 1997).



Site 1232 (proposed Site SEPAC-9A), Shotpoint 686. CBA-3A line 3 0504-0720 97 mar 08

Figure F43. Lithology and physical and chemical data summary, Site 1232. GRA = gamma ray attenuation.

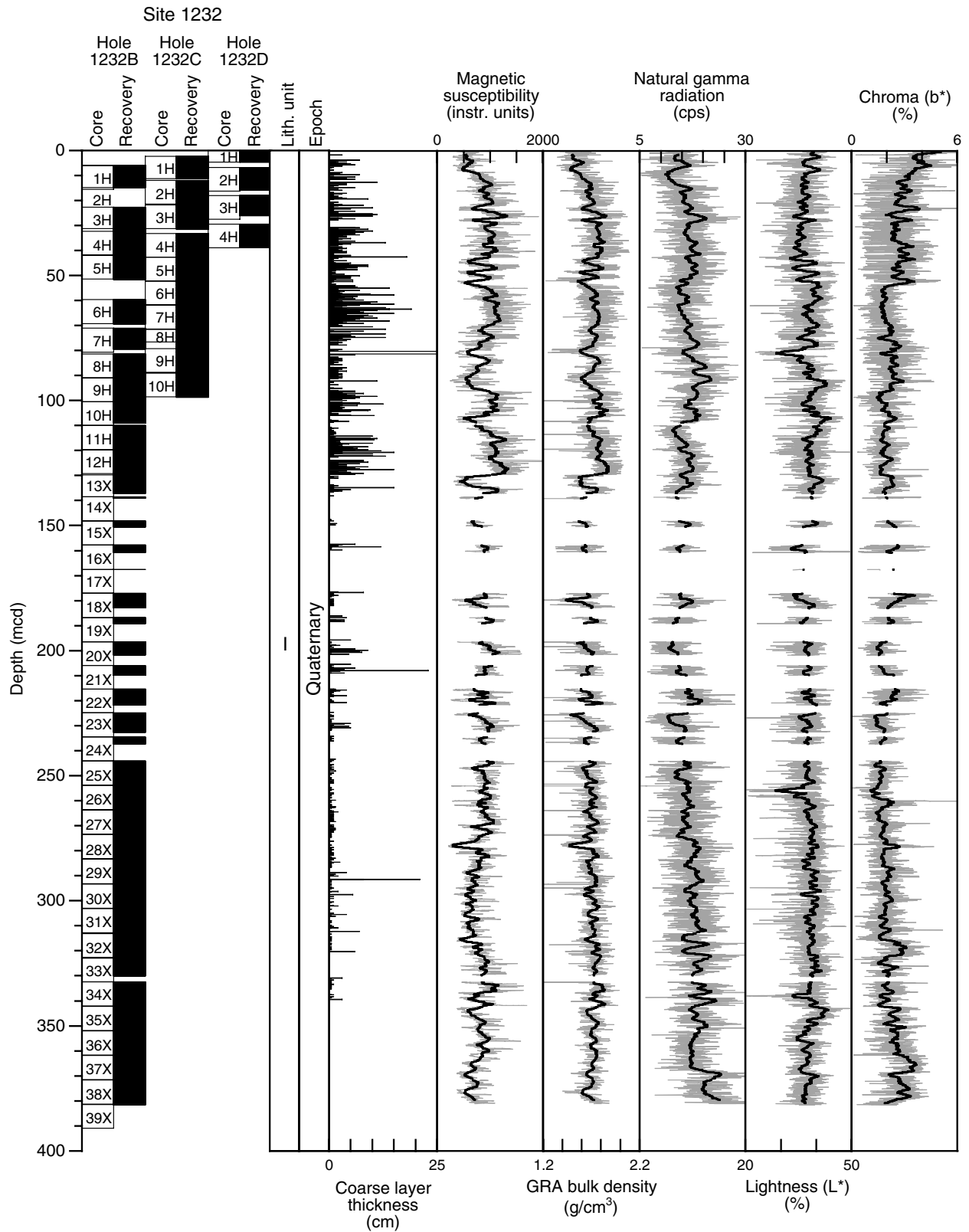


Figure F44. Digital Parasound profile for Site 1233 (Hebbeln et al., 1995). A. East-west profile. B. North-south profile.

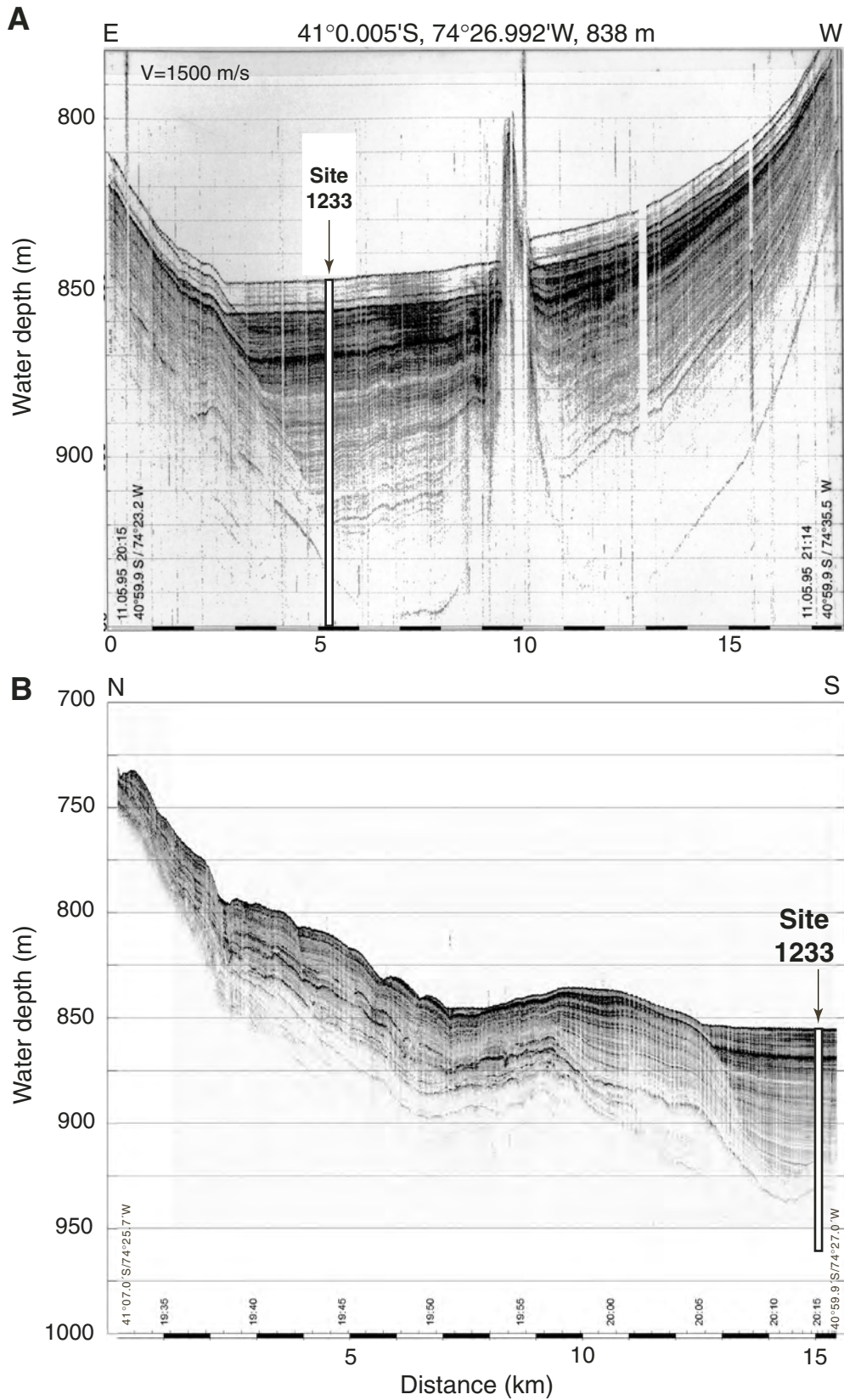


Figure F45. Analog 3.5-kHz profile acquired with the *JOIDES Resolution* during the approach to Site 1233 on 12 April 2002. Depths are represented at 1500 m/s. Reflector numbers appear in boxes.

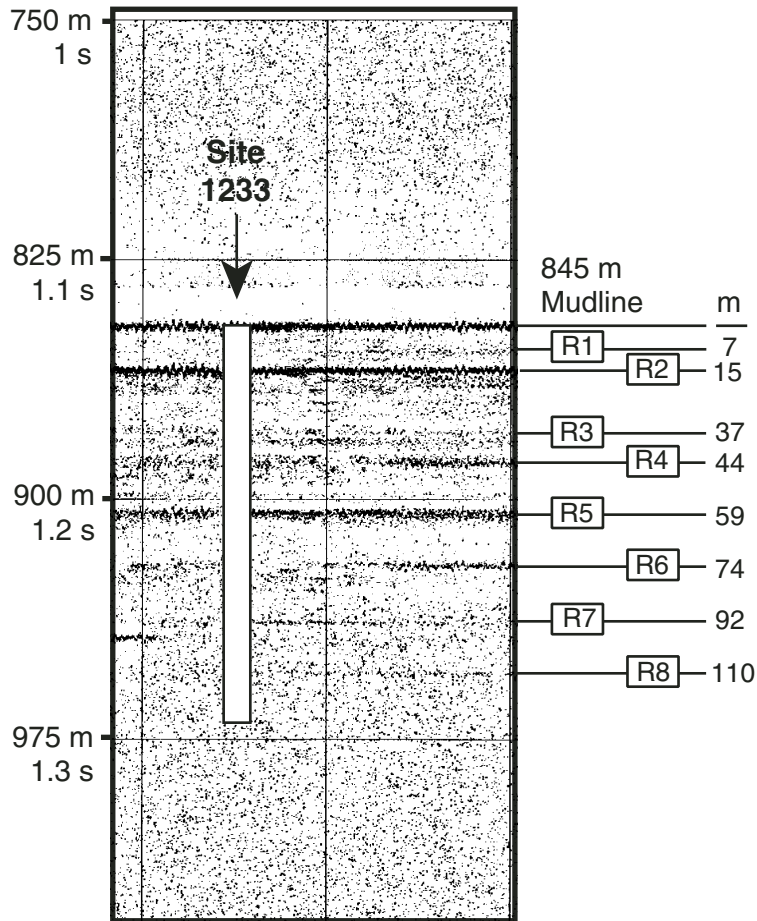


Figure F46. Lithology and physical and chemical data, Site 1233. GRA = gamma ray attenuation.

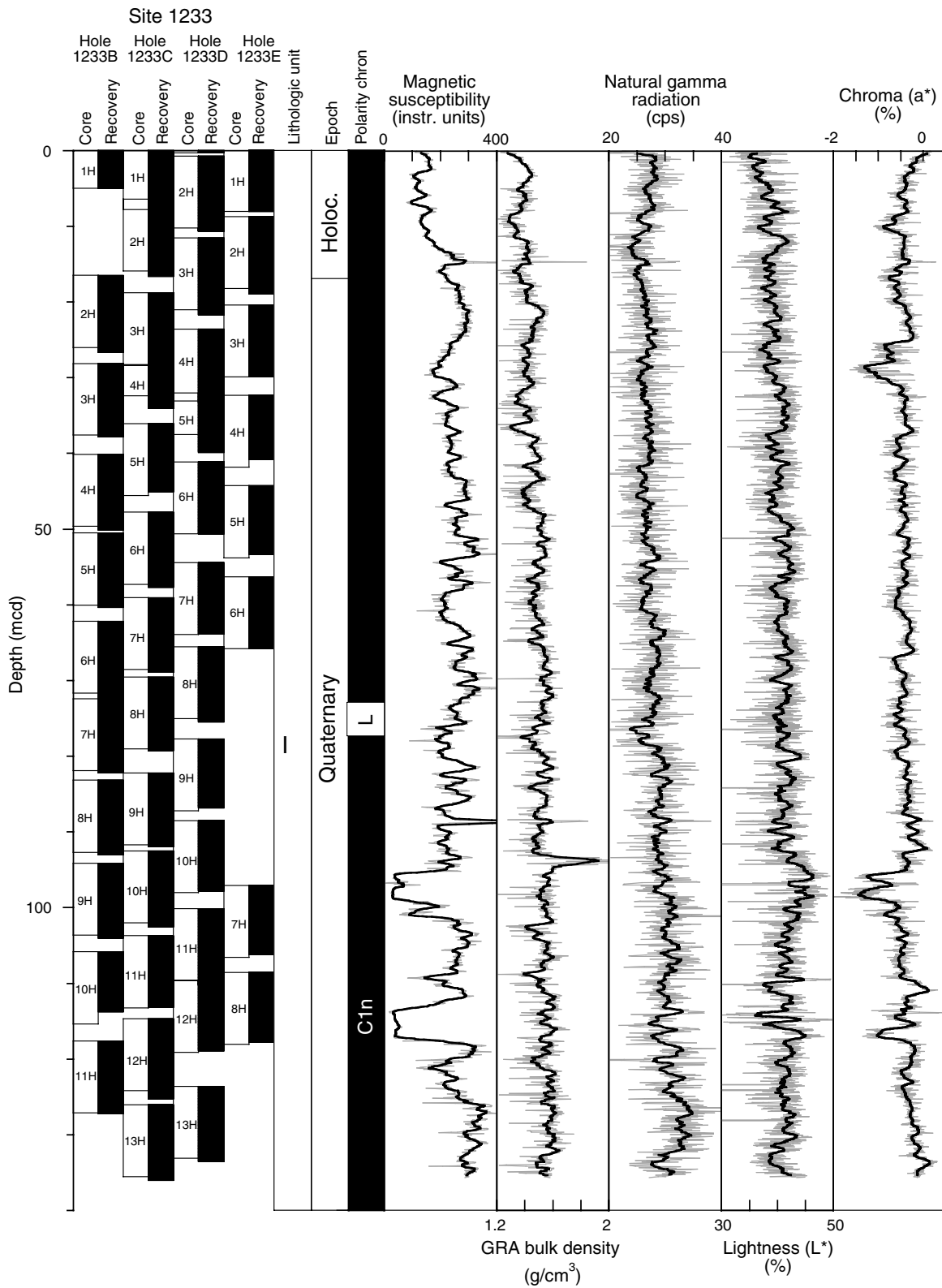


Figure F47. Swath bathymetry of a Chile margin segment, including Sites 1234 and 1235 (Wiedicke-Hombach et al., 2002).

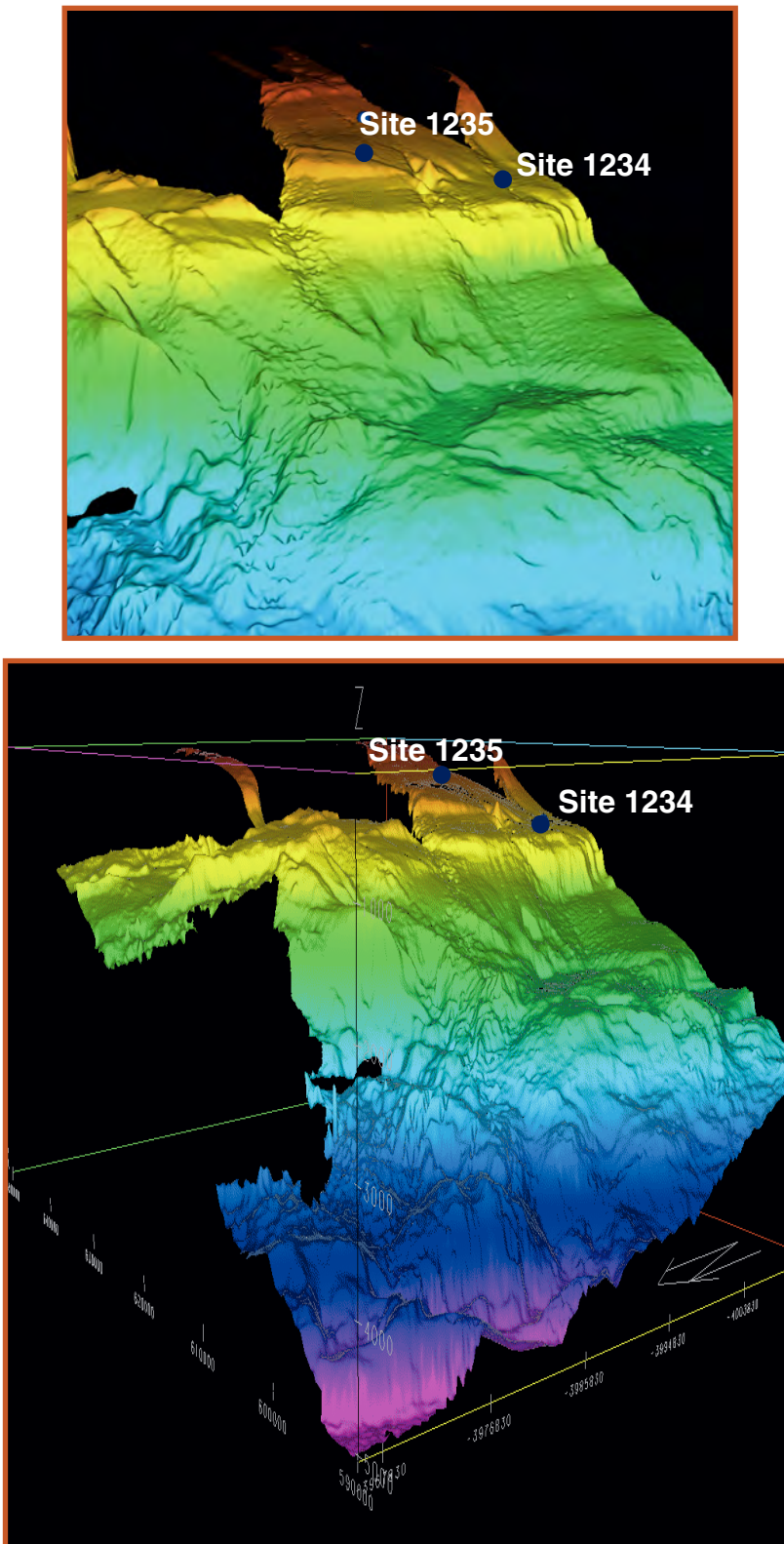
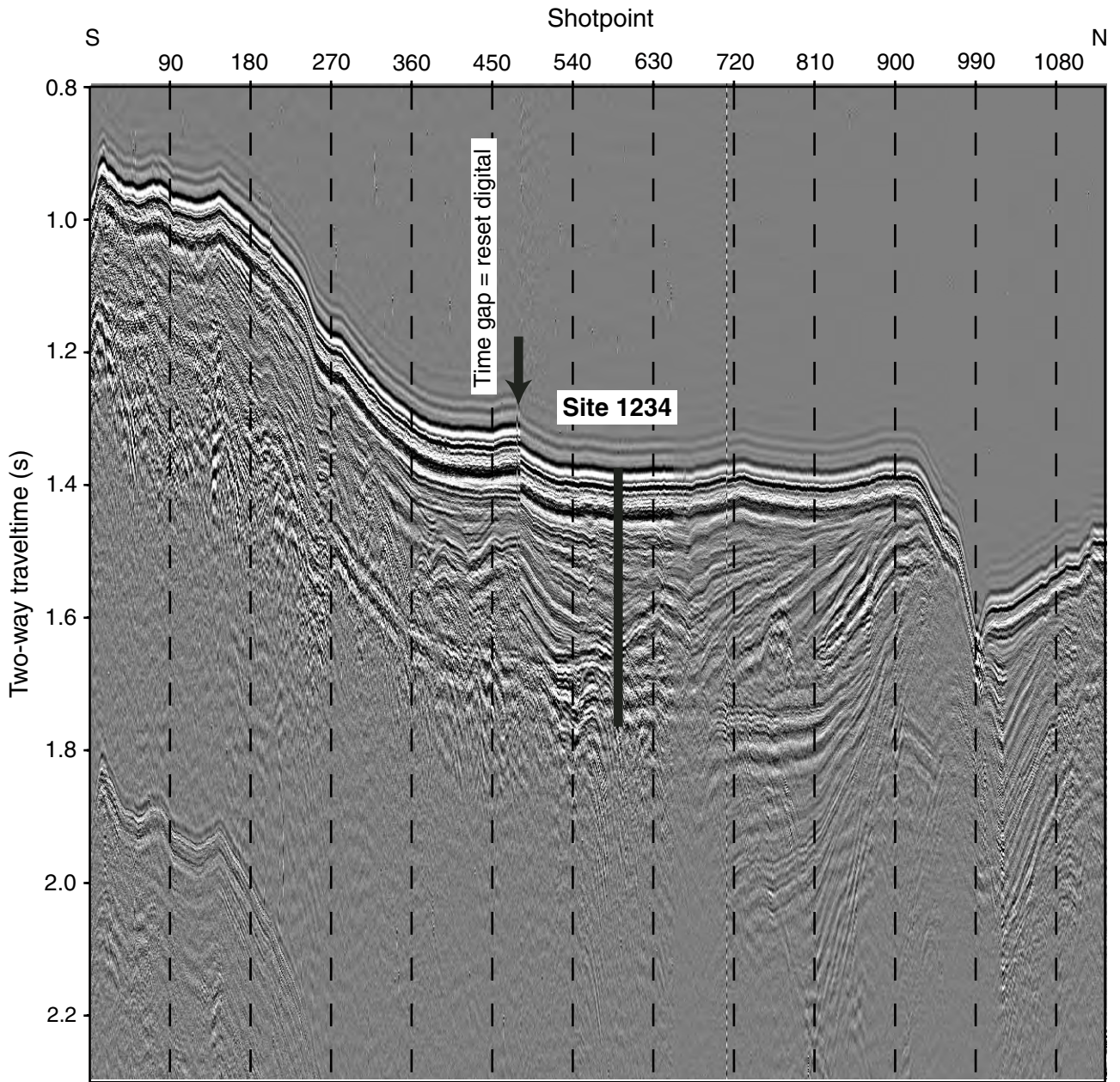


Figure F48. Seismic profile across Site 1234 (Mix et al., 1997).



Site 1234 (proposed Site SEPAC-13B), Shotpoint 585. Survey CBA-3D line 4 Shot within 2100-0018 97 mar 12

Figure F49. Lithology and physical and chemical data, Site 1234. GRA = gamma ray attenuation.

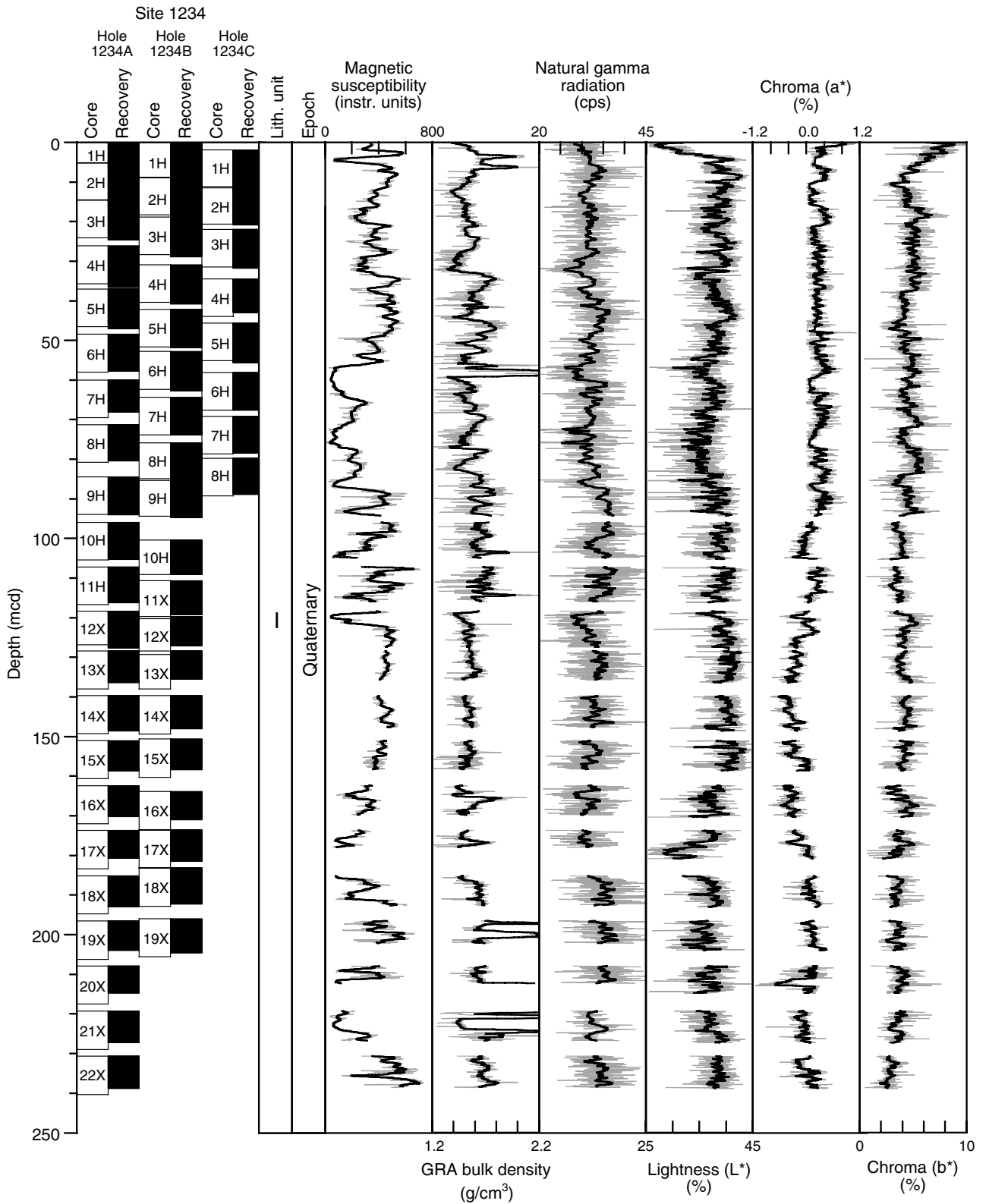
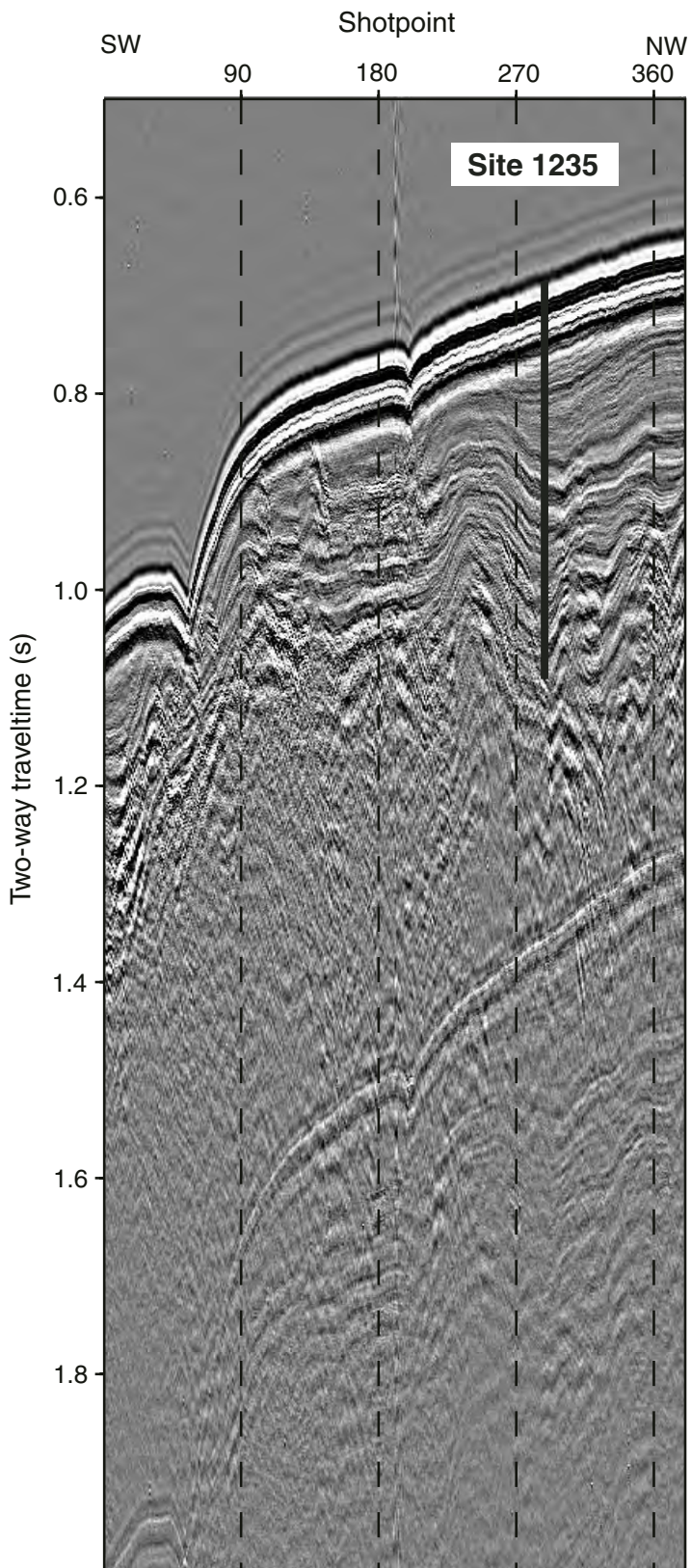


Figure F50. Seismic profile across Site 1235 (Mix et al., 1997).



Site 1235 (proposed Site SEPAC-14A), Shotpoint 295.
Survey CBA-3D line 15 0948-105 97 mar 14.

Figure F51. Lithology and physical and chemical data, Site 1235. GRA = gamma ray attenuation.

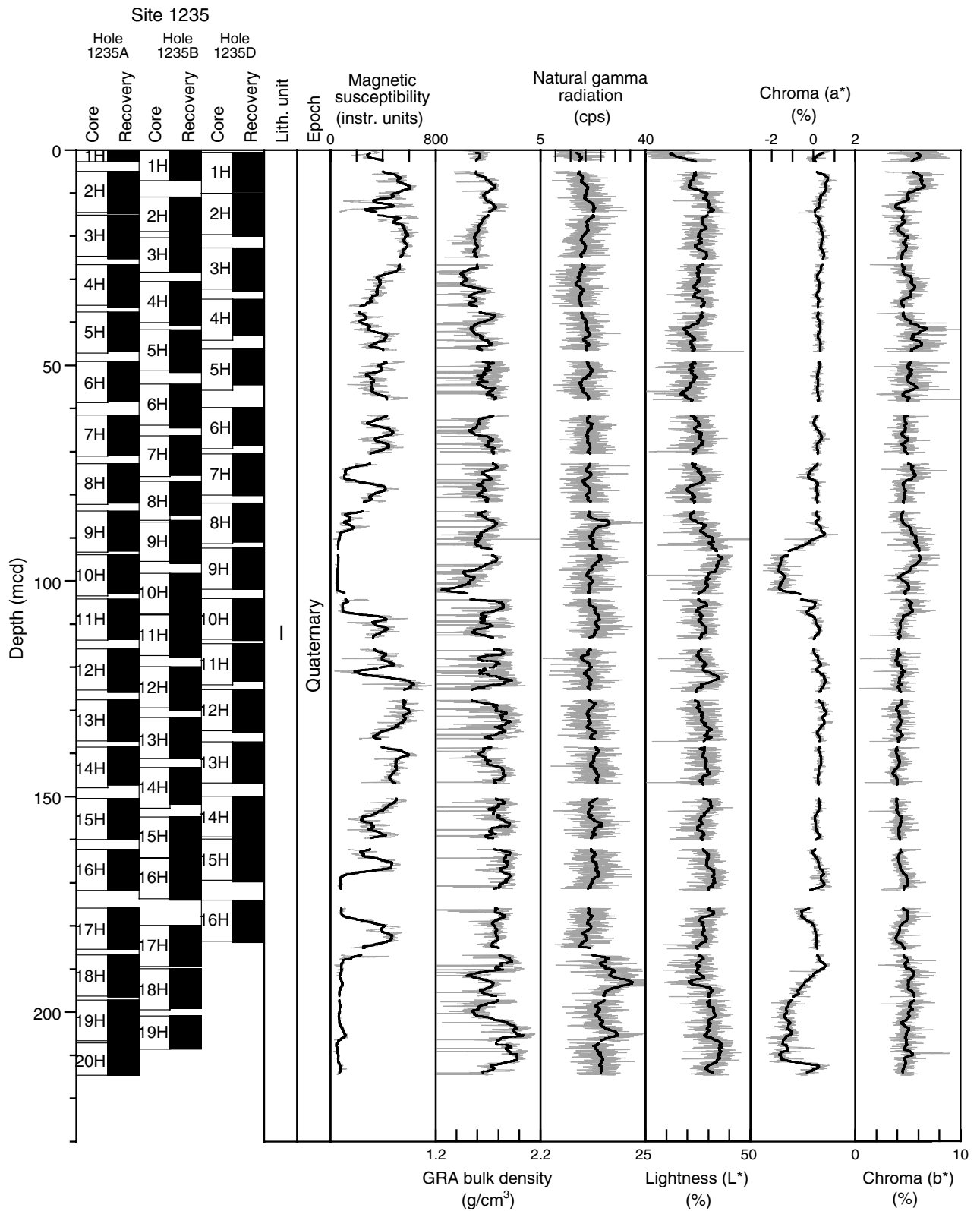


Figure F52. Seismic profile across Site 1236 (Mix et al., 1997).

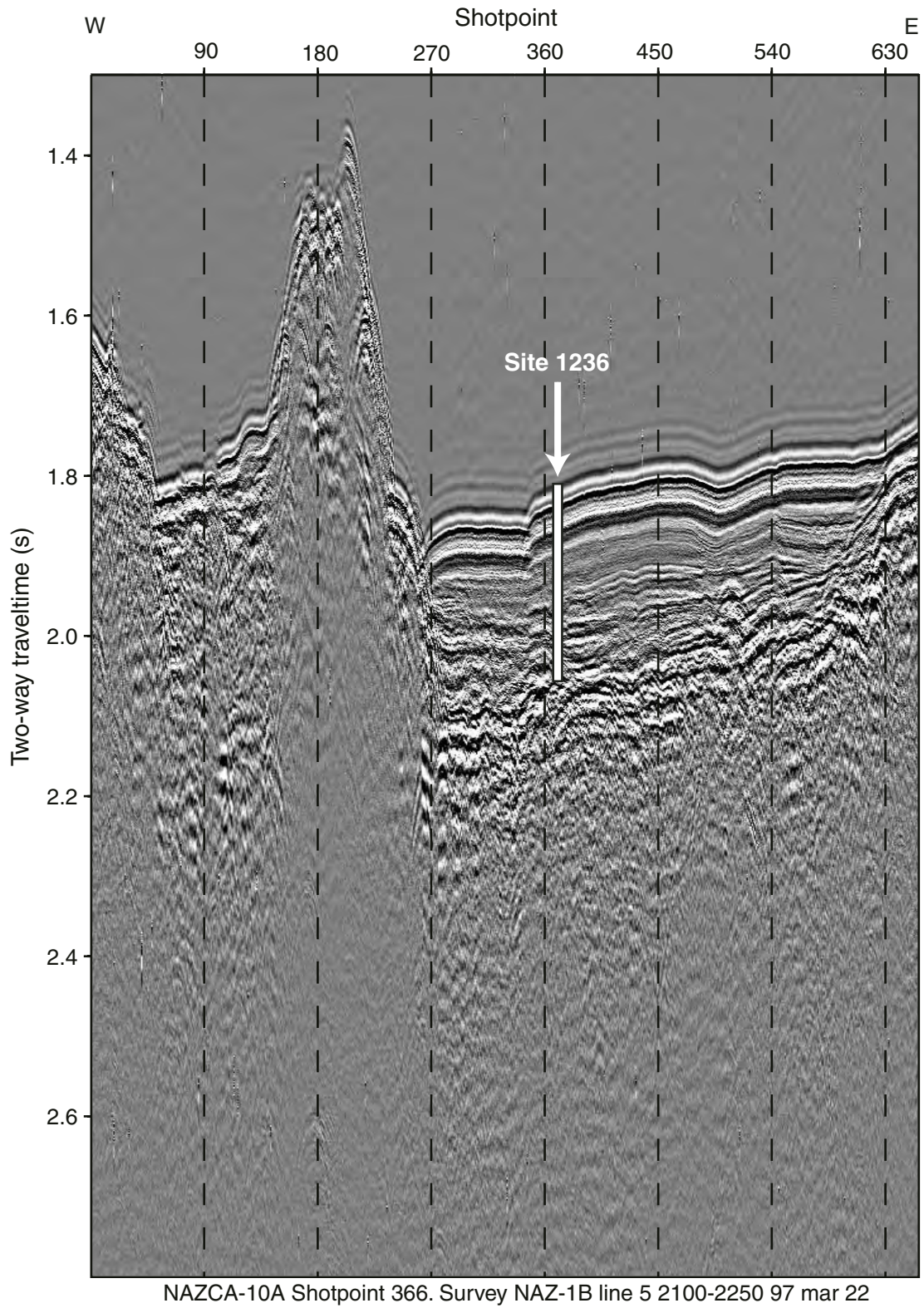


Figure F53. Lithology and physical and chemical data, Site 1236. GRA = gamma ray attenuation.

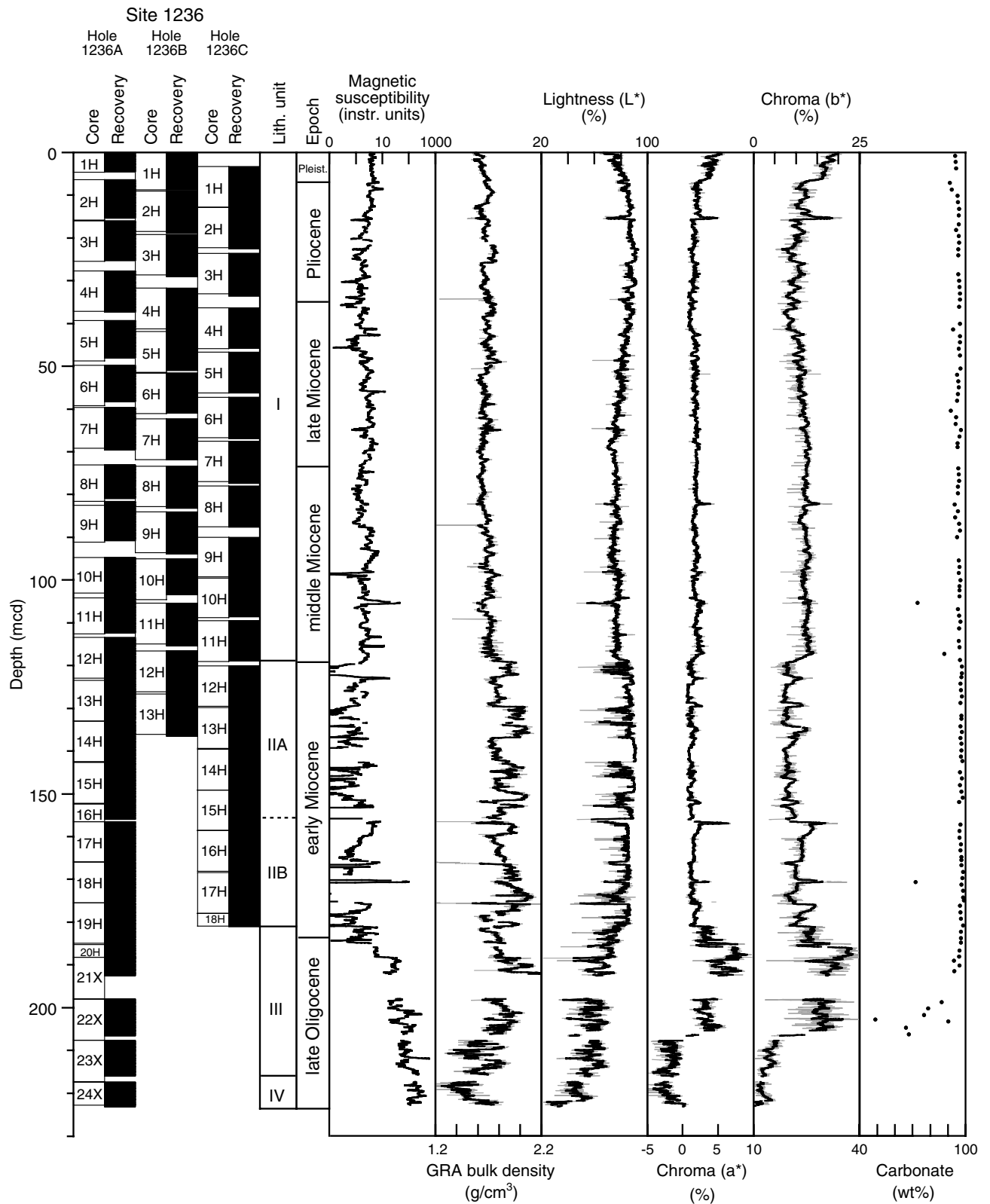
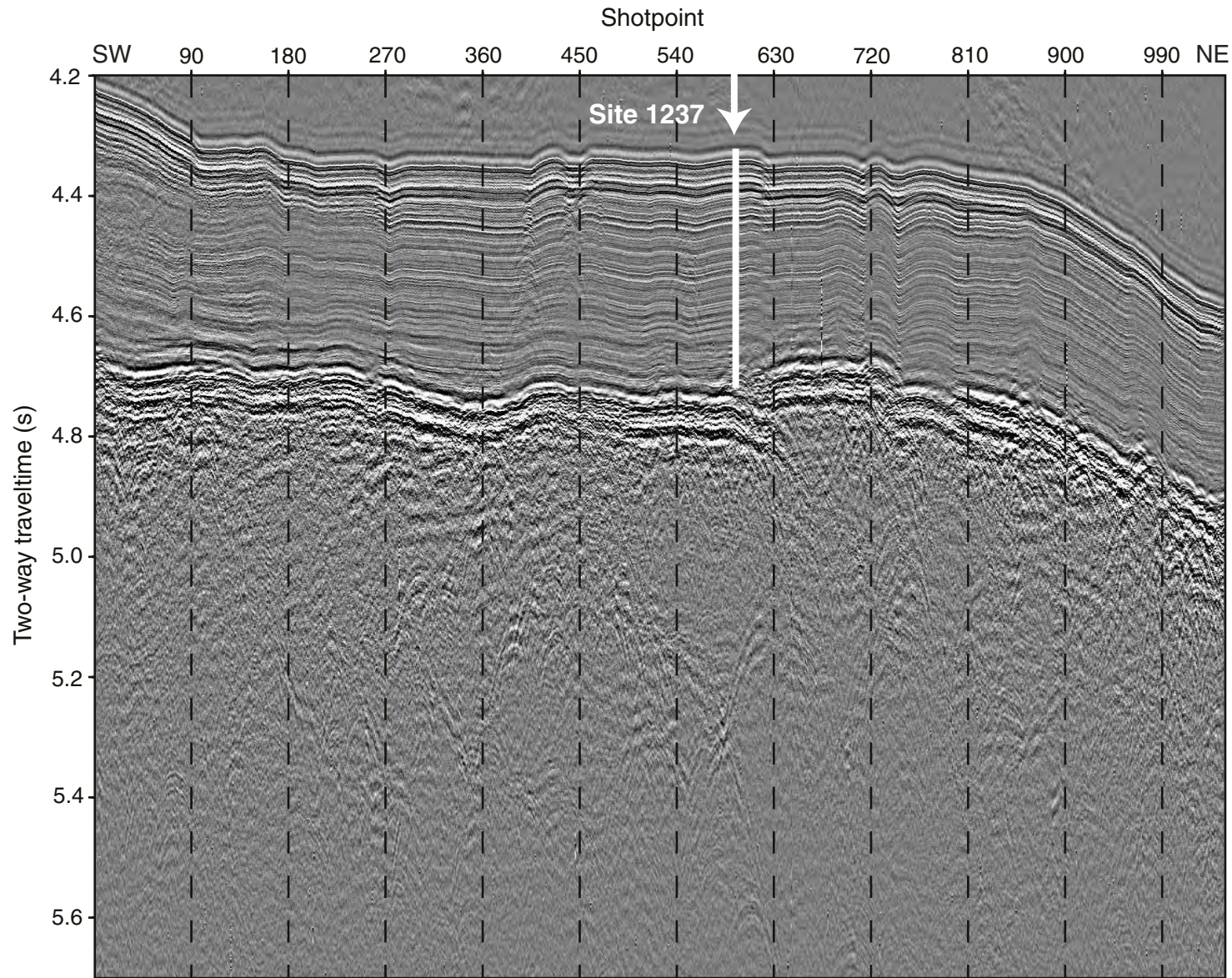


Figure F54. Seismic profile across Site 1237 (Mix et al., 1997).



Shotpoint 589. Survey NAZ-3B line 4 1234-1529z 97 mar 29

Figure F55. Lithology and physical and chemical data, Site 1237. GRA = gamma ray attenuation, MAD = moisture and density, TOC = total organic carbon.

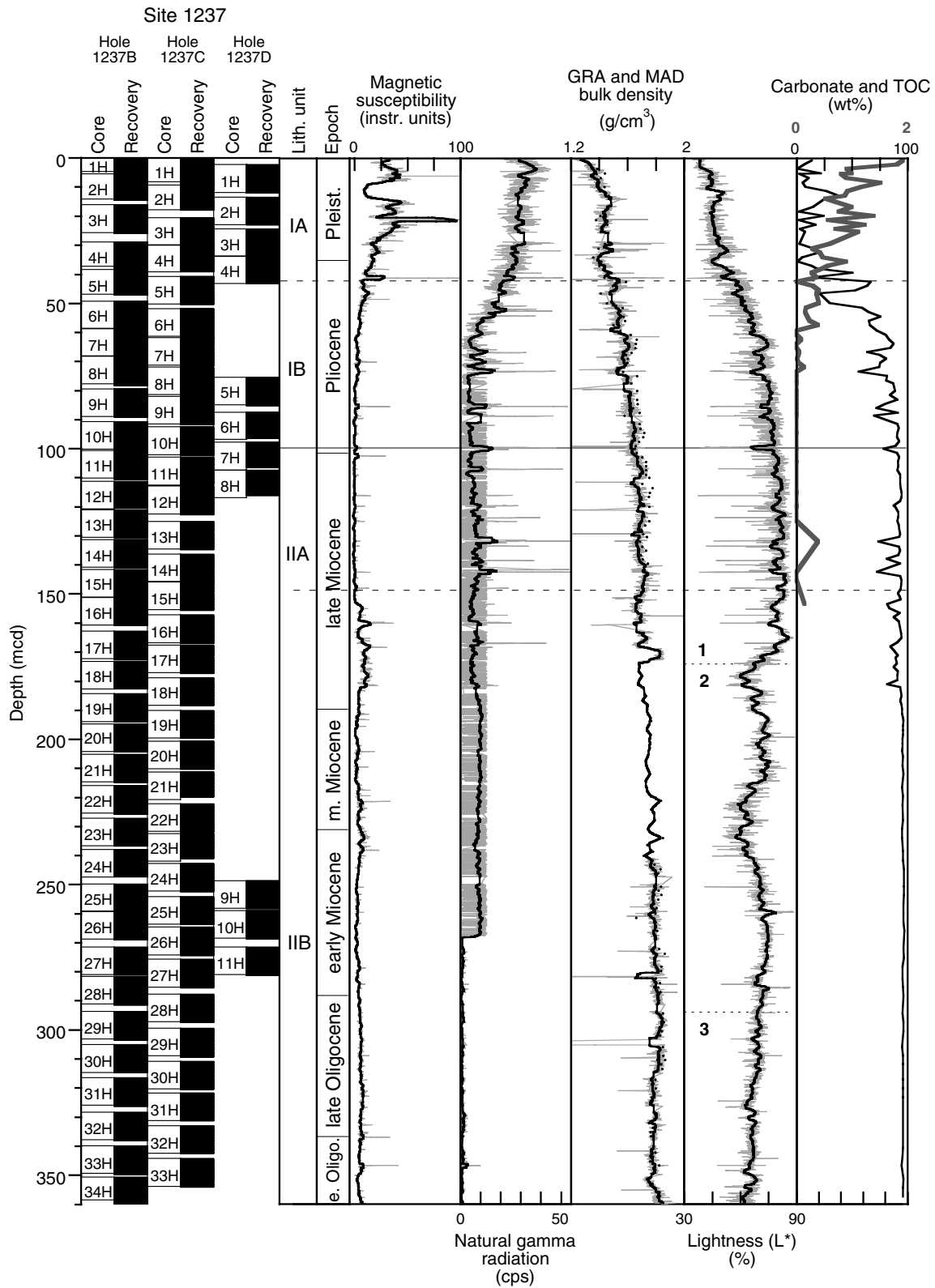


Figure F56. Seismic profile across Site 1238 (Lyle et al., 2000).

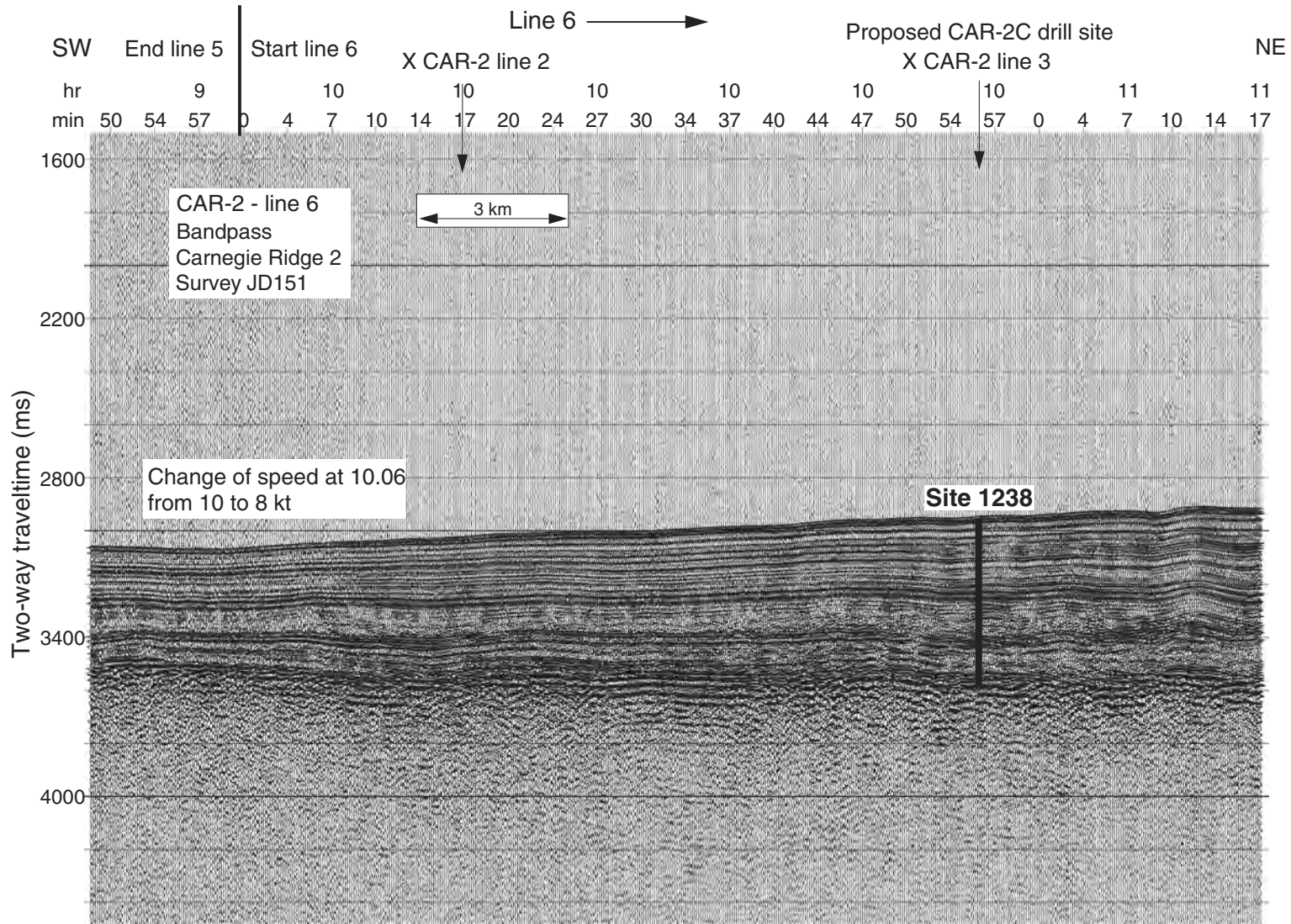


Figure F57. Lithology and physical and chemical data, Site 1238. GRA = gamma ray attenuation, TOC = total organic carbon.

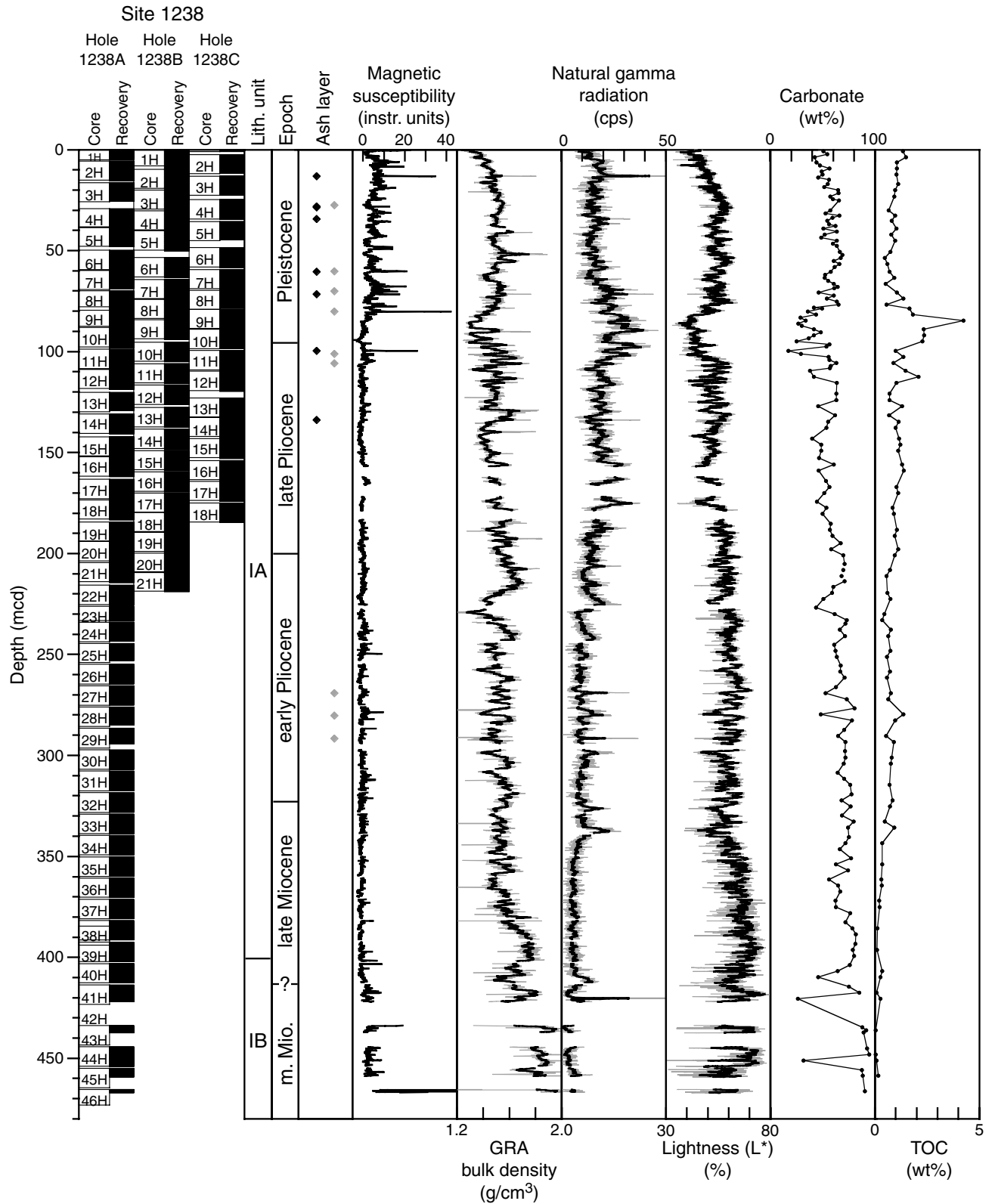


Figure F58. Seismic profile across Site 1239 (Lyle et al., 2000). Reflector numbers appear in boxes.

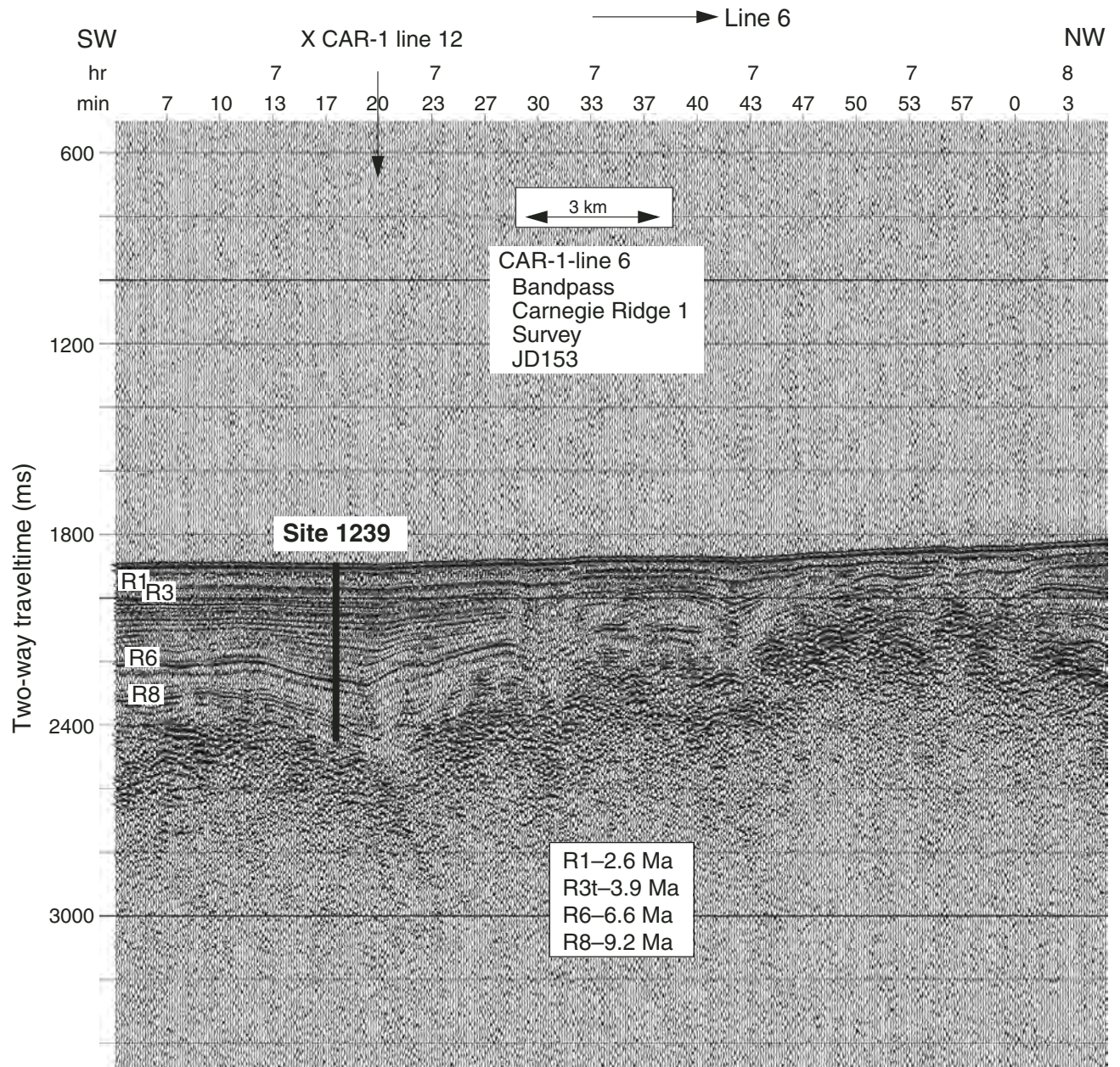


Figure F60. Swath bathymetry of a Panama Basin segment, including Site 1240 (Mix et al., 2000).

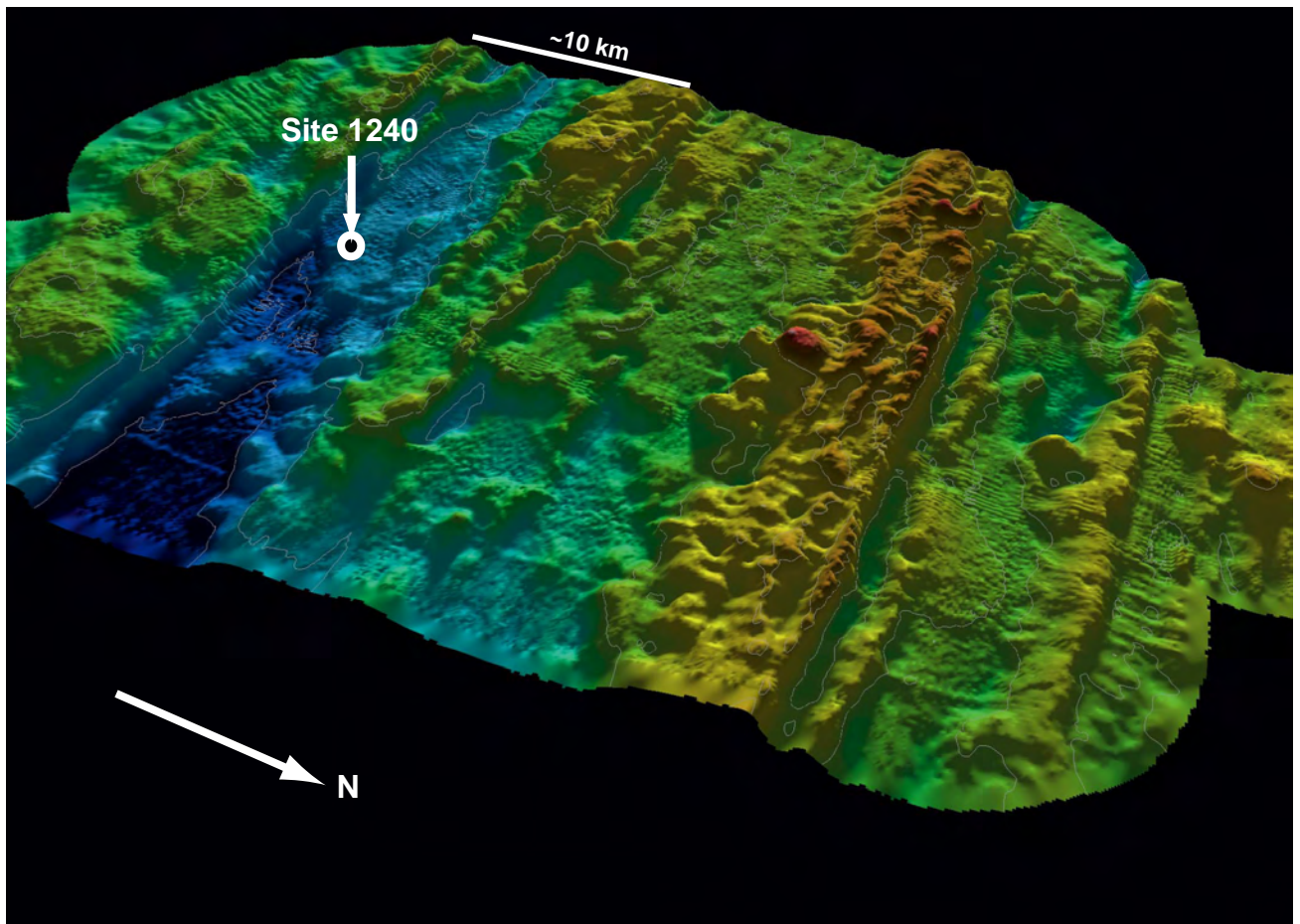


Figure F61. Seismic profile across Site 1240 (Lyle et al., 2000).

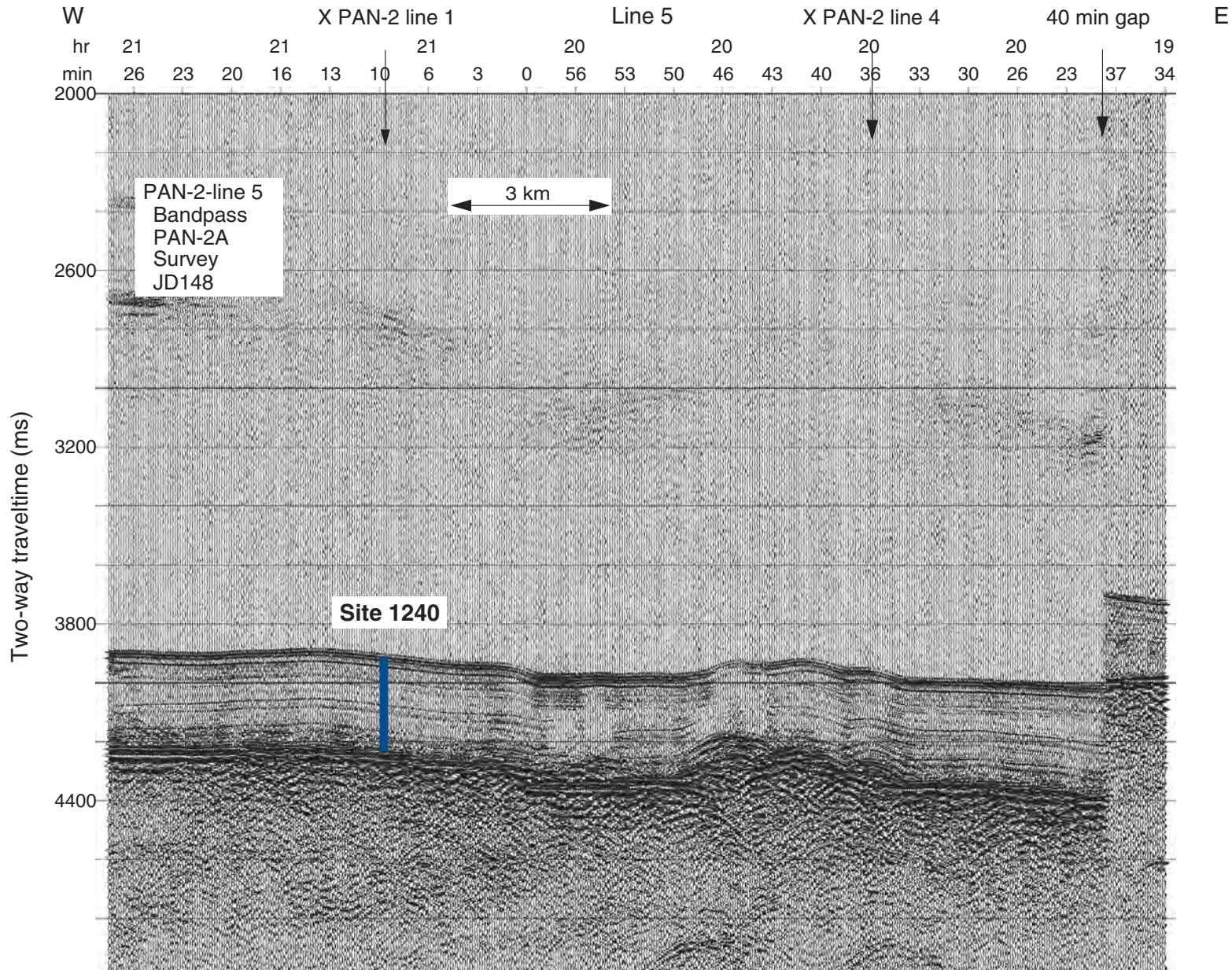


Figure F62. Lithology and physical and chemical data, Site 1240. GRA = gamma ray attenuation, V_p = P -wave velocity, TOC = total organic carbon.

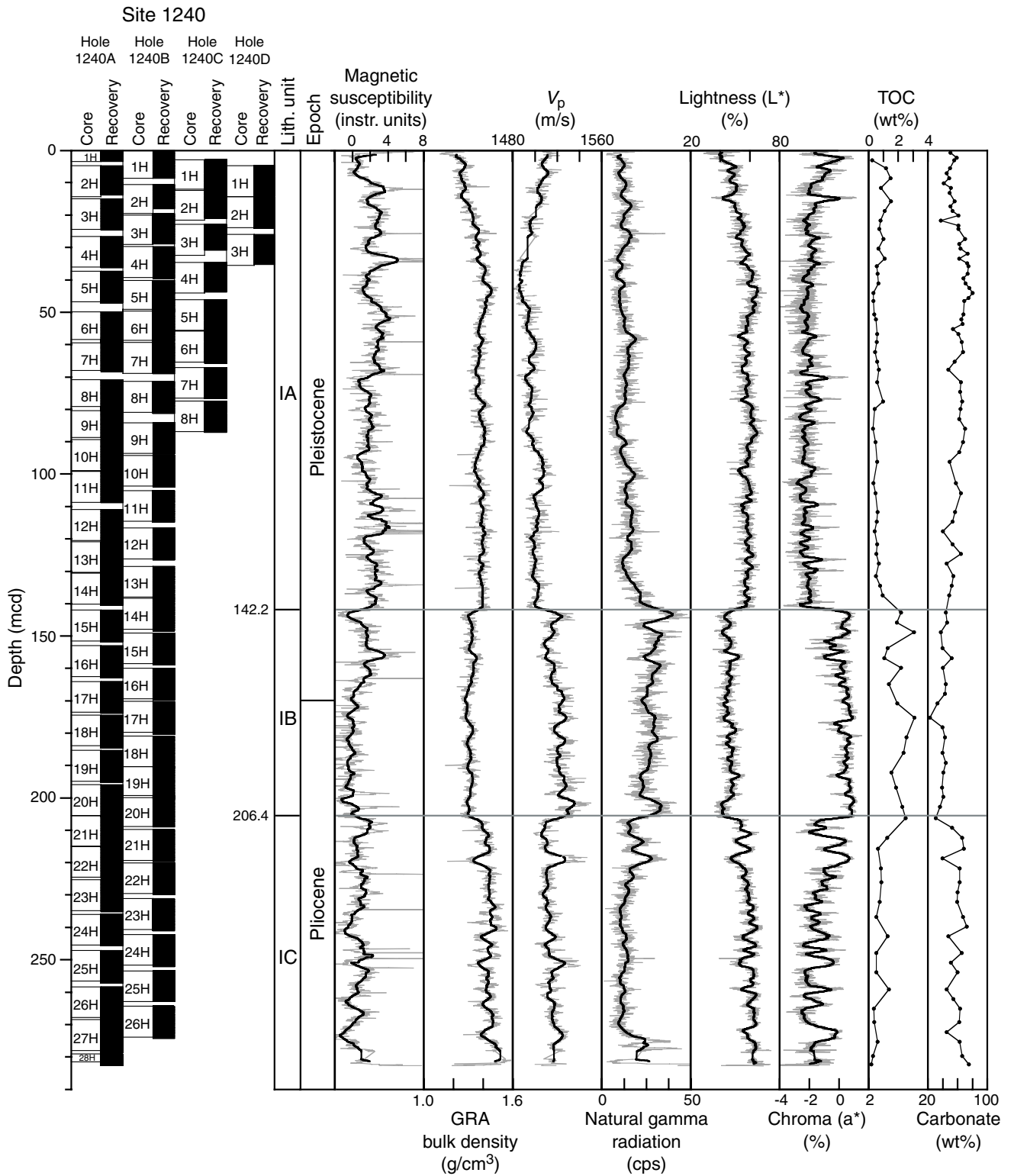


Figure F63. Seismic profile across Site 1241 (Lyle et al., 2000).

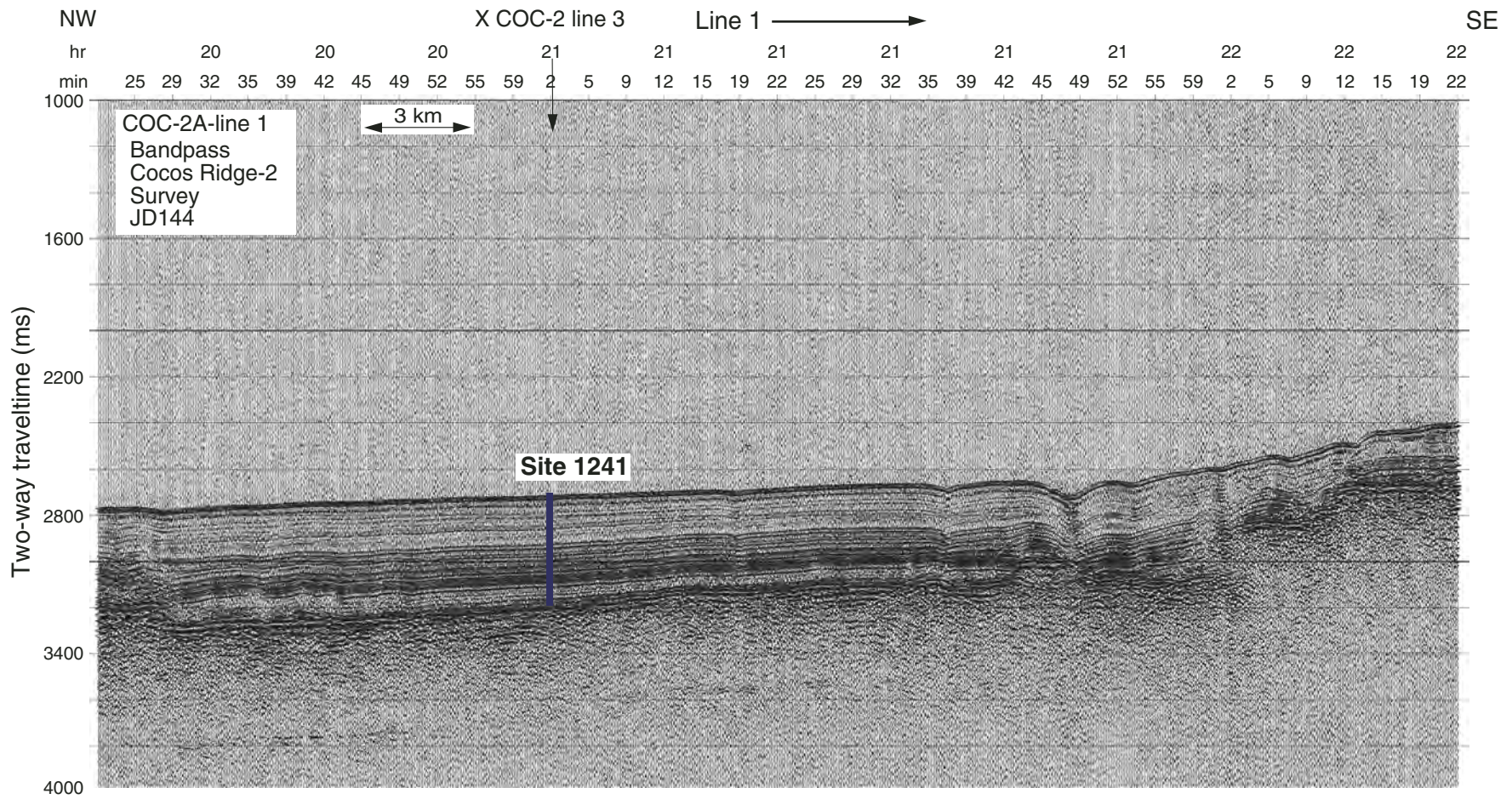


Figure F64. Lithology and physical and chemical data, Site 1241. GRA = gamma ray attenuation, TOC = total organic carbon.

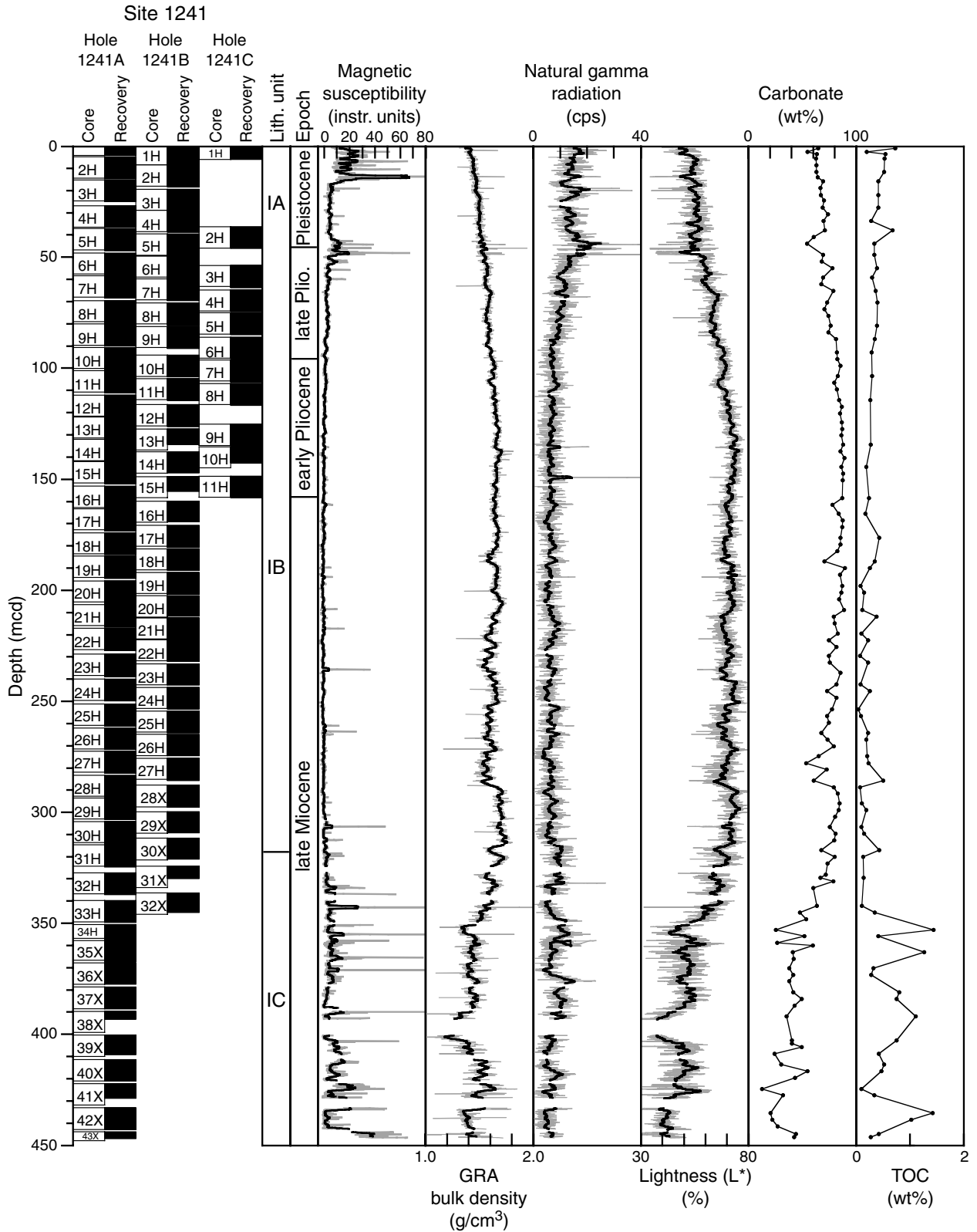


Figure F65. Seismic profile across Site 1242 (Lyle et al., 2000).

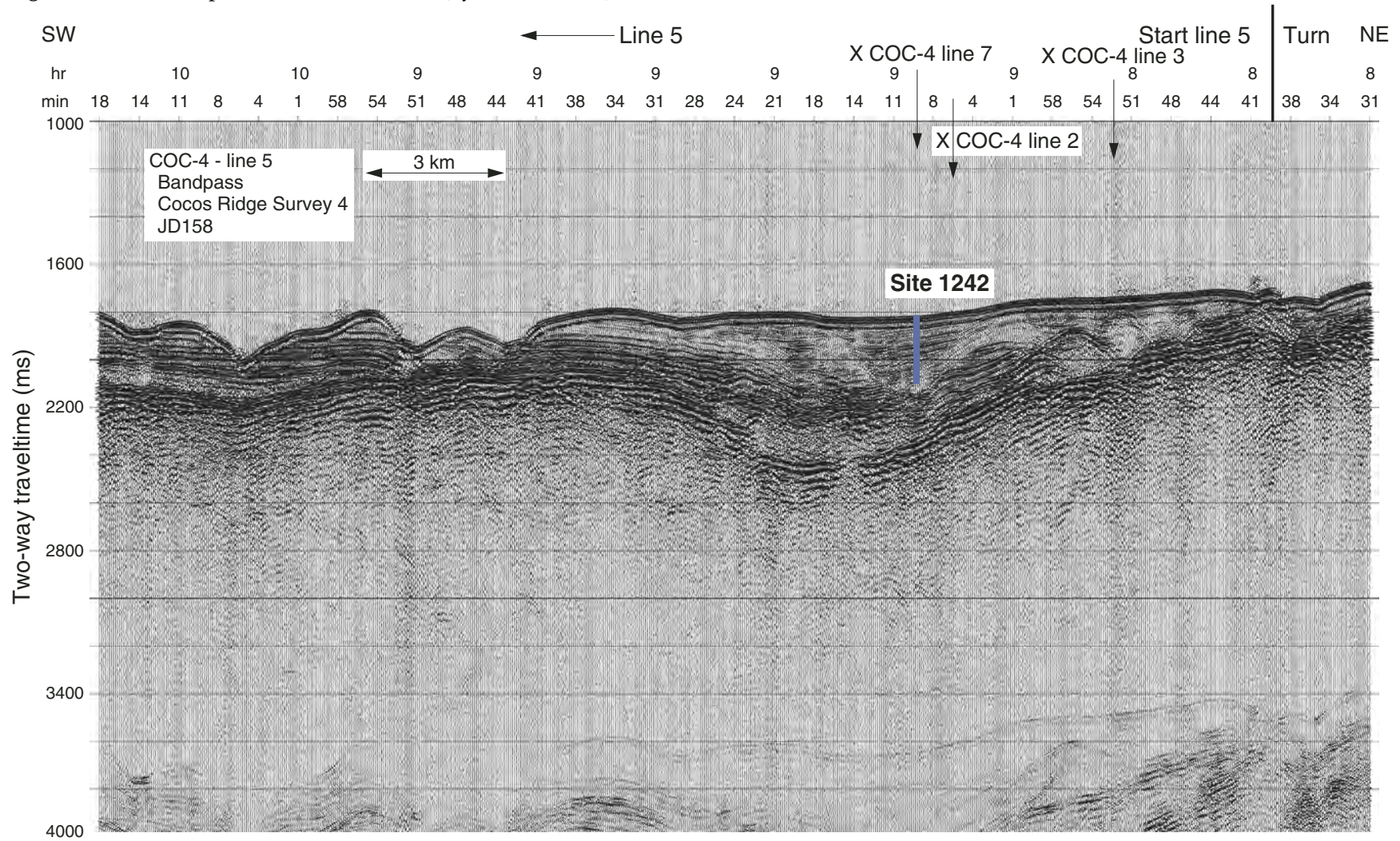


Figure F66. Lithology and physical and chemical data, Site 1242. GRA = gamma ray attenuation.

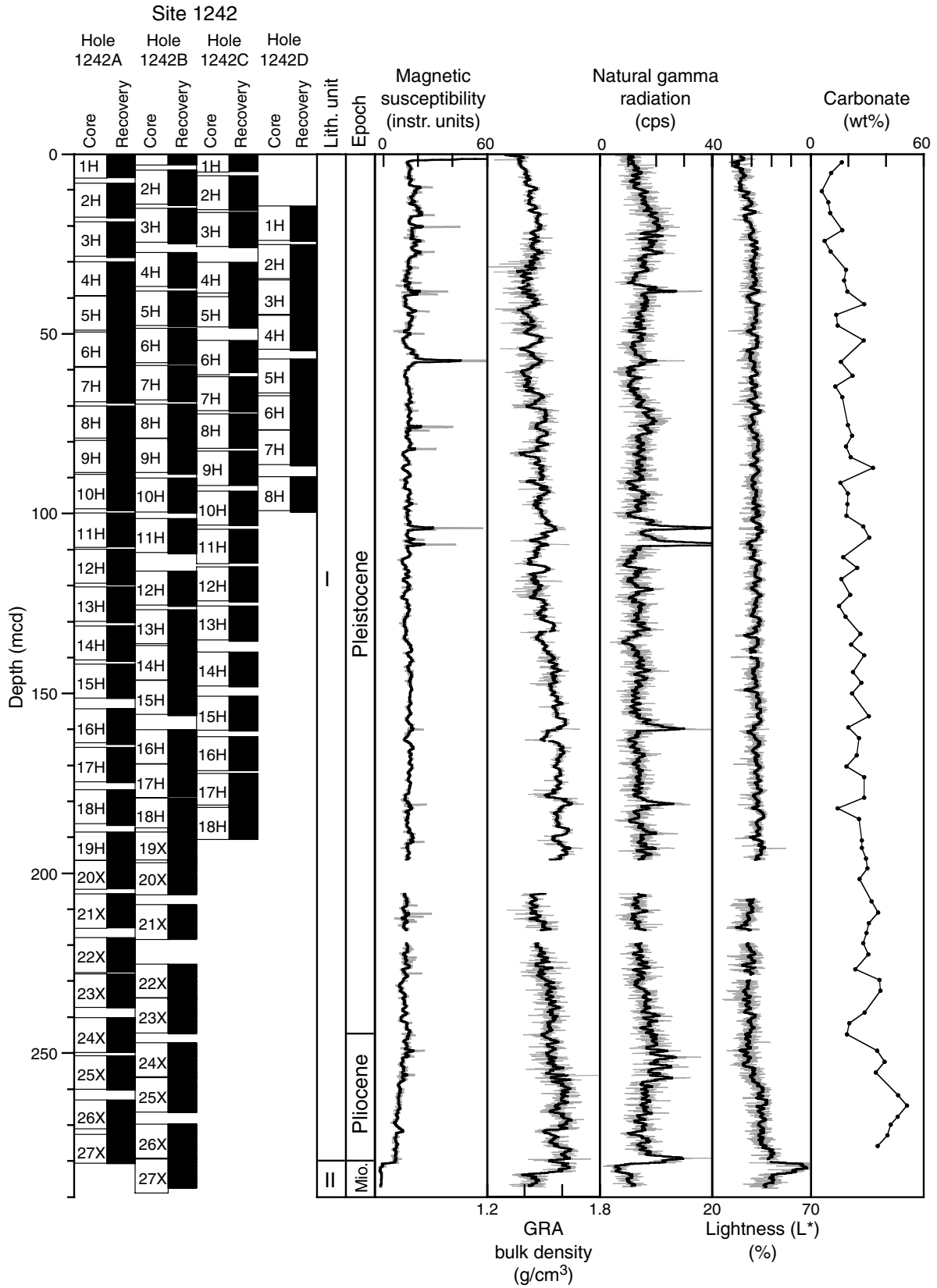


Table T1. Leg 202 coring summary by site.

Site	Number of holes	Average latitude	Average longitude	Average water depth (m)	Maximum penetration (mbsf)	Interval cored (m)	Sum of core recovered (m)	Core recovered (%)	Time on site (days)
1232	3	39°53.45'S	75°54.08'W	4072	371.3	494.6	416.75	84	4.52
1233	5	41°0.01'S	74°26.99'W	838	116.3	411.0	422.23	103	1.76
1234	3	36°13.15'S	73°40.90'W	1015	205.2	461.6	435.15	94	1.67
1235	3	36°9.59'S	73°33.98'W	489	181.3	509.5	513.42	101	1.80
1236	3	21°21.54'S	81°26.17'W	1323	207.7	495.0	490.07	99	2.64
1237	4	16°0.42'S	76°22.69'W	3212	317.4	744.7	771.05	104	5.28
1238	3	1°52.31'S	82°46.93'W	2203	430.6	791.1	787.12	99	4.67
1239	3	0°40.32'S	82°4.86'W	1414	515.4	1026.1	1042.07	102	4.27
1240	4	0°01.31'N	86°27.76'W	2921	253.0	603.7	622.54	103	3.34
1241	3	5°50.57'N	86°26.68'W	2027	395.0	799.0	810.14	101	4.67
1242	4	7°51.35'N	83°36.42'W	1364	256.0	743.8	770.45	104	2.83
Total:						7080.1	7080.99	100	

Table T2. Leg 202 coring summary by hole.

Site	Hole	Latitude	Longitude	Water depth (m)	Penetration (mbsf)	Interval cored (m)	Core recovered (m)	Core recovered (%)	APC cores	XCB cores	Time on site (days)
1232	A	39°53.470'S	75°54.082'W	4078.6	371.3	371.3	288.77	78	12	27	4.52
	B	39°53.453'S	75°54.079'W	4069.5	90.1	90.1	96.30	107	10		
	C	39°53.440'S	75°54.082'W	4068.9	33.2	33.2	31.68	95	4		
1232 totals:	3 holes	39°53.45'S	75°54.08'W	4072.3	371.3	494.6	416.75	84	26	27	
1233	A	41°0.001'S	74°26.998'W	837.5	12.0	9.5	9.94	105	1		1.76
	B	41°0.001'S	74°26.998'W	837.5	109.5	100.0	102.01	102	11		
	C	41°0.003'S	74°26.992'W	837.7	116.3	116.3	121.75	105	13		
	D	41°0.009'S	74°26.991'W	839.2	112.3	110.3	114.88	104	13		
	E	41°0.013'S	74°26.983'W	838.1	101.5	74.9	73.65	98	8		
1233 totals:	5 holes	41°0.01'S	74°26.99'W	838.0	116.3	411.0	422.23	103	46	0	
1234	A	36°13.153'S	73°40.909'W	1015.6	205.2	205.2	189.02	92	11	11	1.67
	B	36°13.150'S	73°40.904'W	1014.0	182.4	182.4	169.71	94	10	9	
	C	36°13.156'S	73°40.894'W	1014.4	79.1	76.0	76.42	101	8		
1234 totals:	3 holes	36°13.15'S	73°40.90'W	1014.7	205.2	461.6	435.15	94	29	20	
1235	A	36°09.591'S	73°33.990'W	489.7	181.3	181.3	182.78	101	20		1.80
	B	36°09.592'S	73°33.983'W	488.5	176.2	176.2	178.81	101	19		
	C	36°09.599'S	73°33.976'W	488.5	152.5	152.0	151.83	100	16		
1235 totals:	3 holes	36°9.59'S	73°33.98'W	488.9	181.3	509.5	513.42	101	55	0	
1236	A	21°21.539'S	81°26.160'W	1323.7	207.7	207.7	197.23	95	20	4	2.64
	B	21°21.541'S	81°26.165'W	1322.5	122.8	122.8	125.10	102	13		
	C	21°21.538'S	81°26.170'W	1322.5	167.3	164.5	167.74	102	18		
1236 totals:	3 holes	21°21.54'S	81°26.17'W	1322.9	207.7	495.0	490.07	99	51	4	
1237	A	16°0.420'S	76°22.680'W	3212.7	10.5	9.5	9.95	105	1		5.28
	B	16°0.421'S	76°22.681'W	3212.7	317.4	317.4	331.35	104	34		
	C	16°0.422'S	76°22.685'W	3211.9	315.3	313.3	323.70	103	33		
	D	16°0.421'S	76°22.693'W	3211.9	253.0	104.5	106.05	101	11		
1237 totals:	4 holes	16°0.42'S	76°22.69'W	3212.3	317.4	744.7	771.05	104	79	0	
1238	A	1°52.310'S	82°46.939'W	2202.2	430.6	430.6	409.77	95	22	24	4.67
	B	1°52.310'S	82°46.934'W	2202.2	201.0	198.0	209.50	106	21		
	C	1°52.310'S	82°46.928'W	2203.2	167.5	162.5	167.85	103	18		
1238 totals:	3 holes	1°52.31'S	82°46.93'W	2202.5	430.6	791.1	787.12	99	61	24	
1239	A	0°40.320'S	82°04.850'W	1414.7	515.4	515.4	515.10	100	19	36	4.27
	B	0°40.321'S	82°04.860'W	1413.3	398.7	396.7	407.32	103	18	24	
	C	0°40.320'S	82°04.870'W	1413.3	117.3	114.0	119.65	105	12		
1239 totals:	3 holes	0°40.32'S	82°4.86'W	1413.8	515.4	1026.1	1042.07	102	49	60	
1240	A	0°01.311'N	82°27.750'W	2922.4	253.0	253.0	264.03	104	28		3.34
	B	0°01.311'N	82°27.756'W	2920.2	248.2	246.2	254.80	103	26		
	C	0°01.311'N	82°27.760'W	2920.2	80.2	76.0	75.30	99	8		
	D	0°01.311'N	82°27.766'W	2920.2	31.7	28.5	28.41	100	3		
1240 totals:	4 holes	0°01.31'N	86°27.76'W	2920.7	253.0	603.7	622.54	103	65	0	
1241	A	5°50.570'N	86°26.670'W	2027.3	394.4	394.4	404.86	103	34	9	4.67
	B	5°50.570'N	86°26.681'W	2025.8	395.0	303.6	302.23	100	27	5	
	C	5°50.570'N	86°26.692'W	2027.2	143.5	101.0	103.05	102	11		
1241 totals:	3 holes	5°50.57'N	86°26.68'W	2026.8	395.0	799.0	810.14	101	72	14	
1242	A	7°51.352'N	83°36.402'W	1363.4	250.8	250.8	260.11	104	19	8	2.83
	B	7°51.353'N	83°36.413'W	1365.2	256.0	250.5	259.24	103	18	9	
	C	7°51.352'N	83°36.424'W	1363.1	172.0	166.5	170.95	103	18		
	D	7°51.353'N	83°36.435'W	1363.1	91.5	76.0	80.15	105	8		
1242 totals:	4 holes	7°51.35'N	83°36.42'W	1363.7	256.0	743.8	770.45	104	63	17	

Note: APC = advanced piston corer, XCB = extended core barrel.

Table T3. Summary of APC drilling over.

Hole	Depth of first excess force (mbsf)	Maximum APC penetration (mbsf)	Added APC penetration by overdrilling (%)	Reason for APC termination	Number of overdrilled APC barrels	APC cores	XCB cores	Total penetration (mbsf)
1232A	103	112.5	9	B2	2	12	27	371.3
1232B				A2		10		90.1
1232C				A2		4		33.2
1233A				A1		1		12.0
1233B				A1		11		109.5
1233C				A1		13		116.3
1233D				A1		13		112.3
1233E				A1		8		101.5
1234A				B1		11	11	205.2
1234B				B1		10	9	182.4
1234C				A2		8		79.1
1235A				B1		20		181.3
1235B				B1		19		176.2
1235C				A2		16		152.5
1236A				A2		20	4	207.7
1236B				C		13		122.8
1236C	154.8	167.3	8	A2	1	18		167.3
1237A				A2		1		10.5
1237B	148	317.4	114	B1	16	34		317.4
1237C	163.3	315.3	93	B1	15	33		315.3
1237D	234	253	8	A2	3	11		253.0
1238A	90.5	204.5	126	B1	10	22	24	430.6
1238B	87	201	131	B1	8	21		201.0
1238C	139	167.5	21	A2	3	18		167.5
1239A	88.9	174.4	96	B2	6	19	36	515.4
1239B	152.3	171.3	12	B2	3	18	24	398.7
1239C				A2		12		117.3
1240A	174.5	253	45	B1	6	28		253.0
1240B	162.7	248.2	53	B1	8	26		248.2
1240C				A2		8		80.2
1240D				A2		3		31.7
1241A	184.4	314.2	70	B1	13	34	9	394.4
1241B	200.4	259.4	29	B2	7	27	5	395.0
1241C				A2		11		143.5
1242A				B1		19	8	250.8
1242B				B1		18	9	256.0
1242C				A2		18		172.0
1242D				A2		8		91.5
Average* (%):			77					

Notes: APC = advanced piston corer, XCB = extended core barrel. Reason for APC termination: A1 = Pollution Prevention and Safety Panel approved depth is reached, A2 = mission accomplished, B1 = incomplete stroke is indicated, B2 = excessive pull out force >100 klb, C = mechanical. * = average from holes with APC refusal.

Table T4. Summary of Leg 202 geochemistry.

Region	Site	Water depth (m)	Sulfate concentration minimum (mM)	Depth (mcd)	Alkalinity concentration maximum (mM)	Depth (mcd)	Phosphate concentration maximum (μM)	Depth (mcd)	Ammonium concentration maximum (mM)	Depth (mcd)	Methane concentration maximum (ppmv)	Shallowest depth (mcd)	Calcium concentration minimum (mM)	Depth (mcd)
Limited to no sulfate reduction														
Nazca Ridge	1236	1323	<26	170–191	2.2	—	2	3	<0.005	—	BDL		Increases with depth	
	1237	3212	<26	5–63	>5	9–20	9	5	>0.25	9–33	8	42–63		
Cocos Rise	1241	2027	Little depletion	—	>5	63–95	5	3	>0.4	53–106	13	189	Increases with depth	
Intermediate sulfate reduction														
Carnegie Ridge	1238	2203	<10	75	>17	83–93	>15	10–64	3	82–386	<100		6.1	54
Panama Basin*	1240	2921	<15	135–200	>17	147–190	>30	147–190	>2	147–200	57	147	<3.5	104–179
Complete sulfate reduction														
Chile Basin	1232	4072	<2	26	>30	26–159	>50	Throughout	>2	37	>10,000	>60	<6	27
Chile margin	1233	838	BDL	21	>60	21–44	>210	11–55	>5	11–77	High	23	<4	93–105
	1234	1015	BDL	10	>63	18–52	>120	10–52	>11	40–88	High	9	<2	5–11
	1235	489	BDL	20	>60	31–42	>200	20–42	>8	31–42	High	20	<2	10–112
Carnegie Ridge	1239	1414	BDL	71	>28	92–123	>20	61–113	>6	133–378	Moderate–high	100	5.5	20–109
Cocos Rise	1242	1364	BDL	23	>25	23–94	60	34	>7.5	94–170	High	35	2.5	71–82
														34

Notes: * = Site 1240 is influenced by fluid flow in the underlying basalt, and its geochemistry is discussed separately in the text as a consequence. BDL = below detection limit. Sulfate detection limit was typically 1 mM or lower.